NASA TECHNICAL
MEMORANDUM

NASA TMX-53389

OCTOBER 15, 1965

NASA TMX-53389

GPO PRICE $ _____

CFSTI PRICE(S) $ _____

Hard copy (HC) 4.00

Microfiche (MF) 1.00

ff 653 July 65

AERO-ASTRODYNAMICS RESEARCH REVIEW NO. 3

AERO-ASTRODYNAMICS LABORATORY
RESEARCH AND DEVELOPMENT OPERATIONS
GEORGE C. MARSHALL SPACE FLIGHT CENTER
HUNTSVILLE, ALABAMA

NASA - GEORGE C. MARSHALL SPACE FLIGHT CENTER

TECHNICAL MEMORANDUM X-53389

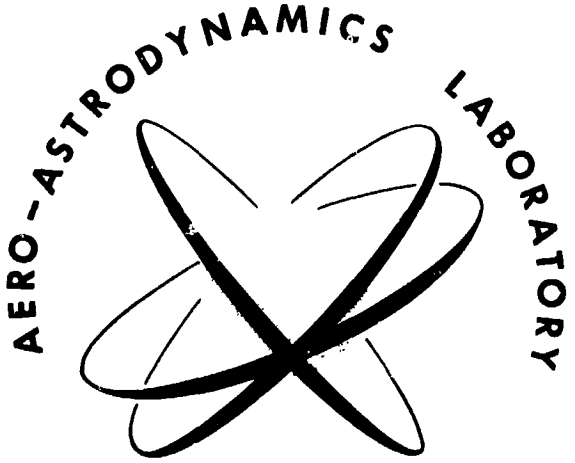

RESEARCH REVIEW NUMBER THREE

January 1, 1965 - June 30, 1965

RESEARCH AND DEVELOPMENT OPERATIONS
AERO-ASTRODYNAMICS LABORATORY

ACKNOWLEDGEMENTS

The articles for this review were contributed by various engineers and physicists of the Aero-Astrodynamics Laboratory, reviewed and compiled by William D. Murphree, and edited by Sarah Hightower.

Grateful acknowledgement is given to the Special Publications Section, Scientific and Technical Information Branch, Management Services Office, MSFC, for preparing the review.

PREFACE

The topics discussed in this third Aero-Astrodynamics Research Review cover a variety of subjects. Included are Acoustics, Aerodynamics, Base Heating, Control, Guidance, Instrumentation, Structural Dynamics, and Orbit Theory. Although many subjects are discussed, all areas of research which are conducted by this laboratory are not treated. Other subjects will be discussed in forthcoming reviews.

It is hoped that these reviews will be interesting and helpful to other organizations engaged in space flight research and related efforts. Criticisms of this review and discussions concerning individual papers with respective authors are invited.

E. D. GEISSLER
Director, Aero-Astrodynamics Laboratory

BLANK PAGE

CONTENTS...

CONTENTS (Continued)...

I. ACOUSTICS

SOUND PRESSURE ESTIMATIONS FROM A POINT DIRECTIONAL ACOUSTIC SOURCE RADIATING IN AN INHOMOGENEOUS MEDIUM

by

Jess H. Jones

SUMMARY

This report concerns a general expression that can be used to make estimates of sound pressures received from a rocket exhaust that radiates in an inhomogeneous medium. The concepts concerning acoustic wave propagation are combined with those having to do with a broad frequency band, directional acoustic source, etc.; in brief, rocket exhaust flow. The ray acoustics approach is used in this paper; there is no attempt to elaborate on the failure of the ray trace method to obtain pressure levels for special conditions. The ray trace technique is used only to describe the relationship between horizontal source-to-receiver distance and the angle of emergence of the sound ray.

LIST OF SYMBOLS

Symbol	Definition
A(f)	Power radiated per unit bandwidth from an equivalent monopole source
B	Area
D.I.	Directivity index
E_A	Attenuation factor
f	Frequency
Δf	Bandwidth
H	Height of ray tube cross section above source elevation
I	Intensity
M_F	Meteorological factor
OB SPL	Octave band sound pressure level
OB AL	Octave band power level
PSL	Pressure spectrum level
$\overline{P^2}/cps$	Space-time mean squared sound pressure per unit bandwidth
P_{ref}	Root mean squared reference sound pressure = 0.00002 newton/(meter)^2
ASL	Power spectrum level
r	Source-to-receiver distance
$S = \widetilde{P^2}/cps$	Time mean squared sound pressure per unit bandwidth
$\overline{SPL}$	Space average sound pressure level
SPL	Sound pressure level
r_o	Radius of source
X_s	Horizontal source-to-receiver distance
α	Azimuth angle of sound ray
β	Directivity angle of sound source
γ	Attenuation function
δ	Azimuth angle of exhaust axis
ζ	Elevation angle of exhaust axis
θ	Elevation angle of sound ray
ξ	Attenuation coefficient in nepers/meter
ϵ	Attenuation coefficient in decibels/meter
ρc	Specific acoustic impedance of the atmosphere
ϕ	Directivity function
ψ	Meteorological function
$\sum$	Summation of all rays arriving at a common location

SUBSCRIPTS

*	Homogeneous conditions
o	Conditions at source
h	Conditions at source for a homogeneous medium
R	Conditions at receiver

SUB-SUBSCRIPT

i	Rays leaving the source arriving at a common location

SECTION I. INTRODUCTION

The purpose of this report is to obtain a general expression which can be used to make engineering estimates of the far-field sound pressures received from a rocket exhaust acoustic source radiating in an inhomogeneous medium [1,2]. This will be accomplished by combining the concepts concerning acoustic wave propagation characteristics [3,4,5,6,7] with those concerning a broad frequency band, point, directional acoustic source, i.e., rocket exhaust flow [8,9].

This discussion will utilize the method of ray acoustics and will not attempt to elaborate on the failure of the race trace method in arriving at meaningful pressure levels for special conditions; i.e., unlimited value of the sound pressure at a focus and scattering of sound into a shadow zone, etc. These areas are important but they are considered as being beyond the scope of the original intent of this report. The ray trace technique will be used only to describe the relationship between the horizontal source-to-receiver distance, X_S, and the angle of emergence of the sound ray, θ_o, i.e., $X_S = f(\theta_o)$.

For the acoustic source in question, i.e., the rocket exhaust flow, the source-to-receiver distance is assumed to be large such that the locally distributed rocket exhaust (acoustic) source appears as a point. Further, the source will be considered as fixed in space and will exhibit highly directional pressure distribution characteristics.

SECTION II. HOMOGENEOUS SOUND PRESSURE EQUATION

Under the ideal conditions of a homogeneous atmosphere, the expression relating the sound pressure to the acoustic source can be derived with little difficulty [9,10]. The resultant equation presented here for a point, directional source radiating in a half space (including atmospheric absorption) is

$$S_* (f,\beta,r) = \frac{\rho c\, A(f)\, \phi(f,\beta)_{\theta_h}}{2\pi\, r^2\, \gamma(f,r)} . \qquad (1)$$

The directivity function $\phi(f,\beta)$ describes the angular deviation of the radiation pattern of the actual rocket source from an equivalent monopole acoustic source $A(f)$. This function modifies the simple monopole source radiation pattern such that the result describes the complex radiation pattern of the rocket exhaust source. The directivity function is defined as

$$\phi(f,\beta) = \frac{\tilde{P}^2(f,\beta)_{r_1}}{\overline{P}^2(f)_{r_1}}$$

where $\tilde{P}^2(f,\beta)_{r_1}$ is assumed to be symmetrical about the rocket exhaust stream and for a given source frequency is a function only of the angle β (Fig. 1). This is evaluated at a far-field distance r_1 which is normally kept constant with respect to β. $\overline{P}^2(f)_{r_1}$ is the space-time mean squared pressure averaged over all space on the surface of a sphere of radius r_1 and consequently is independent of angular orientation. The space average mean squared pressure can be thought of as that due to an equivalent monopole source. For instance, for a monopole source the radiated energy, $\tilde{P}^2(f,\beta)$, is independent of β and the directivity function is therefore unity.

The attenuation function $\gamma(f,r)$ is normally expressed in exponential form and is defined here as $\gamma(f,r) = e^{2\xi(f)r}$, where $\xi(f)$ is the attenuation coefficient expressed in nepers/meters, which is assumed to be a function of frequency only and r is the source-to-receiver distance.

BLANK PAGE

Figure 1 delineates the coordinate system used and also provides an expression relating the directivity angle to the indicated angular functions.

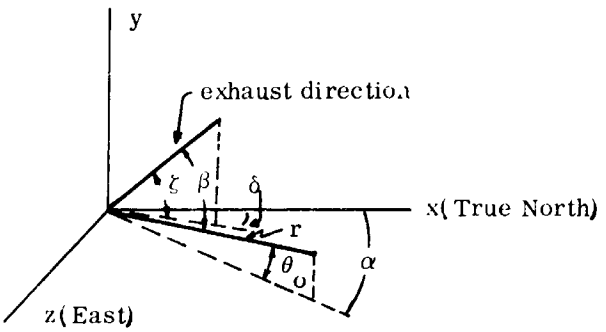

$$\cos\beta = \cos\zeta \cos\theta_o \cos(\alpha-\delta) - \sin\theta_o \sin\zeta$$

FIGURE 1. COORDINATE SYSTEM

Equation 1 provides a means of obtaining estimates of the mean squared sound pressure under homogeneous conditions. However, it is known that when the atmosphere departs from this ideal condition the mean squared sound pressures received at a remote location can vary greatly from the estimates computed by using equation 1. Consequently, a more general form of this expression is highly desirable.

SECTION III. EVALUATION OF THE METEROLOGICAL FUNCTION

It would be highly advantageous to compute independently the sound pressure or sound intensity due to the homogeneous condition and the additional increase or decrease in sound pressure due to the inhomogeneous condition. Using this concept, a meteorological function is defined which accounts for the departure of the atmospheric medium from homogeneous conditions and is given as

$$\psi = \frac{I}{I_*} \qquad (2)$$

where I_* is the sound intensity received under homogeneous conditions (obtained from equation 1 by noting that $I_* = S_*/\rho c$). I is the sound intensity received under inhomogeneous conditions.

A similar approach is followed by Brekhovskikh [3] in which ψ was initially defined as a "focusing factor" and restricted to values of $\psi > 1$. In general, ψ can take on all values. Values of ψ in the range $0 \leq \psi < 1$ indicate a condition which is analogous to a "divergence zone"; i.e., mean squared sound pressure is less than that under ideal conditions. Ideal conditions are achieved when $\psi = 1$.

To evaluate ψ, the sound intensity under inhomogeneous conditions needs to be investigated. This is accomplished by utilizing the concept of ray acoustics. Application of this ray trace procedure is valid if it is assumed that the changes in the properties of the atmosphere are small within a wavelength of the propagating acoustic energy. If this assumption is not satisfied, which is the case at a focus, a modification to the ray trace method is required.

By studying the deformation of a ray tube (Fig. 2)

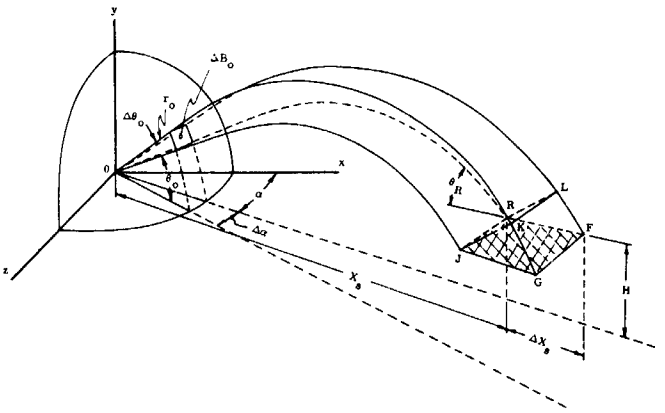

FIGURE 2. RAY TUBE

in an inhomogeneous medium, the intensity I can be evaluated at any point along the tube. For the purpose of this analysis, the ray tube will be confined to lie in the plane which is defined by the y axis and the azimuth angle α. The shaded area at point R, (RFGJ), is parallel to the x - z plane and is separated by a vertical distance H from the x - z plane. The angle θ_R is defined as the acute angle formed by the intersection of the perpendicular to the plane JKLR at R and the plane FGJR.

The area of the wave front contained within the ray tube at R is

$$\Delta B_R = (RJ)(LR)$$

where

$$RJ \cong X_s \Delta\alpha$$

$$LR = RF \sin\theta_R$$

$$LR = \Delta X_s \sin\theta_R .$$

The variable, X_s, is the horizontal source-to-receiver distance of the ray tube and can be expressed as a function of the initial angle, θ_o, of the emerging ray, i.e., $X_s = f(\theta_o)$. When this is done LR can be written as

$$LR = \left(\frac{\partial X_s}{\partial \theta}\right)_{\theta_o} \Delta\theta_o \sin\theta_R .$$

The cross-sectional area of the ray tube at R is then

$$\Delta B_R = X_s \Delta\alpha \left|\left(\frac{\partial X_s}{\partial \theta}\right)_{\theta_o}\right| \Delta\theta_o \sin\theta_R \qquad (3)$$

where the absolute value signs restrict the equation to positive areas or positive energy flux through ΔB_R.

The power radiated by the source through the initial surface area is

$$\Delta A = I_o \Delta B_o$$

where

$$\Delta B_o = (r_o \cos\theta_o \Delta\alpha)(r_o \Delta\theta_o)$$
$$= r^2 \Delta\theta_o \Delta\alpha \cos\vartheta_o$$

and

$$I_o = A(f)\ \phi(f,\beta)_{\theta_o} / 2\pi r_o^2 .$$

(I_o is the intensity of the source of radius r_o.)

The power through ΔB_o becomes

$$\Delta A = A(f)\ \phi(f,\beta)_{\theta_o} \left\{\Delta\theta_o \Delta\alpha \cos\theta_o\right\} / 2\pi . \qquad (4)$$

By accounting for the molecular absorption losses, and assuming that the actual arc length of the ray tube is approximately equal to the horizontal source-to-receiver distance X_s and redistributing the power ΔA at R, the acoustic intensity I at point R becomes

$$I = \frac{\Delta A}{\Delta B_R} = \frac{A(f)\ \phi(f,\beta)_{\theta_o} \cos\theta_o}{2\pi X_s\ \gamma(f,X_s) \left|\left(\frac{\partial X_s}{\partial \theta}\right)_{\theta_o}\right|} \sin\theta_R \qquad (5)$$

For homogeneous conditions, I_*, from equation 1, at point R is

$$I_* = \frac{A(f)\ \phi(f,\beta)_{\theta_h}}{2\pi r^2 \gamma(f,r)} \qquad (6)$$

where $\phi(f,\beta)$ is now evaluated at θ_h with θ_h being defined as $\tan^{-1}\left(\frac{H}{X_s}\right)$ and r is the straight line distance OR from source to receiver.

$$\psi = \frac{I}{I_*} = \left\{\frac{\cos\theta_o\ r^2}{X_s \left|\left(\frac{\partial X_s}{\partial \theta}\right)_{\theta_o}\right|} \sin\theta_R\right\} \left\{\frac{\phi(f,\beta)_{\theta_o}}{\phi(f,\beta)_{\theta_h}}\right\} \qquad (7)$$

The above equation is a completely general expression for ψ and it is valid as long as the fundamental assumption of ray acoustics is satisfied. If it is assumed, as in normal practice [5], that the return angle of the ray, θ_R, is approximately the same as the emerging angle of the ray, θ_o, and that $r >> H$, i.e., $r \approx X_s$, then equation 7 reduces to

$$\psi(f,\alpha,\theta_o,X_s) = X_s \left|\left(\frac{\partial\theta}{\partial X_s}\right)_{\theta_o}\right| \left(\cot\theta_o\right) \left\{\frac{\phi(f,\beta)_{\theta_o}}{\phi(f,\beta)_{\theta_h}}\right\} . \qquad (8)$$

Combining equations 1, 2, and 8, while remembering that $r \approx X_s$, yields

$$S(f,\alpha,\theta_o,X_s) = \left\{\frac{\rho c\ A(f)\ \phi(f,\beta)_{\theta_h}}{2\pi X_s^2\ \gamma(f,X_s)}\right\} \psi(f,\alpha,\theta_o,X_s) \qquad (9)$$

where $S(f,\alpha,\theta_o,X_s)$ is the mean squared sound pressure that is received at a remote location from a point, directional, acoustic source radiating in an inhomogeneous medium. For a nondirectional source, equation 9 can be shown to be identical to the results presented in [1,2].

In examining equation 9, it can be seen that the sound pressure is a function of the initial angle θ_o. This implies that it is the sound pressure associated with an individual ray. To arrive at the true sound pressure, all rays arriving at a common location should be combined. This will be shown in the following paragraphs.

As stated previously

$$X_s = f(\theta_o) . \qquad (10)$$

This expression is normally evaluated by considering that the variation in the propagation velocity of sound,

i.e., the thermodynamic speed of sound plus the wind component, is a function of altitude only. Following along this same line, and using the hypothesis of a layered medium, a typical plot of $X_s = f(\theta_o)$ for a given α, is shown in Figure 3. The discontinuities in Figure 3 are due to the common hypothesis of a layered medium [5, 6] with abrupt changes in the propagation characteristics between the layers.

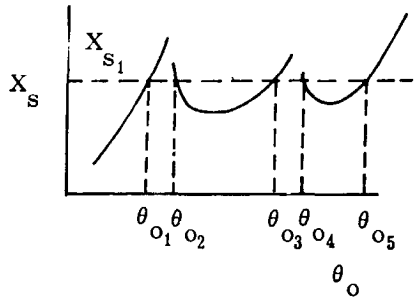

FIGURE 3. SOURCE TO RECEIVER DISTANCE VERSUS EMERGING ANGLE

It can be seen from Figure 3, that for the indicated horizontal source-to-receiver distance, X_s, there will be five rays with initial angles of θ_{o_1}, θ_{o_2} ... θ_{o_5} returning. In theory each ray has an associated mean squared sound pressure and therefore these rays have to be combined to arrive at the resultant mean squared sound pressure. If the pressures from each incoming ray are assumed to be uncorrelated, then the mean squared pressure associated with each ray, with each ray, rather than the instantaneous pressure, will add directly, and equation 2 can then be written as

$$S(f,\alpha,X_s) = \frac{\rho c\, A(f)\, \phi(f,\beta)_{\theta_h}}{2\pi X_s^2\, \gamma(f,X_s)} \sum_{i=1}^{n} \psi(f,\alpha,\theta_{o_i},X_s) \quad (11)$$

where

$\psi(f,\alpha,\theta_{o_i},X_s)$ is given by equation 8 and the symbol $\sum$ implies a summation of all the rays arriving at a common landing distance, i.e., receiver. The summation in equation 11 is defined here, however, to include only "direct" returned rays and not any "reflected" returned rays. With the aid of equation 11, the expected mean squared pressure per unit bandwidth, $\tilde{P}^2$/cps, received at any far-field location from a broad band, point, directional, acoustic source radiating into an inhomogeneous atmospheric medium can be computed.

As noted previously, when the changes in the properties of the atmosphere within a wavelength of the energy under consideration can no longer be considered as negligible, other means of arriving at the mean squared sound pressure have to be employed. This is readily apparent upon examining equation 8 because $\left(\frac{\partial \theta}{\partial X_s}\right)_{\theta_o}$ increases without bond. This does not imply an infinite intensity, but rather that the fundamental assumption of ray acoustics has been violated [2]. The point at which $\left(\frac{\partial X_s}{\partial \theta}\right) = o$, i.e., $\psi(f,\alpha,\theta_{o_i},X_s) = \infty$, is defined as a focus and requires a treatment similar to that presented by Brekhovskikh [3] to obtain an estimate of the pressure field. Likewise, areas in which no ray can be returned is a fundamental fault of the ray trace method [2] and does not imply zero pressure field. These areas are called shadow zones, and sound will be propagated into these areas because of diffraction effects [11, 12].

SECTION IV. INHOMOGENEOUS SOUND PRESSURE EQUATION IN SOUND PRESSURE LEVEL FORM

Sound pressures in acoustics are normally specified in decibel form, i.e., sound pressure level. The sound pressure level is defined as

$$SPL = 20 \log_{10}\left(\frac{\sqrt{\tilde{P}^2}}{P_{ref}}\right) \quad dB \quad (12)$$

where $\sqrt{\tilde{P}^2}$ is the time root mean squared pressure and P_{ref} is the root mean squared reference pressure which is 0.00002 newton/(meter)^2. Equation 12 can also be written as

$$SPL = 10 \log_{10}\left(\frac{\tilde{P}^2}{P_{ref}^2}\right) \quad dB \ . \quad (13)$$

Dividing equation 11 by the reference pressure squared, i.e., (P^2_{ref}), and using the relationship in equation 13, equation 11 becomes the sound pressure spectrum level, or pressure spectrum level, (PSL), in decibels,

$$PSL(f,\alpha,X_s) = 10\log_{10}\left[\left(\frac{\rho c\, A(f)\, \phi(f,\beta)_{\theta_h}}{2\pi X_s^2 P_o^2 \gamma(f,X_s)}\right)\left(\sum_{i=1}^{n} \psi(f,\alpha,\theta_{o_i},X_s)\right)\right]^S \text{ dB} \quad (14)$$

Equation 13 can be expressed in its standard form as follows:

$$PSL(f,\alpha,X_s) = 10\log_{10}\left(\frac{A(f)}{P_o^2/\rho c}\right) + 10\log_{10}\phi(f,\beta)_{\theta_h} - 10\log_{10}(2\pi X_s^2) - 10\log_{10}\gamma(f,X_s) + 10\log_{10}\left[\sum_{i=1}^{n} \psi(f,\alpha,\theta_{o_i},X_s)\right] \text{ dB} \quad (15)$$

Using the units of newtons, meters, and seconds, the ratio $\frac{P_{ref}^2}{\rho c}$ for standard sea level conditions is $\approx 10^{-12}$ watts, which is the standard power reference when the SI system is used. The first term in equation 15 then becomes the sound power spectrum level of the source, i.e., ASL (f) in dB.

From the ideas presented in Section II, the directivity function, now called the directivity index, is

$$D.I.\ (f,\beta)_{\theta_h} = 10\log_{10}\left(\frac{\tilde{P}^2(f,\beta)_{\theta_h}}{\bar{P}^2(f)}\right) \text{ dB} \quad (16)$$

which is also equal to

$$D.I.\ (f,\beta)_{\theta_h} = SPL\ (f,\beta)_{\theta_h} - \overline{SPL}\ (f) \text{ dB} \quad (17)$$

where $\overline{SPL}$ (f) is called the space average sound pressure level.

Similarly, from Section II, the attenuation function, now called the attenuation factor, becomes

$$E_{A(f,r)} = 10\log_{10}\gamma(f,r) = 10\log_{10} e^{2\xi(f)r}. \quad (18)$$

By further reduction and noting the relationship between nepers and decibels and also the fact that $r \approx X_s$, the above becomes

$$E_{A(f,X_s)} = \epsilon\,(f)\, X_s \text{ dB} \quad (19)$$

where ϵ (f) is now the attenuation coefficient in dB/meter and X_s is the horizontal source to receiver distance in meters.

The last term in equation 15 is called the "meteorological factor" and is

$$M_F(f,\alpha,X_s) = 10\log_{10}\left[\sum_{i=1}^{n} \psi(f,\alpha,\theta_{o_i},X_s)\right] \text{ dB}. \quad (20)$$

Equation 15 now becomes

$$PSL(f,\alpha,X_s) = ASL(f) + D.I.\ (f,\beta)_{\theta_h} - 20\log_{10} X_s - E_A(f,X_s) + M_F(f,\alpha,X_s) - 8 \text{ dB}. \quad (21)$$

Due to the broad band frequency characteristics of the source, pressure spectrums in sound pressure level form normally have associated bandwidth characteristics.

In the case of far-field acoustics, the bandwidth associated with the pressure spectrums are usually octave bandwidths. Equation 21 is related to an octave bandwidth analysis as follows

$$PSL(f,\alpha,X_s) + 10\log_{10}\Delta f = O.B.\ SPL(f,\alpha,X_s) \text{ dB} \quad (22)$$

where $\Delta f = 0.707\, f_c$, with f_c being the center frequency of the octave band of interest. Equation 21 then becomes

$$O.B.\ SPL(f,\alpha,X_s) = O.B.\ AL(f) + D.I.\ (f,\beta)_{\theta_h} - 20\log_{10} X_s - E_A(f,X_s) + M_F(f,\alpha,X_s) - 8 \text{ dB} \quad (23)$$

where

$$O.B.\ AL(f) = ASL(f) + 10\log_{10}\Delta f \text{ dB}.$$

Equation 23 is then the standard form in which t' far-field sound pressure level prediction equation is normally presented.

SECTION V. DISCUSSION OF THE FAR-FIELD SOUND PRESSURE LEVEL EQUATION

In "rocket engine generated acoustics," the standard or conventional form of the equation that is used to obtain an estimate of the sound pressure level, in decibel (dB), at a remote far-field location resulting from the operation of a rocket engine, is that which is presented by equation 23. Combining equations 8, 20, and 23 this equation is again presented here and is

$$\text{O. B. SPL}(f,\alpha,X_s) = \text{O. B. AL}(f) + \text{D. I.}(f,\beta)_{\theta_h} - 20\log_{10} X_s - E_A(f,X_s) - 8$$

$$\text{O. B. SPL}(f,\alpha,X_s) = \text{O. B. AL}(f) + \text{D. I.}(f,\beta)_{\theta_h} - 20\log_{10} X_s - E_A(f,X_s) - 8 + 10\log_{10}\left[\sum_{i=1}^{n}\left\{X_s\left|\left(\frac{\partial\theta}{\partial X_s}\right)_{\theta_{o_i}}\right|\left(\cot\theta_{o_i}\right)\left(\frac{\Phi(f,\beta)_{\theta_{o_i}}}{\Phi(f,\beta)_{\theta_h}}\right)\right\}\right] \text{ dB.} \quad (24)$$

In examining equation 24, it can be seen that the first five terms on the right side of the equation can be combined to yield the octave band sound pressure level that is observed under the ideal conditions of a homogeneous atmosphere, i.e. O. B. SPL $(f, \alpha, X_s)_*$.

Equation 24 can therefore be written as

$$\text{O. B. SPL}(f,\alpha,X_s) = \text{O. B. SPL}(f,\alpha,X_s)_* + M_F(f,\alpha,X_s) \text{ dB.} \quad (25)$$

From the above, it is obvious that the "meteorological factor," i.e., $M_F(f,\alpha,X_s)$, describes the effects of the inhomogeneity of the atmosphere on the received O. B. SPL. This term in essence "calibrates" the atmosphere. The unfortunate part, however, is that the M_F term is a function of the directional characteristics of the source under consideration.

If a nondirectional source is considered, the meteorological factor becomes independent of the source characteristics (eq. 24), and is in turn solely a function of the sound propagation velocity. For this case, the meteorological factor could be evaluated for many different types of atmospheric conditions without having any prior knowledge of the characteristics of the source.

A nondirectional source rarely ever exists in actual practice. However, if the directivity ratio in the meteorological factor of equation 24 is made to b unity, this would make the M_F independent of any source characteristics and would allow M_F to be evaluated solely in terms of the existing atmospheric conditions. The amount of error introduced in the computed O. B. SPL, by making the directivity ratio unity, is not presently known. This idea will be investigated and if the errors are small, then it would seem logical to evaluate M_F for many different recurring atmospheric conditions [13].

In any event, equation 24 can be used in its existing form to obtain engineering estimates of the sound pressure level received at a remote far-field location from a broad band, point, directional, acoustic source radiating into an inhomogeneous medium.

SECTION VI. CONCLUSIONS

From the ideas concerning acoustic source characteristics and ray acoustics discussed thus far, an expression has been derived, i.e., equation 24, which is of extreme importance is the area of "far-field acoustics." This equation has a direct application in far-field sound pressure level studies in connection with the static firing and launch of any space vehicle system. Equation 24, although very useful, is by no means the final solution. As stated previously, the "meteorological factor" has a severe limitation which results from the failure of ray acoustics, in that no finite solution can be obtained at a focus point. An alternate approach has to be used [3] in order to obtain a solution in these regions. This factor, i.e., M_F, appears to be extremely sensitive in only the immediate area of a focus (Fig. 3). Another, but not as severe, limitation of the M_F term, is that no solution can be obtained in the regions where no rays are returned, i.e., shadow zones. Even though these regions indicate that no sound rays are present, sound will propagate into these areas because of scattering and diffraction effects [11, 12].

In order to use the far-field sound pressure level equation, three quantities have to be known. The first two, i.e., OBAL (f) and D.I. (f,β), are concerned with the acoustic source in question. These quantities are normally determined by model tests or some reliable empirical method. The third quantity ($X_s = f(\theta_o)$) is somewhat more difficult to evaluate. As indicated earlier, the normal approach, and by far the simplest, is to assume that the sound velocity can be represented by a single profile, which is a function of altitude only, and further, that the linear layer hypothesis is valid. The validity of both assumptions is

questionable especially the latter one. It has been indicated by several authors [14] that very severe anomalies result because of the use of a linear layer model. To mention a few, focal zones appear where they should not, and where these zones should be present, none is indicated. Numerous studies involving very elaborate curve-fitting routines have been performed [15, 16] in an attempt to alleviate this assumption. The necessity in the introduction of many different vertical velocity profiles as a function of horizontal distance [4] would depend upon local environmental conditions. In some areas, the normal assumption is probably adequate. Equation 24 imposes no restriction on how ($X_s = f(\theta_o)$) is to be evaluated. The only restriction is that the sound rays, for a given azimuth, is confined in a vertical plane.

In summary, and with due recognition to the limitations noted above, it is believed that reliable engineering estimates of the sound pressure received at remote far-field locations from a broad band, directional, point source radiating into an inhomogeneous medium can be made with the aid of equation 24 and a functional form of $X_s = f(\theta_o)$, similar to that which is presented in reference 5.

REFERENCES

1. Heybey, Willi H.: On Sound Intensity and Sound Pressure Levels. NASA TMX-53035, 1964.

2. Buell, C. E.: Sound Propagation Prediction. NASA NAS8-11348, 1964.

3. Brekhovskikh, Leonid M.; (Translated by David Leiberman and Robert T. Beyer): Waves in Layered Media. Academic Press, New York, 1960 (Russian edition, 1956).

4. Kinsler, L. E.; and Frey, A. R.: Fundamentals of Acoustics. John Wiley & Sons, New York, 1960.

5. Heybey, Willi H.: Notes on Sound Propagation and Focusing. MTP-AERO-62-17, 1962.

6. Tedrick, R. N.: Studies in Far-Field Acoustic Propagation. NASA TND-1277, 1962.

7. Krammer, R.; Lawrence, L. C., and Murphy, J. E.: A. D. Little, Inc. Rept. No. 1470764 (AD 605328), 1964.

8. Jones, Jess H.: Power Spectrum and Directivity Characteristics of a Single F-1 Engine. Memorandum R-AERO-AU-65-2, 1965.

9. Wilhold, G. A.; Guest, S. H.; and Jones, J. H.: A Technique for Predicting Far-Field Acoustic Environment Due to a Moving Rocket Sound Source. NASA TN D-1832, 1963.

10. Crandall, S. H.: Random Vibration. Dyer, Ira: Sound Induced Missile Vibration. MIT and John Wiley & Sons, New York, 1958.

11. Pridmore-Brown, David C.; and Ingard, Uno: Tentative Method for Calculation of the Sound Field about a Source Over Ground Considering Diffraction and Scattering Into Shadow Zones. NASA TN 3779, 1956.

12. Pridmore-Brown, David C.; and Ingard, Uno: Sound Propagation Into The Shadow Zone in a Temperature-Stratified Atmosphere Above a Plane Boundary. NASA TN-3494, 1955.

13. Perkins, B., Jr.; and Jackson, W. F.: Handbook for Prediction of Air Blast Focusing. Aberdeen Proving Ground, RDT & E Project No. 1M010501A006, 1964, (AD 602112).

14. Pedersen, M. A.: Acoustic Intensity Anomalies Introduced by Constant Velocity Gradients. J. Acoust. Soc. Am., Vol. 33, No. 4, April, 1964.

15. Pedersen, M. A.; Gordon, D. F.; and Keith, A. J.: A New Ray Intensity Procedure for Underwater Sound Based on a Profile Consisting of Curvilinear Segments. U. S. Navy Electronics Laboratory Research Rept. 1105, 1962 (Confidential).

16. Gordon, D. F.: Extensions of the Ray Intensity Procedure for Underwater Sound Based on a Profile Consisting of Curvilinear Segments. U. S. Navy Electronics Laboratory Research Rept. 1217, 1964 (Confidential).

BLANK PAGE

II. AERODYNAMICS

LAUNCH VEHICLE NOSE SHROUD OPTIMIZATION

By

E. S. Hendrix[1]
and
D. L. Bacchus

SUMMARY

The effect of nose fairing shape on vehicle performance has been studied for two-stage and three-stage Saturn V type vehicles. Shroud shapes considered were single and double angle cones with and without cylindrical extensions. Other factors that influence shroud weight and vehicle performance were also investigated. The more important variables were found to be the shroud shape, time of jettisoning, required volume, choice of material, and type of construction. The trends found are generally applicable for any vertically launched space vehicle, having a thrust-to-weight ratio at lift-off of approximately 1.25.

I. INTRODUCTION

A parametric study has been conducted to determine the various factors that influence the design of nose shrouds for large launch vehicles and to determine the effect of these factors on vehicle performance.[2] The study was initiated by MSFC early in 1962 in response to a request from the Jet Propulsion Laboratory to determine from a performance standpoint the most profitable means to package payloads in Saturn-class vehicles. The results of the study can also aid in the selection of the most appropriate nose shape to shroud a given payload.

Fairing shapes considered were single and double angle cones, with and without cylindrical extensions. Although the majority of the study was conducted using a three-stage Saturn V vehicle (Fig. 1), payload weights were also determined for a two-stage Saturn V vehicle to determine the dependence on the "optimum" nose shapes on the launch vehicle and mission selected. Other factors considered in the study were shroud material and type of construction, nose bluntness, jettison time, aerodynamic drag, aerodynamic loads, and aerodynamic heating.

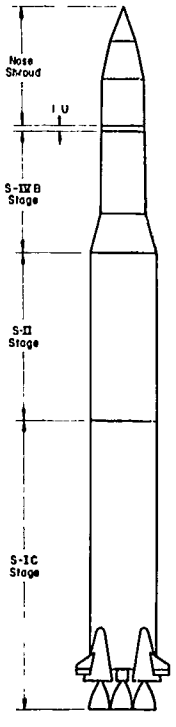

FIGURE 1. SATURN V THREE STAGE VEHICLE WITH TYPICAL NOSE SHROUD

A typical double angle nose shroud showing the basic dimensions is shown in Figure 2. Initial cone angles (θ_1) used were 15°, 20°, 25°, and 30°; frustum angles (θ_2) were 5°, 7.5°, 10°, 15°, and 20°; and diameter ratios (D_1/D_2) were 0.4, 0.6, and 0.8. In addition, single angle cones having half angles from 10° to 25° were studied.

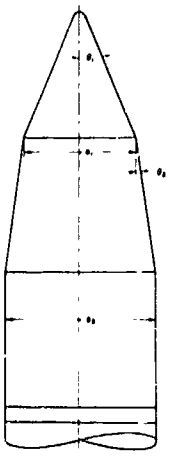

FIGURE 2. SCHEMATIC OF TYPICAL NOSE SHROUD

---

[1]Research Specialist, Lockheed Missiles and Space Company, Huntsville Research and Engineering Center, Huntsville, Alabama.

[2]The study summarized in this report was performed by LMSC/HREC for NASA/MSFC under Contract NAS8-11148.

II. METHOD OF ANALYSIS

The performance of a launch vehicle is both directly and indirectly a function of the shape of the nose fairing which, in most cases, also serves as a protective shroud for some type of payload. Performance is directly affected by the influence of aerodynamic drag which is dependent on the nose shape. Indirectly the performance is affected in that the shape influences parameters such as aerodynamic loads and heating, which in turn influence the weight of the structure.

Numerous investigations have been made to determine minimum drag shapes using the calculus of variations in conjunction with various theoretical means. In general, for a body of given fineness ratio, the minimum drag shape is described by some "power law." However, fabricating a contoured shroud of this type would be highly impractical for the sizes required for large launch vehicles. In addition, the minimum drag configuration does not necessarily give the most performance due to structural weight considerations.

Assuming, then, that an "optimum" shroud would require ease of fabrication, body contours would have to be approximated by a number of straight line segments. To keep the number of variables to a minimum, initial studies considered only conical shapes [1] and were later extended to double angle (cone plus frustum) configurations [2].

By choosing various cone angles, frustum angles, and diameter ratios, the aerodynamic drag, loads, and heating were determined [3, 4, 5]. The structure of each shroud was then designed using computer programs, developed during the course of the study, which minimize shroud weight [6,7].

Fitting the vehicles with various nose fairings and holding stage gross weights constant, ascent trajectories into a 185.2 kilometer circular orbit were optimized. Afterwards, the three-stage vehicle continued on an earth-escape mission. The effect of jettisoning the nose fairing at different times during flight was considered for both vehicles and missions. From the resulting trajectories, maximum payload capabilities were determined.

III. RESULTS

Of the parameters studied, the one having the most influence on performance is the shroud jettison time. For the Saturn V three-stage-to-escape vehicle, the payload can vary as much as 5,000 pounds (2270 kg) (approximately 5 percent) depending on whether the shroud is jettisoned after first stage flight or is carried to escape conditions. Not only does jettison time influence payload weight, but it also greatly influences the "optimum" shroud shape. Considering a conical nose shroud, it can be seen that this is primarily a result of the opposing influence of cone angle on drag and fairing structural weight. As shown in Figure 3,

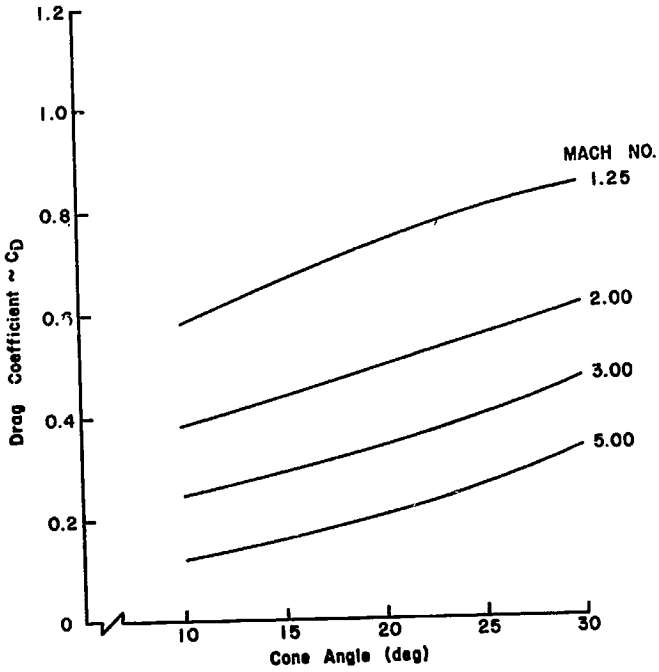

FIGURE 3. EFFECT OF CONE ANGLE ON TOTAL POWER-ON DRAG COEFFICIENT

the total vehicle drag increases with increasing cone angle. However, in Figure 4, it is shown that as the cone angle increases, the shroud structural weight decreases until the cone angle reaches approximately 25°. As would be expected, the resulting performance curves for conical shrouds (Fig. 5) show that when the shroud is ejected early in flight, the aerodynamic drag is of primary importance and a shallow angle shroud gives the most performance. The longer the shroud is carried, the more important weight becomes, and thus the maximum performance cone angle is somewhat higher.

For a given ejection time, varying the shroud shape gives differences in maximum payload of from 1,000 to 4,000 lbm (454 kg to 1814 kg), indicating that nose shape is also an important factor in vehicle performance. Figure 6 shows typical results for double angle fairings having an initial cone angle of 25° and diameter ratio of 0.4. For early jettison times, shallow angle frustums appear to give the most

BLANK PAGE

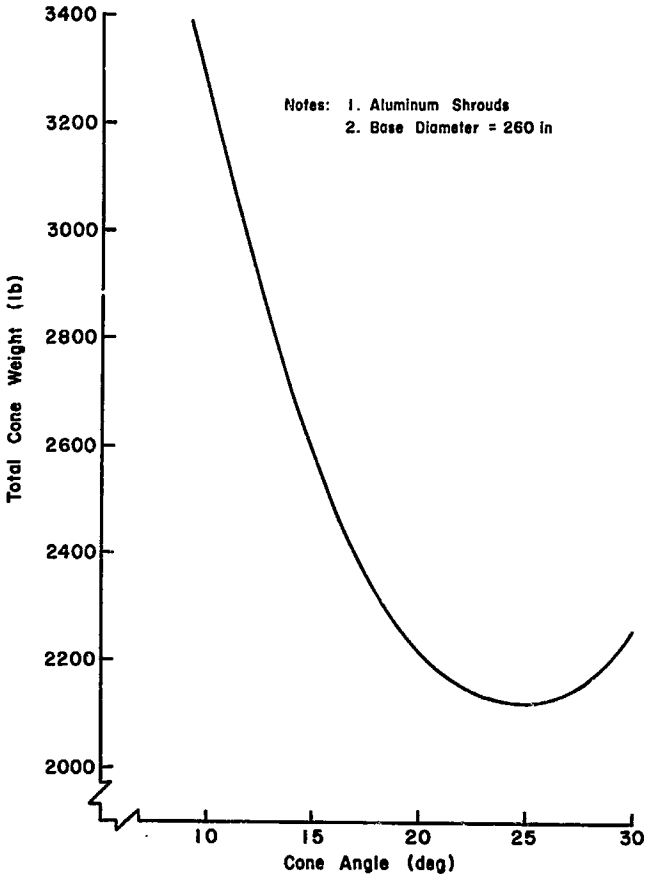

FIGURE 4. EFFECT OF CONE ANGLE ON TOTAL CONE WEIGHT

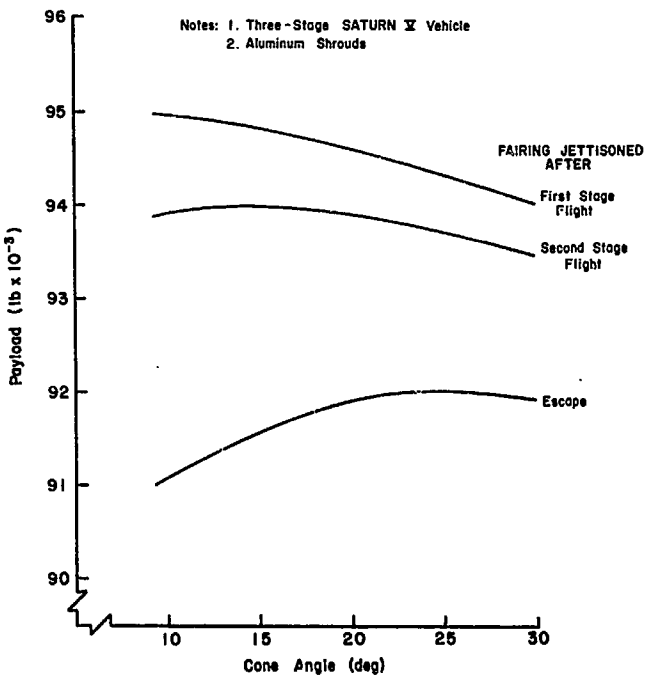

FIGURE 5. EFFECT OF CONE ANGLE ON VEHICLE PAYLOAD COMPABILITY

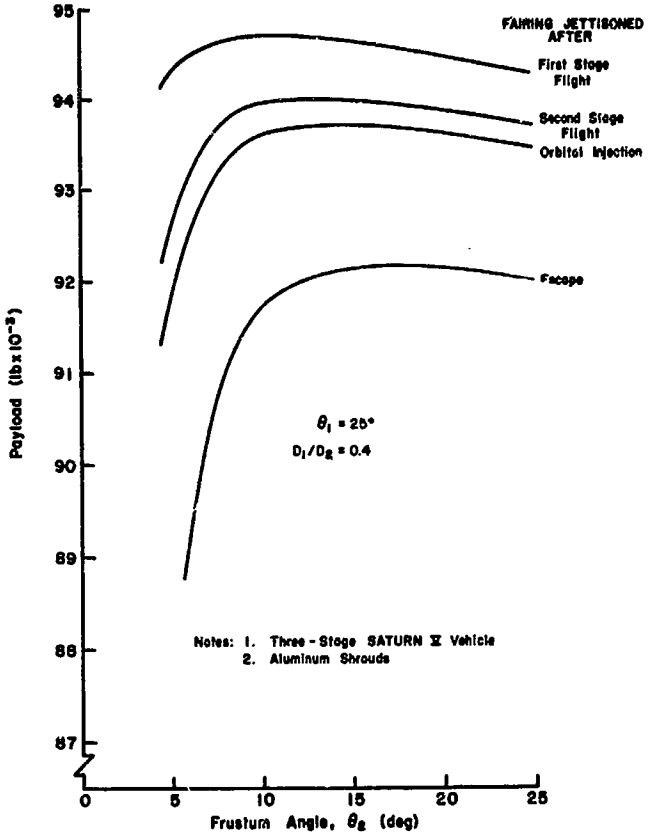

FIGURE 6. EFFECT OF FRUSTUM ANGLE ON PAYLOAD WEIGHT

performance, whereas when the shroud is carried to escape, the most performance is obtained when the frustum angle is closer to the initial cone angle. Again note the marked effect of jettison time on payload weight.

It is to be expected that many low density payloads cannot be contained within the volume of the double angle cone giving the most performance. Thus, to determine the best means of acquiring additional volume, the effect of cylindrical shroud extensions on payload weight was established. A typical result from Reference 2 is shown in Figure 7 where maximum payload weight is presented as a function of the shroud gross volume and geometry. These curves indicate that, for the conditions given, it would be more advantageous not to use cylindrical extensions if the required volume is less than approximately 10,000 ft^3 (283 m^3). However, for greater volume requirements, the use of cylindrical extensions would give the greatest payload capability.

Other factors, mainly, shroud material, type of construction, and internal pressure variations from ambient, were ound to have a pronounced effect on

shroud weight. However, to keep the number of variables within reasonable limits for the time allotted for the study, the bulk of the present work considered only aluminum ring plus skin designs and ambient internal pressure.

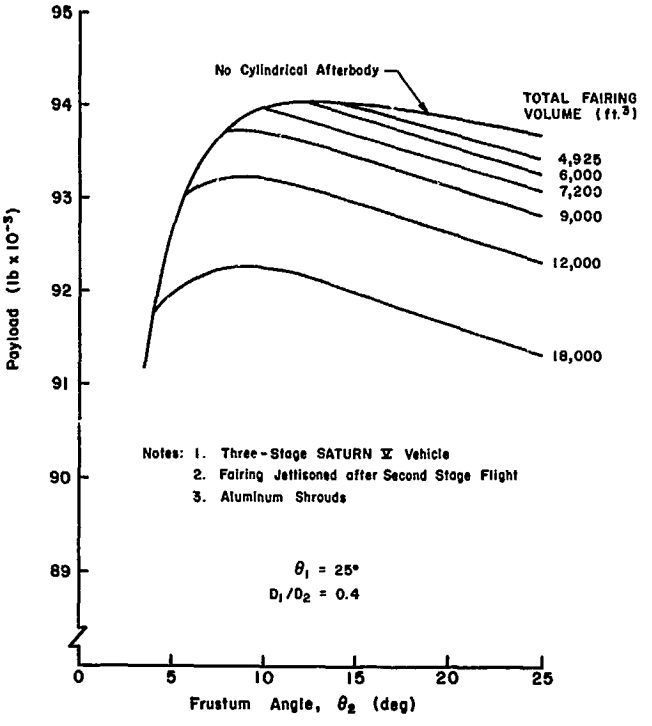

FIGURE 7. EFFECT OF FRUSTUM ANGLE AND TOTAL FAIRING VOLUME ON PAYLOAD WEIGHT

An enlightening result of the studies thus far is the fact that the same trends of payload weight versus body geometry are evident for both the two-stage and three-stage vehicles investigated regardless of their missions. It can thus be conjectured that the trends observed are generally appropriate for any vertically launched space vehicle having an initial thrust-to-weight ratio of approximately 1.25 and similar dynamic pressure histories.

IV. CONCLUDING REMARKS

The nose shroud optimization studies conducted thus far have determined:

a. The factors that most influence shroud weight and vehicle performance.

b. Within limits, the most appropriate payload shroud shapes for maximum performance.

c. The areas where additional effort is necessary and/or desirable.

The factors having the greatest effect on performance were found to be shroud shape, time of jettisoning, required volume, choice of material, and type of construction. Although the two-stage and three-stage Saturn V vehicles gave considerably different payload weights, the same trends have been observed for both vehicles. The results can thus be considered generally applicable for any vertically launched space vehicle having a lift-off acceleration of approximately 1.25 and similar dynamic pressure histories.

In most instances, especially when the shroud is jettisoned early in flight, more performance can be obtained by the use of double angle cones as opposed to pure conical shrouds. In addition, the double angle cones have more volume per unit length for better payload packaging.

Although a great deal of useful information has been derived from the studies thus far, there are several areas where additional effort should prove particularly rewarding. One of these, structural design optimization, is being explored by the Lockheed Missiles and Space Company, Huntsville Research and Engineering Center for the Propulsion and Vehicle Engineering Laboratory at MSFC. The present work has been based upon weights of optimized (weight-wise, subject to practical constraints) ring plus skin designs. Two alternate methods of fairing construction that may be more desirable for certain applications are ring plus stringer plus skin and honeycomb sandwich. Incorporating these materials into a shape optimization study will require that similar structural optimization computer programs be developed.

Since it has been found that the internal pressure in a nose fairing can significantly affect the design of the fairing, an in-flight venting analysis should be performed and included in the design optimization studies. Computer programs are presently available that predict the variation of internal pressure with flight time provided the external flow properties at the vent location are known.

Another area where additional information is needed is in pressure and load distributions at transonic Mach numbers. The present studies have been performed using a set of parametric charts [4] derived from a very limited amount of test data. With additional experimental results, more reliable charts could be developed thus enabling closer approximations to the true minimum weight shroud designs.

There is also a possibility that shapes other than single and double angle cones would be more desirable. The payload gains from parabolic or other contoured configurations could conceivably offset the difficulties of fabrication and thus should be considered in future studies.

V. REFERENCES

1. Hendrix, E. S., Optimum Nose Shape Study-Cone and Cone Plus Cylinder Configurations for Saturn V Vehicles, LMSC-TM-54/20-15, December 1964.

2. Hendrix, E. S., Optimum Nose Shape Study-Cone Plus Frustum and Cone Plus Frustum Cylinder Configuration for Saturn V Vehicles, LMSC-TR-1148-7, May 1965.

3. Hamner, Roger L. and Leff, Alan D., Drag Characteristics of Cone Frustum Configurations at Zero Angle of Attack from Mach 0.7 Through 6.0, LMSC-TM-54/20-35, May 1965.

4. Leff, Alan D. and Lott, Robert A., Frustum Pressure Distributions for Cone-Frustums at Mach Numbers of 1.2, 1.5, and 2.0, LMSC-TM-54/20-38, May 1965.

5. Dean, William G., Thermodynamic Design Curves for Estimating Nose Fairing Skin Thicknesses for a Saturn Ascent Trajectory, LMSC-TM-54/20-7, September 1964.

6. Nevins, Clyde D. and Helton, Benny W., An Investigation of Various Parameters Affecting the Structural Weight of Rocket Vehicle Nose Cones, MTP-P&VE-S-63-4, October 17, 1963.

7. Landis, Ivan M., A Computer Program to Determine the Minimum Weight Design for Ring Stiffened Nose Fairings, LMSC-TR-1148-6, May 1965.

BLANK PAGE

TRISONIC AERODYNAMIC LOADS STUDY

By

Bob G. Dunn

SUMMARY

22332

This study is intended to define the linear aerodynamic load distributions on basic missile and launch vehicle shapes. Since theoretical means are not available in the transonic regime to accurately predict loads, experimental data are being used in the Mach number range from 0.7 to 2.0.

By correlating data from the literature with the results of a supplementary test program, aerodynamic load distributions for cones and cone-cylinders have been obtained and published.

A test program is in progress to define linear local loads on cone-cylinder-flare-cylinder shapes. The analysis of these data has recently begun, the final results of which are to be published in August 1966.

LIST OF SYMBOLS

Symbol	Definition
C_N	Normal force coefficient, $F_N/q_\infty S$
C_{N_α}	Normal force coefficient slope, $\partial C_N/\partial \alpha$
C_N'	Local normal force coefficient, $\partial C_N/\partial (x/D)$
C_{N_α}'	Local normal force coefficient slope, $\partial C_N'/\partial \alpha$
C_M	Pitching moment coefficient, $M/q_\infty SD$
C_{M_α}	Pitching moment coefficient slope, $\partial C_M/\partial \alpha$
C_p	Pressure coefficient, $(p - p_\infty)/q_\infty$
D	Cylinder diameter
F_N	Normal force
L_n	Segment length (n denotes segment number)
M	Pitching moment
M_C	Critical Mach number
M_∞	Freestream Mach number
p	Surface static pressure
p_∞	Freestream static pressure
q_∞	Freestream dynamic pressure, $0.7\ p_\infty\ M_\infty^2$
S	Reference area, $\pi D^2/4$
α	Angle-of-attack, degrees
θ	Cone angle, degrees

Subscripts

1	Cone segment
2	Fore-cylinder segment

I. INTRODUCTION

Missiles and space vehicles are often configurations made up of several conical and cylindrical segments or variations of these shapes. Some examples of these are the Saturn vehicles, Minuteman, Redstone, Jupiter, Juno, Titan, Polaris, and Agena. For the trajectories flown by most of these vehicles, maximum or "design" aerodynamic loading conditions occur at speeds near Mach one.

Even though much testing and analysis are done after initial design to determine exact loading and performance characteristics, the vehicle design and fabrication are commonly based upon aerodynamic loads and characteristics established in the preliminary design analysis. Thus, the importance of having good preliminary design cannot be over-emphasized.

Although theoretical methods are quite adequate for preliminary design in other areas, transonic flow

fields about these configurations do not lend themselves to accurate theoretical analyses. This being the case, the designer must rely upon experimental aerodynamic design curves for initial design information. A parametric representation of these factors is a prerequisite to any practical optimization studies. Such a practical set of design curves which cover broad variations of the significant parameters have not previously been available.

For the past several months, the Huntsville Research & Engineering Center of Lockheed Missiles & Space Company has been engaged in a program to generate an adequate set of aerodynamic design curves for basic shapes in the "Trisonic" Mach number regime (high subsonic, transonic and low supersonic). The Trisonic Aerodynamic Loads Study is under the direction of the Aero-Astrodynamics Laboratory of Marshall Space Flight Center, National Aeronautics and Space Administration.

II. DISCUSSION

A. Published Results

A "building-block" approach to this task was adopted whereby the simplest configuration, a cone, was considered first, and more complicated bodies were considered in the order of complexity of shape. It was planned that the effects of each parameter on the loads for a given segment would be defined such that the total loads for a composite body could be obtained by a summation of segment loads.

A search of the literature was performed to collect published information pertinent to the study. Early in the search, it became apparent that the quantity of useful experimental results was limited and that a test program would be necessary to provide the data required for a comprehensive study. The correlation of available results for cones, cylinders and flares, published in Reference 1, did not provide continuous representation of pressure distributions and stability characteristics for the area of interest.

To define the aerodynamic loads on cone-cylinder configurations, a series of wind tunnel tests was conducted to supplement existing results, thus providing a continuous spectrum of data for the appropriate range of each parameter. Both force and pressure tests were conducted in the MSFC 14 x 14 inch Trisonic Wind Tunnel. A subsequent analysis combined collected results from the literature with those of the associated test and resulted in the design curves presented in Reference 2. The linear aerodynamic characteristics of cones and cylinders are shown in the form of

(1) local normal force coefficient slope, C_{N_α}'

(2) surface pressure coefficient, C_p

(3) normal force coefficient slope buildup, C_{N_α}

(4) pitching moment coefficient slope buildup, C_{M_α}.

The parameters and ranges of each are

(1) Mach number (M_∞) from 0.7 to 2.0

(2) cone semi-vertex angle (θ_1) from 10 to 40 degrees

(3) cylinder lengths up to 6.0 diameters.

Some typical curves are shown in the "carpet plots" of Figures 1 through 4, the experimental points shown being taken from References 3 through 6. The carpet plot method presented here was chosen for two reasons: (1) the coefficients presented are shown varying continuously with two parameters, and (2) for correlation purposes, points which do not fall on one particular curve may be used to define the whole "family" of curves as opposed to the requirement that all parameters but one be duplicated.

Figure 1 presents the variation of cone surface pressure distribution with axial station and cone angle for $M_\infty = 0.8$. A complete cone C_p distribution for any cone angle between 10 and 40 degrees can be faired in by connecting the proper points on each constant station curve.

The cylinder surface pressure for cone-cylinders is shown as a function of axial station and cone angle at Mach 0.8 in Figure 2. It is seen that there is a large pressure drop due to the expansion around the cone-cylinder junction, particularly for the smaller cone angles. The sharp break in the x/D = 0.0 curve just above 20° is characteristic of boundary layer separation at the juncture. For larger cone angles, the flow is separated, whereas it remains attached for smaller cone angles. The Mach number corresponding to the cone angle where separation occurs is termed the critical Mach number and will be discussed later.

Figure 3 depicts the local normal force slopes for cones as being dependent on cone angle and axial station. Integrated values for these curves are compared with cone force data in Reference 2 and are in excellent agreement. It is significant that the presence of a cylindrical afterbody makes little difference on the cone loading.

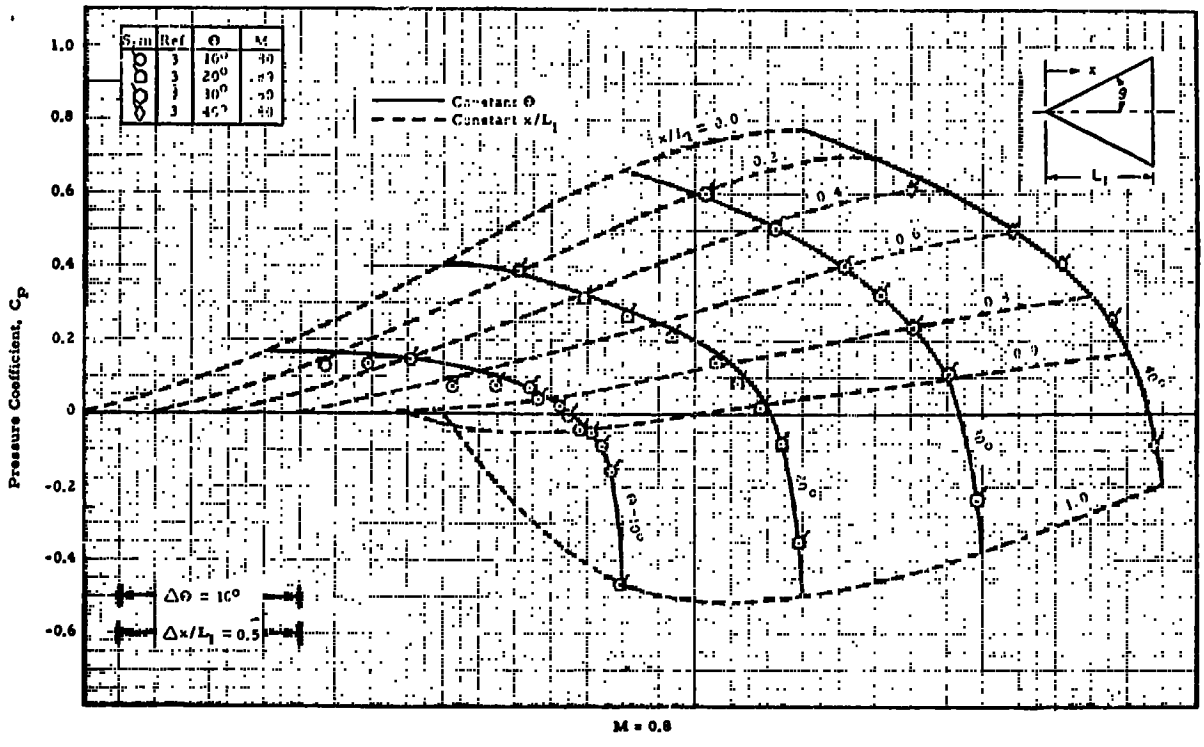

FIGURE 1. VARIATION OF CONE SURFACE PRESSURE DISTRIBUTION WITH SEMI-VERTEX ANGLE FOR ZERO ANGLE-OF-ATTACK

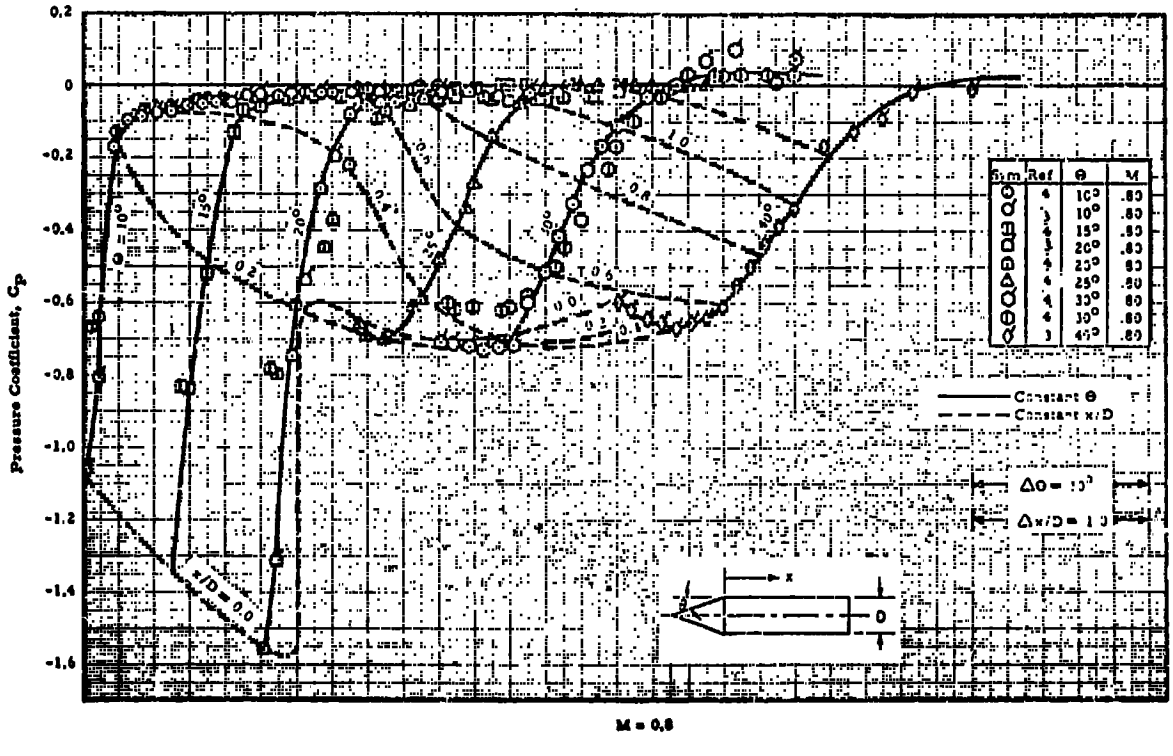

FIGURE 2. VARIATION OF CYLINDER SURFACE PRESSURE DISTRIBUTIONS WITH CONE ANGLE FOR CONE-CYLINDERS AT ZERO ANGLE-OF-ATTACK

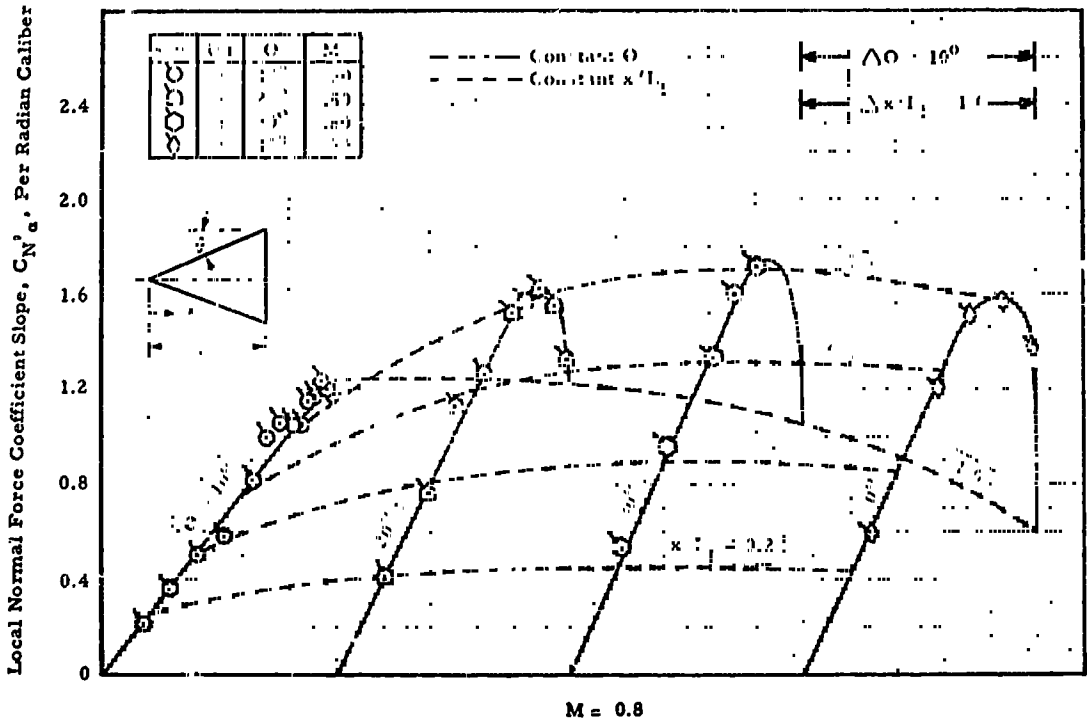

FIGURE 3. THE EFFECT OF SEMI-VERTEX ANGLE ON LOCAL NORMAL FORCE SLOPE DISTRIBUTIONS FOR CONES

The local normal force slopes for the cylinder portions of cone-cylinders are shown in Figure 4. In this case, one sharp break appears in the constant station curves (at $\theta = 20°$) due to flow separation as was seen in the C_p curves. A more detailed survey of data in the vicinity of $\theta = 20°$ might indicate some abrupt change in the trends as was observed in some other cases.

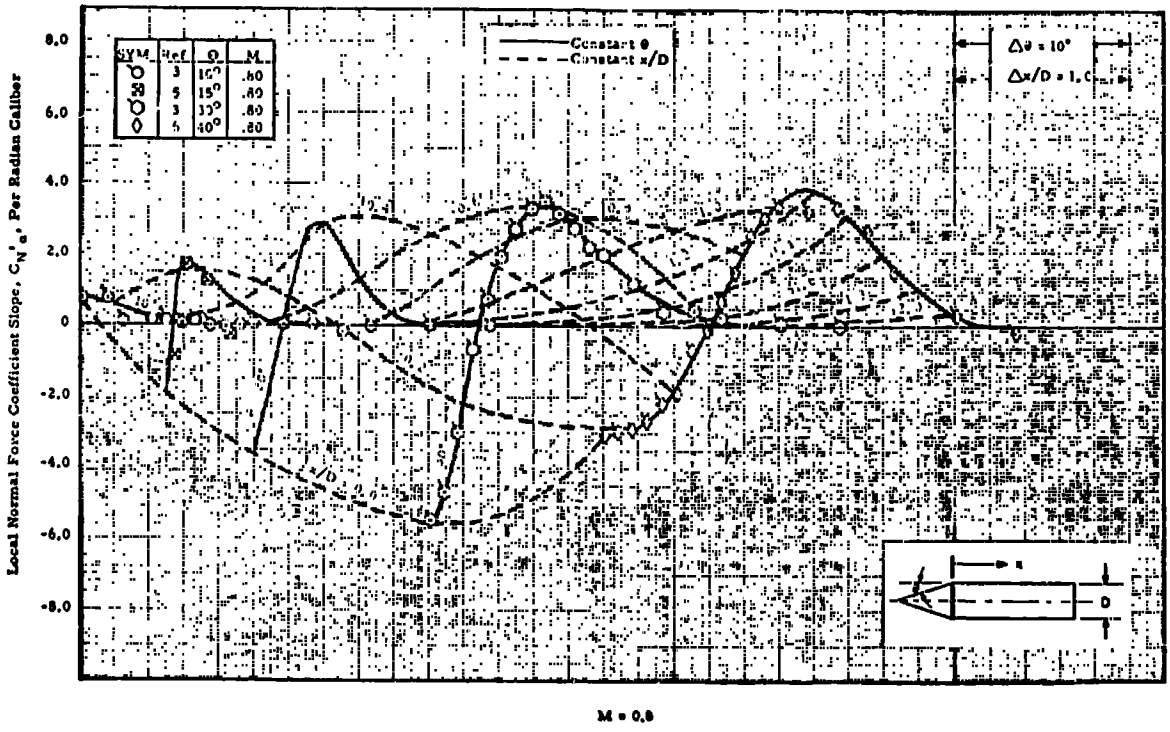

FIGURE 4. THE EFFECT OF CONE ANGLE ON LOCAL NORMAL FORCE SLOPE DISTRIBUTIONS FOR CONE-CYLINDERS

The curves for each segment may be combined to obtain the load distributions for a cone-cylinder; some typical cases are presented in Figures 5 and 6. The pressure distributions are shown in Figure 5 and local normal force slopes in Figure 6 for Mach numbers 0.8, 1.1, and 1.5. The curves for Mach 0.8 are taken directly from interpolated curves faired in Figures 1 through 4. These Mach numbers represent three distinct flow patterns: $M_\infty = 0.8$ is a transonic separated flow case, $M_\infty = 1.1$ is a transonic case with boundary layer completely attached, and $M_\infty = 1.5$ is a supersonic case.

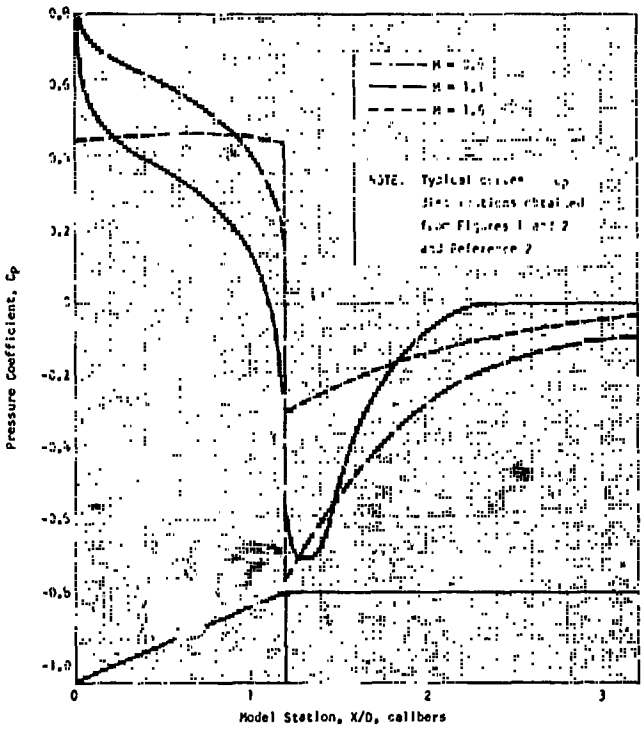

FIGURE 5. SURFACE PRESSURE DISTRIBUTIONS FOR A 22.5 DEGREE CONE-CYLINDER CONFIGURATION AT ZERO ANGLE-OF-ATTACK AND MACH NUMBERS 0.8, 1.1 AND 1.5

For zero angle-of-attack and fixed cone angle, there is an approximate critical Mach number, M_C, above which flow is attached and below which the boundary layer separates at the juncture. Very close to this critical Mach number, alternating flow attachment and separation may occur, but such a phenomenon has not been explored in the present study. Reynolds number and possibly other parameters may have considerable effect upon the critical Mach number. However, this is a problem worthy of a separate research and is not investigated here.

To define the critical Mach number well, the models should be tested at many Mach numbers near

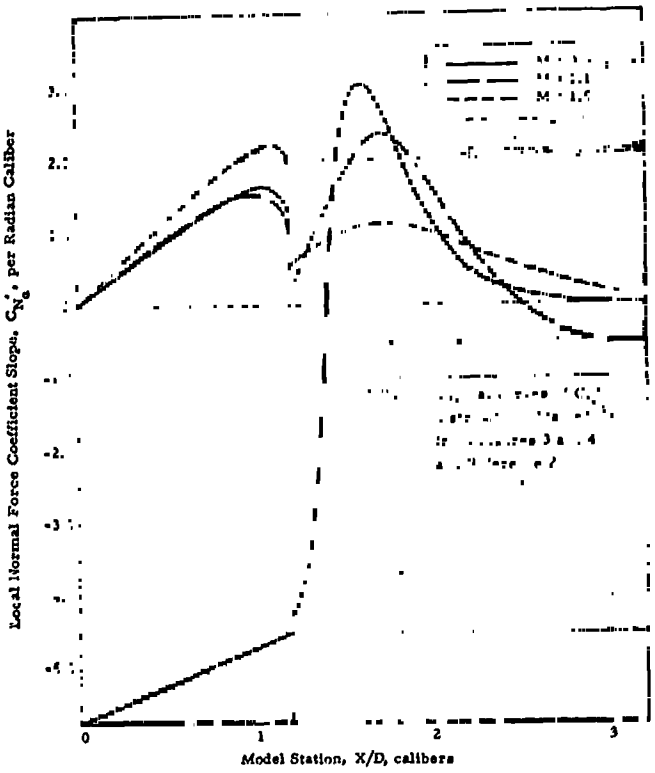

FIGURE 6. LOCAL NORMAL FORCE SLOPE DISTRIBUTIONS FOR A 22.5 DEGREE CONE-CYLINDER CONFIGURATION AT MACH NUMBERS 0.8, 1.1 AND 1.5

M_C, which has not been done for the present investigation. It was observed from the data available, however, that both separated and attached boundary layers existed for given conditions. The Mach numbers for such cases were inferred to be M_C. Figure 7 shows the variation of M_C with cone angle as derived in this manner compared with similar results acquired from the pressure curves of Reference 4. The curves do not agree, but do converge for higher Mach numbers. The discrepancy is probably due to the different wind tunnels or other unexplored factors.

B. Current Activities

The Trisonic Aerodynamic Loads Study is being extended to include the effects of flare-cylinders attached downstream to cone-cylinders. Since the literature provided very few test data which are applicable, a complete test program was scheduled in the MSFC 14-in. (36 cm) Trisonic Wind Tunnel to obtain pressure distributions on cone-cylinder-flare-cylinder configurations. A force was also scheduled to verify integrated pressure loads. Details of these test plans are documented in Reference 7.

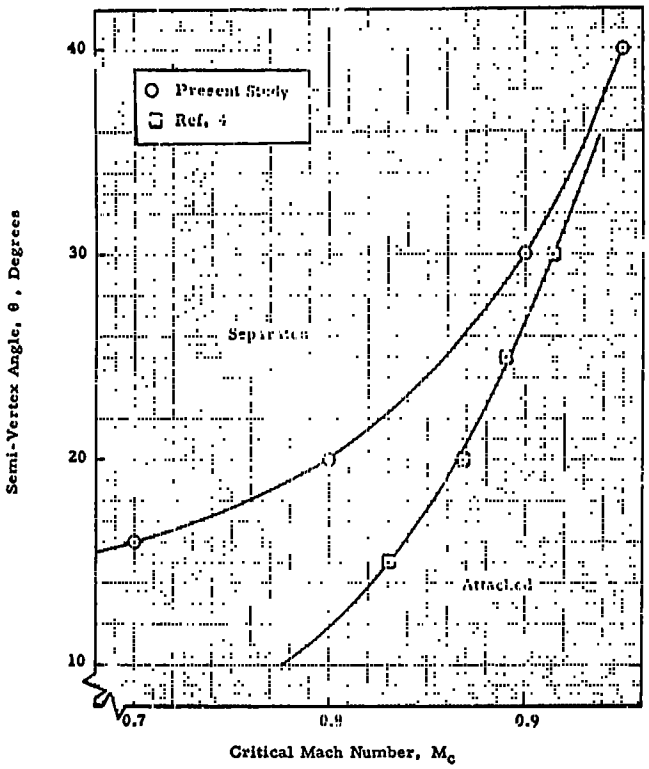

FIGURE 7. THE INFLUENCE OF CONE ANGLE ON CRITICAL FLOW SEPARATION MACH NUMBER

At the present time, a large portion of the pressure test has been completed. A second entry is scheduled for September 1965 to complete the program; the force test will also be completed at that time.

Analysis of the test results generated in the test mentioned above has recently begun. It is the purpose of the current phase of study to derive and present parametric design curves which define linear local aerodynamic load distributions for cone-cylinder-frustum-cylinder bodies. Interest will center about the frustum, and an attempt will be made to isolate the flare effects from the nose shape effects. In this manner, the building-block approach can be followed in the use of these and previously published curves provided judicious restraint is practiced in their application.

The Mach number range covered will be from 0.7 to 2.0. Flare angles of 7.5°, 10°, 15° and 20° and flare base-to-leading-edge diameter ratios of 0.4, 0.6, and 0.8 will be considered in the coming analysis.

It is expected that the results of the current phase of study will be published in a handbook by August of 1966. The planned curves will provide the preliminary designer with a convenient means of evaluating the aerodynamic loads for configurations falling into this general category without time-consuming and expensive tests. The optimization of various parameters with respect to vehicle performance will also be practical with the availability of the final results.

III. REFERENCES

1. Benefield, J. W., R. L. Hamner, R. J. Hauser and A. D. Leff, A Correlation of Transonic and Supersonic Aerodynamic Characteristics for Cones, Cylinders and Flares, TM 54/01-42, Lockheed Missiles & Space Company, Huntsville Research & Engineering Center, Huntsville, Alabama, January 30, 1964, CONFIDENTIAL.

2. Hamner, Roger Lee and Alan D. Leff, Linear Aerodynamic Loads on Cone-Cylinders at Mach Numbers from 0.7 to 2.0, TR HREC/11289-1, Lockheed Missiles & Space Company, Huntsville Research & Engineering Center, Huntsville, Alabama, March 10, 1965.

3. Erickson, E. W. and E. D. Dowling, Transonic Pressure Tests on a Series of 3.480 Inch Diameter Cone-Cylinder Models in the Convair High Speed Wind Tunnel, H51-TR-021-0, Convair Division of General Dynamics, San Diego, California, April 14, 1961.

4. Robertson, J. E. and H. L. Chevalier, Characteristics of Steady-State Pressures on the Cylindrical Portion of Cone-Cylinder Bodies at Transonic Speeds, AEDC-TDR-63-104, Arnold Engineering Development Center, Arnold Air Force Station, Tennessee, August 1963.

5. Pearson, A. O., Surface Pressure Distributions On 0.0628-Scale Models of Proposed Project FIRE Space Vehicles at Mach Numbers From 0.25 to 4.63, TN-D-1961, National Aeronautics and Space Administration, Washington, D. C., September 1963.

6. Hauser, R. J., Experimental Pressure and Normal Force Distribution Data for a Family of Cone-Cylinder Configurations at Test Mach Numbers from 0.7 to 2.0, TM 54/20-5, Lockheed Missiles & Space Company, Huntsville Research & Engineering Center, Huntsville, Alabama, March 17, 1965.

7. Leff, Alan D., Pretest Report for the Trisonic Cone-Cylinder-Frustum-Cylinder Test Series, TM 55/20-31, Lockheed Missiles & Space Company, Huntsville Research & Engineering Center, Huntsville, Alabama, April 1965.

BLANK PAGE

ON SOME AERODYNAMIC ASPECTS OF THE PANEL FLUTTER PROBLEM

By

M. Platzer, R. Beranek, L. Saunders

SUMMARY

Recent panel flutter studies have led to the conclusion that linearized potential flow theory is inadequate to predict panel flutter at low supersonic Mach numbers. Nonlinear transonic flow effects and boundary layer effects were suggested as major reasons for the disagreement between theory and experiment. This paper presents a comparison between linear and nonlinear inviscid supersonic flow past wavy walled planar and cylindrical configurations and discusses their significance toward panel flutter research.

LIST OF SYMBOLS

Symbol	Definition
c	Velocity of sound in the free stream
c_p	Specific heat at constant pressure
c_v	Specific heat at constant volume
C	Euler's constant = 0.5772157
$J_n(\lambda)$	Bessel function of the first kind of order n
$Y_n(\lambda)$	Bessel function of the second kind of order n
$H_o^{(2)}(z)$	Hankel function (Bessel function of the third kind)
$K_o(z)$	Modified Bessel function of the second kind
L	Wave length
M	Mach number
n	Direction normal to a streamline
R	Gas constant
R_o	Radius of cylinder
$\bar{R}$	Surface deformation of the cylinder, positive in the positive r direction
R(x,t)	Radial displacement of the cylinder
s	Entropy
t	Time
u,v,w	Velocity components in the x, r, Θ directions of the velocity V
x,r,Θ	Coordinate system
$\bar{\alpha}$	Wavelength of the advancing acoustic disturbance $\frac{\omega}{c(M+1)}$
α''	Wavelength of the receding acoustic disturbance $\frac{\omega}{c(M-1)}$
γ	Wave number $(2\pi/L)$
ξ	Real, positive variable
ϕ	Velocity potential
ω	Circular frequency of the cylinder vibration
ν	Ratio of specific heats

I. INTRODUCTION

The dynamic aeroelastic instability of surface skin panels that have one side exposed to an airstream and the other side to still air has become of increasing concern to designers of aircraft and missile structures in the last ten years. This problem is commonly referred to as panel flutter and is defined as the self-excited oscillation of a panel in a flow under the action of aerodynamic forces generated by the panel motion. Experiments have shown conclusively that flutter of surface skin panels can exist [1,2]. As a matter of fact, Jordan [3] has suggested that such flutter contributed to early German V-2 rocket failures. More recently, panel flutter has occurred on the X-15 airplane. Figure 1 shows those regions on the X-15 research aircraft which were affected by panel flutter. The variation of the panel response envelope with dynamic pressure as obtained from flight measurements

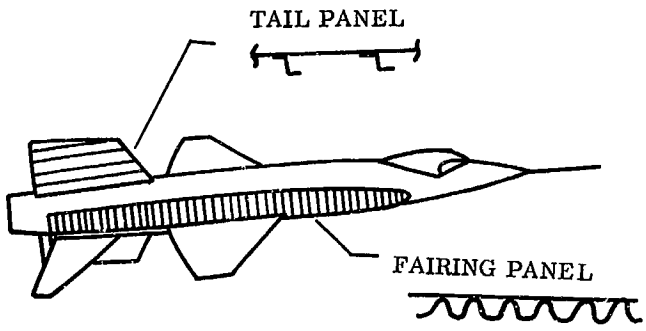

FIGURE 1. REGIONS OF X-15 RESEARCH AIRCRAFT AFFECTED BY PANEL FLUTTER [5]

on an X-15 side-fairing panel is shown in Figure 2. The upper curve exhibits a sudden increase in amplitude at a dynamic pressure of 600 psf due to start of flutter. The lower curve reproduces the measured envelope of the response for the stiffened panel, which

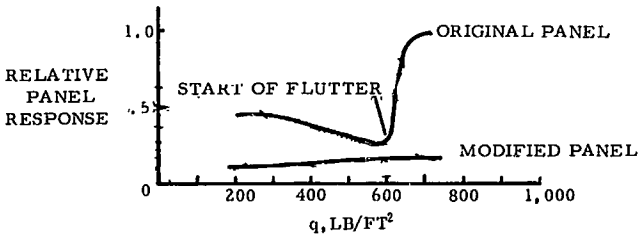

FIGURE 2. VARIATION OF PANEL-RESPONSE ENVELOPE WITH DYNAMIC PRESSURE OBTAINED FROM FLIGHT MEASUREMENTS ON AN X-15 SIDE-FAIRING PANEL [4]

shows that flutter was eliminated. Although, in general, structural nonlinearities strongly tend to limit the flutter amplitudes and therefore cause the modes of structural failure to be those peculiar to fatigue rather than explosive fracture of the skin surface, it is dangerous to regard panel flutter as a fatigue problem only. Tests of the corrugation stiffened X-15 panels, e. g., revealed that flutter was very sudden and very severe. The panels failed unless flutter was stopped in a few seconds [4]. Similar explosive type flutter was encountered in tests of corrugation-stiffened Dyna-Soar panels [6].

Unfortunately, there is no reliable formula or computing program of guaranteed accuracy available today to guide missile and aircraft engineers in designing against panel flutter. Although a substantial amount of theoretical and experimental effort has been devoted to this problem in the last decade, the areas of agreement between theory and experiment are quite limited. As a result of these studies (see Ref. 7 for a recent review) it is generally realized now that in panel flutter many factors are important, e. g., the flow conditions, initial curvature effects, tension and compression loads induced by mechanical or thermal effects, etc. Thus, a comparison between theory and experiment may allow proper interpretation only if all these parameters have been thoroughly analyzed and controlled, an obviously difficult task.

Further progress in the analysis of panel flutter therefore seems to depend upon a careful separation and evaluation of the different factors influencing panel flutter experiments. In this respect, Lock and Fung [8] have suggested that the effects of aerodynamic nonlinearity and of viscosity may be quite important. These aerodynamic aspects of the panel flutter problem are discussed in this report in more detail, along with some results of preliminary in-house studies.

II. PRESSURE DISTRIBUTION ON A VIBRATING CYLINDER

We select a vibrating cylinder for a discussion of the physical significance of various aerodynamic theories. Consider an infinitely long cylindrical shell of radius R_0 which is exposed externally to a uniform airstream parallel to the generators of the cylinder. Assume the cylinder to be vibrating in a sinusoidal axisymmetric standing wave mode within the length L. Thus, the panel deflection is given by

$$R(x,t) = \overline{R} \sin(\gamma x) \cdot e^{i\omega t}, \qquad (1)$$

where $R(x,t)$ is the radial displacement of the shell measured positive in the outward direction, $\overline{R}$ is a real or complex number, and γ is the wave number of the standing wave deflection. The deformation of the shell is assumed to be so small that linearized aerodynamic theory may be employed.

Therefore, adopting a cylindrical coordinate system, we are looking for a solution of the linearized unsteady potential equation.

$$(M^2 - 1)\phi_{xx} - \phi_{rr} - \frac{1}{r}\phi_r + \frac{2i\omega M}{c}\phi_x - \frac{\omega^2}{c^2}\phi = 0 \qquad (2)$$

Such a solution may be obtained by distributing pulsating sources along the axis and summing the effect of the sources. The basic source solution in supersonic flow is well known [9]; e. g.,

$$\phi(x,r,t) = -\frac{1}{2\pi\sqrt{(x-\xi)^2 - \cot^2\alpha \cdot r^2}}\, e^{i[\omega t - \mu(x-\xi)]}$$

$$\cdot \cos\left(\kappa\sqrt{(x-\xi)^2 - \cot^2\alpha \cdot r^2}\right), \qquad (3)$$

where

$$\cot^2\alpha = M^2 - 1, \quad \kappa = \frac{\omega}{c\cot^2\alpha}, \quad \mu = \frac{\omega M}{c\cot^2\alpha}.$$

Thus, by summing over all these sources from 0 to X, we obtain

$$\phi(x,r,t) =$$

$$-\frac{e^{-i\omega t}}{2\pi}\int_0^{x - r\cot\alpha} \frac{q(\xi)\cos\left[\kappa\sqrt{(x-\xi)^2 - \cot^2\alpha \cdot r^2}\right]}{\sqrt{(x-\xi)^2 - \cot^2\alpha \cdot r^2}}$$

$$\cdot e^{-i\mu(x-\xi)}\, d\xi\,. \qquad (4)$$

The source distribution can be determined from the boundary conditions at the cylinder surface, and in our following considerations, we regard it to be known.

Equation (4), unfortunately, is unsuitable for a physical interpretation of the generated flow field. We, therefore, try to generalize Munk's cross-flow concept [10] to this case. Thus, considering first only the flow in a cross section perpendicular to the free-stream, we have the following two-dimensional cross-flow solution

$$\phi_{cross}(x,r,t) = \frac{i}{4} e^{i\omega t}\, q(x) \cdot H_o^{(2)}\left(\frac{\omega}{c} r\right) \qquad (5)$$

which satisfies the two-dimensional Helmholtz equation.

$$\phi_{rr} + \frac{1}{r}\phi_r + \frac{\omega^2}{c^2}\phi = 0 \qquad (6)$$

Obviously, the cross-flow potential equation (5) does not represent a complete solution to our problem. There is an influence of the body pulsation in front of the cross section, x = constant, which has to be taken into account. Generalizing a steady-flow concept first introduced by K. Oswatitsch [11], we may term this part of the flow field "spatial influence" and obtain it by subtracting equation (5) from equation (4).

Since the integrand in equation (4) decreases rapidly with increasing distance of the source-element $q(\xi)$ from the considered station x, we may make an approximation by extending the integration from $x = -\infty$ to $x - r\cot\alpha$ instead of integrating from the leading edge x = 0. This results in a considerable simplification because the integration over the x - direction can now be carried out and we obtain [11]

$$\phi_{spatial}(x,r,t) = \frac{i}{4} e^{i\omega t}\, q_1 e^{i\gamma x}\left\{P_1(r) - H_o^{(2)}\left(\frac{\omega}{c} r\right)\right\}$$

$$+ \frac{i}{4} e^{i\omega t}\, q_2 e^{-i\gamma x}\left\{P_2(r) - H_o^{(2)}\left(\frac{\omega}{c} r\right)\right\} \qquad (7)$$

where

$$P_1(r) = H_o^{(2)}\left[r\cot\alpha\sqrt{(\bar{\alpha} + \gamma)(\alpha'' + \gamma)}\right] \qquad (7a)$$

$$P_2(r) = H_o^{(2)}\left[r\cot\alpha\sqrt{(\bar{\alpha} - \gamma)(\alpha'' - \gamma)}\right] \quad \begin{matrix}\bar{\alpha} > \gamma \\ \alpha'' > \gamma\end{matrix}$$

$$= -H_o^{(1)}\left[r\cot\alpha\sqrt{(\gamma - \bar{\alpha})(\gamma - \alpha'')}\right] \quad \begin{matrix}\gamma > \bar{\alpha} \\ \gamma > \alpha''\end{matrix}$$

$$= \frac{2i}{\pi} K_o\left[r\cot\alpha\sqrt{(\gamma - \bar{\alpha})(\alpha'' - \gamma)}\right] \quad \begin{matrix}\gamma > \bar{\alpha} \\ \alpha'' > \gamma\end{matrix}. \qquad (7b)$$

This expression for the spatial influence gives a much clearer insight into the parameters on which the flow field depends, namely, on the quantities γ, $\bar{\alpha}$, and α''.

Since $\bar{\alpha}$ and α'' represent the wavelengths of the advancing and receding acoustic disturbances in the x - direction, we see that the solution critically depends on the ratio of the cylinder deflection γ to the wave numbers $\bar{\alpha}$ and α''. In particular, if one of the acoustic wavelengths coincides with the deflection wavelength, the spatial influence becomes infinite. Thus a similar singular behavior of this solution is seen to occur as for steady transonic flow. As a matter of fact, this breakdown of linearized theory is due to the same transonic singularity. This can be shown as follows:

The argument in equation (7a) and (7b) can also be written in the form

$$\gamma^2\left[\left(\frac{\omega}{c\gamma} \pm M\right)^2 - 1\right],$$

showing that the solution depends on the "equivalent" steady Mach numbers

$$\left|M \pm \frac{\omega}{c\gamma}\right|.$$

Since the standing wave pulsation can be obtained by superposition of two traveling waves with the velocities $\pm \frac{\omega}{\gamma}$, our problem resolves into two steady flow problems over a wavy walled cylinder with the Mach numbers $M \pm \frac{\omega}{c\gamma}$. The breakdown of linearized theory then occurs when one of these Mach numbers approaches one, which corresponds to the previously stated coincidence condition.

III. STEADY SUPERSONIC FLOW OVER A WAVY WALLED CYLINDER

The foregoing considerations showed that the flow over an infinitely long vibrating cylinder can be reduced to two steady flow problems. Therefore, a study of the steady wavy walled cylinder flow may give considerable insight into the aerodynamic characteristics of vibrating cylinders.

Our objective here is to study the influence of wave-amplitude to wavelength ratio to find the effect of aerodynamic nonlinearities. This will be done by comparing the linearized solutions for an infinitely long cylinder with a nonlinear method of characteristics solution.

Thus, we assume a sinusoidal wave pattern of the form $R(x) = \bar{R} \cos \gamma x$.

Specialization of equation (7) to steady flow yields, after the proper satisfaction of the boundary condition at the body surface, the following expression for the pressure coefficient:

$$C_p = - \frac{2\gamma \bar{R}}{\sqrt{M^2 - 1}} |A| \cos(\gamma x + \Theta), \tag{8}$$

where

$$|A| = \sqrt{a^2 + b^2}, \quad \Theta = \tan^{-1} \frac{b}{a} \tag{9a}$$

$$a = \frac{J_0(\lambda) J_1(\lambda) + Y_0(\lambda) Y_1(\lambda)}{[J_1(\lambda)]^2 + [Y_1(\lambda)]^2} \tag{9b}$$

$$b = \frac{J_0(\lambda) Y_1(\lambda) - J_1(\lambda) Y_0(\lambda)}{[J_1(\lambda)]^2 + [Y_1(\lambda)]^2}, \tag{9c}$$

$$\lambda = \gamma R_0 \sqrt{M^2 - 1}. \tag{9d}$$

From this linearized solution, two limiting cases may be easily obtained by proper expansion with respect to the argument λ, namely, the slender-body solution for values of $\lambda << 1$ and the Ackeret solution for $\lambda >> 1$. By asymptotic expansion for small values [13], we obtain the following "slender-body" expression for the pressure coefficient:

$$C_p = - 2\gamma^2 R_0 \bar{R} \sqrt{(\ell n \frac{\lambda}{2} + C)^2 + \frac{\pi^2}{4}} \cos(\gamma x + \Theta)$$

where

$$\Theta = \tan^{-1} \frac{1}{\frac{2}{\pi}(\ell n \frac{\lambda}{2} + C)}. \tag{10}$$

This result could also have been obtained by using the well known slender body theory for bodies of revolution, e.g., equation 9.34C Reference 12, and applying it to the infinitely long wavy walled cylinder.

On the other extreme, by asymptotic expansion for large values of λ, we obtain the familiar Ackeret solution [12, p. 413]

$$C_p = - \frac{2\gamma \bar{R}}{\sqrt{M^2 - 1}} \sin \gamma x. \tag{11}$$

In Figures 3 and 4 the range of validity of these two asymptotic solutions is compared with linearized theory. Slender-body theory is seen to deviate sharply for higher values of λ, whereas Ackeret theory turns out to be a rather good approximation down to relatively low values of λ.

In panel flutter calculations exact linearized theory or various approximations such as Ackeret theory, piston theory, etc., are used to calculate the generalized aerodynamic forces. Since the flutter amplitudes are usually very small, an analysis of the aerodynamic forces may well be based upon linearized theory, and any deviations of the measured pressure distribution should be attributed to boundary layer effects. However, some recent experiments by McClure [14] and Anderson [15], along with currently planned tests of wavy wall models in the transonic and low supersonic range [16], suggested the desirability of a more accurate flow field analysis.

For this purpose a method of characteristics solution for supersonic flow of an ideal inviscid non-heat-conducting gas has been adapted to the present problem. This solution, worked out by J. L. Sims and L. Saunders*, is based upon the nonlinear non-isentropic equation,

* Aero-Astrodynamics Lab.

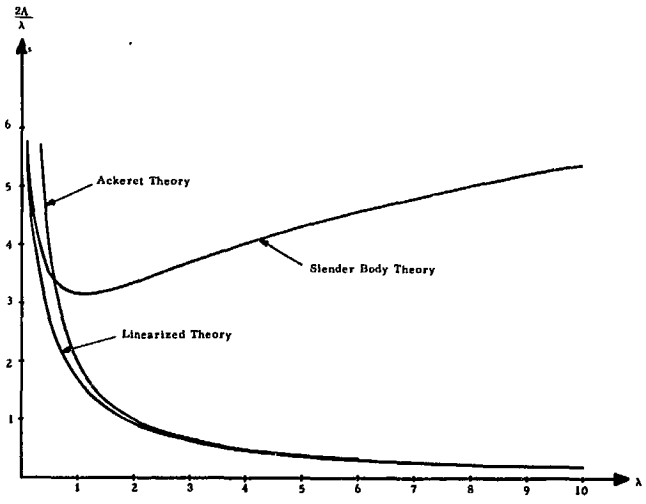

FIGURE 3. ABSOLUTE VALUE OF PRESSURE COEFFICIENT

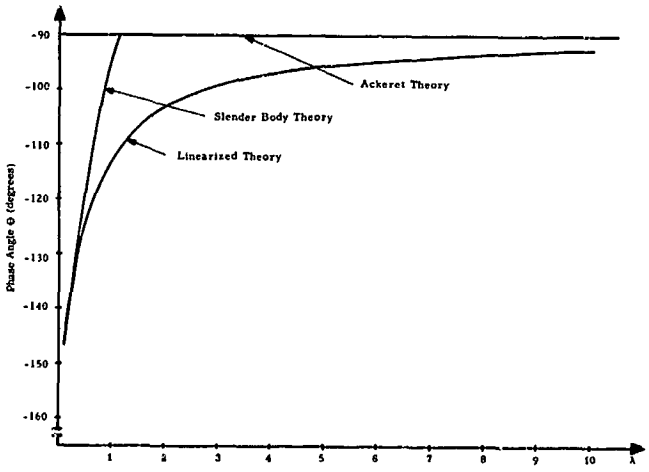

FIGURE 4. PHASE ANGLE OF PRESSURE COEFFICIENT

Phase Angle Θ (degrees)

$$\left(1-\frac{u^2}{c^2}\right)\frac{\partial u}{\partial x}+\left(1-\frac{v^2}{c^2}\right)\frac{\partial v}{\partial r}-\frac{2uv}{c^2}\frac{\partial u}{\partial r}+\frac{v}{r}$$

$$=\frac{uv}{\nu VR}\frac{\partial s}{\partial n}\,, \qquad (12)$$

where x, r, and Θ are cylindrical coordinates, u, v, w are the velocity components of the velocity V, c the speed of sound, R the gas constant, s the entropy and n the direction normal to the streamline.

We will apply this numerical method of characteristics solution to a wavy walled cylinder whose dimensions are shown in Figure 5. This model has been extensively studied by Anderson [15], and we refer to his report for details of his experimental investigations. Our purpose here is to show a comparison

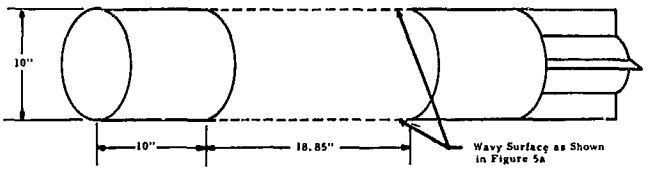

FIGURE 5. WAVY WALL CYLINDER INVESTIGATED BY ANDERSON IN HIS WIND-TUNNEL TESTS

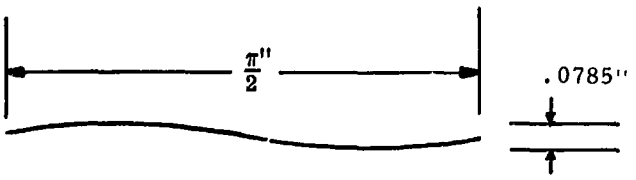

FIGURE 5a. SKETCH SHOWING DIMENSIONS OF ONE WAVELENGTH OF THE ANDERSON MODEL

between nonlinear theory for a finite length model and linear theory for an infinitely long cylinder. Figure 6 shows the variation of the pressure coefficient for supersonic flow at M = 3.0 over the first seven waves. Linear theory, of course, is a pure sine wave. Nonlinear theory also exhibits the same sinusoidal pattern and, in particular, shows no leading edge effect. The only effect here of aerodynamic nonlinearity is an overall shift in pressure levels which causes an integrated compressive loading of the shell. A similar comparison for M = 4.62 shows the same general characteristics (Figure 7). However, nonlinear theory begins to show a slight leading edge effect and a noticeable deviation from the sinusoidal variation. Furthermore, a small upstream phase shift of the peak amplitude is to be observed. These characteristics are further enhanced for flow at M = 10.0 as shown in Figure 8. Here a quite significant leading edge effect is seen to occur.

In exploring the lower supersonic Mach number range, computer runs for M = 2.0 and M = 1.5 show essentially the same results as for M = 3.0. A further extension to the range $1 < M < \sqrt{2}$, however, could not be obtained for the present configuration (Figure 5) because the flow is soon decelerated to local subsonic Mach numbers in going through the first shock wave. This prohibits further analysis by the method of characteristics. Only a sharp decrease in wave amplitude allowed a further analysis in this Mach number range.

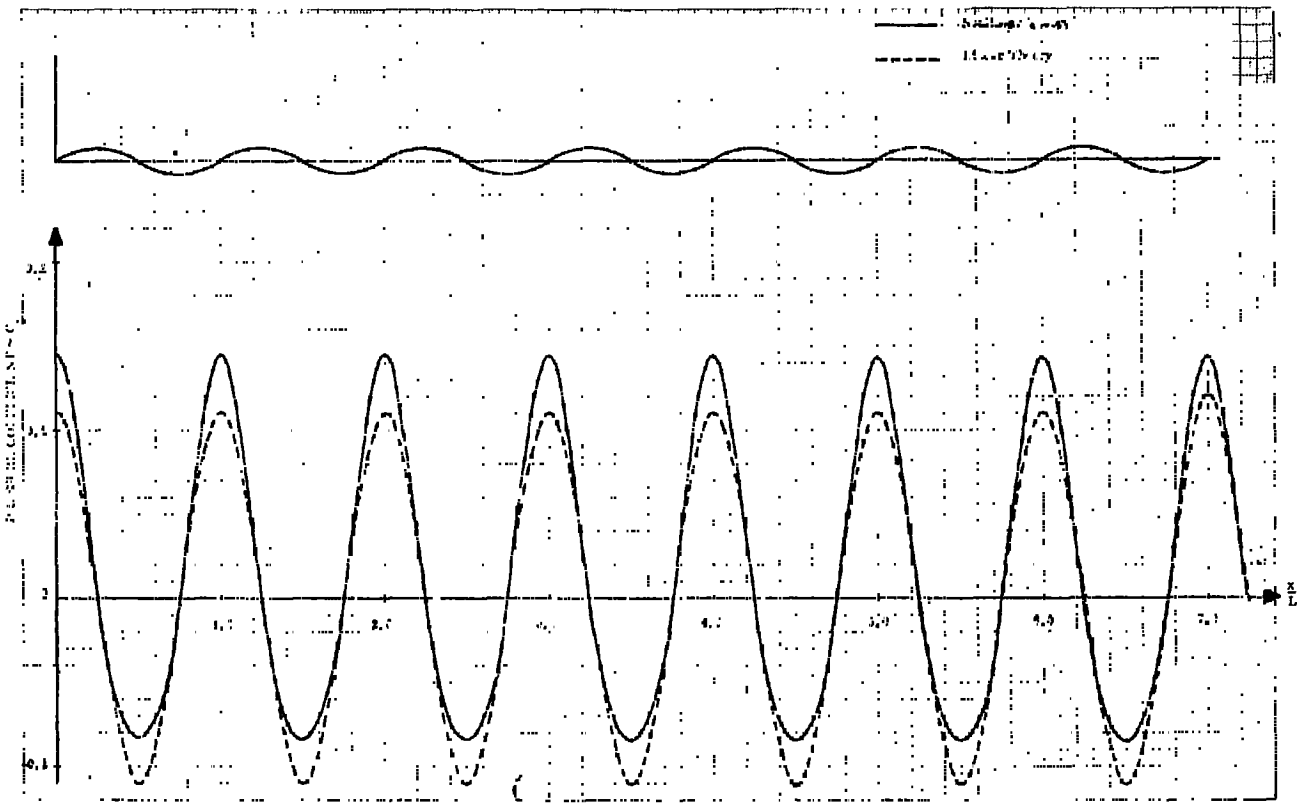

FIGURE 6. PRESSURE DISTRIBUTION ALONG WAVY WALLED CYLINDER OF FIGURE 5
$M_\infty = 3.0$ $a/L = 0.025$

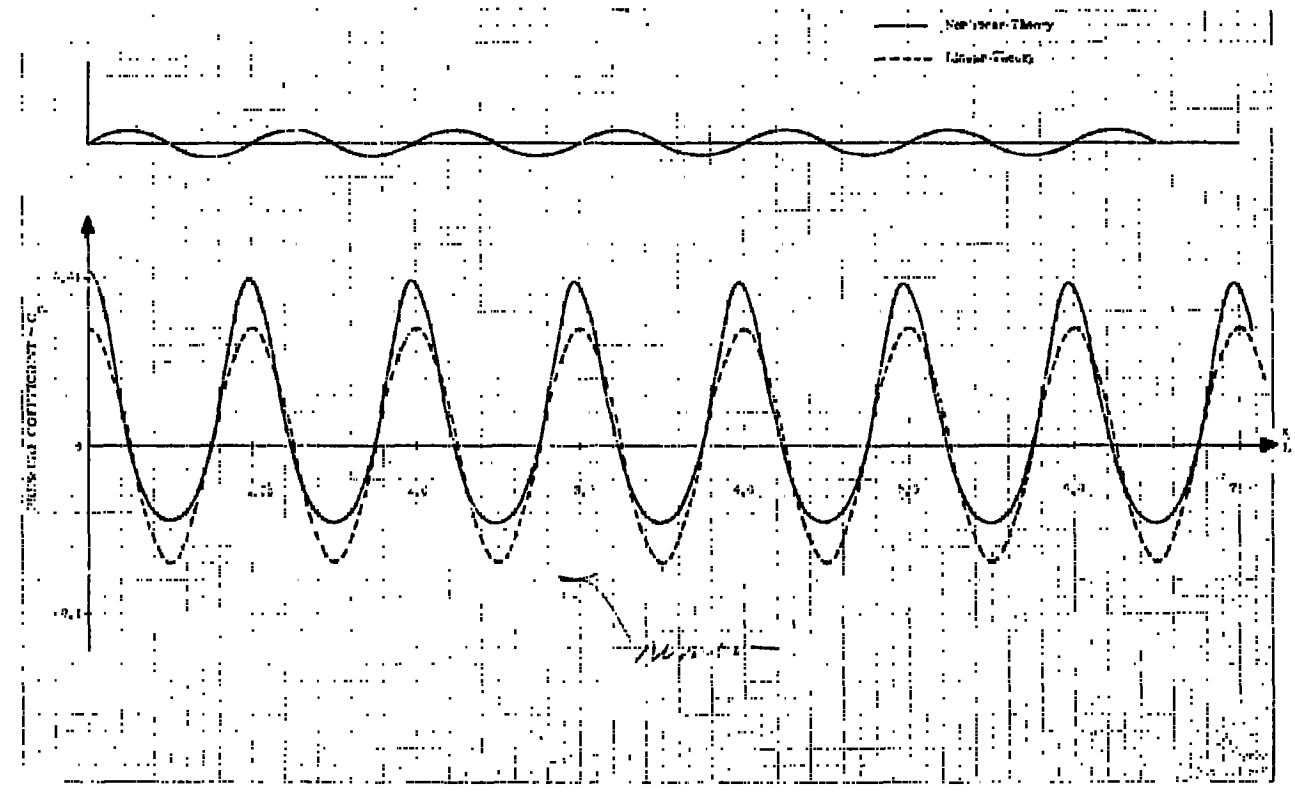

FIGURE 7. PRESSURE DISTRIBUTION ALONG WAVY WALLED CYLINDER OF FIGURE 5
$M_\infty = 4.62$ $a/L = 0.025$

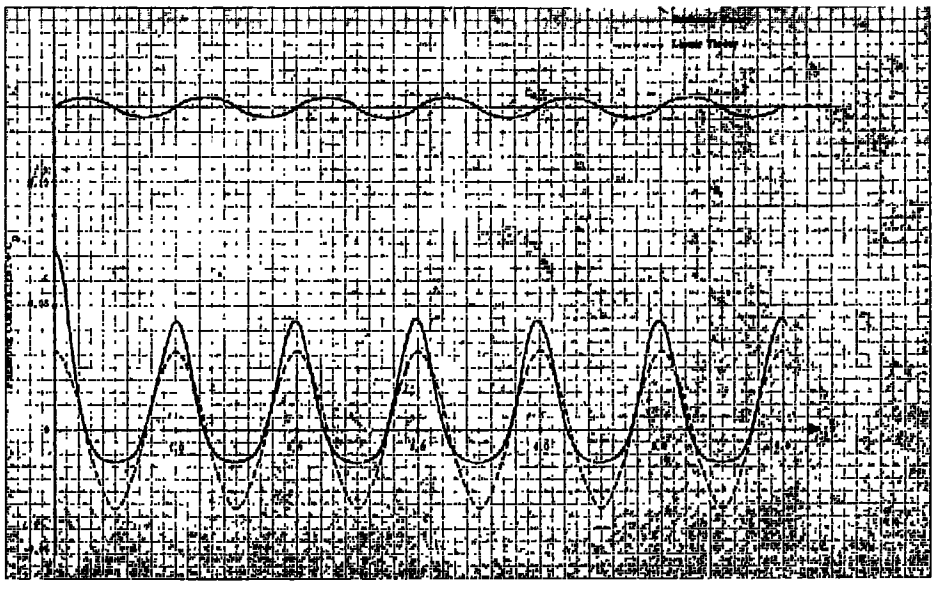

FIGURE 8. PRESSURE DISTRIBUTION ALONG WAVY WALLED CYLINDER OF FIGURE 5
$M_\infty = 10.0$ a/L = 0.025

IV. STEADY SUPERSONIC FLOW OVER A TWO-DIMENSIONAL WAVY WALL

The foregoing results for the wavy cylinder flow shall now be further substantiated by an analysis of the two-dimensional wavy wall flow. Here again the same basic features are found as for the cylinder flow, namely, no leading edge effect for medium Mach numbers and an overall shift in pressure levels. As an example, Figure 9 shows the pressure distribution along a two-dimensional wavy wall at M = 1.6 and an amplitude to wave length ratio a/L = 0.02 by linear and nonlinear theory. For this Mach number, the nonlinear method of characteristics solution predicts supersonic flow throughout the whole flow field. Reducing the free-stream Mach number to M = 1.405, however, already leads to subsonic flow right after the seventh shock (Figure 10). Lines of constant Mach number for this particular case are shown in Figure 11. A similar analysis for an amplitude to wave length ratio a/L = 0.01, on the other hand, reestablishes supersonic flow throughout the whole flow field at M = 1.405. To illustrate this amplitude dependence of the flow field a little further, Figures 12 and 13 show a third example, an amplitude to wavelength ratio a/L = 0.04. At this higher amplitude, the flow becomes subsonic already at M = 1.6 in going through the second shock wave.

McClure [14] gives measurements of the pressure distribution over two-dimensional wavy walls with amplitude to wavelength ratios of 0.02 and 0.01 at M = 1.405. The present calculations may point out the appreciable effects of aerodynamic nonlinearities in the low supersonic flow regime. The available experimental and analytical information in this particular

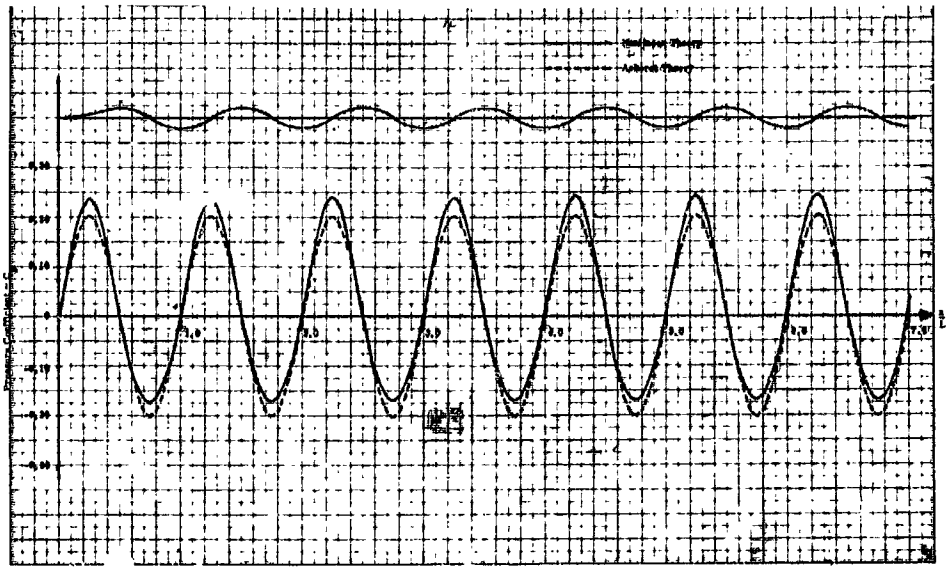

FIGURE 9. PRESSURE DISTRIBUTION ALONG A TWO-DIMENSIONAL WAVY WALL
$M_\infty = 1.60$ a/L = 0.02

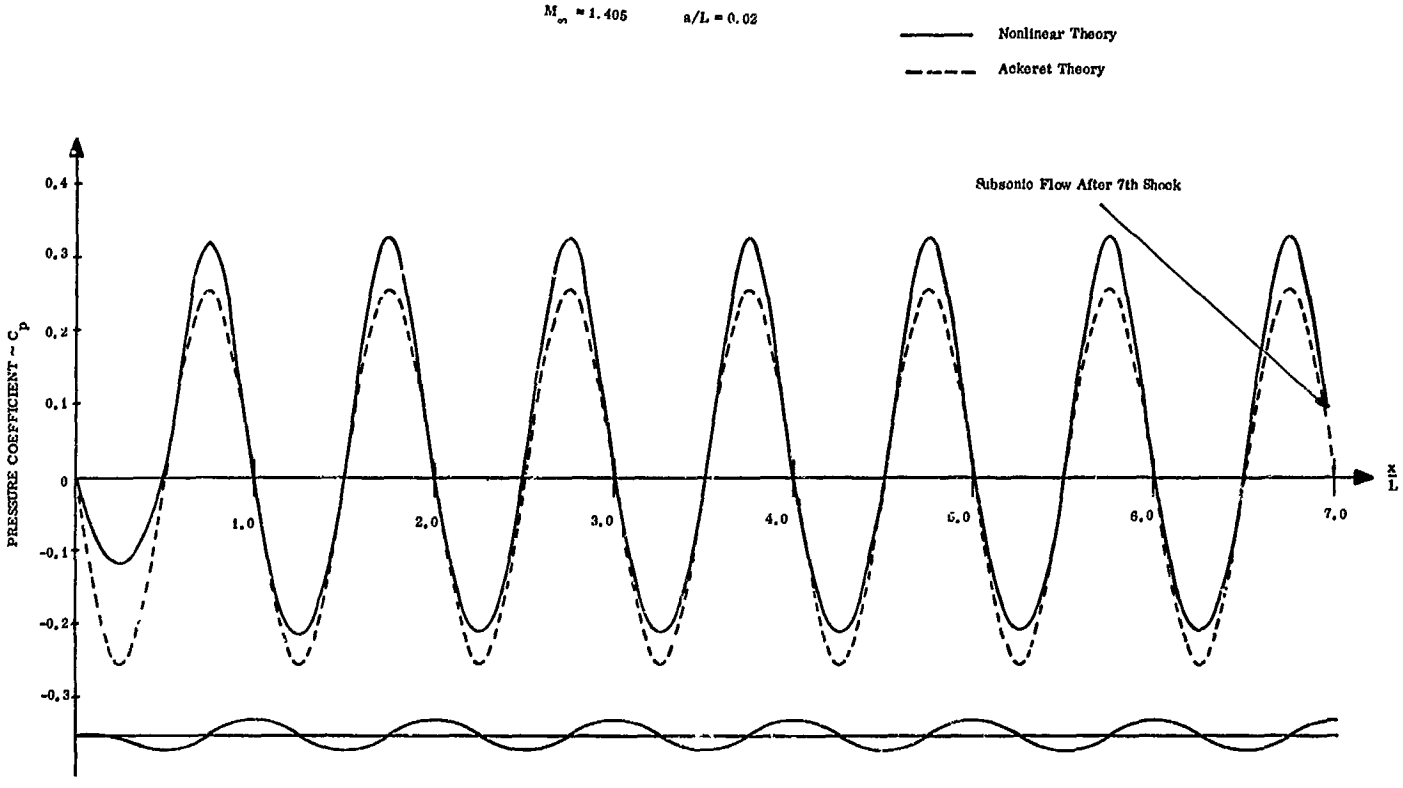

FIGURE 10. PRESSURE DISTRIBUTION ALONG A TWO-DIMENSIONAL WAVY WALL
M_∞ = 1.405 a/L = 0.02

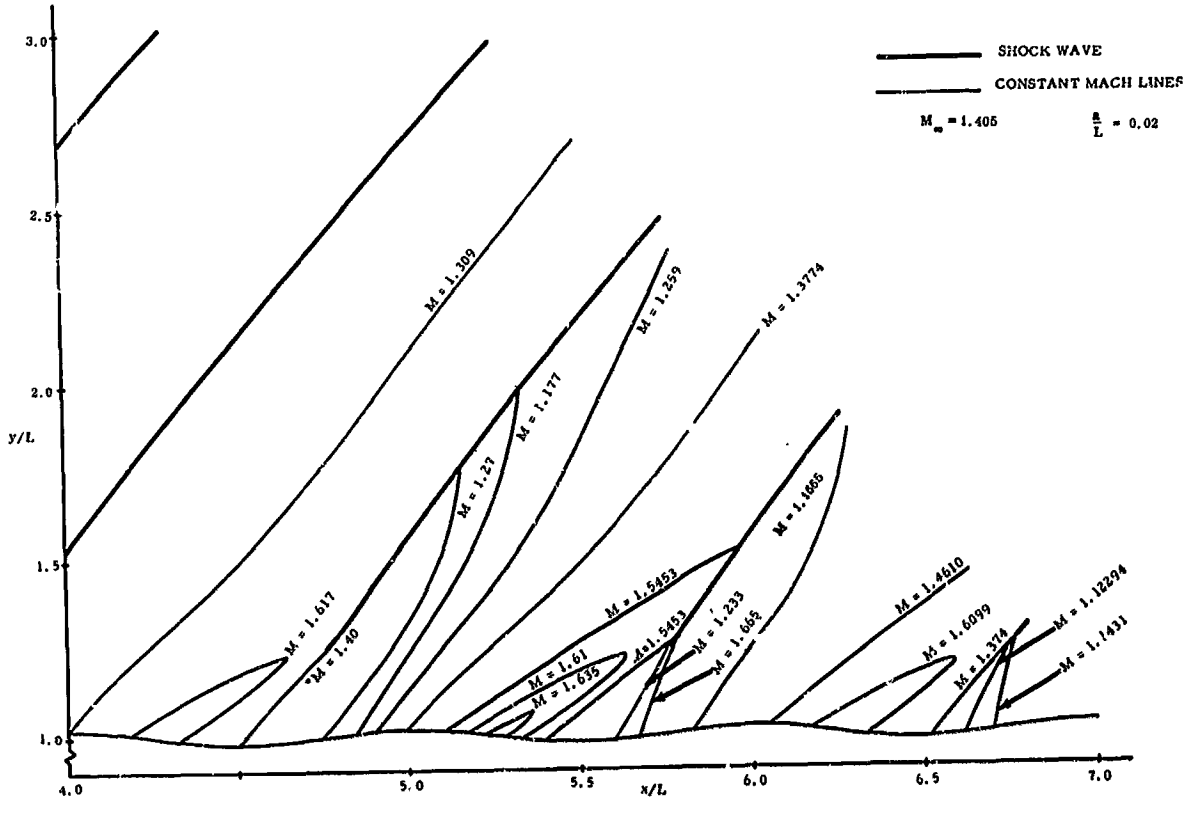

FIGURE 11. FLOW FIELD OVER WAVY WALL MODEL
M_∞ = 1.405 a/L = 0.02

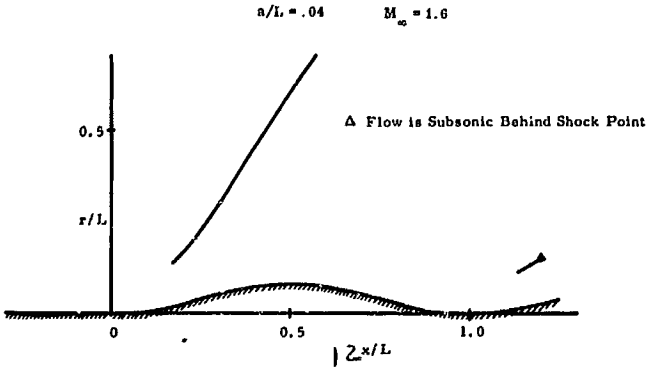

FIGURE 12. NONLINEAR FLOW FIELD OVER TWO-DIMENSIONAL WAVY WALL
$a/L = 0.04$ $M_\infty = 1.6$

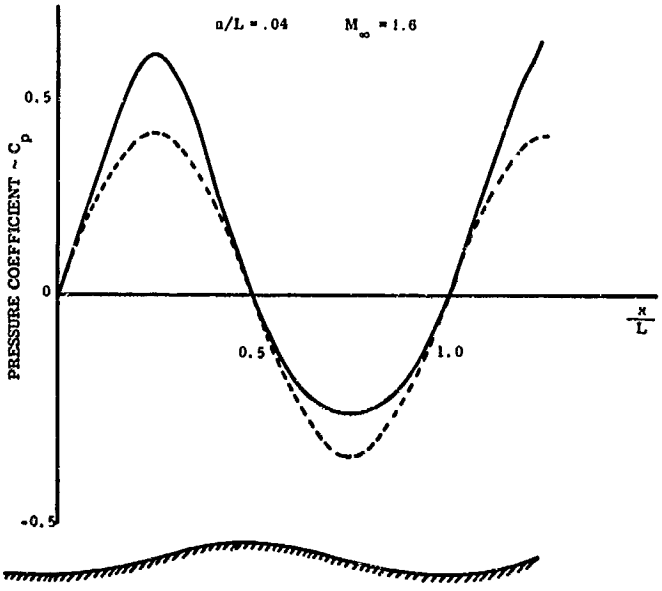

FIGURE 13. PRESSURE DISTRIBUTION ALONG A TWO-DIMENSIONAL WAVY WALL
$a/L = 0.04$ $M_\infty = 1.6$

speed range is unfortunately not sufficient to evaluate this effect in more detail. It is, therefore, one objective of the currently planned experimental program [16] to investigate these flow aspects very carefully.

V. CONCLUSIONS

Recent panel flutter studies [7, 8, 14] have led to the conclusion that linearized potential flow theory is inadequate for an accurate description of the flutter phenomenon at the low supersonic Mach numbers. Two phenomena were suggested as the main reasons for the apparent disagreement between theory and experiment, i.e., the effect of aerodynamic nonlinearity and the boundary layer effect. Since the flutter displacements are usually very small, it seems plausible to ignore the nonlinear transonic flow effects and to ascribe the dominant effect to the neglect of viscosity. Recent studies by McClure [14] and Anderson [15, 17] attempted to predict this boundary layer influence and to verify it by measuring the flow over wavy surfaces.

For the purpose of this study, the steady supersonic flow over wavy walled planar and cylindrical configurations was analyzed by means of a nonlinear method of characteristics solution and compared with linearized solutions. There is an appreciable dependence of the flow characteristics upon the amplitude to wavelength ratio causing mixed flow phenomena for low supersonic free-stream Mach numbers.

A more detailed analysis using transonic flow theories is necessary in order to evaluate the significance of transonic nonlinearities upon panel flutter. Conceivably, large amplitude flutter, flutter of buckled panels, and flutter of slightly curved panels could be appreciably influenced by such transonic flow effects.

VI. REFERENCES

1. Sylvester, M. A., and Baker, J. E.: Some Experimental Studies of Panel Flutter at Mach Number 1.3. NACA TN 3914, February 1957.

2. Eisley, J. G.: The Flutter of a Two-Dimensional Buckled Plate with Clamped Edges in a Supersonic Flow. AFOSR T. N. 56-296, 1956.

3. Jordan, P. F.: The Physical Nature of Panel Flutter. Aero. Digest., February 1956, p. 34.

4. Kordes, E. E., and Noll, R. B.: Flight Flutter Results for Flat Rectangular Panels. NASA TN D-1058, February 1962.

5. Kordes, E. E., Tuovila, W. J., and Guy, L. D.: Flutter Research On Skin Panels. NASA TN D-451, September 1960.

6. Rich, R.: Private Communication.

7. Fung, Y. C.: Some Recent Contributions To Panel Flutter Research. AIAA J., vol. 1, no. 4, April 1963, pp. 898-909.

8. Lock, M. H., and Fung, Y. C.: Comparative Experimental and Theoretical Studies of the Flutter of Flat Panels in a Low Supersonic Flow. Cal Tech, AFOSR TN-670, May 1961.

9. Garrick, I. E.: Nonsteady Wing Characteristics, Section F, Vol. VII, p. 677, of High Speed Aerodynamics and Jet Propulsion, Princeton University Press, Princeton, N. J . 1957.

10. Munk, M. M.: The Aerodynamic Forces on Airship Hulls. NACA Rept. 184, 1924.-

11. Platzer, M. F.: On An Extension of Oswatitsch's Equivalence Rule To Unsteady Flow. NASA TM X-53189, October 1964.

12. Liepmann, H. W., and Roshko, A.: Elements of Gasdynamics. John Wiley & Sons, Inc., New York, N. Y., 1958.

13. Beranek, R. G., Saunders, L., and Platzer, M. F.: Report to be published.

14. McClure, J. D.: On Perturbed Boundary Layer Flows. M. I. T. Rept. 62-2, June 1962.

15. Anderson, W. J.: Supersonic Wind Tunnel Tests of Wavy-Walled Cylinders. Report to be published.

16. Cooperative research program between Ames Research Center, Marshall Space Flight Center and Georgia Institute of Technology.

17. Anderson, W. J.: Experiments on the Flutter of Flat and Slightly Curved Panels at Mach Number 2.81. GALCIT Rept. SM 62-34, AFOSR 2996, June 1962.

III. AEROTHERMODYNAMICS

CONTINUOUS CARBON ABSORPTION STUDIES

By

C. C. Ferriso*, C. B. Ludwig*, and Robert M. Huffaker

SUMMARY

For thick optical paths of interest for Saturn type 1st stage boosters, carbon contributes more than 50 percent of the total emission. The absorption coefficient of this carbon produced in a RP-1/oxygen rocket engine combustion chamber has been experimentally determined and an analytical model developed which accurately expresses the absorption coefficient as a function of temperature, density, and wavelength. These measurements were made on a small rocket motor with the perfect nozzle designed by the method of Foelsch. This nozzle produces homogeneous, shock-free, axially parallel exit gases.

I. INTRODUCTION

The radiative heating of the base of large booster vehicles using a hydrocarbon-oxygen propellant is primarily due to emission from three constituents of the exhaust gases; CO_2, H_2O, and solid carbon. The emission from the molecules is restricted to the various vibration rotation bands and has a complex dependency on frequency. The solid carbon, on the other hand, gives rise to a continuous and smoothly varying spectrum. Water and carbon dioxide are equilibrium products of the combustion; solid carbon is not. Thermodynamic calculations predict no solid carbon for the mixture ratios at which the engine is normally operated.

An estimate of the relative importance of the different radiating species may be obtained from an examination of available data for the total hemispherical emissivities for conditions characteristic of the exhaust. It is found that, for the thick optical paths of interest for Saturn type boosters, carbon contributes more than 50 percent of the total emission. The data for solid carbon used in this estimate were obtained from theoretical values for the absorption coefficients (Fig. 1) of carbon particle clouds which, in turn, were based on the properties of pure bulk graphite. The experimental determination of these absorption coefficients for the carbon produced in RP-1/oxygen rocket engine combustion chambers is the primary purpose of this work.

* Employed by General Dynamics/Convair
San Diego, California

The determination of the emissive properties of volumes of gas containing dispersed carbon particles is, in some aspects, much simpler than the equivalent problem for the molecular emitters, and in some aspects much more difficult. The molecular absorption spectra, when observed at high spectral resolution, generally show a highly complex functional dependence on wavelength. In contrast to this the carbon absorption spectra are expected to vary smoothly with wavelength. Thus Beer's law applies to transmission or emission measurements made at moderately low spectral resolution and measurements made on thin samples of gas may therefore be extrapolated reliably to any desired thickness. This greatly simplifies the experimental problem since only the temperature and not the pathlength need be varied.

Since carbon is present in particulate form, the particles will scatter, as well as absorb light. If the particles are not small compared to wavelength, this scattering may significantly affect the radiant heat transfer. In general, the effect of scattering will be to lower the total energy radiated by the gas from that expected when scattering is neglected, although the radiation in particular directions may actually be enhanced at the expense of that in other directions for some flow field configurations.

One of the most difficult aspects of the present problem is the establishment of the relation between the amount and properties of the carbon particles produced in the small scale rocket engines with those of the full scale engines. The solid carbon produced in the combustion of a fuel-rich mixture and oxygen is a nonequilibrium product. In the absence of reliable quantitative methods for predicting the amount formed in a given situation, some measurements on the full scale engine will be required.

II. SCOPE OF THE PRESENT EXPERIMENTAL PROGRAM

The experiments consist of measuring the emission from small, hydrocarbon-fueled rocket engines operated in combustion regimes where carbon is formed. These measurements are made at the exit plane using the techniques and equipment applied to

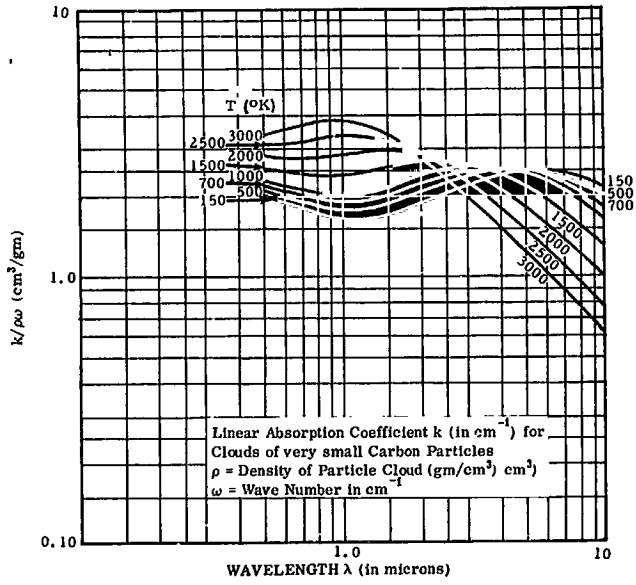

FIGURE 1. LINEAR ABSORPTION COEFFICIENT FOR CARBON PARTICLE CLOUDS

measurements of emissivities of gases. By holding combustion constant and varying the expansion ratio of the engine, one can vary the temperature of the system while holding the mass fraction of carbon nearly constant. The data are reduced to the form of absorption coefficient as a function of combustion conditions: temperature and wavelength. Since the carbon is produced by an essentially unknown process in the combustion chamber, the application of data taken in small scale experiments to the full scale motor must be carried out with some care. Although it is not possible to duplicate the combustion conditions of the large engine in the small scale engine, part of the program is devoted to examining the effect on carbon content and the spectral distribution of the absorption coefficient of varying different combustion parameters. The object is to identify those design parameters that control the carbon formation, such as mixture ratio, chamber pressure, chamber length, injector pattern, injector hold size, throat diameter, state of oxidizer (LOX or GOX), and cooling water flow rate.

III. TEST APPARATUS AND MEASUREMENT

A. ROCKET BURNER

Absorption coefficient measurements require homogeneous samples of gas of known temperature, pressure, and composition, containing measurable quantities of carbon particles. These gas-particle systems are produced by small rocket motors with contoured nozzles burning RP-1 and oxygen as propellants.

An exploded view of a typical motor is shown in Figure 2. The motor is rated at 160 lb (715 N) nominal thrust (0.6 lb/sec [0.27 kg/sec]mass flow rate). The motor consists of an electrolytic copper injector, a machined electrolytic copper combustion chamber-nozzle piece (the "liner"), and a stainless steel cooling jacket.

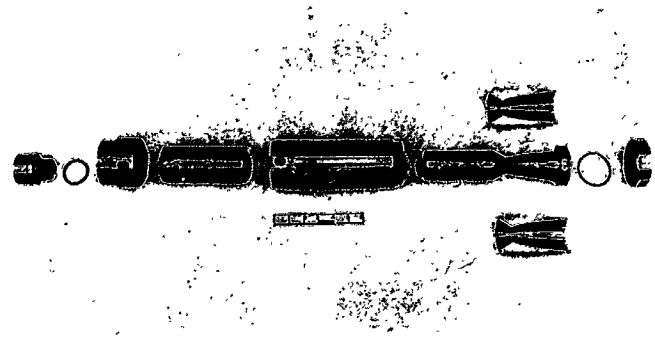

FIGURE 2. EXPLODED VIEW OF MOTOR

The liner can be made with different area ratios. All liners are constructed with the same chamber dimensions and nozzle contour to the throat. The diverging sections are perfect nozzles designed by the method of Foelsch, using an IBM 7090 computer program; this computes the nozzle contour for a given area ratio, throat diameter, and combustion product ratio of specific heats. These nozzles produce homogeneous, shock-free, axially parallel exit gases, as shadowgraph studies have shown. Figure 3 shows some of the shadowgraph results.

B. INFRARED EMISSIVITY APPARATUS

Spectral emissivity measurements are made of the carbon continuum between 0.7 μ and 4.0 μ using spectrometer equipment. (Fig. 4).

The energy emitted by the burner exit gases is focused on the entrance slit of Perkin-Elmer Model 99 double-pass monochromator. A thermocouple de-detector or a cooled PbS detector, and a CaF_2 prism is used in the monochromator. A wave number calibration of the monochromator is made using known absorption bands of various gases. For the energy calibration, the two-position diagonal mirror is rotated to fill the monochromator aperture with radiation from a Barnes Engineering Model RS6A 1000°C (1270°K) blackbody calibration source. A temperature measurement is made of the source during calibration with a Pt-Rh thermocouple placed on the cavity surface. The optical system is enclosed and flushed with dry nitrogen to reduce atmospheric absorption.

BLANK PAGE

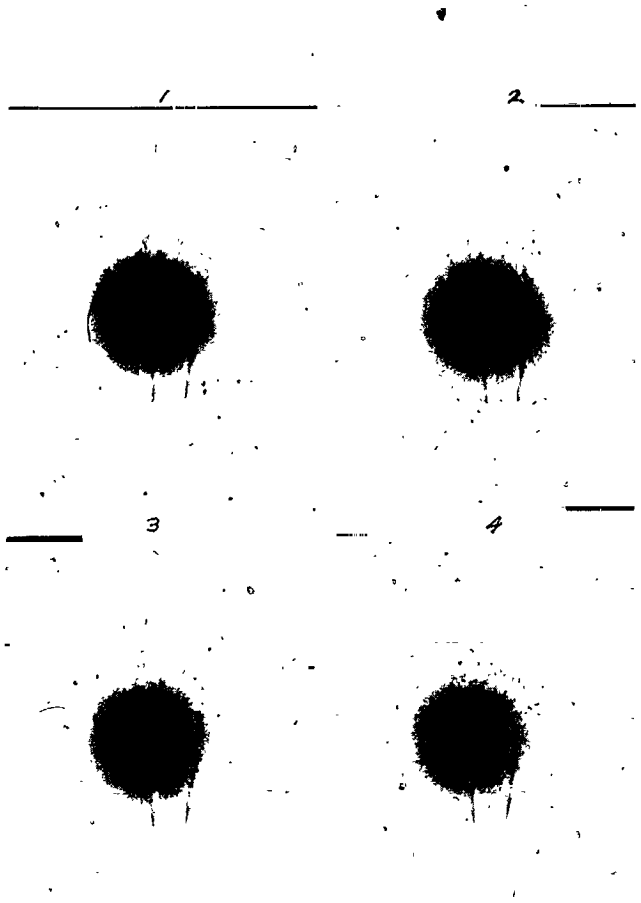

FIGURE 3. SHADOWGRAPHS OF BURNER EXITS

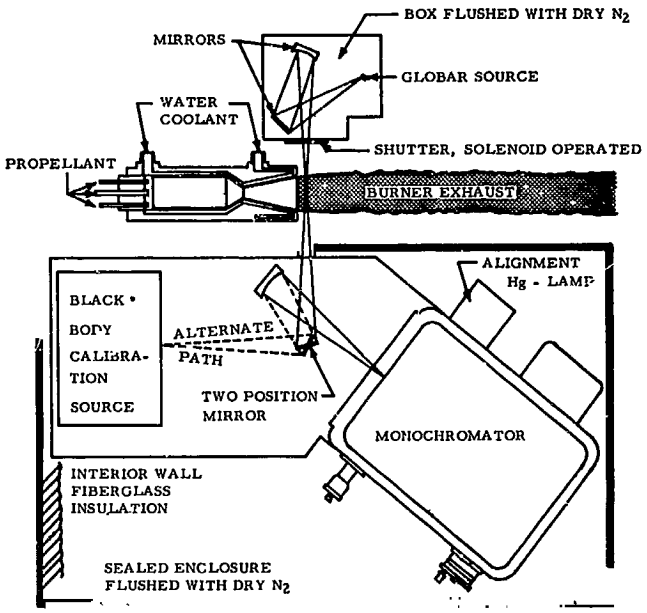

FIGURE 4. SPECTROMETER FOR SPECTRAL EMISSIVITY MEASUREMENTS

C. TEMPERATURE MEASUREMENTS

Temperatures, both in the continuum and molecular spectral regions, are measured with an absorption-emission technique. The spectral emissivity, $\epsilon(\nu)$, is calculated from the measured transmission with

$$\epsilon(\nu) = 1 - \frac{I(\nu)}{I_o(\nu)} \qquad (1)$$

where $I_o(\nu)$ is the incident globar energy and $I(\nu)$ is the transmitted energy of the source (globar) attenuated by the hot exhaust gas. The temperature can then be determined from the corresponding Planck blackbody function.

D. SPECTRAL EMISSIVITIES MEASUREMENTS

The spectral emissivities are determined from emission measurements and the experimental gas temperature measurements. The energy emitted by the exhaust gas is obtained on a calibrated energy basis by relating the recorder deflection to the blackbody calibration source. Readings from the recorder traces (exhaust gas and calibration source) are made at constant monochromator drum settings and serve as input to a computer data reduction program that converts drum settings into wave numbers by using the original wave number calibration curve. The computer program then evaluates the spectral emissivities at a particular wave number, ν, from

$$\epsilon(\nu, T) = \frac{G(\nu) N^\circ(\nu, T_B)}{B(\nu)\, N^\circ(\nu, T)} \qquad (2)$$

where $G(\nu)$ and $B(\nu)$ are the voltage deflections at a particular wave number for the hot gas and blackbody source, respectively; $N^\circ(\nu, T_B)$ is the Planck blackbody energy value for the calibration source at its temperature, T_B; and $N^\circ(\nu, T)$ is the Planck blackbody energy value for the hot gas where T at the measured mixture ratio is taken from a curve fit to the experimental temperature data points. The data reduction program is also set up to give total emissivities, spectral absorption coefficients, and simple radiance (energy) spectra.

IV. RESULTS

Data have been collected on two liners having area ratios of 5.25:1 and 3:1. The exit temperatures versus mixture ratios are plotted in Figure 5, together with theoretical values, assuming complete equilibrium in the chamber and shifting equilibrium expansion to the exit plane, which represents an upper limit. It is interesting to note that the experimental values exceed the theoretical predicted values. It is believed that this behavior is, in part, due to the non-equilibrium process of condensing carbon in the chamber.

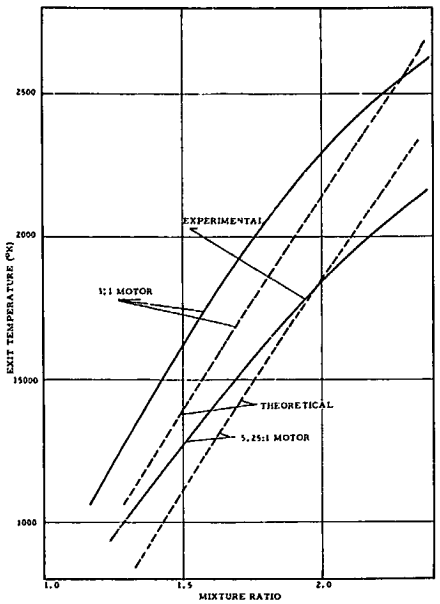

FIGURE 5. PLOT OF EXPERIMENTAL AND THEORY VALUES OF EXIT TEMPERATURES VS MIXTURE RATIOS FOR THE 3:1 AND 5.25:1 ROCKET MOTORS

In Figures 6 and 7 we show typical traces of the measured spectral emissivities at a mixture ratio of 1.42 for the 5.25:1 and the 3:1 area ratio number, respectively. The molecular emission at 4.3 μ and 2.7 μ

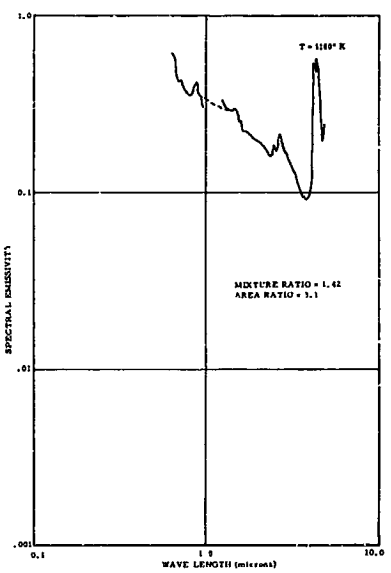

FIGURE 6. TYPICAL TRACE OF THE MEASURED SPECTRAL EMISSIVITIES AT A MIXTURE RATIO OF 1.42 FOR THE 5.25:1 AREA RATIO MOTOR

is clearly indicated. These traces are reduced to pure continuum radiation by subtracting the molecular radiation from CO_2 and H_2O. In Figure 8 is plotted the "effective spectral absorption coefficient" of carbon

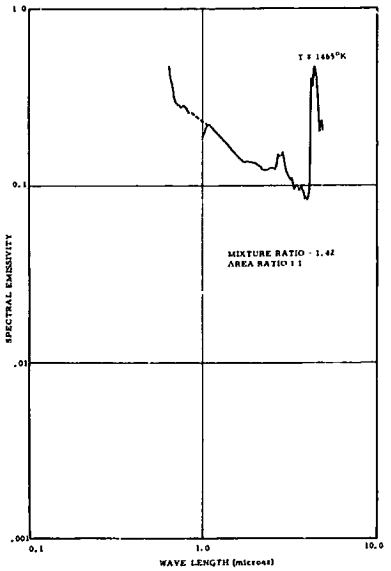

FIGURE 7. TYPICAL TRACE OF THE MEASURED SPECTRAL EMISSIVITIES AT A MIXTURE RATIO OF 1.42 FOR THE 3:1 AREA RATIO MOTOR

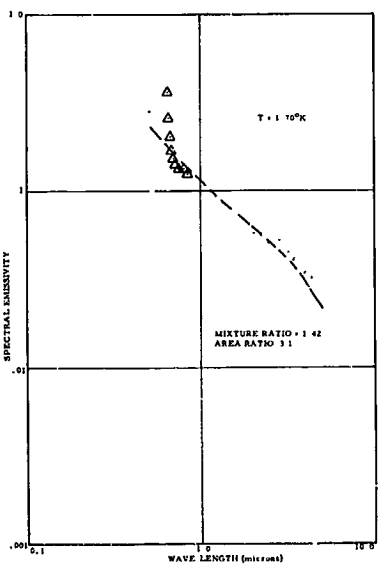

FIGURE 8. COMPARISON OF EXPERIMENTAL AND THEORETICAL DATA WHERE THEORETICAL CALCULATIONS ARE ADJUSTED AT 2.2 MICRONS

times the carbon density, ρ_c, as dots. The spread indicates the experimental uncertainty, as well as the uncertainty in the data reduction procedures. The dashed lines represent the model calculations taken from Figure 1. These lines were placed to give the best agreement with the experimental points. There is good agreement in the shape of these curves. The scaling factor is the unknown carbon concentration, using the theoretical absorption coefficients. The carbon concentration is given in Figure 9 for all mixture ratios investigated. The agreement between the

values of the two different engines indicates the proper temperature dependency of the absorption coefficients.

It is found that the carbon concentration is strongly dependent on the mixture ratio.

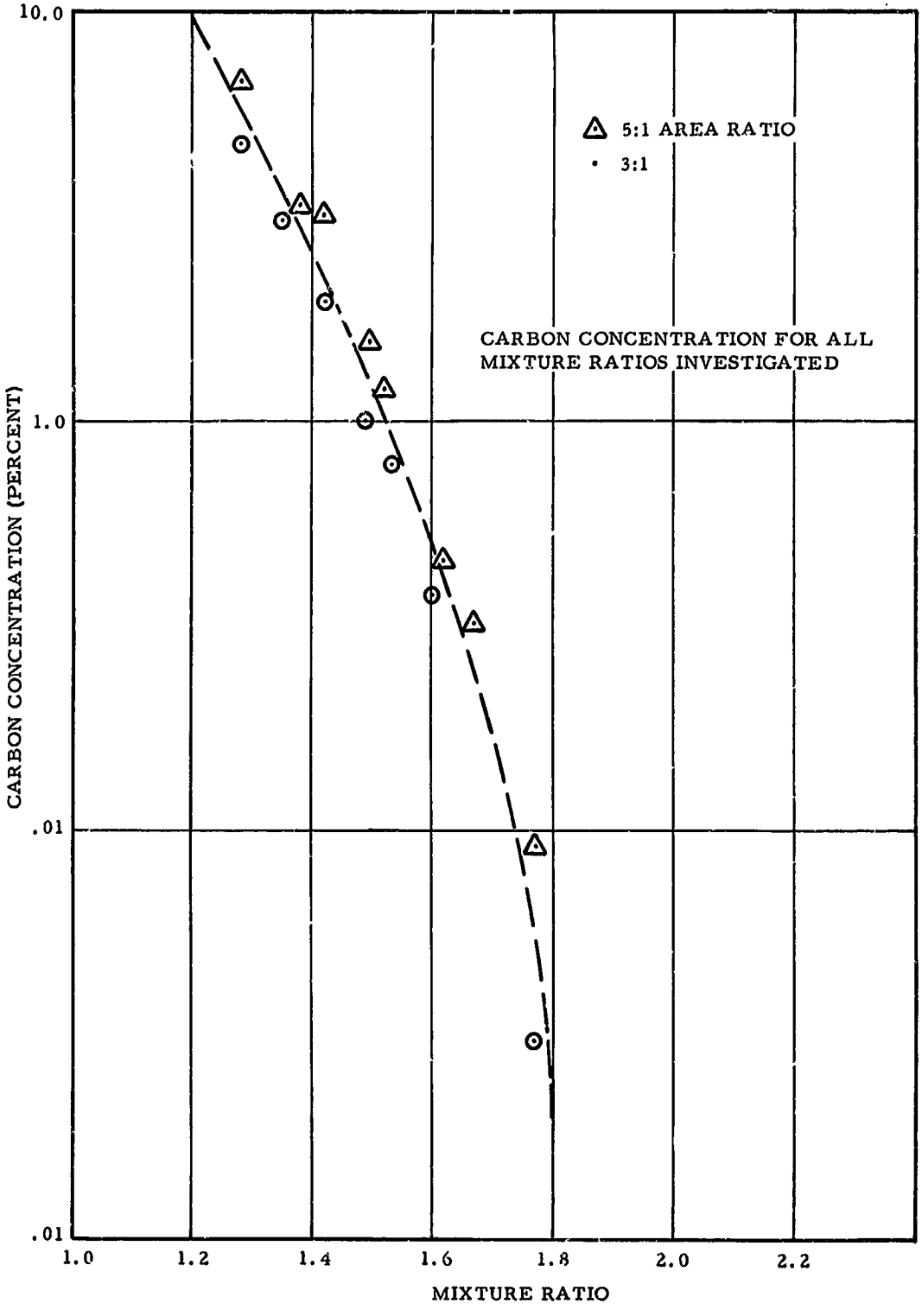

FIGURE 9. CARBON CONCENTRATION FOR ALL MIXTURE RATIOS INVESTIGATED

BLANK PAGE

INFRARED SPECTRAL TRANSMITTANCES FOR DETERMINING RADIANT FLUX OF INHOMOGENEOUS GASES

By

Robert M. Huffaker

SUMMARY

A general method has been developed to calculate spectral transmittances of inhomogeneous gases from the properties of homogeneous gases. Thus, any calculation of spectral transmittance for a particular inhomogeneous gas path can be done by properly combining known "band model" data on gases at constant temperature, pressure, and concentration. The method developed is based principally on two special spectroscopic concepts: (1) the molecular band-model, and (2) the Curtis-Godson approximation. This method has been experimentally verified over the temperature, pressure, and wavelength range typical of Saturn V exhausts.

I. INTRODUCTION

Heat transfer to the base of a launch vehicle can occur through two modes: convection and radiation. There is evidence that, on large vehicles burning RP-1 (kerosene) and oxygen, these two modes are both important. There currently exists no satisfactory technique of calculating base heating for a given engine array at various altitudes and vehicle velocities. We therefore require both better means of measuring heat transfer to the base region of vehicles actually under test, and more rigorous and reliable means of predicting heat transfer to vehicles before testing.

Convection to the base region depends upon the properties of the gas flow close to the surface being heated. Simple models of the flow, together with boundary layer correlations for the heat transfer coefficient, have been used in the past to arrive at local heating rates on the heat shield. Radiation, on the other hand, is sensitive to the entire flow field not occluded by the vehicle structure. Here predictions have been made either by representing the exhaust plume as a surface with a given emissivity, temperature, and configuration, or by assuming a simple geometrical configuration for the hot gas, which is presumed to be uniform, and integrating the equation of transfer with a simplified absorption coefficient.

The exhaust plume from a multiple-engine configuration like the Saturn-V is an extraordinarily complex gas-dynamical structure. The exhaust jets from the different engines interact with the atmosphere and with each other through an intricate series of shock waves and turbulent mixing layers. Some of the exhaust material flows back into the base region. Wherever the exhaust material mixes with the atmosphere, it can burn, and, at low altitudes, it does. With such a complicated flow field controlling the heat transfer to a base region, it is not surprising that simple models of the heat transfer must be tied strongly to empirical data.

In an effort to learn more about the base heating problem and to provide both mathematical techniques and values of parameters required for solution of the problem, a number of studies have been undertaken. These involve descriptions of the flow field, the radiative properties of its constituents, and a radiation calculation method for inhomogeneous gases.

Water vapor, carbon dioxide, and solid carbon particles (soot) are the principal radiators in the first-stage plume. Water vapor is the only radiator of importance in the plumes of the hydrogen-fueled stages. Extensive experimental and theoretical studies of the emission of CO_2 under various conditions have been made, and the properties of this molecule are well understood. Much less is presently known about H_2O. A NASA sponsored program, directed by Dr. Carmine Ferriso, is now underway at General Dynamics/Convair. The program was set up to measure the emission and absorption characteristics of water vapor for temperatures from 300°K to 3000°K and for pressures of 0.1 atmospheres to 1.0 atmospheres. Band model parameters will also be obtained for water vapor from this experimental data and additional theoretical studies.

To calculate the radiant heating to a rocket base by the exhaust plumes, one must know the spectral transmittances of the plume gases. Since plumes are strongly inhomogeneous, one must determine spectral transmittances of inhomogeneous gases explicitly to develop a calculation method. A general method has now been developed with the Warner and Swasey Company Contract under the direction of Dr. Richard Tourin, to calculate spectral transmittances of

inhomogeneous gases from the properties of homogeneous gases. Thus, any calculation of spectral transmittance for a particular inhomogeneous gas path can be done by properly combining known data on gases at constant temperature, pressure, and concentration.

The method developed is based principally on two special spectroscopic concepts: (1) the molecular band model, and (2) the Curtis-Godson approximation. The molecular band model is a mathematical representation of the effective radiant energy in portions of the spectrum where gas molecules emit and absorb energy. The band model yields an explicit, closed formula for the molecular radiation within each selected spectral region of interest, which uses as input data the averaged line strength, the averaged line spacing and the averaged line half width. An average of 25 wave numbers is considered sufficient. An exponential line intensity distribution or a delta function distribution is also used in the band model. The use of a band model is critically important for practical calculations of gas radiation. Without a band model, one would have to deal individually with each of the many thousands of spectral lines that contribute to molecular radiation, a much bigger and more difficult problem, parts of which are beyond solution at present. The Curtis-Godson approximation is a method of combining the parameters that appear in the band model formulae in such a way that the parameters needed for an inhomogeneous gas calculation are obtained solely from homogeneous gas data. This is also a critical factor, because the necessary parameters need be calculated or measured in the laboratory only for uniform gas samples. Without the Curtis-Godson, or some equally good approximation, one would have to treat each inhomogeneous gas path as a special case.

II. THEORY

A. PROBLEM STATEMENT AND DEFINITION

We wish to predict the radiant energy transferred from an inhomogeneous mass of hot gases. The radiated energy is distributed irregularly over a broad range of the spectrum, mainly at wave numbers (the frequency divided by the velocity of light) between 2000 cm^{-1} and 10,000 cm^{-1}. Once the energy is obtained along a line of sight, the radiant flux is then integrated over all spectral regions for this line of sight, and integrated over solid angle to obtain the total radiant flux. In this report we are concerned with the first part: how to determine the radiant flux incident upon the base in any spectral range, contributed by the hot gases along a line of sight like the one in Figure 1. The key variable turns out to be the spectral transmittance of the inhomogeneous gas. The method used to calculate radiant flux for a homogeneous gas will be outlined first; this should clear the approach to the inhomogeneous case.

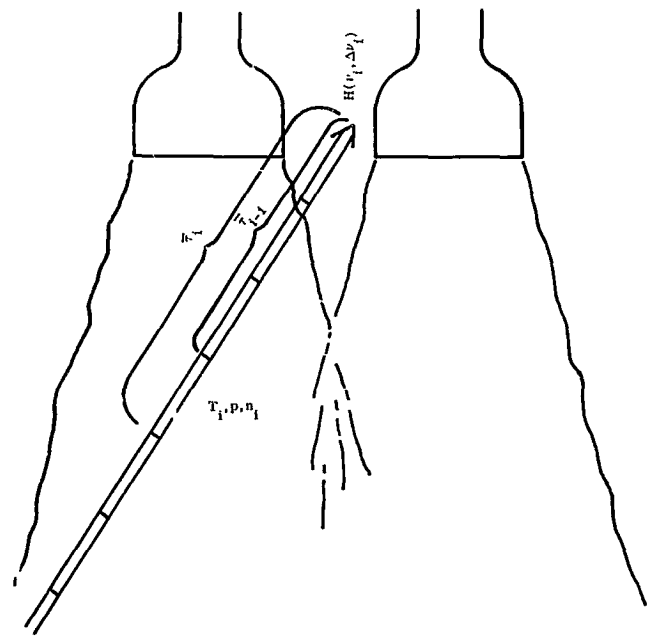

FIGURE 1. SCHEMATIC OF ROCKET EXHAUST PLUMES. THE ARROW REPRESENTS A TYPICAL INHOMOGENEOUS GAS PATH

Assume a mass of homogeneous hot gas, which emits and absorbs radiant energy at wave number ν. A beam of radiant energy at wave number ν, of arbitrary magnitude $I_o(\nu)$ is sent through the hot gas. Some of this beam is absorbed in the gas, and the remainder $I(\nu)$ emerges. The gas itself emits radiant energy at wave number ν, of magnitude $N_g(\nu, T)$.

The spectral radiance of the hot gas $N_g(\nu, T)$ is defined as the radiant power per unit area, per unit solid angle, per unit wave number interval, in watt-cm^{-2}-steradian^{-1}-$cm_{\Delta\nu}$.

The spectral transmittance $\tau_{(\nu)}$ is the fraction of incident radiant energy emerging from the gas; i.e.,

$$\tau(\nu) = \frac{I(\nu)}{I_o(\nu)} \quad . \tag{1}$$

The spectral absorptance $\alpha(\nu)$ is the fraction of incident radiant energy absorbed in the gas; i.e., the fraction not transmitted, or

$$\alpha(\nu) = 1 - \tau(\nu) = 1 - I(\nu)/I_o(\nu). \tag{2}$$

The spectral emissivity $\epsilon(\nu)$ is the ratio of the gas radiance, $N_g(\nu,T)$ to the radiance of a blackbody, $N_b(\nu,T)$. Kirchhoff's law states that

$$\epsilon(\nu) = \alpha(\nu) \quad , \tag{3}$$

from which one can easily get $\epsilon(\nu)$ by measuring $\alpha(\nu)$. In radiant transfer studies of isothermal gases, attention is focused on the spectral emissivity, because if one knows $\epsilon(\nu)$ and the temperature, the radiance is easily computed; thus,

$$N_{gas}(\nu,T) = \epsilon(\nu,T)\, N_b(\nu,T) \quad . \tag{4}$$

In considering strongly inhomogeneous gases, the radiance calculation is formulated quite differently, because the emission and absorption within the gas must be considered explicitly. The equation of radiative transfer becomes

$$H(\nu,\Delta\nu_j) = \sum_{i=1}^{n} N_b(\nu_j,T_i)\left[\bar{\tau}_{i-1}(\nu_j,\Delta\nu_j) - \bar{\tau}_i(\nu_j,\Delta\nu_j)\right] \quad , \tag{5}$$

where the terms are understood by reference to Figure 1. One now considers the inhomogeneous structure of the line of sight, and considers it subdivided into a series of zones, each of which is homogeneous. The quantities in equation (5) are then; $H(\nu_j,\Delta\nu_j)$ is the irradiance at the point of interest within wave number $\Delta\nu_j$ centered at wave number ν_j; $N_b(\nu_j,T_i)$ is the blackbody spectral radiance at ν_j, at the temperature T_i of the ith zone; $\bar{\tau}_{i-1}(\nu_j,\Delta\nu_j)$ is the spectral transmittance of the inhomogeneous path comprising all zones between the ith zone and the point of interest; and $\tau_i(\nu_j,\Delta\nu_j)$ is the spectral transmittance of the path including the ith zone and all other zones between the ith zone and the target point. The Planck radiance functions are well known, and tabulated, so that the quantities we seek are the inhomogeneous transmittances; Warner and Swasey Company has accomplished this by applying the Curtis-Godson approximation. First, the band model method for a homogeneous gas will be defined. Then it will be shown how these homogeneous gas parameters are combined to get the corresponding parameters for the inhomogeneous case.

B. THE STATISTICAL BAND MODEL

While many band models have been studied, the statistical model best represents the spectra of water vapor and carbon dioxide. The need for band models is illustrated in Figure 2 where two small spectral intervals $\Delta\nu_1$ and $\Delta\nu_2$ are illustrated showing typical spectral lines of a molecular spectrum. A band model is a mathematical formula which gives the transmittances, for intervals $\Delta\nu$ in which one is interested, without the need to deal with the individual spectral lines. The band model is vitally necessary

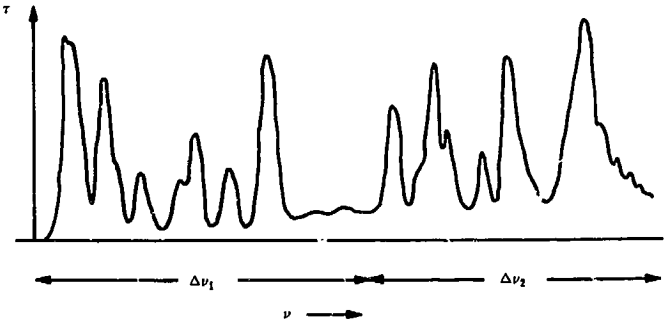

FIGURE 2. SCHEMATIC INFRARED SPECTRUM OF A HOT GAS IN TWO NARROW INTERVALS, PLOTTED AS TRANSMITTANCE VERSUS WAVE NUMBER

in radiant heat transfer calculations for two reasons: (1) the number of spectral lines involved in a practical problem may run into hundreds of thousands, and for most of these not enough is known for accurate calculations; and (2) practical spectroscopic instruments distort the spectral lines, so that the "true" spectrum cannot be measured. The statistical band model formula for the spectral transmittance τ at wave number ν is

$$\ln \frac{1}{\tau} = 2\pi \frac{\gamma}{d} f(x) \quad , \tag{6}$$

where

$$x = \frac{(S/d)\ell}{2\pi\frac{\gamma}{d}} \quad . \tag{7}$$

The term $\frac{\gamma}{d}$ is the ratio of average line width to average line spacing in the spectral interval $\Delta\nu$ at ν; $\frac{S}{d}$ is the ratio of average line strength to average line spacing in the same interval; $f(x)$ is the Ladenberg-Reiche function; and ℓ is the path length in the gas. The strength parameter $\frac{S}{d}$ is proportional to P_a, the partial pressure of absorbing gas; thus,

$$\frac{S}{d} = \frac{S^\circ}{d} P_a \quad .$$

Then, if we define

$$M = P_a \ell \quad ,$$

equation (7) can be rewritten as

$$x = \frac{\frac{S^\circ}{d}\, M}{2\pi\, \frac{\gamma}{d}} \quad . \tag{7a}$$

To apply the statistical model to calculating transmittances of homogeneous gases, we need only two parameters: the strength parameter S/d, and the width parameter γ/d, averaged over each spectral interval of interest. This information is being obtained under contract to General Dynamics/Convair.

C. COMBINATION OF ISOTHERMAL BAND MODEL PARAMETERS TO GET INHOMOGENEOUS TRANSMITTANCES

Several techniques were investigated by Warner and Swasey for combining isothermal band model parameters to predict the transmittance through an inhomogeneous path. The Curtis-Godson approximation gave the best results.

The Cutris-Godson method is based on the premise that one can substitute a hypothetical homogeneous gas path that would have the same spectral path will have the same spectral transmittance as an inhomogeneous path if the parameters $(\gamma/d)'$ and X' as defined by equations (8) and (9) below are used in the band model formulas for the transmittance of a homogeneous gas, equations (6) - (7a).

$$\left(\frac{\gamma}{d}\right)_i' = \frac{\sum_{h=1}^{i} p_a^h \left(\frac{S^\circ}{d}\right)_h \ell_h \left[\left(\frac{\gamma_a^\circ}{d}\right)_h p_a^h + \left(\frac{\gamma_b^\circ}{d}\right)_h p_b^h\right]}{\sum_{h=1}^{i} \left(\frac{S^\circ}{d}\right)_h p_a^h \ell_h} \tag{8}$$

$$X_i' = \frac{\left\{\sum_{h=1}^{i} \left(\frac{S^\circ}{d}\right)_h p_a^h \ell_h\right\}^2}{2\pi \sum_{h=1}^{i} \left(\frac{S^\circ}{d}\right)_h p_a^h \ell_h \left[\left(\frac{\gamma_a^\circ}{d}\right)_h p_a^h + \left(\frac{\gamma_b^\circ}{d}\right)_h p_b^h\right]} \tag{9}$$

The subscript h in equations (8) and (9) stands for each of the homogeneous zones into which the inhomogeneous path has been divided. The limits indicate that the number of zones in the inhomogeneous path is i. Substituting equations (8) and (9) into equations (6) and (7) will give $\bar{\tau}_i$ for use in equation (5). When the limit i-1 is used instead of i, one can calculate $\bar{\tau}_{i-1}$ of equation (5). P_b is the pressure of nonradiating gas in each zone, such as nitrogen, and $\left(\frac{\gamma_b^\circ}{d}\right)$ is the line-width parameter for this gas. The derivation of equations (8) and (9) is given in G. R. Harrison, Practical Spectroscopy, Chapter 14. Equations (8) and (9) are derived by requiring that the mean transmittance of the inhomogeneous path is exactly equal to the mean transmittance of the homogeneous path for the extreme cases of infinitesimally small path lengths and very large path lengths. For intermediate path lengths, the equality is only approximate.

D. RECAPITULATION

The Curtis-Godson method is based on the premise that one can substitute a hypothetical homogeneous gas path that would have the same spectral transmittance as a real, inhomogeneous path encountered in a rocket exhaust plume. These parameters were shown to be calculable from the band model parameters of the homogeneous zones. Once the parameters of the hypothetical path were determined, the spectral transmittance was calculable from the statistical band model formula for spectral transmittance. The complex problem of determining transmittances of inhomogeneous gases has thus been reduced to the simpler problem of determining band model parameters of homogeneous gases.

III. EXPERIMENTS AND RESULTS

Experiments were carried out at Warner and Swasey to test the theory, determine the accuracy, and obtain values of band model parameters for specific cases. Band model parameters were measured for isothermal gases at various temperatures, the results were used to predict transmittances of known inhomogeneous paths, and the inhomogeneous path transmittances were compared to the theoretical prediction.

Using a furnace-gas cell arrangement, numerous transmittances of water vapor inhomogeneous paths were measured and compared to transmittances calculated by the Curtis-Godson combination method in conjunction with the statistical band model. Each inhomogeneous path consisted of two zones, of different temperature, pressure, and composition. Zone path lengths varied from 1 1/2 inches to 24 inches, and total paths from 3 inches to 48 inches. Typical results are given in Table 1. Table 1 also shows two-zone transmittances calculated from the transmittances of the individual zones by the commonly used Beer-Lambert law, which gave an order of magnitude larger error than did the Curtis-Godson method.

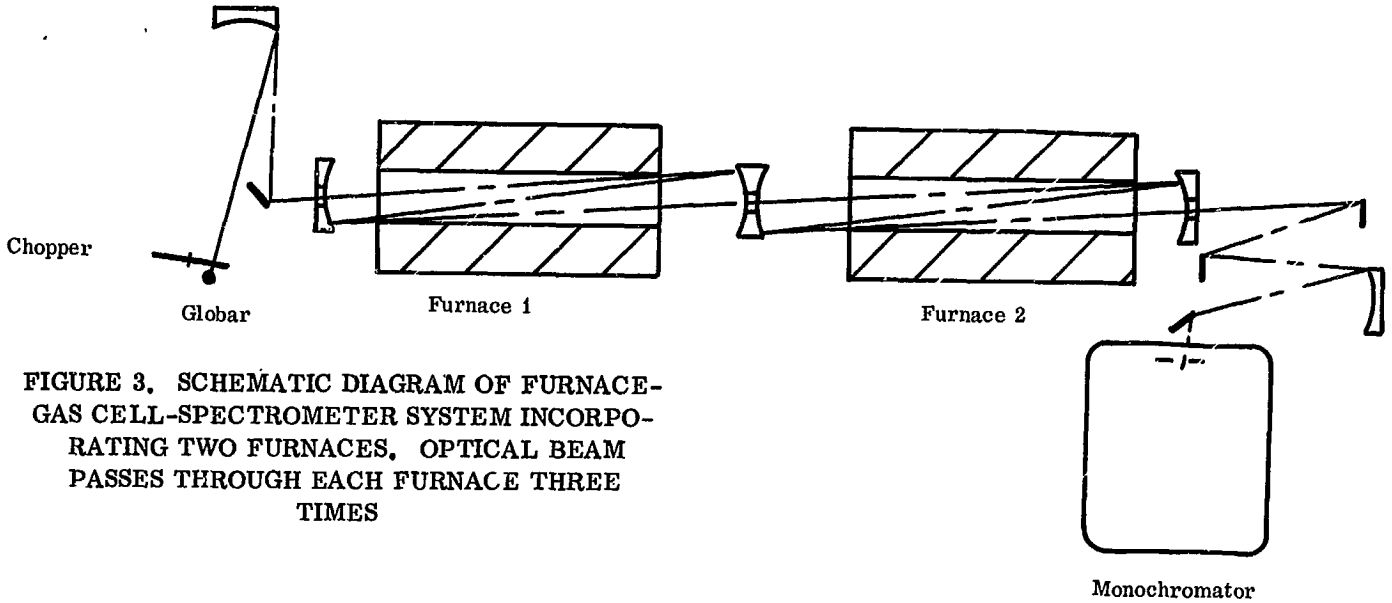

FIGURE 3. SCHEMATIC DIAGRAM OF FURNACE-GAS CELL-SPECTROMETER SYSTEM INCORPORATING TWO FURNACES. OPTICAL BEAM PASSES THROUGH EACH FURNACE THREE TIMES

TABLE I

Two Zone Water Vapor Transmittances

$\nu = 3990\ cm^{-1}$

$T_1 = 637°K$ $T_2 = 1273°K$

$\ell_1 = 24$ inches $\ell_2 = 24$ inches

	Zone 1		Zone 2		Measured	Two Zone Transmittances Calculated	
Case No.	H_2O Pressure (mm Hg)	Zonal Trans. τ_1	H_2O Pressure (mm Hg)	Zonal Trans. τ_2	τ_{12}	Curtis-Godson Method	Beer-Lambert Law
1	53	.711	49	.747	.625	.631	.531
2	53	.711	49	.745	.622	.630	.530
3	51	.722	101	.573	.501	.518	.414
4	51	.714	105	.563	.492	.507	.402
5	50	.720	148	.460	.413	.424	.331
6	52	.710	148	.452	.402	.415	.321
7	104	.503	100	.597	.398	.414	.300
8	100	.519	106	.564	.384	.409	.293
9	112	.474	102	.570	.363	.383	.270
10	102	.508	147	.459	.327	.348	.233
11	101	.520	154	.436	.317	.339	.227
12	138	.395	138	.474	.276	.294	.187
13	151	.358	151	.443	.247	.260	.159
14	147	.373	153	.437	.243	.267	.163
15	152	.358	154	.436	.240	.258	.156

BLANK PAGE

IV. CONTROL STUDIES

SOME SUFFICIENT CONDITIONS FOR MINIMAX CONTROL

By

Thomas E. Carter

SUMMARY

Presented are the initial efforts of a mathematical investigation to determine sufficient conditions for solution of a class of optimal control problems in which the quantity to be minimized is the peak value of some measure of performance of the control. This work was motivated by the fact that many guidance and control problems can be formulated as problems of this class, yet very little theoretical work has been done in this area. Some theorems are developed which apply to this class of problems. A simplified version of a booster control problem known as the "constrained bending moment minimax drift problem" is used as a model for application of the theorems. Some conjectures are made regarding extending the work to other minimax problems.

I. INTRODUCTION

A class of problems which has received very little attention in the literature of optimal control theory is that in which the function to be minimized is given by the peak value of a function over a time interval. Problems such as this belong to a class which have been called "minimax" problems at MSFC. These include guidance and control problems of space vehicles in which it is desirable to minimize peak values of some selected index of vehicle performance such as lateral drift or bending moment.

Since control theory so far has had so little to say about cost functions of this type, it was necessary to go back to the basic techniques of real analysis to investigate this type of problem. By use of this approach, several theorems have been developed which are applicable to minimax type problems. These theorems can be used to find a solution to some simple minimax problems, but no systematic method can yet be claimed. It is hoped that other theorems can be added to those in this report so that a general theory of minimax control elements can be built up similar to that which exists in other areas of optimal control.

This report gives a mathematical statement of the problems including definitions of minimax elements and supreme minimax elements. The general theorems are then developed and applied to a simplified booster control problem which has been under consideration at MSFC for some time. This problem is known as the constrained bending moment minimax drift problem. A minimax control law is developed for a simplified version of this problem.

II. DEFINITIONS AND STATEMENT OF THE PROBLEMS

Consider the following set of equations,

$$\dot{x} = f(x, t, u(t)), \tag{1}$$

defined over a closed interval $I_F \subset R$ where R is the set of real numbers. Differentiation is with respect to $t \in I_F$. The real valued function $u(t)$ belongs to a class U called the set of "admissible controls." The state vector x belongs to region X called an "admissible set" of n-vectors. For each $x_o \in X$ and $u(t) \in U$ and subinterval $I \subset I_F$, it is assumed that only one solution $\chi(x_o, t; u(t))$ exists such that $\chi(x_o, t_o; u(t)) = x_o$.

Associated with (1) is a scalar $y(t,u(t))$ which denotes the "cost" of $u(t)$ for each x_o. This is given by the equation

$$\dot{y} = h(t, \chi(x_o, t; u(t)), u(t)). \tag{2}$$

For a given $x_o \in X$ this may be written as

$$\dot{y} = g(t, u(t)). \tag{3}$$

For $y(t_o, u(t)) = y_o$, we have

$$y(t, u(t)) = \int_{t_o}^{t} g(\tau, u(\tau))d\tau + y_o . \tag{4}$$

Minimax elements with respect to (1) and (3) are defined as follows:

Consider a closed interval $I \subset I_F$ and a point $t_o \in I$ such that $\chi(x_o, t_o; u(t)) = x_o$ and $y(t_o; u(t)) = y_o$. If there exist a control $u'(t, I) \in U$ and a point $y' \in R$ with the property that

$$y' = \min_{u \in U} \max_{t \in I} y(t, u(t)),$$

then

(1) $y'(I)$ is called a minimax value of $y(t, u(t))$ with respect to I,

(2) $u'(t,I)$ is called a minimax control, and

(3) $\chi(x_o, t; u'(t,I))$ is called a minimax trajectory through x_o.

These are called the minimax elements of equations (1) and (3) with respect to x_o, y_o, and I.

It may be desirable to define minimax elements which do not depend on the time interval under consideration. Thus, supreme minimax elements are defined as follows.

Consider the collection $\{I\}$ of all closed intervals in I_F which contain t_o where $x(t_o) = x_o$ and $y(t_o) = y_o$. If there exist a control $u^*(t) \in U$ and a point $y^* \in R$ with the property that

$$y^* = \max_{I \in \{I\}} \min_{u \in U} \max_{t \in I} y(t, u(t)),$$

then

(1) y^* is called a supreme minimax value of $y(t,u(t))$,

(2) $u^*(t)$ is called a supreme minimax control, and

(3) $\chi(x_o, t; u^*(t))$ is called a supreme minimax trajectory through x_o.

The two types of problems considered in this paper are as follows:

Given equations (1) and (3) and sets U, X, and I_F:

(1) For $t_o \in I \subset I_F$, $x_o \in X$, $y_o \in R$, and $u'(t,I) \in U$, show that $u'(t,I)$ is a minimax control and find the other minimax elements.

(2) For $t_o \in I_F$, $x_o \in X$, $y_o \in R$, and $u^*(t) \in U$, show that $u^*(t)$ is a supreme minimax control and find the other supreme minimax elements.

In view of these problems, several theorems were developed which provide sufficient conditions for minimax control and supreme minimax control. The proofs of these theorems are presented in the next section. After that, the use of the theorems is illustrated by showing that certain elements are supreme minim x elements for a simplified booster control problem known as the constrained bending moment minimax drift problem.

III. SOME GENERAL THEOREMS

Some sufficient conditions for minimax control are presented in this section. Of the theorems presented here, the first two are probably the most important since the example in the next section depends heavily upon the use of these two theorems. Theorem 3.1 makes use of an integral cost function. To apply this theorem, it is important to express the cost as an integral function, hence the expression (3) for the cost. An examination of (4) reveals that a control making $y(t, u(t))$ attain its minimax value is equivalent to making

$$\int_{t_o}^{t} g(\tau, u(\tau))\, d\tau$$

a minimax value since they differ by y_o, which is independent of t and $u(t)$. The four theorems are as follows:

THEOREM 3.1: Given a real-valued piecewise continuous function $g(t,u(t))$ defined on a closed interval I and $u(t) \in U$. If there exists $u'(t) \in U$ such that $g(t, u'(t)) \leq g(t, u(t))$ for each $t \in I$ and each $u(t) \in U$ and if

$$\left| \int_{t_o}^{\tau} g(t,u(t))\, dt \right|$$

is bounded over I and U, then

$$\min_{u(t) \in U} \sup_{\tau \in I} \int_{t_o}^{\tau} g(t,u(t))\, dt \text{ occurs for } u(t) = u'(t).$$

Proof: Let $u(t)$ be any control in U. From the hypothesis there exists $u'(t) \in U$ such that $g(t,u'(t)) \leq g(t,u(t))$ for each $t \in [t_o, \tau] \subset I$. Then it follows that

BLANK PAGE

$$\int_{t_o}^{\tau} g(t,u'(t))dt \leq \int_{t_o}^{\tau} g(t,u(t))\ dt.$$

Let $\int_{t_o}^{\tau} g(t,u(t))\ dt = G(\tau)$, $\int_{t_o}^{\tau} g(t,u'(t))\ dt = G'(\tau)$.

Then $G'(\tau) \leq G(\tau)$ for any $\tau \in I$;

hence, $\sup_{\tau \in I} G'(\tau) \leq \sup_{\tau \in I} G(\tau)$ for each $\tau \in I$.

In terms of the original functions,

$$\sup_{\tau \in I} \int_{t_o}^{\tau} g(t,u'(t))\ dt \leq \sup_{\tau \in I} \int_{t_o}^{\tau} g(t,u(t))dt$$

for each $u(t) \in U$, which is equivalent to

$$\sup_{\tau \in I} \int_{t_o}^{\tau} g(t,u'(t))\ dt = \min_{u \in U} \sup_{\tau \in I} \int_{t_o}^{\tau} g(t,u(t))\ dt$$

and the proof is complete.

THEOREM 3.2: Given a real-valued function $y(t,u(t))$ defined on a closed interval I and $u(t) \in U$. If there exist a subinterval $I_s \subset I$ and a control $u_1(t)$ defined on I_s such that there exists $T \in I_s$ where

$$y(T,u_1(T)) = \min_{u \in U} \max_{t \in I_s} y(t, u(t)),$$

and if there exists a control $u_2(t)$ defined on the complement of I_s in I (denoted $C_I(I_s)$) such that $y(t, u_2(t)) \leq y((T, u_1(T))$ for each $t \in C_I(I_s)$, then there exists a minimax control on I given by

$$u'(t) = \begin{cases} u_1(t), & t \in I_s \\ u_2(t), & t \in C_I(I_s) \end{cases}.$$

Proof: Assume $u'(t)$ is not a minimax control on I. Then there exists a control $u(t) \in U$ on I such that $\max_{t \in I} y(t,u(t) < \max_{t \in I} y(t,u'(t))$. Furthermore, $\max_{t \in I} y(t,u(t)) = y(t_m,u(t_m))$ where $t_m \in C_I(I_s)$ because $y(T,u_1(T))$ is a minimax value for all admissible controls on I_s. It follows that

$y(t_m,u(t_m)) > \max_{t \in I_s} y(t,u(t))$ because t_m does not belong to I_s and $\max_{t \in I_s} y(t,u(t)) \geq \max_{t \in I_s} y(t,u_1(t))$ because $u_1(t)$ is a minimax control on I_s. Furthermore, by definition of $u'(t)$,

$$\max_{t \in I_s} y(t,u_1(t)) = \max_{t \in I} y(t,u'(t));$$

hence, $\max_{t \in I} y(t,u(t)) > \max_{t \in I} y(t,u'(t))$ which contradicts the assumption; hence, $u'(t)$ is a minimax control on I.

THEOREM 3.3: If $I_1 \subset I_2$ then $y'(I_1) \leq y'(I_2)$.

Proof: Let $u'(t)$ be a minimax control on I_2. Assume that the maximum occurs at $T \in I_2$. Then

$\max_{t \in I_2} y(t,u'(t)) = y(T,u'(T))$. Therefore,

$y(T,u'(T)) \geq y(t,u'(t))$ for each $t \in I_2$. Since $I_2 \supset I_1$, this expression holds for each $t \in I_1$, so, in particular,

$y(T,u'(T)) \geq \max_{t \in I_1} y(t,u'(t))$. It follows that

$$\max_{t \in I_2} y(t,u'(t)) \geq \max_{t \in I_1} y(t,u'(t)) \text{ or}$$

$y'(I_2) \geq y'(I_1)$, and the proof is complete.

THEOREM 3.4: If $u^*(t)$ is a supreme minimax control with respect to x_o and y_o where $x(t_o,u^*(t_o)) = x_o$ and $y(t_o,u^*(t_o)) = y_o$, then for any $t_o' \in I_F$, $u^*(t)$ is also a supreme minimax control with respect to $x(t_o',u^*(t_o'))$ and $y(t_o',u^*(t_o'))$.

Proof: Let $y'(I)$ be a minimax point with respect to I where I is any closed interval in I_F containing t_o. Let y^* be the supreme minimax value associated with $u^*(t)$. Since t_o and t_o' are both in I_F, there exists $I_o \in \{I\}$ which is sufficiently large to contain both; hence, $y^* = \max_{I \in \{I\}} y'(I) = \max_{I \supset I_o} y'(I) = \max_{I' \in \{I'\}} y'(I')$

where $\{I'\}$ is the set of all closed intervals in I_F containing t_o'. Hence, $u^*(t)$ is a supreme minimax control with respect to $x(t_o', u^*(t'))$ and $y(t_o', u^*(t'))$ for each $t_o' \in I_F$.

IV. APPLICATION TO A SIMPLIFIED BOOSTER CONTROL PROBLEM

Application of the previous theorems to a booster control problem known as the constrained bending moment minimax drift problem is presented in this section. This is the problem of minimizing the maximum lateral drift from a reference trajectory along flight time where the magnitude of the bending moment cannot exceed a critical value.

A. FORMULATION OF THE CONSTRAINED BENDING MOMENT PROBLEM

The rigid body equations of a typical vehicle are given in the following form:

$$\ddot{\varphi} + C_1 \alpha + C_2 \beta = 0$$

$$\ddot{z} = K_1 \varphi + K_2 \alpha + K_3 \beta \qquad (5)$$

$$\alpha = \varphi - \frac{\dot{z}}{V} + \alpha_w ,$$

where φ, α, β, z represent angular deviation from reference, angle of attack, engine gimbal angle, and lateral positional deviation from reference, respectively. The wind contribution of the angle of attack is denoted by α_w and the vehicle speed by V.

The bending moment, given by a linear combination of α and β, is constrained as follows:

$$\left|M'_\alpha \alpha + M'_\beta \beta\right| \leq M_{max}, \qquad (6)$$

where M'_α and M'_β are bending moment coefficients and M_{max} is the allowable bending moment. The problem is to minimize the function

$$\max_{t \in I} \left|\dot{z}(t)\right|$$

subject to the subsidiary conditions (5) and (6).

To obtain a model more amenable to analysis, two simplifying assumptions are made. It will be assumed that the wind angle of attack is zero and the quantity $\frac{\dot{z}}{V}$ will be neglected. The latter assumption may not be unrealistic since the object is to keep the maximum of $|\dot{z}(t)|$ as small as possible. Under these assumptions, the problem under consideration is the following:

Minimize $\max_{t \in I} |\dot{z}(t)|$ subject to the conditions

$$\ddot{\varphi} + C_1 \varphi + C_2 \beta = 0$$

$$\ddot{z} = (K_1 + K_2)\varphi + K_3 \beta \qquad (7)$$

$$\left|M'_\alpha \varphi + M'_\beta \beta\right| \leq M_{max} .$$

Observe that the bending moment can, in this problem, be treated as a control variable in a very natural way. Define the new variable v in such a way that

$$M_{max} v = M'_\alpha \varphi + M'_\beta \beta . \qquad (8)$$

Using v as the control variable, the system (7) becomes

$$\ddot{\varphi} = \mu\varphi - Mv$$

$$\ddot{z} = \nu\varphi + \rho M v \qquad (9)$$

$$|v| \leq 1,$$

where

$$\mu = (-C_1 + C_2 \frac{M'_\alpha}{M'_\beta}), \quad \nu = (K_1 + K_2 - K_3 \frac{M'_\alpha}{M'_\beta})$$

$$\rho = \frac{K_3}{C_2} \text{ and } M = \frac{C_2}{M'_\beta} M_{max}.$$

The equations can now be put in state variable form by making the substitutions $x_1 = \varphi$, $x_2 = \dot{\varphi}$, and $x_3 = \frac{\dot{z}}{\nu+\rho}$. A constant K is defined by $K = \frac{\nu}{\nu+\rho}$. The constrained bending moment problem can thus be put in the following state variable form:

$$\dot{x}_1 = x_2$$

$$\dot{x}_2 = \mu x_1 - Mv(t) \qquad (10)$$

$$\dot{x}_3 = Kx_1 + (1-K)\, Mv(t)$$

$$|v(t)| \leq 1, \quad 0 \leq K \leq 1,$$

where the object is to find a v(t) which minimizes $\max_{t \in I} |x_3(t)|$.

Since the purpose in this report is to illustrate the use of the theorems presented in the previous section on a minimax problem we will choose K=1. It is

felt that the same general techniques can be used on the more general problem ($0 \leq K \leq 1$), but the analysis becomes more complicated. Choosing $K = 1$ yields the original version of the constrained bending moment minimax drift problem. In this problem the state variable equations are

$$\dot{x}_1 = x_2 \tag{11}$$

$$\dot{x}_2 = \mu x_1 - Mv(t), \quad \mu > 1, M > 1 \tag{12}$$

$$\dot{x}_3 = x_1, \tag{13}$$

where $v(t) \in V = \{v(t) \mid |v(t)| \leq 1\}$ and each element in V is a piecewise continuous function of t. The quantities x_1, x_2, and x_3 represent attitude angle, its time rate of change, and lateral drift, respectively. The control variable v(t) represents a normalized bending moment. The problem is to find a control in V for which $\max_{t \in I} |x_3(t, v(t))|$ is minimized. The interval I is chosen sufficiently small such that μ and M can be considered constant.

Equations (11), (12), and (13) are in the form of (1) and (3) if we interpret y as $|x_3|$ and U as V.

Let $y = |x_3| = x_3 \operatorname{sgn} x_3$ for $x_3 \neq 0$. Then $\dot{y} = \dot{x}_3 \operatorname{sgn} x_3 = x_1 \operatorname{sgn} \left(\int_{t_o}^{t} x_1 \, d\tau + x_3(t_o) \right)$.

For this problem, equations (1) and (3) become

$$\begin{pmatrix} \dot{x}_1 \\ \dot{x}_2 \end{pmatrix} = \begin{pmatrix} 0 & 1 \\ \mu & 0 \end{pmatrix} \begin{pmatrix} x_1 \\ x_2 \end{pmatrix} + \begin{pmatrix} 0 \\ -M \end{pmatrix} v(t) \tag{14}$$

$$\dot{y} = x_1 \operatorname{sgn} \left(\int_{t_o}^{t} \chi_1 d\tau + x_3(t_o) \right) \tag{15}$$

where

$$\int_{t_o}^{t} x_1 \, d\tau + x_3(t_o) \neq 0$$

and (4) becomes

$$y(t, v(t)) = \int_{t_o}^{t} x_1 \operatorname{sgn} \left(\int_{t_o}^{\tau} x_1 d\rho + x_3(t_o) \right) d\tau + y_o \tag{16}$$

where x_1 is a function of v(t) through (14).

Consider in V the "extreme controls" $v(t) = +1$ and $v(t) = -1$ on I. The trajectories $\chi(t, x_o; v(t))$ of these two controls are seen in the phase plane as hyperbolas. The asymptotes of the hyperbolas intersect forming a closed region containing the origin (Fig. 1). Let the region of admissible trajectories X be defined as the interior of this region. In other words, X is the region in which the control $u = \operatorname{sgn} x_1$ provides stable trajectories. Formally, X is defined as follows:

$$X = \left\{ x \in R^2 \;\middle|\; |x_1| + |\sqrt{\mu}\, x_2| < \frac{M}{\mu} \right\} .$$

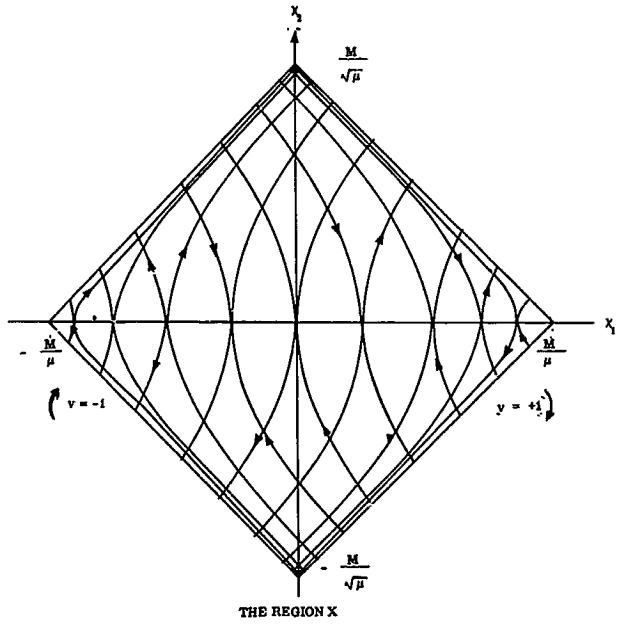

FIGURE 1. THE TRAJECTORIES $\chi(t, x_o; \pm 1)$ SEEN IN THE PHASE PLANE

B. SOME THEOREMS ON THE CONSTRAINED BENDING MOMENT MINIMAX DRIFT PROBLEM

Some theorems dealing with the problem of finding minimax values of $y(t, v(t)) = |x_3(t)|$ subject to equations (11), (12), and (13) are presented at this point. Let $x_1(t_o)$, $x_2(t_o)$ and $x_3(t_o)$ be denoted by x_{10}, x_{20}, and x_{30}, respectively. The first theorem is as follows:

THEOREM 4.1: Let $\begin{pmatrix} x_{10} \\ x_{20} \end{pmatrix} \in X$ and $x_{10} = 0$. If $x_{20} \neq 0$, then $v(t) = \operatorname{sgn} x_1$ is a minimax control over any closed interval (t_o, t_1). If $x_{20} = 0$, then $v(t) = 0$ is a minimax control.

Proof:

(a) If $x_{20} = 0$, then for the control $v(t) = 0$ everywhere on $[t_o, t_1]$ a solution to the differential equations (11), (12), and (13) is $x_1 = 0$, $x_2 = 0$, $x_3 = x_{30}$ on $[t_o, t_1]$. Hence, $|x_3(t)| = |x_{30}|$ is certainly

a minimal value of $y(t, v(t))$. Hence, $v(t) = 0$ is a minimax control under the condition $x_{10} = x_{20} = 0$.

(b) Assume $x_{20} \neq 0$, $x_{10} = 0$.

Equations (11) and (12) can be integrated by variation of parameters to reveal the following solution for x_1:

$$x_1(t, v) = \frac{x_{20}}{\sqrt{\mu}} \sinh \sqrt{\mu}\,(t - t_o) - \frac{M}{\sqrt{\mu}} \int_{t_o}^{t} \sinh \sqrt{\mu}\,(t-\tau)\, v(\tau)\, d\tau. \qquad (17)$$

Let $x_{20} > 0$. For any $t \in [t_o, t_1]$, $\min_{v \in V} x_1(t,v)$ occurs for the control $v(\tau) = +1$, $\tau \in [t_o, t]$. This is because $\sinh \sqrt{\mu}(t-\tau) \geq \sinh \sqrt{\mu}(t-\tau) v(\tau)$ for $v(\tau) \leq 1$. For the control $v(\tau) = +1$, equation (17) becomes

$$x_1(t,+1) = \frac{x_{20}}{\sqrt{\mu}} \sinh \sqrt{\mu}\,(t-t_o) + \frac{M}{\mu}\,(1-\cosh \sqrt{\mu}\,(t-t_o)) \qquad (18)$$

Since $\begin{bmatrix} 0 \\ x_{20} \end{bmatrix} \in X$ and $x_{20} > 0$, if t_1 is sufficiently large there exists a unique $T_p \neq t_o$ such that $x_1(T_p, +1) = 0$. Furthermore, $x_1(T_p, +1) \leq x_1(T_p, v)$ for each $v \in V$. For each $t \in [t_o, T]$, the condition $0 \leq x_1(t,+1) \leq x_1(t,v)$ holds. It follows from equation (13) that $x_3(t,v)$ is monotonically increasing on $[t_o, T_p]$ for each $v \in V$. It should be observed that for any $T \in [t_o, T_p]$ the maximum of $x_3(t,+1)$ over the interval $[t_o, T]$ occurs either at $t=t_o$ or at $t=T$.

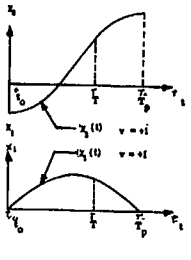

FIGURE 2. SKETCH OF $x_1(t,+1)$ and $x_3(t,+1)$

Consider equation (16) over the interval $[t_o, T]$ where $y(t, v(t)) = |x_3(t, v(t))|$. We will use Theorem 3.1 to show that $v(t) = +1$ is a minimax control over $[t_o, T]$ where $t_o \leq T \leq T_p$. We are given $\dot{y} = g(t, v(t))$ where

$$g(t, v(t)) = x_1 \operatorname{sgn} \left(\int_{t_o}^{t} x_1\, d\tau + x_3(t_o) \right) \text{ where}$$

$x_1 = x_1(t, v)$ as given by equation (17). Equation (17) shows that $x_1(t,+1) \leq x_1(t,v)$ where $|v(t)| \leq 1$. For this reason, $\int_{t_o}^{t} x_1(\tau,+1)\, d\tau \leq \int_{t_o}^{t} x_1(\tau, v)\, d\tau$

from which it follows that

$$\operatorname{sgn} \left(\int_{t_o}^{t} x_1(\tau,+1)\, d\tau + x_3(t_o) \right) \leq \operatorname{sgn} \left(\int_{t_o}^{t} x_1(\tau, v)\, d\tau + x_3(t_o) \right).$$

If the equality holds, then $g(t,+1) \leq g(t, v)$ because $x_1(t,+1) \leq x_1(t,v)$. If the strict inquality holds, then since $x_1(t,v) \geq 0$ on $[t_o, T]$, it follows that $g(t,+1) \leq 0$, whereas $g(t, v) \geq 0$ on (t_o, T); hence, $g(t,+1) \leq g(t,v)$. It has been established that, for $t \in [t_o, T]$ where $t_o < T \leq T_p$, $g(t,+1) \leq g(t,v)$ for each $v \in V$. It follows from Theorem 3.1 that $v(t) = +1$ is a minimax control on $[t_o, T]$ where $T \in [t_o, T_p]$.

The problem now is to find a minimax control over the entire interval $[t_o, t_1]$ which reduces to $v(t) = +1$ on the subinterval $[t_o, T_p]$. Consider as a possibility the control $v'(t) = \operatorname{sgn} x_1$. For this control x_1 given by equation (17) is a periodic function of t. In fact, $x_1(T_p + t) = -x_1(t)$. Hence, $y(t, v'(t))$ is also periodic and never exceeds its maximum value on $[t_o, T_p]$; that is, $y(t, v'(t)) \leq \max_{t \in [o, T_p]} y(t,+1)$ for each $t \in (T_p, t_1)$. Hence, by Theorem 3.2, the control $v'(t) = \operatorname{sgn} x_1$ is a minimax control over the entire interval (t_o, t_1). A minimax control law has thus been found for $x_{10} = 0$, $x_{20} > 0$ which is independent of the final time t_1. For the case $x_{10} = 0$, $x_{20} < 0$, an argument similar to the preceding can be used.

It can be shown further that, under the conditions of this theorem, the control $v'(t) = \operatorname{sgn} x_1$ is, in fact, a supreme minimax control. This is stated as the following lemma.

LEMMA: The control $v = \operatorname{sgn} x_1$ is a supreme minimax control with respect to $x_o \in X$ and $y_o \in R$ where $x_{20} \neq 0$ and $x_{10} = 0$.

Proof: It has been established that $v = \operatorname{sgn} x_1$ is a minimax control over $[t_o, t_1]$ for any real t_1. Furthermore, the functions $x(t, \operatorname{sgn} x_1)$ and $y(t, \operatorname{sgn} x_1)$ are both periodic. If the interval $[t_o, t_1]$ is chosen sufficiently large to include a complete period, then

$$\max_{t\in[t_0,t_1]} y(t, \operatorname{sgn} x_1) = \max_{t\in I} y(t, \operatorname{sgn} x_1),$$

where I is any interval in I_F which contains $[t_0, t_1]$.

Hence

$$\max_{t\in[t_0,t_1]} y(t, \operatorname{sgn} x_1) = \max_{I\in\{I\}} \min_{v\in V} \max_{t\in I} y(t,v) = y^*.$$

The control $v = \operatorname{sgn} x_1$ is thus a supreme minimax control with respect to $x_0 = \begin{pmatrix} 0 \\ x_{20} \end{pmatrix} \in X$ and $x_{30} \in R$ where $x_{20} \neq 0$.

This lemma along with Theorem 3.4 establishes the key theorem for use on the constrained bending moment problem.

THEOREM 4.2: The control $v = \operatorname{sgn} x_1$ is a supreme minimax control with respect to any point $(x_0 \neq 0) \in X$ and $y_0 \in R$.

Proof: Consider a point $x_0 \in X$ such that $x_0 \neq 0$. Consider the control $v = \operatorname{sgn} x_1$ and the corresponding trajectory $x(t, \operatorname{sgn} x_1)$ through x_0. Let $x(t_0) = x_0$, $y(t_0) = y_0$. There exists $t_0' \in I_F$ such that $x_1(t_0') = 0$ and $x_2(t_0') \neq 0$. Hence, the previous lemma shows that $v = \operatorname{sgn} x_1$ is a supreme minimax control with respect to $x(t_0')$ and $y(t_0')$. It follows from Theorem 3.4 that $v = \operatorname{sgn} x_1$ is also a supreme minimax control with respect to x_0 and y_0.

C. SOME CONCLUSIONS ON THE CONSTRAINED BENDING MOMENT PROBLEM

The final result is that $v^* = \operatorname{sgn} x_1$ is a supreme minimax control for each nonzero $x_0 \in X$ and $x_3(t_0) \in R$. If the limit cycle trajectory is undesirable, an approximate supreme minimax control can be obtained by setting $v = \operatorname{sgn}(x_1 + \epsilon x_2)$ where ϵ is a sufficiently small positive number.

The concept of supreme minimax control was introduced because of certain advantages it holds over an ordinary minimax control in the constrained bending moment problem. The principal advantages are its independence of the time interval I and of the initial conditions x_0 and y_0. A supreme minimax control does not have the following shortcomings that some ordinary minimax controls may have:

(1) A control which is minimax over I may, in general, lead to a poor control over some larger interval containing I. For this reason, piecing together minimax controls over various intervals may not lead to a minimax control over the union of these.

(2) Minimax control over a fixed I can lead to different control laws for different initial conditions x_0 and $x_3(t_0)$.

(3) For one set of initial conditions, a minimax value can be less than for another admissible set of initial conditions. The most practical interest, however, is in the "worst" minimax value.

V. A SUMMARY OF SEARCH PROCEDURES FOR MINIMAX CONTROL

An outline of methods for seeking a minimax control or supreme minimax control which are based primarily on Theorems 3.1 and 3.2 is presented for a class of minimax problems.

No claim is made that these techniques can be applied in each case. They are presented merely as suggestions as to how Theorems 3.1 - 3.4 might be used in constructing a minimax control law.

Consider the class of problems in which equation (1) is linear in x and u.

$$\dot{x} = Ax + bu(t) + Cw(t), \quad x(t_0) = x_0 \tag{19}$$

$$\dot{y} = h(t,x,u(t)), \quad y(t_0) = y_0 \tag{20}$$

In this problem, w(t) is a known function of time, A is an nxn matrix, b and c are n-vectors. Given a region X and x_0 for which there exists at least one control in U such that the solution trajectory remains in X for all $t \in I$ and given $y_0 \in R$, the problem is to find a minimax control over I. A possible approach is as follows:

(1) Solve equation (19) by the method of variation of parameters and obtain $x = \varphi(t,u(t))$. For this solution equation (20) becomes

$$\dot{y} = h(t, \varphi(t,u(t)), u(t)) = g(t,u(t)), \quad y(t_0) = y_0 \tag{21}$$

(2) Pick a subinterval $I_s \subset I$ in which the peak value of y is expected to occur. For example, if w(t) has a peak, for many physically meaningful cost functions, the peak of y might be expected to occur near the peak w(t). In these cases, I_s should contain the peak time of w(t).

(3) Find, if possible, a control $u_1(t) \in U$ such that $g(t,u_1(t)) \leq g(t,u(t))$ for any $t \in I$ and $u(t) \in U$. Then by Theorem 3.1, $u_1(t)$ is a minimax control on I_s. Let $y'(I_s)$ denote the minimax value on I_s.

(4) Find any control $u_2(t) \in U$ defined on $C_I(I_s)$ for which the peak value of $y(t,u_2(t))$ is less than or equal $y'(I_s)$. Then by Theorem 3.2, the control

$$u'(t) = \begin{cases} u_1(t), & t \in I_s \\ u_2(t), & t \in C_I(I_s) \end{cases}$$

is a minimax control over I.

(5) If possible, pick $u_2(t)$ such that the function $u'(t)$ is independent of the interval I. In this case, $u'(t)$ is a supreme minimax control.

VI. CONCLUSION

Control problems in which the object is to minimize the peak value of a functional constitute a very practical class of problems having many applications in aerospace vehicle guidance and control. In this report some sufficient conditions for solution of problems in this class were stated and applied to a simplified version of a booster control problem. Some conjectures for application to other problems were also presented. It is hoped that further study in this area will lead to more systematic procedures for determining minimax control elements.

BLANK PAGE

V. GUIDANCE STUDIES

CONCEPTS OF THE ITERATIVE GUIDANCE LAW FOR SATURN LAUNCH VEHICLES

By

Clyde D. Baker

SUMMARY

Beginning with the V2 rockets in the mid-1940's and continuing through the Redstone, Jupiter and Pershing missiles, the delta minimum concept was employed successfully. The delta minimum concept requires that both nominal and perturbed trajectories fly essentially the same geometrical trajectory regardless of other considerations. Analog computation was employed for the execution of the delta minimum concept.

In 1960, research work was begun to develop new guidance concepts for the Saturn space vehicles. This work was motivated by the development of new mathematical techniques for maximization of payload through optimization methods and by the development of digital computers to replace analog computers as on-board hardware. It was also obvious that space trajectories would require greater flexibility to cope with sudden changes, such as engine out, and that more flexibility must be permitted in the selection of flight profiles.

This paper presents the basic concepts of the iterative guidance law developed for Saturn launch vehicles to meet these new requirements of space age guidance. The development of the iterative guidance law and the results and ideas presented in this paper are due primarily to Mr. Helmut J. Horn and his associates in the Dynamics Analysis and Flight Mechanics Division of the Aero-Astrodynamics Laboratory.

I. INTRODUCTION

A typical space guidance problem is that of placing a space vehicle into a specified circular orbit around the earth. The particular iterative guidance solution of this problem is presented in this paper to illustrate the basic principles and concepts involved. Among many other applications, iterative guidance will inject a spacecraft into a specified lunar orbit or will soft land a vehicle at a specified point on the surface of the moon. The discussion here will be limited primarily to the problem of injection into a circular orbit about the earth since the principles of the guidance scheme are essentially the same for all specific applications.

The accomplishment of any of these missions requires proper functioning of the control, navigation, and guidance systems. Since these functions are intercoupled, in the final analysis they must be considered simultaneously. However, for the purpose of explanation we will discuss each as a separate function.

The control system then has as its primary function the supervision of the rotational motion of the vehicle, subject to the constraint of the prescribed reference attitude while maintaining structural loads within acceptable bounds in the presence of disturbances such as wind. Pitch and yaw attitude angles are prescribed by the guidance system and are then introduced as reference angles into the control system. The control system then rotates the vehicle into the prescribed reference direction while simultaneously insuring that maximum allowable bending moments are not exceeded and that propellant sloshing does not reach disastrous amplitudes. Simply stated, the control system maintains the desired vehicle attitude angles and angular rates while preventing the structural destruction of the vehicle.

The purpose of the navigation system is to provide accurate information describing the current position, velocity and acceleration of the vehicle as a function of flight time, or some other convenient variable. This information is provided with respect to some reference coordinate item. Thus it may be position, velocity, and acceleration of the vehicle with respect to the launch site or it may be given with respect to the target point. Such information may be provided by an inertial platform together with integrating accelerometer as in the Saturn vehicles or it may be provided by radar measurements, or visual tracking, etc.

Finally, it is the purpose of the guidance system to use the position, velocity, and acceleration information provided by the navigation system to determine the reference attitude for the control system. This means essentially that, on the basis of known position, velocity and acceleration of the vehicle, the guidance system prescribes the required direction of the thrust vector necessary to achieve the mission of the flight.

In the beginning of the Saturn guidance studies, it was assumed that guidance would become active only after the burnout of the first stage. Trajectory shaping of the first stage was constrained primarily to prevent excessive aerodynamic structural loads and aerodynamic heating. Within these constraints, a zero-lift

first stage trajectory was then computed to maximize the payload when connected to an optimized second stage to orbit. More recently, angles of attack during the first stage have been permitted in order to further increase the payload delivered to orbit.

For the specific guidance problem of entering a circular earth orbit discussed here, it is necessary to cut off the engines when the specified altitude is reached with zero degrees path angle and circular velocity. All three of these conditions must be satisfied simultaneously.

To illustrate the solution of the iterative guidance problem, the complete equations of motion of the vehicle are presented first. These equations are then simplified step by step to illustrate the essential elements of the problem.

II. EQUATIONS OF MOTION

The equations of motion of the Saturn vehicle are usually written in the following form:

$$\ddot{x} = F_1^{(1)}\frac{F}{m} + n_1^{(1)}\frac{N}{m} - C_1^{(1)}\frac{A}{m} + G_1^{(1)} g \qquad (1)$$

$$\ddot{y} = F_2^{(1)}\frac{F}{m} + N_2^{(1)}\frac{N}{m} - C_2^{(1)}\frac{A}{m} + G_2^{(1)} g \qquad (2)$$

$$\ddot{z} = F_3^{(1)}\frac{F}{m} + N_3^{(1)}\frac{N}{m} - c_3^{(1)}\frac{A}{m} + g_3^{(1)} g \qquad (3)$$

where

$F^{(1)}$ is a unit vector in the direction of thrust force, F,

$N^{(1)}$ is a unit vector in the direction of normal force, N,

$C^{(1)}$ is a unit vector in the direction of axial force, A,

$G^{(1)}$ is a unit vector in the direction of gravitational force, g, and

m is the mass of the vehicle.

Subscripts 1, 2, and 3 indicate components of the unit vectors along the x, y, and z coordinates, respectively. These coordinates have their origin at the center of the earth with the y-axis parallel to the gravity vector at launch. The x-axis is parallel to the downrange direction and the z-axis completes a right-handed system.

Since guidance is initiated after the vehicle is out of the atmosphere, $\frac{N}{m}$ and $\frac{A}{m}$ are both zero and the equations may be simplified to

$$\ddot{x} = F_1^{(1)}\frac{F}{m} + g_1 \qquad g_1 = G_1^{(1)} g \qquad (4)$$

$$\ddot{y} = F_2^{(1)}\frac{F}{m} + g_2 \qquad g_2 = G_2^{(1)} g \qquad (5)$$

$$\ddot{z} = F_3^{(1)}\frac{F}{m} + g_3 \qquad g_3 = G_3^{(1)} g \quad . \qquad (6)$$

The values of the thrust force unit vector components are given by

$$F_1^{(1)} = \cos\chi \cos\tau \cos\beta_\xi \cos\beta_\zeta - \sin\chi \cos\beta_\zeta \sin\beta_\xi - \cos\chi \sin\beta_\zeta \sin\tau \qquad (7)$$

$$F_2^{(1)} = \sin\chi \cos\tau \cos\beta_\xi \cos\beta_\zeta - \sin\chi \cos\beta_\zeta \sin\beta_\xi + \cos\chi \cos\beta_\zeta \sin\tau \qquad (8)$$

$$F_3^{(1)} = \sin\tau \cos\beta_\xi \cos\beta_\zeta + \cos\tau \sin\beta_\zeta \qquad (9)$$

where

χ is the vehicle attitude angle in the pitch plane,

τ is the vehicle attitude angle in the yaw plane,

β_ξ is the engine gimbal angle in the pitch plane, and

β_ζ is the engine gimbal angle in the yaw plane.

Equations (7), (8), and (9) are exact representations of the respective directions of thrust. However, since these equations are coupled in the pitch and yaw axes, the above definitions of χ, τ, β_ξ, and β_ζ are not strictly correct. Because of the coupling, they may not correctly be referred to as being in the pitch and yaw planes. Using the fact that the angles τ, β_ξ and β_ζ are small, the definitions given above are approximately true and allow a visualization of these equations.

BLANK PAGE

The values of g_1, g_2, and g_3 are somewhat complicated functions of the vehicle altitude and latitude and will not be given explicitly here.

Equations (4), (5), and (6) are the precise equations of motion of a vehicle in vacuum on a rotating spheroidal earth and may include a full six degrees of freedom with the inclusion of the dynamics equations relating gimbal angles and attitude angles. These equations may also be simplified at this point to three degrees of freedom by making certain simplifications concerning the dynamics of rotational motion. For guidance studies, the latter choice is adequate.

Accordingly, the dynamics of angular motion will be neglected, and the thrust direction will be assumed along the longitudinal axis of the vehicle. Furthermore, guidance will be assumed to restrict the trajectory to a plane so that the equations of motion may be reduced to

$$\ddot{x} = \frac{F}{m}\cos\chi(t) + g_1 \tag{10}$$

$$\ddot{y} = \frac{F}{m}\sin\chi(t) + g_2 \ . \tag{11}$$

For injection into a circular orbit about the earth, the following conditions must be satisfied.

$$x_c^2 + y_c^2 = r_c^2 \tag{12}$$

$$\dot{x}_c^2 + \dot{y}_c^2 = v_c^2 \tag{13}$$

$$x_c\dot{x}_c + y_c\dot{y}_c = 0 \tag{14}$$

where the subscript c refers to engine cutoff time at injection into orbit.

The guidance problem then is to prescribe the angle $\chi(t)$ so that equations (12), (13), and (14) are satisfied simultaneously at injection. This problem as stated does not have a unique solution. There are, in general, many trajectories and corresponding steering angles $\chi(t)$ which will fulfill these end conditions given by equations (12), (13), and (14).

By imposing the requirement that these terminal conditions be fulfilled in minimum time, or equivalently, that they be fulfilled by minimum fuel consumption, the steering law becomes unique, and may be solved by the use of calculus of variations. However, the calculus of variations solution to this problem is too complicated to be carried out in flight by an on-board computer. Consequently, further simplifications are made to reduce the complexity of the problem while maintaining the desired accuracy and minimum fuel consumption.

III. THE NATURE OF THE MODIFICATION OR SIMPLIFICATION

As pointed out earlier, the calculus of variation solution of the optimum thrust direction to maximize payload on a rotating, spheroidal earth requires computation facilities far in excess of those available with an on-board computer.

The iterative guidance concept derives the optimal thrust direction law for a flat earth model with constant gravitational field and then applies this law in the realistic earth model. It is important to note that only the optimal control law from the simplified model is used. The equations of motion for Saturn are calculated on a rotating spheroidal earth.

Obviously, a careful check must be made to determine if the optimal guidance law derived for the simplified model provides optimal performance and accuracy for the actual Saturn trajectories. Many numerical calculations demonstrate that the optimality can be preserved.

IV. THE ITERATIVE GUIDANCE MODE CONCEPT

Since equations (10) and (11) are too complicated for on-board computation, further simplifying assumptions are made that

$$g_1 = 0 \tag{15}$$

$$g = \text{constant} \tag{16}$$

and equations (10) and (11) then become

$$\ddot{x} = \frac{F}{m}\cos\chi \tag{17}$$

$$\ddot{y} = \frac{F}{m}\sin\chi - g. \tag{18}$$

Equations (17) and (18) may be written as a system of first order equations in the form

$$\dot{x}_1 = \frac{F}{m}\cos\chi = \ddot{x} \tag{19}$$

$$\dot{x}_2 = x_1 \qquad = \dot{x} \tag{20}$$

$$\dot{x}_3 = \frac{F}{m}\sin\chi - g = \ddot{y} \tag{21}$$

$$\dot{x}_4 = x_3 \qquad = \dot{y} \quad . \tag{22}$$

To apply the maximal principle to this system of equations, define

$$\dot{x}_5 = 1 \tag{23}$$

where the quantity to be minimized now is

$$J = \int_0^{t_c} x_5\, dt \ ,$$

subject to the end conditions

$$x(t_c) \text{ unspecified} \qquad x_2(t_c) \text{ unspecified} \tag{24}$$

$$y(t_c) = y_{tc} \qquad x_4(t_c) = x_{4_{tc}} \tag{25}$$

$$\dot{x}(t_c) = \dot{x}_{tc} \qquad x_1(t_c) = x_{1_{tc}} \tag{26}$$

$$\dot{y}(t_c) = \dot{y}_{tc} \qquad x_3(t_c) = x_{3_{tc}} \quad . \tag{27}$$

These equations are the flat earth equivalents of equations (12), (13), and (14).

The Hamiltonian of this system of equations then is

$$H = P_1\frac{F}{m}\cos\chi + p_2x_1 + P_3\left(\frac{F}{m}\sin\chi - g\right)$$

$$+ P_4x_3 - 1 \ . \tag{28}$$

To maximize the Hamiltonian with respect to the control variable χ, calculate

$$\frac{\partial H}{\partial \chi} = -P_1\frac{F}{m}\sin\chi + P_3\frac{F}{m}\cos\chi = 0 \tag{29}$$

which implies

$$\tan\chi = \frac{P_3}{P_1} \ . \tag{30}$$

From the canonical equations,

$$\dot{P}_1 = \frac{-\partial H}{\partial x_1} = -P_2 \tag{31}$$

$$\dot{P}_2 = \frac{-\partial H}{\partial x_2} = 0 \tag{32}$$

$$\dot{P}_3 = \frac{-\partial H}{\partial x_3} = -P_4 \tag{33}$$

$$\dot{P}_4 = \frac{-\partial H}{\partial x_4} = 0 \quad . \tag{34}$$

Hence,

$$P_1 = -P_{20}t + P_{10} \tag{35}$$

$$P_2 = P_{20} \tag{36}$$

$$P_3 = -P_{40}t + P_{30} \tag{37}$$

$$P_4 = P_{40} \ . \tag{38}$$

Thus, equation (30) may be written

$$\tan\chi = \frac{-P_{40}t + P_{30}}{-P_{20}t + P_{10}} \quad . \tag{39}$$

From the transversality conditions

$$\left(\sum_{i=1}^{4} p_i\right)\Big|_{x_i = x_{ic}} dx_i = 0 \ . \tag{40}$$

Since $x(t_c)$ is unspecified, $P_{20} = 0$ and equation (39) may be written

$$\tan\chi = \frac{-P_{40}t + P_{30}}{P_{10}} = A + Bt \quad , \tag{41}$$

where

$$A = \frac{P_{30}}{P_{10}} \tag{42}$$

$$B = \frac{-P_{40}}{P_{10}} \quad . \tag{43}$$

Equation (41) then is the optimum steering law to maximize payload for a trajectory on a flat nonrotating earth with constant gravitational field. This expression is further simplified by assuming that

$$\chi = a + bt \quad . \tag{44}$$

This expression may be substituted into equations (17) and (18) to obtain

$$\ddot{x} = \frac{F}{m} \cos (a + bt) \tag{45}$$

$$\ddot{y} = \frac{F}{m} \sin (a + bt) \quad . \tag{46}$$

Integrating equations (45) and (46) yields

$$\dot{x}_c = \int_o^{t_c} \frac{F}{m} \cos (a + bt)\, dt + \dot{x}_o \qquad \text{and} \tag{47}$$

$$\dot{y}_c = \int_o^{t_c} \frac{F}{m} \sin (a + bt)\, dt - gt + \dot{y}_o \quad . \tag{48}$$

and integrating equations (47) and (48) yields

$$x_c = \int_o^{t_c} \int_o^{t} \frac{F}{m} \cos (a + bt)\, dt^2 + \dot{x}_o t + x_o \tag{49}$$

and

$$y_c = \int_o^{t_c} \int_o^{t} \frac{F}{m} \sin (a + bt)\, dt^2 - \frac{gt^2}{2} + \dot{y}_o t + y_o \quad . \tag{50}$$

Equations (47), (48), and (50) may be substituted into equations (26), (27), and (25), respectively, to obtain three simultaneous equations in the three unknowns a, b, and t_c.

The simultaneous solution of these three equations provides the values of a, b, and t_c required for calculating the optimal payload for the flat earth case. This is an open loop solution to the problem. This process may be made a closed loop process by repeating it and recomputing new values of a, b, and t_c, at each second or so of flight. This is the desired solution sought from the beginning of the problem. Using the values of a, b, and t_c, the resulting value of χ is taken as an approximate solution to equations (4) and (5). This is the basic concept of the iterative guidance mode. The remainder of this paper is concerned with three topics:

(a) Methods for solving the three simultaneous transcendental equations in three unknowns.

(b) Methods of applying the flat earth optimal solution to the realistic case and improving the optimality in this application. It will later be shown that accuracy is not a problem because of the sequence of computation.

(c) Stability and accuracy of the iterative guidance mode.

V. SOLVING THE SIMULTANEOUS EQUATIONS

Returning to the transversality condition of equation (40), assume for the moment that $y(t_c)$ is unspecified as well as $x(t_c)$. Then both P_{20} and P_{40} are equal to zero, and the optimum steering law is given by

$$\tan\chi = \frac{P_{30}}{P_{10}} = \tilde{\chi} \text{ a constant.} \tag{51}$$

Equation (51) states that, for a flat earth, the optimum steering program to achieve a given velocity, without position constraints, is a constant.

For this case, equations (45) and (46) can be written

$$\ddot{x} = \frac{F}{m} \cos\tilde{\chi} \tag{52}$$

$$\ddot{y} = \frac{F}{m} \sin\tilde{\chi} - g \ . \qquad (53)$$

Integrating equations (52) and (53)

$$\dot{x}_c = v_{ex} \ln \left(\frac{\tau_o}{\tau_o - \tau_c} \right) \cos\tilde{\chi} + \dot{x}_o \qquad (54)$$

$$\dot{y}_c = v_{ex} \ln \left(\frac{\tau_o}{\tau_o - \tau_c} \right) \sin\tilde{\chi} + \dot{y}_o - g t_c \qquad (55)$$

where

$$\frac{F}{m} = \frac{v_{ex}}{\tau - t} \qquad (56)$$

$$\tau = \frac{m(t)}{\dot{m}} \qquad (57)$$

$$v_{ex} = I_{sp} g_o = \text{characteristic velocity.} \qquad (58)$$

Equations (54) and (55) may be solved for $\tilde{\chi}$

$$\tilde{\chi} = \arctan \left[\frac{\dot{y}_c - \dot{y}_o + g t_c}{\dot{x}_c - \dot{x}_o} \right] \qquad (59)$$

Equation (59) gives the value of the constant steering angle $\tilde{\chi}$ which is required to guide a vehicle from its initial point to specified values of velocity $\dot{x}(t_c)$ and $\dot{y}(t_c)$ in minimum time. These are the same values of velocity components which are required when the position constraint is imposed where, of course, the time will be increased. This angle $\tilde{\chi}$ represents the major part of the angle χ so that χ may be divided into its principal part $\tilde{\chi}$ plus a second smaller part $(-k_1 + k_2 t)$.

By adding this angle $(-k_1 + k_2 t)$, χ is changed so that, in principle, it might not be expected that the same terminal velocity components are obtained after the addition. However, since two parameters are added, the two may be chosen simultaneously so that the velocity requirements may be preserved while meeting the position constraint.

It may be observed that this same argument holds without the introduction of $\tilde{\chi}$ in the first place. The introduction of this angle in the manner described makes possible the further simplification described below in equations (60), (61), (62), and (63).

Equations (45) and (46) can now be written as

$$\ddot{x} = \frac{F}{m} \cos\left(\tilde{\chi} - k_1 + k_2 t\right) \qquad (60)$$

$$\ddot{y} = \frac{F}{m} \sin\left(\tilde{\chi} - k_1 + k_2 t\right) - g \ . \qquad (61)$$

Simplifying, assuming that $(-k_1 + k_2 t)$ is a small angle,

$$\cos\chi \approx \cos\tilde{\chi} + k_1 \sin\tilde{\chi} - k_2 t \sin\tilde{\chi} \qquad (62)$$

$$\sin\chi \approx \sin\tilde{\chi} - k_1 \cos\tilde{\chi} + k_2 t \cos\tilde{\chi} \ . \qquad (63)$$

Substitute these values into equation (61) and integrate to obtain

$$\dot{y}_c = f_1(k_1, k_2, t_c) \ . \qquad (64)$$

Integrate once again to obtain

$$y_c = f_2(k_1, k_2, t_c) \ . \qquad (65)$$

Equate (64) with (55) and solve the resulting equation simultaneously with equation (65) for k_1 and k_2.

Thus, the equation $\chi = \tilde{\chi} - k_1 + k_2 t$, where $\tilde{\chi}$, k_1, and k_2 are derived in this manner, fulfills both altitude and velocity conditions.

To solve for t_c, consider the velocity to be gained at a given instant of time.

$$\Delta v = \left[(\dot{x}_c - \dot{x})^2 + (\dot{y}_c - \dot{y} + g t_c)^2 \right]^{\frac{1}{2}} \qquad (66)$$

together with the characteristic velocity equation

$$t_c = \tau[1 - e^{-\Delta v/v_{ex}}] \quad . \tag{67}$$

Equations (66) and (67) may be solved simultaneously for t_c. Thus, k_1, k_2, and t_c have been obtained for the flat earth case.

VI. GUIDANCE OVER A SPHERICAL EARTH

The methods employed in the derivation of the guidance equations for a spherical earth are essentially the same as those used with a flat earth model. However, the equations of motion must be modified to account for the constantly changing magnitude and direction of the gravity force. An average gravity magnitude g^*, and an average gravity direction ϕ^*, between the current point on the trajectory and the final injection point are updated at the beginning of each computation cycle.

For deriving the guidance equations on a spherical earth, it is convenient to change coordinate systems so that the terminal conditions expressed in equations (12), (13), and (14) may be expressed in a more convenient form. The new coordinate system is chosen so that the η axis coincides with the local vertical at the injection point. The ξ axis is chosen parallel to the local horizontal at injection. In this coordinate system, the equations of motion are

$$\ddot{\xi} = \frac{F}{m}\cos\chi_{\xi} - g^* \sin\phi^* \tag{68}$$

$$\ddot{\eta} = \frac{F}{m}\sin\chi_{\xi} + g^* \cos\phi^* \quad . \tag{69}$$

The terminal conditions in this coordinate system are

$$\xi_c \text{ unspecified} \tag{70}$$

$$\dot{\xi}_c = v_c \tag{71}$$

$$\dot{\eta}_c = 0 \tag{72}$$

$$\eta_c = h_c . \tag{73}$$

These equations may now be solved exactly as in the x, y coordinate system.

VII. SUMMARY OF GUIDANCE EQUATIONS AND REQUIRED INPUT CONSTANTS

For the calculation of the guidance of a single stage to earth orbit, the input constants are

$$v_{ex},\ \eta_{t_c},\ \dot{\eta}_{t_c},\ \dot{\xi}_{t_c} \text{ and } t_c \ .$$

The initial measured values are

$$\frac{F}{m},\ x_o,\ y_o,\ \dot{x}_o,\ \dot{y}_o,\ v_o,\ \phi_o \ .$$

Calculate

$$\tau = v_{ex}/\frac{F}{m}$$

$$A_1 = -v_{ex}\,\ell n\,(1 - \frac{t_c}{\tau})$$

$$A_2 = A_1\tau - v_{ex}\,t_c$$

$$A_3 = -A_2 + t_c A_1$$

$$A_4 = A_3\,\tau - \frac{v_{ex}\,t_c^{\,2}}{2}$$

$$\phi_{t_c} = \frac{A_3 + v_o t_c}{\eta_{t_c}}$$

$$\xi_o = x_o \cos(\phi_o + \phi_{t_c}) - y_o \sin(\phi_o + \phi_{t_c})$$

$$\eta_o = x_o \sin(\phi_o + \phi_{t_c}) + y_o \cos(\phi_o + \phi_{t_c})$$

$$\dot{\xi}_o = \dot{x}_o \cos(\phi_o + \phi_{t_c}) - \dot{y}_o \sin(\phi_o + \phi_{t_c})$$

$$\dot{\eta}_o = \dot{x}_o \sin(\phi_o + \phi_{t_c}) + \dot{y}_o \cos(\phi_o + \phi_{t_c})$$

$$g^* = \tfrac{1}{2}(g_o + g_{t_c})$$

$$\phi^* = \tfrac{1}{2}\,\phi_{t_c}$$

$$\left.\begin{aligned} \Delta v_o^2 &= (\dot{\xi}_{t_c} - \dot{\xi}_o - g^* t_c \sin\phi^*)^2 \\ &\quad + (\dot{\eta}_{t_c} - \dot{\eta}_o + g^* t_c \cos\phi^*)^2 \\ \Delta v_0 &= -v_{ex}\, n\,(1 - t_c/\tau) \end{aligned}\right\} \text{Solve simultaneously for } t_c$$

$$\tilde{\chi}_\xi = \tan^{-1}\left[\frac{\dot{\eta}_{t_c} - \dot{\eta}_0 + g^* t_c \cos\phi^*}{\dot{\xi}_{t_c} - \dot{\xi}_o - g^* t_c \sin\phi^*}\right]$$

$$P = A_3 \cos\tilde{\chi}_\xi$$

$$Q = A_4 \cos\tilde{\chi}_\xi$$

$$R = \eta_{t_c} - \eta_o - \dot{\eta}_o t_c + \tfrac{1}{2} g^* t_c^2 \cos\phi^* - A_3 \sin\tilde{\chi}_\xi$$

$$k_1 = \frac{A_2 R}{A_1 Q - A_2 P}$$

$$k_2 = \frac{A_1 R}{A_1 Q - A_2 P}$$

$$\chi_\xi = \tilde{\chi}_\xi - (k_1 - k_2 t)$$

$$\chi = \chi_\xi - \phi_o - \phi_{t_c} .$$

This angle χ is introduced into the control system, and the computation cycle is started over again. As the computation progresses through the flight, computation of k_1 and k_2 is stopped when $t_c < 20$ seconds. Cutoff is given when $t_c = 0$. The system of equations listed above is calculated repeatedly throughout the flight, treating each time point as new initial conditions. Errors of the approximation introduced tend to zero at terminal time, and terminal conditions are fulfilled precisely.

VIII. STABILITY, ACCURACY, AND OPTIMALITY OF THE I. G. M.

The partial derivatives of attitude with respect to the state variables are the most significant criteria for stability and accuracy. The F/m derivative is small during the entire flight, eliminating this usually rather noisy measurement as a trouble source. However, because the trajectory optimization is based on a predicted relation of the future thrust profile for a stage to the instantaneously measured value, any major thrust change will cause a performance loss.

The other derivatives start at low values and increase approximately inversely proportional to the time-to-go (for velocity errors) or its square (for displacement). The tightening of the guidance loop toward the end of flight is very desirable because it keeps residual errors small. However, it creates a potential stability problem. This problem was eliminated without causing a significant error by stopping computation of the steering equations at a given time-to-go (e. g., $t_c = 20$ seconds) and flying open loop. A better method is to freeze the time-to-go at a minimum value and continue guidance.

The low guidance gains at early flight make the system very tolerant to major disturbances, noise and time lags during this phase.

Guidance scheme errors for realistic variations of initial conditions (Table I) are very small. The effects of performance variations, changes in air density, and winds are equally insignificant.

TABLE I. GUIDANCE SCHEME ERRORS FOR REALISTIC VARIATIONS OF INITIAL CONDITIONS

Initial Stage Variable				Payload Loss	Injection Errors		
Δx_1 km	$\Delta \dot{x}_1$ m/s	Δy_1 km	$\Delta \dot{y}_1$ m/s	percent	Altitude m	Velocity m/s	Path Angle degrees
+2.7	0	0	0	.11	.1	0	+.001
0	+143	0	0	.32	.13	-.04	0
0	- 57	0	0	.07	.1	+.01	+.001
0	0	1.0	0	.11	.1	0	+.001
0	0	0	+78	.14	.1	-.01	0
0	0	0	-80	.11	.1	0	+.001

A time lag of 5 seconds from measurement to steering command causes no error and no loss of weight in orbit. A 40 second lag caused 3 km altitude error and 11 percent payload load loss.

Periodic thrust fluctuations with a maximum amplitude of 65 percent of nominal and periods of 5 - 100 seconds create no serious stability problem.

IX. REFERENCES

1. Hoelker, R. F., The Evolution of Guidance Theory and Trajectory Analysis into a Single Scientific Discipline, prepared for presentation at the Meeting of the Institute of Navigation in Williamsburg, Va., June 1961. Marshall Space Flight Center, Huntsville, Alabama.

2. Miner, W. E., Schmieder, D. H., and Braud, N. J., The Path-Adaptive Mode for Guiding Space Flight Vehicles, ARS Guidance, Control and Navigation Conference, Stanford, California, August 1961. Revised March 1962, Reprint from Progress in Astronautics and Rocketry, 1962 Academic Press, New York, New York.

3. Baker, C. D., A Minimum Fuel Reserve Guidance System, Aero-Internal Note 3-64 (Limited Distribution) January 14, 1964.

4. Smith, I. E., Hart, J. J., and Chandler, D. C., Procedure for Implementing a Simplified Path Adaptive Scheme, Marshall Space Flight Center, Aeroballistics Internal Note #25-62, July 31, 1962.

5. Horn, H. J., Martin, D. T., and Chandler, D. C., An Iterative Guidance Scheme and Its Application to Lunar Landing, Marshall Space Flight Center report, MTP-AERO-63-11 (Limited Distribution) February 6, 1963.

6. Horn, H. J., Application of An Iterative Guidance Mode To A Lunar Landing, Paper No. 1504 (63) presented at the Third European Space Flight Symposium and 15th Annual Meeting of the DGRR in Stuttgart, Germany, May 22-24, 1963. Reprinted in: Raumfahrtforschung, Heft 2, April-Juni 1964, pp. 49-54.

7. Smith, I. E., and Deaton, Jr., E. T., An Ite ative Guidance Scheme For Ascent To Ori (Suborbital Start of The Third Stage), Marsh Space Flight Center report, MTP-AERO-63-4 May 29, 1963.

8. Fried, B. D., On the Powered Flight Trajector of an Earth Satellite, Jet Propulsion, Vol. 2 June 1957, pp. 641-643.

9. Lawden, D. F., Optimal Rocket Trajectorie Jet Propulsion, Vol. 27, December 195 p. 1263.

10. Fried, Burton D., Trajectory Optimization fo Powered Flight in Two or Three Dimensions, i Space Technology, Edited by H. Seifert, 195 p. 4-9.

11. Perkins, F. M., Flight Mechanics of Ascendin Satellite Vehicles, Jet Propulsion, Vol. 2 May 1956, pp. 352-358.

12. MacPherson, D., An Explicit Method of Guidin A Vehicle From An Arbitrary Initial Positio and Velocity To A Prescribed Orbit, Aerospac Corporation, TDR-594 (1565-01) TN-1, Febru ary 13, 1961.

13. Cherry, G. W., Orbit Insertion Guidance Tech nique, Space Guidance Analysis Memo #30, MIT Instrumentation Laboratory, November 2 1962.

14. Cherry, G. W., A Unified Explicit Technique for Performing Orbital Insertion, Soft Landing and Rendezvous with a Throttleable Rocket-Propelled Space Vehicle, AIAA Guidance and Control Conference; August 12-14, 1963.

15. Perkins, F. M., Optimum Guided Ascent, Aerospace Corporation, SSD-TDR-64-120, Jun 1964.

VI. INSTRUMENTATION

DEVELOPMENT OF A LASER DOPPLER FLOWMETER FOR GAS VELOCITY MEASUREMENT

By

W. Foreman* and Robert M. Huffaker

SUMMARY

The measurement of gas velocity for a gas that has variations in pressure and density has proven to be very difficult using the more conventional methods of probes such as electron beams, gamma rays or x-rays. These methods require the detecting apparatus to be exposed to the radiation for long periods of time, or they have pressure limitations. The large magnitudes of the Doppler shifts obtainable, using a CW gas laser, suggest that local velocity vectors can be measured by using the visible light from the laser. Optical heterodyning of the laser light scattered from the flowing gas with a portion of the incident laser beam split off from a beam splitter will produce a beat signal at the frequency of the Doppler shift due to the motion of the gas. Measurement of the beat signal frequency, together with the geometry of the optical system, determines the flow velocity of the gas. A probeless velocity measuring technique has been developed based on this principle. This technique has been checked in a wind tunnel at speeds up to 500 ft/sec (150 m/sec). Work is continuing to determine velocity limitations. This technique also gives a distribution of velocities due to the turbulence level of the gas flow. This technique is also applicable for the measurement of velocity of any moving surface. Some applications will be the measurement of panel flutter and for a calibration of dynamic pressure transducers or other applications where knowledge of particle flow is desired.

I. INTRODUCTION

Overlapping of the exhaust plumes from the various exhaust nozzles of high-thrust rocket engines gives rise to an undesirable flow characteristic called "reverse flow" in which some of the hot exhaust gases flow back toward the base of the rocket. Impingement of the hot reverse flow on the base region causes local heating. The effect becomes more pronounced at high altitude, where the exhaust plumes expand due to the low ambient pressure. To achieve a satisfactory thermal balance in the base region of the rocket, the heating effects due to reverse flow must be taken into account. Unfortunately, the problem is so complex that application of ordinary analytical techniques to the reverse flow phenomenon cannot be made with complete confidence. Experimental measurements of the local temperature, density, and flow velocity of the exhaust gases in the vicinity of the base region are required to supplement the analytical treatment.

Reverse flow phenomena also occur in cold flow models of rocket engines -- that is, scale models of rocket nozzle clusters in which ordinary air at room temperature is forced through the nozzles at high speed. Both the analytical and experimental approaches to the reverse flow problem are simpler in the cold flow case. For this reason, it is logical to begin a study of reverse flow phenomena with a cold flow model.

This paper is concerned with the development of a new experimental technique for measuring one of the variables associated with reverse flow fields in cold flow models, namely, local flow velocities in the neighborhood of the base region.

II. THE LASER DOPPLER FLOWMETER

The following are the two principal conditions which a cold flow velocity measurement must satisfy:

(1) It is necessary to measure local flow velocities with reasonable accuracy.

(2) The perturbation induced in the flow pattern by the measurement technique must be negligible.

In addition to these requirements, it is highly desirable to measure the complete velocity vector $\vec{v}$ at a given point, rather than a single component of $\vec{v}$ along a given direction. This could be done, for example, by measuring simultaneously the components of $\vec{v}$ along three noncoplanar axes which intersect at the given point.

None of the gas flow velocity measurement techniques currently in use fully satisfy the requirements listed above. One promising approach to the problem which has not yet been seriously exploited is the optical

* Employed by Brown Engineering Co., Huntsville, Alabama

Doppler technique. In this approach, use is made of the fact that when monochromatic light is scattered from moving particles, the frequency of the scattered light differs from that of the incident light (Doppler effect). The Doppler frequency shift depends both on the velocity of the moving particles and on the geometry of the scattering. If the scattering geometry is fixed, measurement of the Doppler shift gives sufficient information to determine the velocity of the moving particles.

Before the development of the continuous-wave gas laser, there was no monochromatic light source with sufficient intensity to serve as the source in an optical Doppler flowmeter. Furthermore, even if a suitable source had been available, the best spectrographic techniques could not have furnished the resolution necessary to measure the small Doppler shifts associated with ordinary flow velocities. For example, if monochromatic light of wavelength $\lambda = 6000$ Å is reflected at normal incidence from a body moving at a speed of 10 ft/sec (3 m/sec) the resulting Doppler shift is 10 MHz, which corresponds to a wavelength shift of approximately 0.0001 Å. A wavelength shift this small is well beyond the range of ordinary spectographic resolution.

The development of the continuous-wave gas laser furnished a light source which meets the stringent requirements of the optical Doppler flowmeter. The concomitant development of the technique of optical heterodyning furnished a Doppler shift detection mechanism which possesses the necessary resolution. In optical heterodyning, two coherent, monochromatic light beams with different frequencies are directed simultaneously onto the photosensitive surface of a photodetector (for example, the photocathode of a photomultiplier tube). The intrinsic square-law response of the photodetector leads to an electrical output signal the frequency of which is equal to the frequency difference between the two incident light beams. Optical heterodyning thus allows a direct measurement of the frequency difference between two coherent, monochromatic light beams from a few Hertz up to the maximum frequency response of the photodetector (typically several hundred mega-Hertz for fast photomultiplier tubes). The development of these two basic tools brought the optical Doppler flowmeter into the realm of feasibility.

A laser Doppler flowmeter designed to measure liquid flow rates has been operated by Yeh and Cummins [1] at the Radiation Laboratory of Columbia University. A simplified diagram of the Yeh-Cummins laser flowmeter is shown in Figure 1. Polystyrene spheres of diameter 0.557μ were placed in water to form a dilute colloidal suspension (1 part solid to

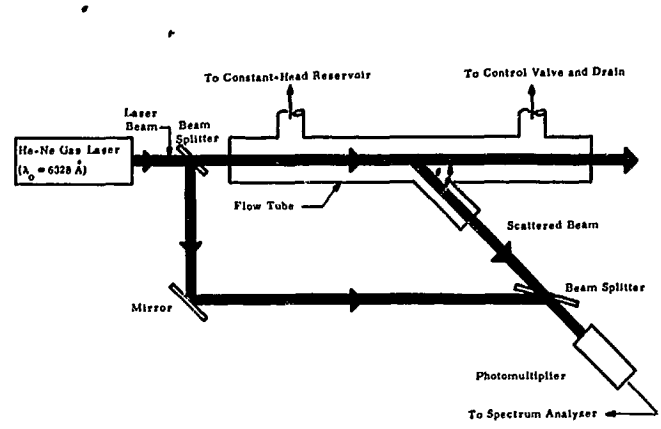

FIGURE 1. A SIMPLIFIED DIAGRAM OF THE LASER FLOWMETER OF YEH AND CUMMINS

30,000 parts water by volume). These spheres served as optical scattering centers for the light beam generated by a He-Ne gas laser operating at a wavelength of 6328 Å. The continuous power output of the laser was approximately 5 mW in the TEM_{00} mode. The contaminated water flowed from a large, constant-head reservoir through a flow tube of circular cross section. The flow rate was controlled by an outlet needle valve. The laser beam passed axially down the flow tube, and the light scattered at an angle θ by the scattering centers lying within a small linear segment of the laser beam was collected by an optical system, combined with a fraction of the incident laser beam by a system of beam splitters, and focused on the photocathode of a photomultiplier tube. The scattered light suffered a Doppler shift of frequency f_D given by

$$f_D = \frac{2 v n}{\lambda_o} \sin^2 \frac{\theta}{2} , \qquad (1)$$

where n is the index of refraction of the liquid, v is the flow velocity, and $\lambda_o = 6328$ Å is the vacuum wavelength of the incident laser beam. Optical heterodyning of the scattered and unscattered beams on the photocathode gave rise to a sinusoidal signal in the photomultiplier output at the difference frequency f_D. Measurement of this frequency allowed the flow velocity v to be calculated from equation (1). By translating the beam back and forth across the diameter of the flow tube, Yeh and Cummins were able to measure the velocity profile across the tube. They obtained a parabolic velocity distribution in excellent agreement with the theory of laminar flow. The minimum detectable velocity in this experiment was estimated to be about 4×10^{-3} cm/sec.

An experimental feasibility study was initiated within the Brown Research Laboratories to verify the feasibility of applying the laser Doppler flowmeter to

BLANK PAGE

gas flow fields. In May 1965, the Doppler shift due to scattering of visible gas laser radiation from a contaminated flowing gas was detected for the first time by Foreman, George, and Lewis [2], thereby verifying the basic feasibility of the laser flowmeter. Further experiments have since been conducted to verify the feasibility of applying the laser Doppler flowmeter to cold flow model studies. The experimental results to date are summarized, and some planned future experiments are discussed briefly.

III. BASIC FEASIBILITY EXPERIMENTS

Since the initial feasibility experiments on the laser Doppler flowmeter have been discussed in detail in Reference 2, only a brief summary will be presented here. The experimental arrangement used to detect the Doppler shift in laser light scattered from a flowing contaminated gas is shown in Figure 2. It is necessary to add an optical scattering contaminant (such as smoke) to the flowing gas to increase the intensity of the scattered light up to a usable level.

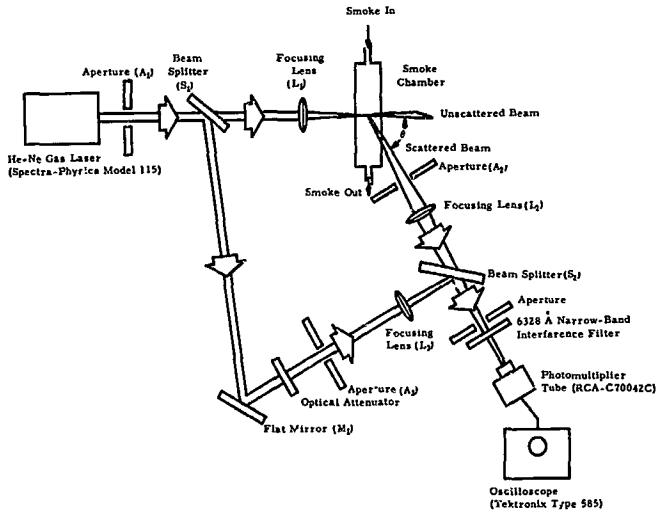

FIGURE 2. DETAILS OF THE EXPERIMENTAL SETUP FOR BASIC FEASIBILITY DEMONSTRATION

The coherent, monochromatic light beam emerging from a He-Ne gas laser passes through an aperture A_1 to remove the blue haze which surrounds the red laser beam. The beam is then split into two parts by the beam splitter S_1. The deflected beam is reflected off a flat mirror M_1, after which it is attenuated by passage through a set of neutral density filters. It then passes through an aperture A_3 and a focusing lens L_3, and is finally deflected into a photomultiplier tube by the beam splitter S_2. The rest of the original laser beam passes through S_1, and is focused to a point by the lens L_1. A glass chamber filled with air contaminated with smoke is placed at the focal point of L_1. The lens L_2 collects the light scattered from the smoke chamber at an angle θ with the forward direction of the unscattered beam. The aperture A_2 limits the total solid angle over which the scattered light is intercepted by L_2. The scattered light collected by L_2 passes through the beam splitter S_2 and enters the photomultiplier. The lenses L_2 and L_3 are positioned in such a way that the two beams are focused at the same spot on the photocathode, and the optical system is aligned so that the axes of the two converging beams entering the photomultiplier are coincident.

When the smoke-filled air in the chamber was set into motion by means of a small air compressor, a high frequency heterodyne signal appeared on the oscilloscope screen. A typical waveform is shown in Figure 3. The frequency of the signal agreed approximately with that to be expected for the Doppler shift

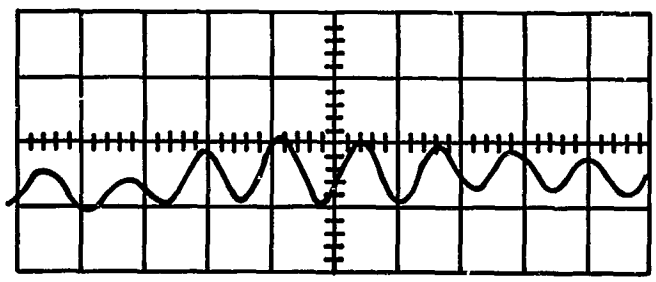

Sweep Speed: 200 μsec/cm
Sensitivity: 20 mv/cm

FIGURE 3. DOPPLER WAVEFORM FROM MOVING SMOKE AT LOW VELOCITY

from particles moving with the estimated smoke velocity. The signal disappeared when the reference beam (reflected from minor M_1) was blocked off proving that a true heterodyne signal was being observed. The signal also disappeared when the smoke was at rest. When the flow speed through the chamber was varied, the heterodyne signal frequency tracked the flow speed linearly. These results verified the basic feasibility of a laser Doppler flowmeter for measurement of contaminated gas flow velocities.

IV. QUANTITATIVE FLOW MEASUREMENTS AT LOW VELOCITIES

It is anticipated that in cold flow model studies, velocities up to Mach 2 will be encountered. It is therefore necessary to verify that the laser Doppler flowmeter can be used up to hypersonic velocities before attempting to apply it directly to a cold flow model. Following the initial feasibility demonstration described in the previous section, a program was begun to make careful quantitative flow measurements from low velocities up to hypersonic velocities.

The first quantitative flow measurements were made with the apparatus shown in Figure 4. The laser beam is focused at the center of a 5 mm inside diameter glass tube through which air is drawn by an exhaust blower. Smoke is added to the air upstream from the optics to provide the necessary light scattering contaminant. The laser beam emerging from the glass tube is intercepted by a lens, attenuated, and focused on the photocathode of an RCA-C70042C photomultiplier tube. Light scattered at an angle θ by the moving smoke is collected by a lens and also focused on the photocathode. The heterodyne signal from the photomultiplier is fed into a wideband amplifier, the bandpass of which is cut off below 1 kHz by an external high-pass filter. The Doppler shift frequency f_D is read out on an analog frequency meter (General Radio Type 1142-A).

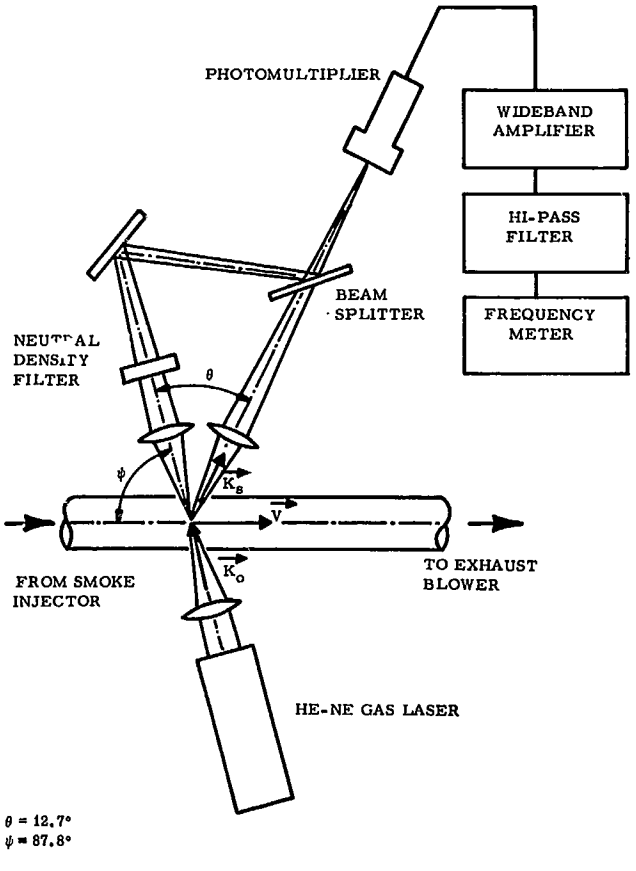

FIGURE 4. EXPERIMENTAL ARRANGEMENT FOR LOW-VELOCITY MEASUREMENTS

The Doppler frequency shift f_D is given in the general case by the expression [3]

$$f_D = (2\pi)^{-1} [\vec{k}_s - \vec{k}_o] \cdot \vec{v} , \qquad (2)$$

where $\vec{k}_s$ and $\vec{k}_o$ are the wave vectors of the scattered and incident beams, respectively, and $\vec{v}$ is the velocity of the scattering particles. Application of equation (2) to the scattering geometry shown in Figure 4 gives

$$f_D = \frac{2v}{\lambda_o} \sin \frac{\theta}{2} \sin \left(\psi + \frac{\theta}{2}\right) , \qquad (3)$$

where $\lambda_o = 6328$ Å is the vacuum wavelength of the incident laser beam. In deriving equation (3) use has been made of the fact that $k_s \approx k_o$, and the directional spreads in $\vec{k}_s$ and $\vec{k}_o$ due to focusing have been neglected.

As an independent check on the laser flowmeter results, the flow velocity was measured directly by timing the passage of the leading edge of the injected smoke stream between two points 70 cm apart, one upstream and one downstream from the optics. It was not possible to measure the flow with high accuracy by this method, but the flow speed (~ 1 cm/sec to ~ 100 cm/sec) was too small to allow the use of a Pitot tube. The frequencies f_D measured with the laser Doppler flowmeter are plotted as a function of the directly measured velocities in Figure 5. A theoretical curve calculated from equation (3) is also shown. The results are quite satisfactory, especially considering the inaccuracies inherent in the direct velocity measurements. Above a velocity of 100 cm/sec the direct velocity measurements became too inaccurate to be useful. The Doppler signal could be tracked, however, all the way up to the maximum velocity v ~ 14.4 m/sec (corresponding to f_D ~ MHz which the blower system could produce. At heterodyne frequencies higher than the 1.5 MHz upper limit of the analog frequency meter, the heterodyne signal was monitored on an oscilloscope.

Auxiliary experiments have been performed which indicate that the efficiency of optical heterodyning goes through a steep maximum in the immediate neighborhood of the focal point of the incident laser beam. A

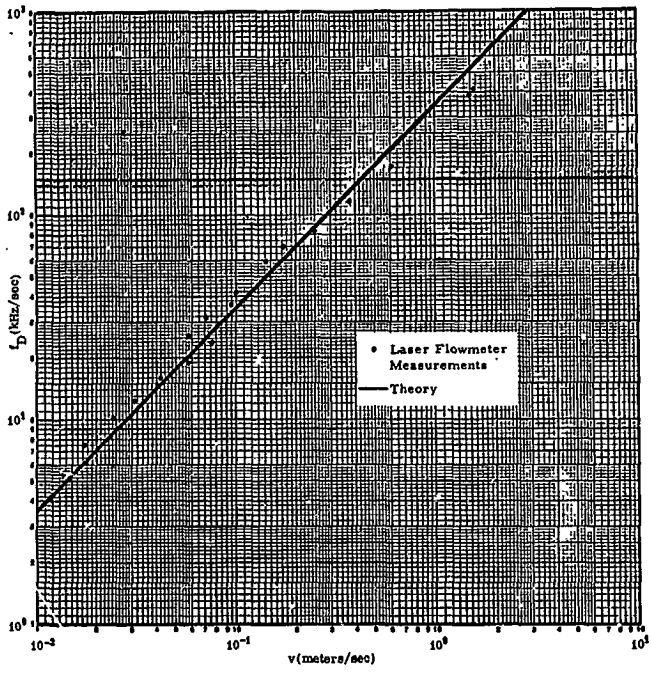

FIGURE 5. COMPARISON OF LASER FLOWMETER RESULTS WITH THEORY

similar observation has been made by Kroeger [4] using laser light scattered from moving diffuse surfaces. As a consequence of this effect, the Doppler shift, which is observed with the laser Doppler flowmeter, is due to the flow velocity only in the immediate neighborhood of the focal point of the incident beam -- that is, the laser flowmeter gives a local velocity measurement. By moving the focal point across the diameter of large flow tubes, velocity profiles have been measured. The flow fields which have been used thus far have not been sufficiently laminar, however, to allow a good comparison between the measured velocity profiles and those predicted by the theory of laminar flow.

Following the low velocity measurements made with the arrangement shown in Figure 4, a similar optical system was set up on a small wind tunnel in the Brown Research Laboratories designed to produce a maximum flow velocity of about 50 m/sec. The experimental setup is shown in Figure 6. A continuous air flow is maintained through the system by an exhaust blower located on the roof of the building. Air is drawn into the intake through a set of three porous air filters located at the base of the tunnel. Smoke is generated in the base region by burning commerical smoke candles. The smoke mixes with the incoming air and passes through a series of contractions into the test section, which has a 1" × 3" rectangular cross section. A Pitot tube is provided to supply an independent measurement of the flow velocity at the center of the test section. Flat optical entrance and exit windows for the laser and scattered beams are mounted flush with the inside walls of the test section to avoid perturbing the flow pattern. Above the test section, the wind tunnel cross section gradually expands to a 10" × 10" square shape. The tunnel is then joined to a 10" × 10" vent which connects the tunnel to the exhaust blower on the roof. A bleeder vent is connected in parallel with the wind tunnel. By adjusting a control

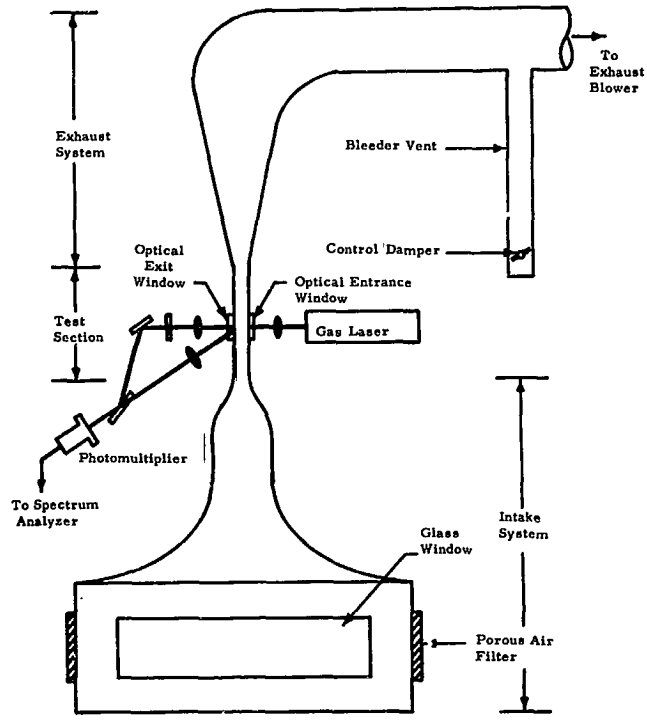

FIGURE 6. LOW-VELOCITY WIND TUNNEL

damper in the bleeder vent, the flow velocity in the wind tunnel can be varied over a wide range.

Velocity measurements on the wind tunnel have just begun. The Doppler heterodyne signal has been detected from low velocities up to the highest velocity (~ 50 m/sec) which the tunnel can produce, but careful quantitative data have not yet been taken.

V. PROPOSED FUTURE EXPERIMENTS

After the completion of the low-velocity wind tunnel work described above, it will be necessary to extend the measurements to velocities in the sonic and hypersonic range. Preparations are now underway to make use of a high speed wind tunnel at Marshall Space Flight Center for this purpose. The tunnel in question covers the Mach number ranges from 0.3 to 0.85 and 1.5 to 4.5. The major problem at high

velocities is expected to be the generation and injection of sufficient quantities of smoke into the flow stream.

One possible remedy for the smoke problem is the use of a gas laser with considerably higher power than that available from the He-Ne laser used in the low velocity experiments. As the laser power output increases, the density of smoke required to maintain a given scattered light intensity decreases proportionately. The possibility of using the recently developed Argon gas laser (with an output power of about 330 mW in a single blue line) is also being investigated.

Following the hypersonic velocity measurements, attention will be turned to the development of a multidimensional velocity measurement system. Two orthogonal components of local velocity vectors can be measured by a trivial extension of the system used to measure one component. Although the design of a system to measure three noncoplanar components will be somewhat more complex, it does not appear to be impractical.

The laser Doppler flowmeter should eventually find application in a wide variety of gas flow measurements. Its practical ramifications extend far beyond cold-flow model studies, although it was for this purpose that the present experimental program was begun.

REFERENCES

1. Yeh, Y.; and Cummins, H. Z.: Localized Fluid Flow Measurements with an He-Ne Laser Spectrometer. App. Phys. Lett., 4, 176, 1964.

2. Foreman, J. W., Jr.; George, E. W.; and Lewis, R. D.: Feasibility Study of a Laser Flowmeter for Local Velocity Measurements in Gas Flow Fields. Tech. Note R-149, Brown Eng. Co., Inc., Huntsville, Ala., May 1965. (The preliminary results were to be published in the August 1 issue of the J. Appl. Phys.).

3. Lee, K. S. H.: On the Doppler Effect in a Medium. Tech. Rep. No. 29, Antenna Lab., Calif. Inst. of Technology, Dec. 1963.

4. Kroeger, R. D.: Motion Sensing by Optical Heterodyne Doppler Detection from Diffuse Surfaces. Proc. IEEE, 53, 211, 1965.

MEASUREMENT OF GAS TEMPERATURE AND THE RADIATION COMPENSATING THERMOCOUPLE

By

Glenn E. Daniels

SUMMARY

To achieve a high degree of accuracy in gas temperature measurement, a method is devised whereby several thermocouples may be wired together to make the Radiation Compensating Thermocouple. This thermocouple is designed so that the errors of measurement from the radiation environment will cancel out; results of tests, equations, and information are presented to aid in its fabrication.

I. INTRODUCTION

To evaluate the tests and operation of the Radiation Compensating Thermocouple described later in this report, the first section has been used for a brief discussion of the theory of gas temperature measurement. The available literature covering the theoretical problems of heat transfer around a cylinder and the derivation of a theoretical expression for the error of a thermometer used in measuring a gas temperature under the various situations which may occur is scarce. Because of the complexity of the theory, the actual design of the Radiation Compensating Thermocouple has been based on empirical data obtained by laboratory and field measurements.

The accurate measurement of gas temperatures presents many problems because of the large errors usually present. An object immersed in a gas reaches thermal equilibrium at a temperature which is frequently different from that of the gas.

The problem of precise temperature measurement can best be described as follows:

The temperature which a temperature sensor (thermometer) indicates is not usually the temperature of a gas, but a temperature which is a result of heat transfer from the gas and its surroundings to the sensor by radiation and convection-conduction balanced against the rate of heat transfer from the sensor by radiation and convection-conduction to the gas and surroundings and by conduction from the sensor to its support (Fig. 1).

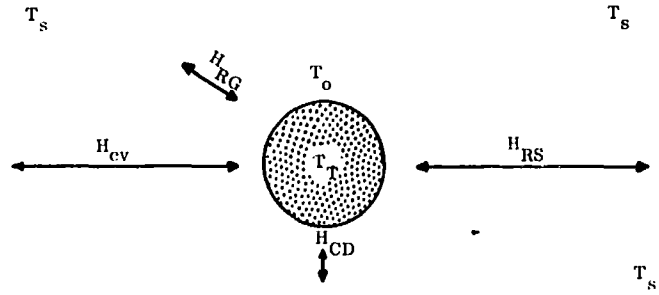

where: T_o = gas temperature

T_s = surrounding temperature

T_T = temperature of the sensor

H_{cv} = heat transfer by convection and conduction between the gas and sensor

H_{RS} = heat transfer by radiation between the sensor and the surroundings

H_{CD} = heat transfer by conduction between the sensor and support

H_{RG} = heat transfer by radiation from gas molecul to sensor

FIGURE 1. HEAT TRANSFERS BETWEEN AN OBJECT AND GAS

If the temperature of the gas changes rapidly, the response time of the temperature sensor (i.e., the time required for the individual heat transfer rates to again come into equilibrium) is another factor which influences the correctness of the temperature indicated by the sensor with respect to the true gas temperature.

The knowledge that thermometers do not usually measure the correct temperature of a gas is not new; William Charles Wells [1] in his studies of the formation of dew at the beginning of the 19th Century (1800 to 1815) realized that the air temperatures measured by his thermometers were not always correct. The Annual Report of the Chief Signal Officer [2] for the year 1887 includes a detailed discussion of the errors

of thermometers used to measure air temperatures and of the errors of air temperature measurements when weather shelters are used.

Since these early reports were made, a large number of studies and tests on the problems of gas temperature measurement have been reported in the literature; for example, Circular 513 [3] of the National Bureau of Standards lists approximately 400 references to papers on the measurement of gas temperatures published during the period between 1929 and 1951. Since 1951, many additional reports have been published on the subject.

In many published articles, the factors which cause a sensor to indicate a temperature different from the gas temperature have been described as errors of the sensor. Actually, the temperature indicated by the sensor is a very accurate measurement of the equilibrium temperature the sensor has reached while exposed to the gas and to its surroundings, if properly calibrated.

The amount by which the temperature of the sensor differs from the actual temperature of the gas is a result of the various heat transfers reaching a balance different from the balance of the heat transfers which would result if the temperature of all the surroundings were the same as the gas temperature. This amount will be referred to as an error in this paper (not an error of the sensor, but a result of the sensor temperature being different from the gas temperature).

The various factors which enter into the measurement of a temperature affect a temperature sensor in a gas in the following ways:

1. Radiation heat transfer (H_{RS}) between the sensor and the surrounding objects occurs when the surroundings have a different temperature from the gas; i.e., the sun, as a source hotter than the sensor, will cause the unshielded thermometer to indicate too high a temperature, while a clear sky, as a source colder than the sensor, will result in temperature indications which are too low. The addition of thermal radiation shields reduces, but does not eliminate, the radiation error because the shield (a surrounding object) becomes a source for heat transfer by radiation.

Reduction of the amount of heat transfer by radiation (i.e., a cloudy day) will reduce the error of measurement. Radiation heat transfer can occur in a vacuum.

2. Radiation heat transfer between the sensor and the surrounding gases (H_{RG}) is an error negligible in meteorological measurements because air is transparent to radiation transfer; but luminous particles in gases in furnaces, from certain fuels, cause errors the same way that solid objects cause radiation errors.

3. Convection-conduction heat transfer between the sensor and the gas (H_{CV}) is the main process through which the temperature sensor approaches the gas temperature. If this were the only method of heat transfer, the sensor would always reach the gas temperature very closely if its response time were fast enough. This heat transfer will vary with the speed of motion of the gas across the sensor, being lowest with calm winds and increasing as a function of the wind speed. The greater this heat transfer the faster and closer the temperature sensor will approach the desired gas temperature.

4. Conduction heat transfer from the sensor to the sensor supports (H_{CD}) is a loss of heat (or gain) that could cause large errors. This is the flow of heat from a thermocouple along the wire leads, or the flow of heat from a thermometer bulb to the glass stem. This heat transfer increases as the thermal conductivity increases, but decreases with decrease of the cross section of the supports. Such heat transfer needs to be small for accurate temperature measurement.

5. The impact of gas molecules on a sensor can cause an error by heating the sensor. For low gas velocities (normal wind speeds), these errors are negligible, but at high velocities, such as space vehicle velocities, these errors can be important.

6. The response time of a sensor can be a factor which introduces an error in measurement when a sudden change in gas temperature occurs. The faster the sensor response, the smaller the magnitude of this error and the shorter the time in which it occurs.

There are several ways in which the errors can be reduced:

1. When the sensor size is reduced, the heat transfer per unit area from radiation will be the same. The response time will also be shortened. The heat transfer per unit area from conduction and convection to the gas will increase. Therefore, the smaller sensor will more closely approach the true gas temperature; i.e., it will have a smaller error. Margaret Fishenden and Owen A. Saunders [4] have given a

BLANK PAGE

comprehensive discussion of heat transfer on cylinders of various sizes. This reference should be consulted if more information is desired.

W. J. Waggener [5], at a scientific meeting in Germany in 1898, proposed, probably for the first time, the use of a group of thermocouples of various wire sizes to determine the true temperature of a Bunsen burner flame (a hot gas surrounded by colder objects). His method was to place several thermocouples of different sizes in the flame; the various temperatures obtained were plotted versus the size of the thermocouple wires. By extrapolating the temperature curve obtained, to zero wire size, the true gas temperature is determined, because a thermocouple of zero mass and size will theoretically indicate the correct gas temperature. This is illustrated in Figure 2.

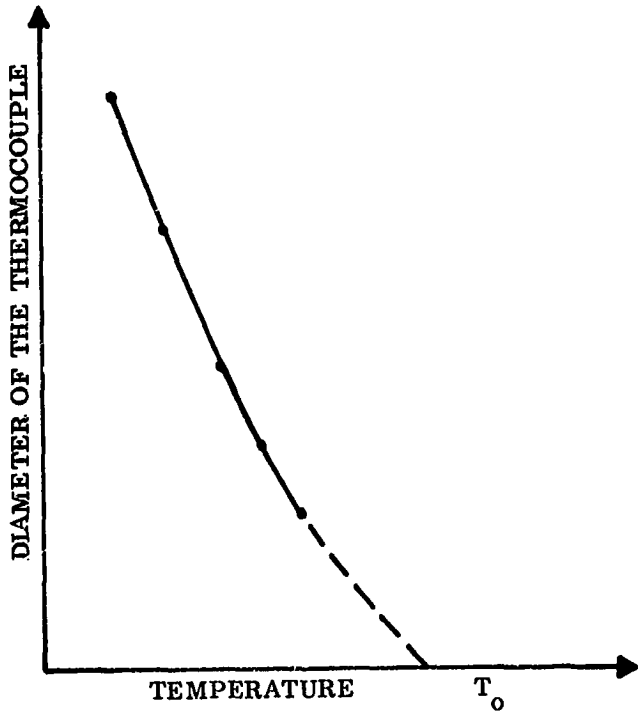

FIGURE 2. USE OF THERMOCOUPLES OF VARIOUS SIZES TO FIND THE GAS TEMPERATURE, T_o

Henry Kreisinger and J. K. Barkley [6] conducted a series of tests, using thermocouples of various sizes to measure temperatures of gases in boilers. They found that when measuring temperatures of hot gases surrounded by cooler surfaces the temperatures measured by small thermocouples were higher than those of large thermocouples. They also found that the higher the gas temperature in relation to the temperature of the boiler walls, the greater the error of measurement of the true gas temperature for a sensor of a specific size. When using a thermocouple 0.020 cm in diameter, errors exceeding 55°C (100°F) were found when the gas temperature was about 1090°C (2000°F).

Data collected at Fort Huachuca, using copper and constantan butt-joined thermocouples of various sizes in measurement of air temperatures, have shown that, when the thermocouples are used without shields or special reflective coatings, errors can reach 1°C for AWG No. 35 gage wire (0.014 cm diameter) during clear days and one-half this value on clear nights. If the thermocouple is reduced in size sufficient to provide accuracies of air temperature measurements of ±0.06°C (0.1°F), as stated in many requirements for accuracy of air temperatures, a thermocouple no larger than 0.0008 cm diameter (AWG wire size about No. 58) will be required. Such a thermocouple would be difficult to fabricate, install, and maintain and could not be expected to remain intact for more than a short period of time.

2. If the surface emissivity of the sensor is reduced (reflectivity increased), the absorption of radiation will be lower (heat transfer from radiation is less). Therefore, the sensor will read closer to the temperature of the gas. One difficulty with using high reflectivity coatings is that many of them have high values of reflectivity in the visible region of the spectrum (appear white), yet in the infrared region of the spectrum they have a low reflectivity, and thus act as a black body [7].

Considerable study of the problem of coatings for temperature sensors for radiosondes has been made by the University of Michigan and published in an annual progress report [7]. One of the best coatings they found, with a high reflectivity in both the visible and infrared region of the spectrum, is aluminum. It has a reflectivity of 94 percent. Such a coating on a thermocouple made of AWG No. 35 gage wire would result in the error of measurement, because of radiation, of about 0.17°C (0.3°F) when used in the sun without shields. This error is much smaller than normal measurements, and continuous measurements of air temperatures for micrometeorological use with this small error would be of great value. The disadvantage of such a thermocouple is that a very small thermocouple is required, and even small particles of dust accumulating on the thermocouple will greatly increase the measurement errors.

3. Since increasing the speed of the gas over the sensor increases the heat transfer from conduction and convection in the gas, aspiration of sensors has

long been a favorite method of reducing the error of gas temperature measurement. The "high velocity" thermocouple is most useful in measurement of gases in furnaces where errors of 200°C are common on the large thermocouples, where an appropriate design of the sensor and shields to accelerate the flow of gas is used. The "high velocity" thermocouple when thus used can be placed parallel to the flow of the gases. In meteorological measurements of air temperatures, especially near the surface of the ground, aspiration will obtain air samples, not from a point or horizontal plane outside the shield but from a sphere of air, with its radius depending on the rate of aspiration. Wind, with its changing direction and velocity, will distort the sphere so that the center of the sphere will not coincide with the location (height above the ground) where the measurement is required. J. Bartel [8] and Alf Nyberg [9] have discussed this problem in detail.

Many methods have been reported in the literature to eliminate, reduce, or correct the error by which sensors differ from true gas temperatures. E. Marston Moffatt, [10] Andrew I. Dahl, [11, 15] W. L. Bolles, [12] W. L. Servinghouse, [13] Marvin D. Scadron, Isidore Warshawsky, and Clarence C. Gettelman, [14] have all discussed these gas temperature errors in detail and give methods for estimating the errors. The National Advisory Committee for Aeronatuics (now Lewis Research Center, National Aeronautics and Space Administration) conducted studies on this problem, to use in research on jet engines, and presented the results in Technical Reports [16, 17, 18]. In NACA Technical Note 3766 [17] the following equation was given for computing the error of bare-wire thermocouples:

$$\text{Radiation Correction} = \frac{K^*_{rad}}{\sqrt{M_P}} \left(\frac{T_w}{T_R}\right)^{-0.18} \left[\left(\frac{T_w}{T_R}\right)^4 - \left(\frac{T_d}{T_R}\right)^4\right], \quad (1)$$

where

$K^*_{rad} \approx 27 e_w \sqrt{d}$

T_w = indicated thermocouple junction temperature

T_R = 1000°R, reference temperature

T_d = temperature of duct (surroundings)

M_P = velocity of gas (in terms of Mach number)

e_w = emittance of wire

d = diameter of wire

If we examine equation (1), we see that many of the parameters in the equation would be the same for two thermocouples of different size but of identical construction (type, same materials, etc.), if they were exposed close together. Therefore, we can rewrite equation (1) as follows for forced convection:

$$\text{Radiation correction} = \text{function} \left(\sqrt{\frac{d}{v}}\right), \quad (1a)$$

where

d = diameter of thermocouple wire

v = velocity of gas across the sensor.

Equation (1a) shows that the smaller the sensor the smaller the error; likewise, the higher the aspiration rate the smaller the error. For a short enough period of time the velocity of the gas could be assumed constant and then the radiation correction is a function only of wire size.

If the gas is at a temperature, T_O, and the surrounding objects are at a different temperature, T_S, (represented as the sum of all the objects at temperatures T_{S_1}, T_{S_2}, T_{S_3}, ..., T_{S_n}) lower (colder) than T_O, we can illustrate the various heat transfers and the flow of heat as shown in Figure 1.

The condition for equilibrium of the sensor in Figure 1 can be shown by

$$H_{CV} + H_{RG} + H_{RS} + H_{CD} = 0 \quad (2)$$

where

H_{CV} = heat transfer by convection-conduction between the gas and the sensor.

H_{RG} = heat transfer between the gas molecules and the sensor by radiation

H_{RS} = heat transfer by radiation between the sensor and the surroundings.

H_{CD} = heat transfer by conduction between the sensor support and the sensor.

Some terms are negative or positive depending on whether surrounding objects are warmer or colder than the gas, and whether the sensor is warmer or colder than the gas or the supports. If the gas is transparent to radiation (as is air), H_{RG} is zero, then we can write equation (2) as

$$h_c (T_O - T_t) A_1 + \sigma e e_S (T_S^4 - T_t^4) A_1 X + (KA_2/a)(T_t - T_S) = 0, \quad (3)$$

where

h_c = coefficient of heat transfer by convection-conduction

T_o = gas temperature

T_T = sensor temperature

T_s = temperature of surrounding objects

A_1 = surface area of sensor

A_2 = cross-sectional area of sensor

σ = Steffan-Boltzmann constant

e = surface emissivity of sensor

e_s = emissivity of surrounding objects

X = fraction of total solid angle over which the junction sees the surrounding objects

K = coefficient of thermal conductivity of sensor and support

a = depth of immersion of sensor and support in the gas.

The term $\sigma e e_s (T_s^4 - T_T^4) A_1 X$ will nearly always consist of a sum of several terms, one term for each variety of surrounding source of radiation, of temperature, or of emissivity. The term for conduction $(KA_2/a)(T_T - T_s)$ likewise may consist of several terms, one for each type of material used in the sensor or support.

Equations (1) and (2) show that, when the net temperature of the surroundings differs from the gas temperature, a sensor will indicate not the temperature of the gas, but some temperature between the gas temperature and the surrounding temperatures.

Therefore, theoretically a single temperature sensor never reads the true temperature of a gas except in a special case where no heat transfer occurs. This fact is important because we do not have a direct method of precisely measuring the correct temperature of a gas and therefore have no reference to use to determine directly the error of any gas thermometer from the true gas temperature. Too often experiments state that their thermometers have no error when they actually have no way of knowing the errors of their measurements. But it is possible, by proper selection of several sensors, identical except for size and properly connected such that the error on each sensor when summed up with proper sign will cancel out, that the gas temperature can be measured directly with a negligible error. This is the principle of the Radiation Compensating Thermocouple. Its design is such that it can be connected directly in place of any single thermocouple of like materials, but will give measurements directly of gas temperatures with much smaller errors. Any shields or aspiration required on the single thermocouple can be eliminated.

II. THE RADIATION COMPENSATING THERMOCOUPLE

If we look at Figure 3, which is Figure 2 redrawn for a condition where the gas temperature (air temperature) is lower than the surrounding source (sun,

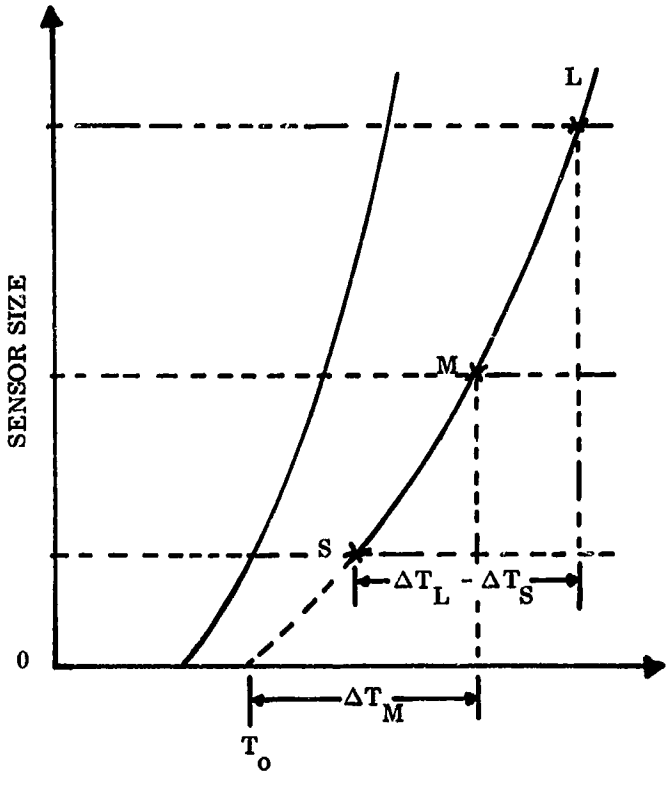

FIGURE 3. THEORY OF RADIATION COMPENSATING THERMOCOUPLE - STATIC CONDITION

on a clear day plus the sky), we have a curve of temperature where the temperature increases with sensor size (thermocouple wire size). The extrapolation of the curve to zero sensor size gives the true air temperature (T_0). In this case we are considering one individual static case of an unchanging air temperature and surrounding temperatures such as that which occurs for a short time on a clear day. For this condition, we can select three sensors of three sizes (small, medium, and large). The temperatures measured by these three sensors can be represented by T_S, T_M, and T_L, respectively, with errors ΔT_S, ΔT_M, and ΔT_L from the true gas temperature.

Therefore,

$$T_s = T_o + \Delta T_s \tag{4a}$$

$$T_M = T_o + \Delta T_M \tag{4b}$$

$$T_L = T_o + \Delta T_L . \tag{4c}$$

The three thermocouples may be wired together such that thermocouple T_L is opposing the other thermocouples electrically. Then these three thermocouples will read some temperature T_x, and we can write

$$T_x = (T_o + \Delta T_M) - (T_o + \Delta T_L) + (T_o + \Delta T_s), \tag{5a}$$

or, simplifying,

$$T_x = T_o + \Delta T_M - (\Delta T_L - \Delta T_s). \tag{5b}$$

If we select these three thermocouples such that the errors satisfy the equation

$$\Delta T_M = \Delta T_L - \Delta T_s, \tag{6}$$

then from equation (5b) we have

$$T_x = T_o. \tag{7}$$

In other words, by proper selection of the three thermocouples, the system can be made to read the true gas temperature directly. The wiring of such a system is shown in Figure 4.

The previous discussion is based on a single static condition of radiation error. If we look at equation (1a) we see that the radiation correction (radiation error) is a function of the square root of the diameter of the thermocouple and therefore a change of radiation from the surroundings, change of gas temperature, or change of wind speed to new constant values (for new static conditions) will shift the curve in Figure 4 to a new position with the same mathematical shape. The individual errors of each single thermocouple may be smaller or larger, but because the intersection of the new curves by the same wire sizes will be by parallel lines, the ratio

$$\frac{\Delta T_M}{\Delta T_L - \Delta T_s} \tag{8}$$

will remain a constant and equal to "one" for the ideal thermocouple design.

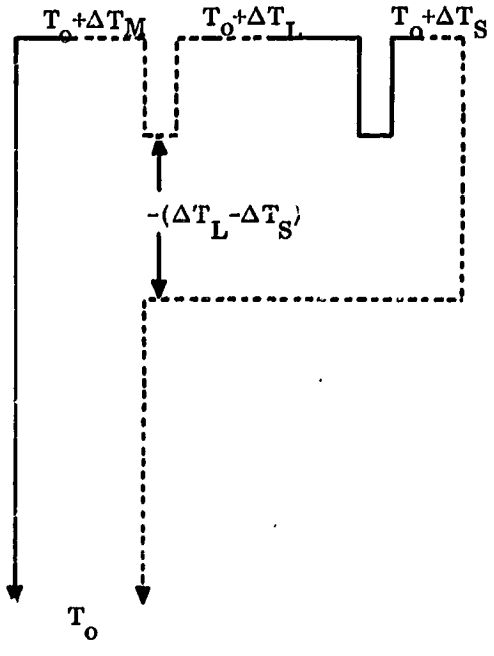

FIGURE 4. WIRING OF RADIATION COMPENSATING THERMOCOUPLE

The theoretical description of the Radiation Compensating Thermocouple has been simple, but the actual design of a working unit, i.e., finding the correct wire sizes, required careful and precise tests to evaluate all phases of construction.

The Radiation Compensating Thermocouple, when evaluated in terms of the errors discussed earlier, gives the following:

1. The error, from heat transfer by radiation between the sensor and the surroundings, and the heat conduction-convection between the gas and sensor not being in balance, can be reduced to any accuracy desired depending on the precision of design and fabrication.

2. The error from heat conduction between the sensor and support can be considered in the design. This error is small enough to be ignored, with the present design.

3. The Radiation Compensating Thermocouple does not compensate for response time error; in fact, if the thermocouples selected vary too greatly in size, the compensating balance will change for short periods of time with rapid temperature changes. It was for this reason that the original design using three thermocouples was changed to one using five thermocouples. With five thermocouples, we can rewrite equation (6) as

$$\Delta T_M = (\Delta T_{L_1} - \Delta T_{s_1}) + (\Delta T_{L_2} - \Delta T_{s_2}). \quad (6a)$$

But, if the two large and two small thermocouples are the same size,

$$\Delta T_M = 2(\Delta T_L - \Delta T_s) \quad (6b)$$

or

$$\frac{1}{2}\Delta T_M = \Delta T_L - \Delta T_s, \quad (6c)$$

This permits fabrication with thermocouples more nearly the same size and reduces the effect of response time error.

III. RESULTS OF TEST IN THE METEOROLOGICAL REGIME

The tests which led to the discovery and were used in development of the Radiation Compensating Thermocouple were conducted in the atmosphere in the temperature regime used for meteorological measurements. The equipment available for recording and for tests strongly influenced the physical design of the prototype models. Copper-constantan type thermocouples were used, mounted on a tower with the thermocouples facing south. This required a design of the Radiation Compensating Thermocouple with the five junctions and the wire leads connecting the junctions forming a flat surface parallel to the ground (Fig. 5 and 6). The five junctions were along the south-facing edge of the plane and the leads horizontal. In this way, all the thermocouple junctions had similar exposure to the sun (the largest contribution of point type radiation). If the thermocouple is rotated around the north-south axis, there will be little change in the compensating ability except for convection between individual thermocouples unequally affecting other thermocouples in the thermocouple system. This convection would exist in its worst condition when the plane of the thermocouple system is vertical since the lowest thermocouple receives no convection from the other thermocouples. Yet all of the other four thermocouples would be affected by different amounts of convection.

All tests conducted were controlled by five individual thermocouples to give a reference true air temperature. Except for size, these thermocouples were as identical in construction as possible (Table 1).

To obtain the largest possible errors on each single thermocouple, each thermocouple element in the Radiation Compensating Thermocouple was given a thin coating of flat black paint (Kodak black brushing lacquer was used) to make the absorption of radiation as great as possible.

TABLE 1.

DIMENSIONS OF SINGLE THERMOCOUPLES USED IN TESTS

SIZE OF THERMOCOUPLES		
AWG Wire Size	Wire Diameter* (Inches)	Width of Thermocouple Between Bands (Inches)
36	0.006	0.025
28	0.012	0.050
24	0.020	0.100
20	0.032	0.150
18	0.041	0.190

* Thermocouples whose diameters exceeded these values by more than 0.003 inch were rejected.

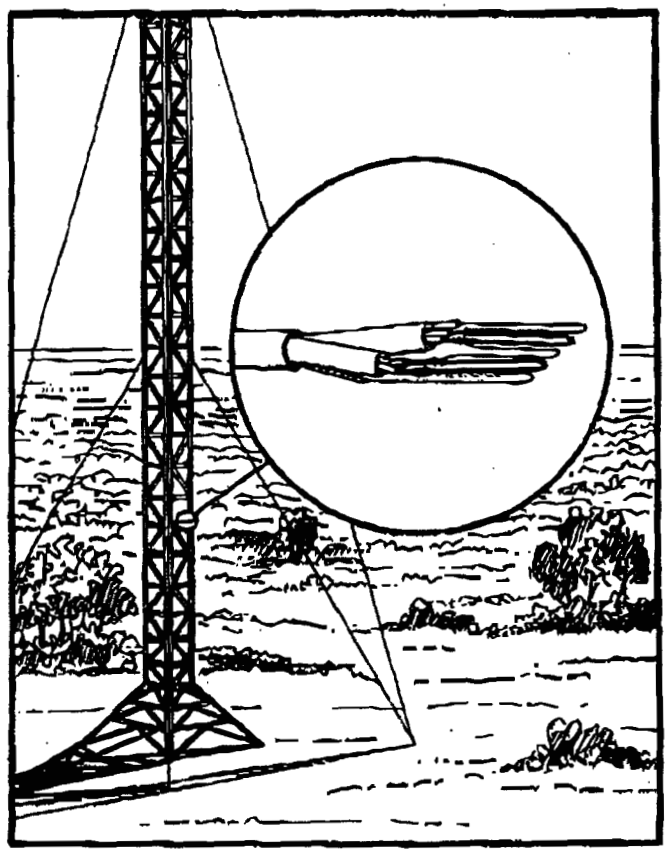

FIGURE 6. INSTALLATION OF RADIATION COMPENSATING THERMOCOUPLE

In the early tests at the Meteorological Department, Fort Huachuca, Arizona, the only recording potentiometers available for data collection were multiple print recorders with a printing cycle of 15 seconds between each print. Because of this, one minute and 15 seconds was required to obtain temperature readings from the five single thermocouples

FIGURE 6. MODEL OF RADIATION COMPENSATING THERMOCOUPLE

and one Radiation Compensating Thermocouple. Much of the data collected during the day time when the sun was out was unsatisfactory because of turbulence which frequently caused air temperature changes of as much as 10°F in a few seconds during each test cycle. The early morning data did provide short periods of data that could be used in design of the early test models. Some useable data were also obtained by watching the recorder and determining the temperature difference between each reading. Later a syncroprint recorder (with printing speed usually less than one second per point) was available. The data obtained in the morning hours with this recorder were frequently excellent, and by studying the records, periods of high stability and calm winds could be found which had repeated cycles of data where each thermocouple would read nearly the same temperature during successive printouts.

Data collected on one of the tests with the syncroprint recorder was selected as the best data for use in designing models of the Radiation Compensating Thermocouple for future tests. The data given in Table 2 are values averaged over several cycles of the recorder and represent data where the radiation error on each single thermocouple was the largest observed. The use of this data for design of the Radiation Compensating Thermocouple for regular use in measurement of air temperatures would mean that most of the time the errors on each single thermocouple would be less than that used for design; therefore, the Radiation Compensating Thermocouple would usually be performing better than the design data indicated.

Using the data in Table 2 and assuming a relationship of

$$T = a + b D + c D^2 \qquad (9)$$

where

T = air temperature

D = (diameter of wire),

constants a, b, c, were determined by least squares solution and the following equation was obtained:

$$T = 69.112 + 279.832D - 1033.06D^2 \qquad (10)$$

If we substitute a wire diameter of zero into the equation, then we find a value for T_o (zero wire size) of 69.11°F; i.e., the air temperature was 69.11°F at the time.

TABLE 2.

AVERAGE VALUES OF TEMPERATURE RECORDED AT FORT HUACHUCA, ARIZONA, 09:00 A. M. APRIL 8, 1960, BY VARIOUS SIZE THERMOCOUPLES (ALL THERMOCOUPLES PAINTED BLACK AND EXPOSED WITHOUT SHIELDS)

Thermocouple		Average Temperature (°F)
Wire Size (AWG Size)	Diameter**	
16	0.053	81.06
20	0.0335	77.26
24	0.022	74.79
28	0.014	72.91
35	0.006	70.70
Model 42 Radiation Compensating Thermocouple		68.91

** Actual wire diameter measured after painting.

Now, let

$$\Delta T = T - T_o$$

where ΔT = temperature difference from T_o. Substituting into equation (10), we obtain

$$\Delta T = 279.832D - 1033.06D^2 \text{ for } \Delta T \text{ in } °F, \text{ and } D \text{ in inches} \qquad (11a)$$

or

$$\Delta T = 6.1205D - 0.88958D^2 \text{ for } \Delta T \text{ in } °C, \text{ and } D \text{ in millimeters.} \qquad (11b)$$

Equations (11a) and (11b) are empirical equations which can be used to find the error of any small black temperature sensor in the sun. See Table 3 for errors of thermocouples computed from equation (11a) and shown in Figures 7 and 8. If the error is desired for a sensor which has an emittance different from a black body, the error can be found by correcting the error obtained from equation (11a) or (11b) by the value of the emittance.

TABLE 3.

TEMPERATURE ERRORS OF SINGLE THERMOCOUPLES OBTAINED FROM DATA IN TABLE 2 EQUATION (11a) COMPARED TO ACTUAL MEASURED ERROR IF $T_0 = 69.11$

COMPUTED FROM

$\Delta T(°F) = 279.83\ D\ (INCHES)\ 1033.06\ D^2(INCHES^2)$,

OR

$\Delta T(°C) = 6.1205\ D\ (mm) - 0.88958\ D^2(mm^2)$

Wire Size (D)			ΔT	
AWG	(INCH)	(mm)	°F	°C
16	0.0508	1.2903	11.54	6.41
18	0.0403	1.0236	9.60	5.33
20	0.032C	0.8128	7.89	4.38
22	0.0254	0.6452	6.43	3.57
24	0.0201	0.5105	5.20	2.89
26	0.0159	0.4039	4.19	2.33
28	0.0126	0.3200	3.36	1.87
30	0.0100	0.2540	2.70	1.50
32	0.0080	0.2032	2.17	1.21
34	0.0063	0.1600	1.72	0.96
35	0.0060	0.1524	1.64	0.91
36	0.0050	0.1270	1.37	0.76
50	0.0010	0.0254	0.28	0.16

The actual errors of the single thermocouples can be compared to the errors computed from equation (11a), as shown in Table 4.

To construct a Radiation Compensating Thermocouple, equation (11a) or (11b) can be used to determine the wire combinations. The method used in the tests was to select a specific size thermocouple for the largest thermocouple; and then, by trial and error, the measuring thermocouple and the small thermocouple sizes were found such that the measuring thermocouple was approximately halfway between the large and small thermocouples on the error curves.

TABLE 4.

ERRORS OF SINGLE THERMOCOUPLE SENSORS (BLACK, BUTT-JOINED) FOR VARIOUS WIRE SIZES, EXPOSED IN BRIGHT SUNLIGHT

Thermocouple				
Wire Size AWG	Diameter (inches)	Computed °F	Actual °F	Computed Minus Actual °F
16	0.053	11.93	11.95	-0.02
20	0.0335	8.21	8.15	+0.06
24	0.022	5.65	5.68	-0.03
28	0.014	3.72	3.80	-0.08
35	0.006	1.60	1.59	+0.01

NOTE: Model 42 of the Radiation Compensating Thermocouple (data is Table 2) had an error of 0.20°F from the computed T_0. This is within the measuring accuracy of the equipment being used.

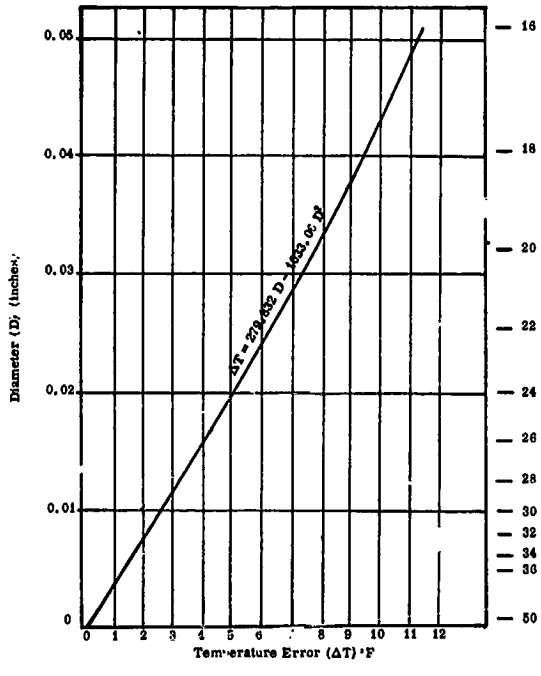

FIGURE 7. ERRORS OF SINGLE THERMOCOUPLE SENSORS (BLACK, BUTT-JOINED) FOR VARIOUS WIRE SIZES, U.S. CUSTOMARY UNITS

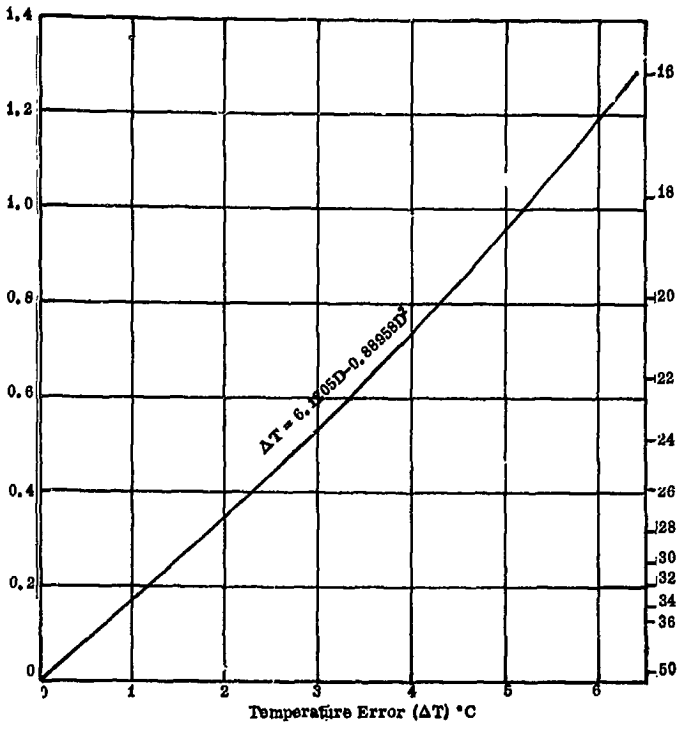

FIGURE 8. ERRORS OF SINGLE THERMOCOUPLE SENSORS (BLACK, BUTT-JOINED) FOR VARIOUS WIRE SIZES, METRIC UNITS

As examples of verification of the amount of error in specific designs of the Radiation Compensating Thermocouples, the following designs are analyzed with equations (11a), (6a), and (8).

DESIGN I

Thermocouple	Wire Size (AWG)	Wire Size (INCHES)	ΔT	$\Delta T_L - \Delta T_S$
S	24	0.0201	5.20	2.69
L	20	0.032	7.89	
M	22	0.0254	6.43	
L	20	0.032	7.89	2.69
S	24	0.0201	5.20	
$\Sigma (\Delta T_L - \Delta T_S)$				5.38

Using equation (8), we obtain

$$\frac{\Delta T_M}{\Delta T_L - \Delta T_S} = \frac{6.43}{5.38} = 1.20 .$$

This means the Design I has a residual error of about 20 percent still in the measurement. In other words, it has removed 80 percent of the error.

DESIGN II

Thermocouple	Wire Size (AWG)	Wire Size (INCHES)	ΔT	$\Delta T_L - \Delta T_S$
S	28	0.0126	3.63	4.53
L	20	0.032	7.89	
M	24	0.0201	5.20	
L	20	0.032	7.89	3.70
S	26	0.0159	4.19	
$\Sigma (\Delta T_L - \Delta T_S)$				8.23

Using equation (8), we obtain

$$\frac{\Delta T_M}{\Delta T_L - \Delta T_S} = \frac{5.20}{8.23} = 0.63 .$$

In Design II, the Radiation Compensating Thermocouple is overcorrecting the error by about 37 percent. This means that the Radiation Compensating Thermocouple will read a temperature lower than the actual gas temperature when a radiation source hotter than the surroundings is present; i.e., the temperature indicated by the Radiation Compensating Thermocouple will be higher when shaded than when in the sun.

DESIGN III

Thermocouple	Wire Size (AWG)	Wire Size (INCHES)	ΔT	$\Delta T_L - \Delta T_S$
S	28	0.0126	3.36	1.84
L	24	0.0201	5.20	
M	26	0.0159	4.19	
L	24	0.0201	5.20	2.50
S	30	0.0100	2.70	
$\Sigma (\Delta T_L - \Delta T_S)$				4.34

From equation (8), we obtain

$$\frac{\Delta T_M}{\Delta T_L - \Delta T_S} = \frac{4.19}{4.34} = 0.97 .$$

Design III will provide a Radiation Compensating Thermocouple that will have approximately 3 percent error in measurement of the true gas temperature indicated being lower than the actual gas temperature.

All computations and discussions of the designs were based on the worst conditions: a clear, sunny, calm day and black thermocouples. To get an idea of the Radiation Compensating Thermocouple compared to a single thermocouple under similar conditions, let us examine Design III. The single thermocouple, designated "M," would normally be used in measurement. If all thermocouples are black, the "M" thermocouple would have an error of 4.19° F on a clear day in the sun. At the same time, the Radiation Compensating Thermocouple would have an error of 4.19 - 4.34 = - 0.15° F; i.e., it would read 0.15° F too low.

This is the "worst" error to expect. Also, these computations were made on the assumption that the fabrication would not increase any of the diameters of the wires. Actually, about 0.001 inch should be added to each wire size before making computations.

Design II has provided the best data in tests because of the adjustment in diameters of the wires for fabrication.

These tests were carried on over a period of about two years. During this time, about 25 models of the Radiation Compensating Thermocouple were fabricated by hand using ordinary jewelry tools, pliers, small files, silver solder and a propane torch. Besides comparing the Radiation Compensating Thermocouple with single thermocouples, two identical Radiation Compensating Thermocouples, designed to give very small errors, were fabricated. One was painted black, and the other white using a flat white paint that was white not only in the visible region of the spectrum but also in the infrared region of the spectrum. When these two thermocouples were placed in the sun, the air temperatures recorded were almost exactly the same from each Radiation Compensating Thermocouple under stable air conditions. This is an excellent example of the usefulness of the Radiation Compensating Thermocouple in gas measurements, since contamination or changes in the surface color do not change the accuracy of the Radiation Compensating Thermocouple unless the contamination is not uniform and thus changes the balance between the individual thermocouples.

Since the original tests, operational tests have been made at Fort Huachuca by Mr. A. V. Carlson of the Meteorology Department [19]. In these tests various test models of the Radiation Compensating Thermocouple were compared with a single AWG No. 24 gage thermocouple. These tests were recorded on a two-pen recorder permitting simultaneous recording of temperature data from the single thermocouple and the Radiation Compensating Thermocouple. These tests were run with various radiation conditions - clear and cloudy days and nights with the thermocouples inside and outside the standard instrument shelter.

The results of these tests were as follows:

1. The performance of the test models of the Radiation Compensating Thermocouple was as predicted. (These predictions were based on the data given in this report.)

2. A properly designed Radiation Compensating Thermocouple used without shields or shelter is superior to a single thermocouple even when the single thermocouple is mounted in an instrument shelter.

3. The single thermocouple read 4 to 5 degrees Fahrenheit higher than the Radiation Compensating Thermocouple when both were exposed in direct sunshine even in winds up to 15 miles per hour.

One more remark is needed on the data in Table 2. These data are only one sample from one morning; but this is the best set of data obtained for the worst conditions during the two years of tests. All other data agreed closely with this data within the errors of data measurement, and because of the excellent fit of this data by a second-degree curve, these data should provide adequate information for preliminary design of Radiation Compensating Thermocouples within the thermocouple wire size range given and general meteorological temperature range. The tests at Fort Huachuca [19] have further substantiated the validity of this data. For temperatures outside the meteorological range, tests should be made with five or more single thermocouples of various sizes in the desired temperature ranges to verify or correct the curves.

As a check for faulty construction, all Radiation Compensating Thermocouples fabricated should have a laboratory or field test to compare them with the extrapolated temperature for wire size zero, using a group of single thermocouples. This could be done in a laboratory test chamber.

Patent 3,049,012 on this device was issued August 14, 1962, with rights assigned to the United States Government., inventor Glenn E. Daniels.

IV. EFFECTS OF PRESSURE CHANGES

The NACA equation, discussed in this report as equation (1), for computing the radiation error of a thermocouple does not include any term for gas pressure, and is valid only at standard atmospheric pressure. Actually, the radiation error increases with

decreasing atmospheric pressure and becomes very large at low pressures. This is because the major factor which opposes and reduces the radiation error, heat transfer convection-conduction between the gas and sensor, becomes smaller with decreasing air pressure, because there are fewer molecules for the convection and conduction. The values of error with sensor size, which are given in Table IV, were obtained at Ft. Huachuca, Arizona. The average station pressure at Ft. Huachuca is about 0.8 of an atmosphere; therefore, the measured temperature errors in the tests at Ft. Huachuca will be a little larger than at sea level, but smaller than higher elevation stations.

V. CONCLUSIONS

Current gas temperature measurements have large errors. The Radiation Compensating Thermocouple can provide data on the temperature of a gas much more representative of the actual gas temperature than either a single thermocouple, with or without shields, or an aspirated thermocouple. Even if the Radiation Compensating Thermocouple is crudely made, and the error is not completely compensated out, the data from this thermocouple are superior to data collected by the sensors currently in use.

Additional tests should be made in the laboratory and in the field on the Radiation Compensating Thermocouple to better understand the theory of heat transfer and to determine the optimum design for its use in various types of gas measurements.

Tests made at Ft. Huachuca, Arizona, proved the feasibility of the Radiation Compensating Thermocouple in gas temperature measurement.

For immediate use, the information given in this report can be used to design Radiation Compensating Thermocouples which have small errors in gas temperature measurements when used without shields.

REFERENCES

1. Wells, William Charles: Essay on Dew. Constable, 1815.

2. Annual Report of the Chief Signal Officer of the Army to the Secretary of War of the Year 1887. Part 2 of two parts. Appendix 46, Treatise on Meteorological Apparatus and Methods by Cleveland Abbe, A. M. Government Printing Office.

3. Freeze, Paul K.: Bibliography on the Measurement of Gas Temperatures. Circular 513, Nat. Bur. Standards, Aug. 20, 1961.

4. Fishenden, Margaret; and Saunders, Owen A.: The Calculation of Heat Transmission. His Majesty's Stationary Office, London, 1932.

5. Waggener, W. J.: Über die Messung von Flammentemperaturen durch Thermoelemente, insbesondere über die Temperaturen im Bunsen' schen Blaubrenner. Verhandlungen der Physikalischen Gesellschaf zu Berlin, vol. 14, pp. 78-83.

6. Kreisings, Henry; and Barkley, J. F.: Measuring the Temperature of Gases in Boiler Settings. Dept. of the Interior, Bureau of Mines, Bulletin No. 145, 1918.

7. Annual Progress Report and Technical Reports, September 1, 1956 to September 1, 1957, Contract Nonr. 710 (22), Atmospheric Physics Univ. of Minnesota, pp. 103-106.

8. Bartals, J.: Temperaturmeasring in Bodennahe und Aspiration. Met. Zerschr. Braunschweig, 1930.

9. Nyberg, Alf: Temperature Measurements in an Air Layer Very Close to a Snow Surface. Hydrologick Bibliografi, Communications Series of Papers No. 27, Statens Meteorologish Hydrografiska instalt.

10. Moffatt, E. Marston: Methods of Minimizing Errors in the Measurement of High Temperatures in Gases. Instruments, vol. 22, no. 2, Feb. 1949, pp. 122-132.

11. Dahl, Andrew I.: Measurement of High Temperature in Gas Streams. Petroleum Refiner, vol. 29, no. 3, Mar. 1959, pp. 112-115.

12. Bolles, W. L.· Measurement of Gas Temperatures by Means of Thermocouples. Petroleum Refiner, vol. 29, no. 2, Feb. 1948, pp. 120-126.

13. Severinghaus, W. L.: Reducing Radiation Errors in Gas Temperature Measurement. Mech. Eng., vol. 59, no. 5, May 1937, pp. 334-358.

14. Scadron, Marvin D.; Warshawsky, Isidore; and Gettelman, Clarence C.: Thermocouples for Jet Engine Gas Temperature Measurement. Proc. Inst. Soc. of America, vol. 7, paper 52-12-3, 1952, pp. 142-148.

15. Dahl, A. I.; and Flock, E. F.: Shielded Thermocouples for Gas Turbines. Trans. ASME Feb. 1949, pp. 153-161.

REFERENCES (Concluded)

16. Scadron, Marvin D.; and Warshawsky, Isidore: Experimental Determination of Time Constants and Nusselt Numbers for Bare-Wire Thermocouples in High Velocity Air Streams. NACA TN 2599, Jan. 1952.

17. Glawe, George E.; Simmons, Frederick S.; and Stickney, Truman M.: Radiation and Recovery Corrections and Time Constants of Several Chromel-Alumel Thermocouple Probes in High-Temperature, High-Velocity Gas Streams. NACA TN 3766, Oct. 1956.

18. Simmons, Frederick S.: Recovery Corrections for Butt-Welded, Straight-Wire Thermocouples in High-Velocity, High-Temperature Gas Streams. NACA RM E54G22a, Sept. 25, 1954.

19. Carlson, A. V.: An Evaluation of Radiation Compensating Thermocouple Temperature Sensors. USAERDAA-MET-10-64, Sept. 1964, Meteorol. Dept., Hdqtrs, U. S. Army Elec. Res. and Devel. Activity, Fort Huachuca, Ariz.

BLANK PAGE

OPTICAL INTEGRATION OVER CORRELATION AREAS IN TURBULENT FLOWS

By

F. R. Krause and M. J. Fisher*

SUMMARY

Statistical analyses of turbulent fluctuations are needed to provide inputs for dynamical and structural response calculations. Previous experimental investigations of area-integrated correlation functions are limited because they were based on point measurements with standard solid probes like hot wires and dynamic pressure transducers. In this paper the use of the integrating features of optical beams for a "one shot" estimate of area integrated correlation functions is discussed.

INTRODUCTION

The statistical analysis of turbulent fluctuations is needed to provide inputs like aerodynamic forcing functions, turbulent fluxes, and Mach wave sound sources for dynamical and/or structural response calculations. The mathematical description of all these inputs is identical insofar as they are expressed by an area integral over a space-time correlation function. The same integrals are needed in the statistical theory of turbulence, if one wants to calculate true three-dimensional wave number components instead of their one-dimensional approximation based on line integrals and symmetry assumptions [1].

Previous experimental investigations of area integrated correlation functions are limited because they were based on point measurements with standard solid probes like hot wires and dynamic pressure transducers. The inherent numerical integration procedures require a large number of points. The experimental and numerical effort in providing these pointwise estimates of correlation functions is then prohibitive, even if an instrument could be found that combines the necessary temporal and spatial resolution with a sufficiently linear and time invariant frequency response [2].

We propose to use the integrating features of optical beams for a "one shot estimate" of area integrated correlation functions. The cross correlation of light intensities gives the three-dimensional wave number components of light extinction coefficients for any wave front propagating normal to the plane of the crossed optical beams. The wave-length and the spectroscopic resolution of the received light may be adjusted to represent a selected thermodynamic property such as density. An application to Mach wave sound emission leads to a one shot estimate of Ffows Williams' Mach wave sound sources [3].

I. WAVE NUMBER COMPONENTS OF LIGHT EXTINCTION COEFFICIENTS

Electromagnetic theory shows that the light extinction coefficient μ is uniquely determined by the thermodynamic properties of the flow. Its space-time correlation might therefore be used to study the turbulent fluctuations of thermodynamic flow properties.

Consider the experimental arrangement in Figure 1. Two narrow beams of white light traverse a jet in

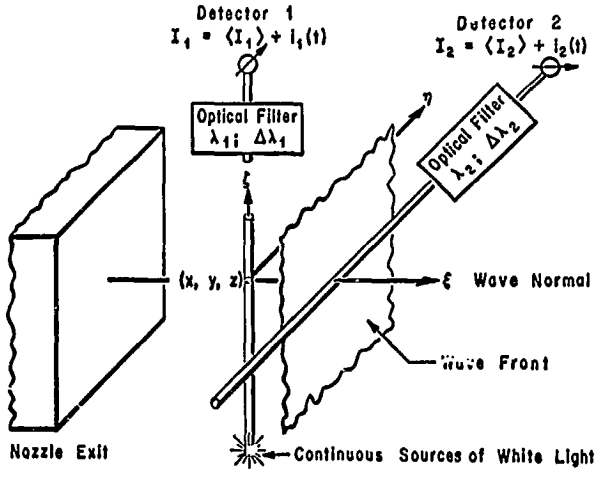

FIGURE 1. OPTICAL MEASUREMENT OF THREE DIMENSIONAL WAVE NUMBER COMPONENTS

the y and z directions. Using an optical filter in front of the photo-detectors, we limit the received radiative power to the wavelength interval $\Delta\lambda$ centered around the wave length λ. The light extinction coefficient μ then accounts for the power loss through the interval Δx centered around the point $\vec{x}$ and is defined by

$$\mu(\vec{x}, t, \lambda, \Delta\lambda) = \frac{\text{Filtered power loss along } \Delta x}{\text{Filtered energy flux} \cdot \Delta x \cdot \Delta\lambda} \quad (1)$$

* Research Physicist, Illinois Institute of Technology Research Institute.

The turbulence causes temporal fluctuations

$$\mu'(\vec{x}, t, \lambda, \Delta\lambda) = \mu - \langle \mu \rangle \qquad (2)$$

which lead to a fluctuation of the received spectral radiance (power/solid angle, area and wavelength interval)

$$I_y(t) = \langle I_y \rangle + i_y(t) \ . \qquad (3)$$

The intensity fluctuations of the y and z beams are now correlated. The resulting normalized temporal cross correlation function G is then related to the light extinction coefficients μ' by an integral which can be derived by calculating the time histories of $I_y(t)$ and $I_z(t)$ through a quadrature of equation (1).

$$G(\xi, \tau)_{\vec{x}} = \frac{\langle i_z(t)\, i_y(t+\tau) \rangle}{\langle I_y \rangle \cdot \langle I_z \rangle} \qquad (4)$$

$$= \int_{-\infty}^{+\infty}\int \langle \mu'(x, y, z+\zeta, t)\, \mu'(x+\xi, y+\eta, z, t+\tau) \rangle \, d\eta \, d\xi \ .$$

This area integration is extremely useful in many applications as will now be demonstrated by interpreting equation (4) in terms of three-dimensional wave number components. Consider the fluctuations around a point $\vec{x}$, which is defined by the intersection of the upstream beam and the line of minimum beam separation. The space-time correlation function around this point,

$$\langle \mu'(x, y, z, t)\, \mu'(x+\xi, y+\eta, z+\zeta, t+\tau) \rangle \ , \qquad (5)$$

could then be used to describe the correlated fluctuations in its vicinity through a system of standing waves. We are interested in the wave fronts which are parallel to the beams. The contributing waves are characterized by the spatial and temporal wave numbers (frequencies) k, ω. The mean square amplitude ("energy") E of these wave number components is then given by [1]

$$E_\mu(k, \omega)_{\vec{x}} = \qquad (6)$$

$$\frac{1}{8\pi^3} \int_{-\infty}^{+\infty}\int e^{-i(kx+\omega\tau)} \left(\int_{-\infty}^{+\infty}\int R_\mu(\vec{\xi}, \tau)_{\vec{x}} \, d\eta \, d\xi \right) d\xi \, d\tau \ .$$

The inner integral resembles the measurable quantity G, equation (4), very much. The functional similarity is now made complete by assuming that there is at least one line inside the wave front, along which the turbulent fluctuations are spatially homogeneous. Without loss of generality, this line could be the ζ axis, since a rotation around the wave normal will not change equations (4) and (6). By making this assumption, equation (5) becomes

$$\langle \mu'(x, y, z+\zeta, t)\, \mu'(x+\xi, y+\eta, z, t+\tau) \rangle$$

$$= \langle \mu'(x, y, z, t)\, \mu'(x+\xi, y+\eta, z-\zeta, t+\tau) \rangle . \qquad (7)$$

Substitution of equation (7) into equation (4) and transformation of ζ to $-\zeta$ shows that the measurable signal is equal to the area integral over the space-time correlation function

$$G(\xi, \tau)_{\vec{x}} = \int_{-\infty}^{+\infty}\int R_\mu(\vec{\xi}, \tau)_{\vec{x}} \, d\eta \, d\xi \ . \qquad (8)$$

The wave number component E can thus be measured directly by repeating the cross correlation of light intensities for various beam separations ξ. Substituting equation (6) gives the final result:

$$E_\mu(k, \omega)_{\vec{x}} = \frac{1}{8\pi^3} \int_{-\infty}^{+\infty}\int G(\xi, \tau) e^{-i(k\xi+\omega\tau)} d\xi \, d\tau . \qquad (9)$$

Obviously, the measurement of three-dimensional wave number components is not restricted to the streamwise direction. Exactly the same result holds for any other wave front to which the beams can be aligned parallel. Furthermore, the cross correlation could be measured for other light wavelengths λ and wavelength resolutions $\lambda/\Delta\lambda$ by recording more than two phototubes either simultaneously or in repeated runs. In this way, one obtains an absorption and/or emission spectrum of the wave number component $E(k, \omega)$, which could then be resolved into the wanted thermodynamic property.

II. MACH WAVE SOUND EMISSION

To demonstrate the potentialities of the optical cross correlation, we now discuss a well known example, which has so far defied a direct measurement. This is Mach wave sound emission. Consider the mean square pressure fluctuations $\langle p^2(\vec{x}_f) \rangle$ in the far field of a supersonic jet as shown in Figure 2. These pressure fluctuations receive a contribution from Mach wave sound sources at position $\vec{x}$ on the jet, which has been given by Ffows Williams [2]. In our notation, his superposition of Mach wave sound is given by a volume integral

$$\langle p^2(\vec{x}_f) \rangle = \frac{1}{16\pi^2} \int_{-\infty}^{+\infty}\int\int \frac{(x_f - x)^2 (z_f - z)^2}{|\vec{x}_f - \vec{x}|^6} \left| \frac{\partial u(\vec{x})}{\partial z} \right|^2 F(\vec{x}) \, d\vec{x} \qquad (10)$$

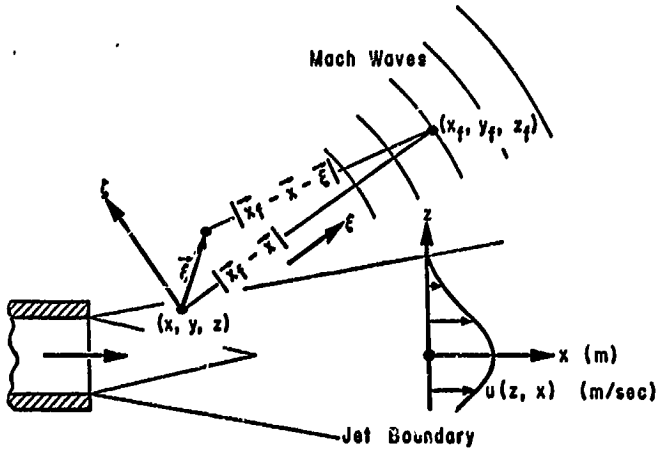

FIGURE 2. MACH WAVE SOUND EMISSION

over the volume integrated space-time correlation function of the density time derivatives.

$$F(\vec{x}) = \iiint_{-\infty}^{+\infty} \left\langle \frac{\partial \rho}{\partial t}\left(\vec{x}, t - \frac{|\vec{x}_f - \vec{x}|}{a_o}\right) \frac{\partial \rho}{\partial t}\left(\vec{x} + \vec{\xi}, t - \frac{|\vec{x}_f - \vec{x} - \vec{\xi}|}{a_o}\right) \right\rangle d\vec{\xi} . \quad (11)$$

Here a_o denotes the far field velocity of sound. The problem is to measure the combined source strength or forcing function F. Obviously, the beams should be aligned parallel to the front of the Mach waves; that is, we turn the coordinate system (ξ, η, ζ) until the ξ axis coincides with direction of Mach wave emission. In this case the vectors $\vec{x}_f - \vec{x}$, and $\vec{x}_f - \vec{x} - \vec{\xi}$ are almost parallel to the ξ axis, as shown in Figure 2, and we may simplify the retarded times in equation (11) by the approximation

$$|\vec{x}_f - \vec{x}| - |\vec{x}_f - \vec{x} - \vec{\xi}| = \xi . \quad (12)$$

For stationary time series, the absolute values of the retarded times are unimportant; only their difference ξ/a_o affects the correlation. Furthermore, the correlation of density derivatives can be expressed by the second derivative of the density correlations.

$$\left\langle \frac{\partial \rho}{\partial t}\left(t - \frac{\vec{x}_f - \vec{x}}{a_o}\right) \frac{\partial \rho}{\partial t}\left(t - \frac{|\vec{x}_f - \vec{x}|}{a_o} + \tau\right) \right\rangle$$

$$= \frac{\partial^2}{\partial \tau^2} \langle \rho'(t)\, \rho'(t + \tau) \rangle . \quad (13)$$

The Mach wave sound might therefore be expressed in terms of the directly accessible density cross correlation function

$$F(\vec{x}) = \int_{-\infty}^{+\infty} \frac{\partial^2}{\partial \tau^2} \iint_{-\infty}^{+\infty} \langle \rho'(\vec{x}, t)\, \rho'(\vec{x} + \vec{\xi}, t + \tau(\xi)) \rangle \, d\eta \, d\xi \Big) \, d\xi , \quad (14)$$

where $\tau(\xi) = \xi/a_o$. The inner integral is identical with the area-integrated correlation function of equation (8), except that the extinction coefficient fluctuations μ' have been replaced by th density fluctuations ρ'. In most flows with frozen composition the spectral region of the detected light may be adjusted to make these fluctuations directly proportional:

$$\rho' = C(\lambda, \Delta\lambda)\, \mu' . \quad (15)$$

In this case, the inner integral is directly proportional to the normalized optical correlation function G. The Mach wave sound sources follow from substituting equations (15) and (8) into equation (14):

$$F(\vec{x}) = C^2 \int_{-\infty}^{+\infty} \frac{\partial^2}{\partial \tau^2} G(\xi, \tau(\xi))_{\vec{x}} \, d\xi . \quad (16)$$

The argument $(\xi, \tau(\xi))$ describes the temporal correlation between the space-fixed position $\vec{x}$ and one moving wave front. For almost frozen patterns of turbulence, the temporal changes are concentrated at th space-fixed observer and might be approximated with the flashlight image $(\tau = 0)$ of all waves along the same normal. All of these waves could be recorded simultaneously by aligning many beams parallel to the η axis, or, by using one thick "y" beam. Therefore, a quick look at the exact line integral of equation (16) might be obtained from a "one shot estimate" employing a beam, with a slit shaped cross section.

$$F(\vec{x}) \cong C'^2 \frac{\partial^2}{\partial \tau^2} G^*(\tau = 0) . \quad (17)$$

The asterisk denotes that the slitted section of one beam must be enlarged to cover the whole correlation volume around the point $\vec{x}$.

III. REFERENCES

1. Batchelor, G. K., The Theory of Homogeneous Turbulence, Cambridge, The University Press, Students edition, 1960.

2. Krause, F., Wall Pressure Fluctuations and Skin Vibrations with Emphasis on Free Shear Layers and Oscillating Shocks, NASA TM X-53189, October 1964.

3. Ffowcs Williams I.E., G. Maidanik, The Mach Wave Field Radiated by Supersonic Turbulent Shear Flows, J. Fluid. Mech., (1965) Vol. 21, pp. 641-657.

BLANK PAGE

VII. STRUCTURAL DYNAMICS

ELASTIC STABILITY OF A SLENDER BAR UNDER DYNAMIC LOADS

By

Frank C. Liu

SUMMARY

This research is concerned with the elastic stability problems of a space rocket under nonconservative, dynamic loads. The mathematical analysis is made on a simple model, a uniform bar with free-free ends with one end subjected to a time-varying thrust load. This work consists of three parts: The first presents the critical thrust of the bar together with an outline of various other buckling criteria under different assumptions; the second shows the elastic stability of a spacecraft due to the coupling of longitudinal and transverse vibrations; and the third part deals with the critical thrust of the bar subjected to high speed aerodynamic load. The variation of frequency of transverse vibration due to the thrust and flight velocity is also illustrated.

I. INTRODUCTION

The means of finding the static buckling load of a slender column is the well known Euler's method. If the external forces have a potential, they are called conservative forces, in which case this method is applicable [1]. The theory of elastic stability of nonconservative problems is based on the investigation of the small oscillation of the system about its equilibrium position. Thorough discussion and many practical examples of the so-called dynamic method may be found in V. V. Bolotin's books listed as References 1 and 2. This approach is now used to deal with elastic stability problems of space vehicles.

The space vehicle is treated as a uniform, slender cylindrical bar, and such that the shell effect, local buckling, and panel flutter are disregarded. We are mainly interested in the elastic stability of the vehicle under dynamic loads. This bar has both ends free and is subjected to a thrust force at the tail end along the direction of the body axis; i.e., the rocket engine gimbal is clamped. Thus, this load is nonconservative, because it vibrates together with the bar. Two dynamic stability problems are presented here.

First, we consider the dynamic coupling of longitudinal vibration and transverse vibration of the vehicle. The velocity of stress waves traveling in a solid rod is equal to the speed of sound in the rod; in general, the frequency of the stress wave traveling back and forth in a solid metal rod is much greater than the natural frequency of transverse vibration of the rod, and hence, the coupling effect is negligible. However, a rocket usually has great mass density with a small effective load-carrying cross-sectional area. Its longitudnial frequency may be of the same order of magnitude as its transverse vibration frequency. Thus, the elastic coupling becomes significant.

Second, we are concerned with the elastic stability of the space vehicle under the combined action of a thrust and an aerodynamic load. For a space rocket of large cross-sectional area, the aerodynamic force and damping effect caused by its transverse oscillation in supersonic air flow may have some significance to its dynamic stability. Such information may be helpful to structural design engineers.

II. THE CRITICAL THRUST

Presented is the analysis of the dynamic approach on elastic stability of a slender bar while the well-known static approach is also given for comparison.

A. THE DYNAMIC ELASTIC STABILITY

When the load is not acting along a fixed direction due to the motion of the bar, equilibrium of the bar cannot be obtained without taking into account the inertia force. In other words, the dynamic elastic stability of the bar is governed by the differential equation of transverse vibration [2],

$$EI \frac{\partial^4 w}{\partial x^4} + \frac{\partial}{\partial x}\left(N \frac{\partial w}{\partial x}\right) + m \frac{\partial^2 w}{\partial t^2} = 0 \qquad (1)$$

where $N = P_o(1 - x/L)$ is the axial force along the bar, EI is the bending stiffness, m is the mass per unit length, and L is the length. Two types of boundary conditions are treated.

Case 1. The motion of two ends constrained along a fixed direction: As shown in Figure 1e. the solution of equation 1 gives the critical load [3]

$$P_o^* = 2\bar{P}$$

where $\bar{P} = \pi^2 EI/L^2$ is the buckling of a bar with hinged ends (Fig. 1a).

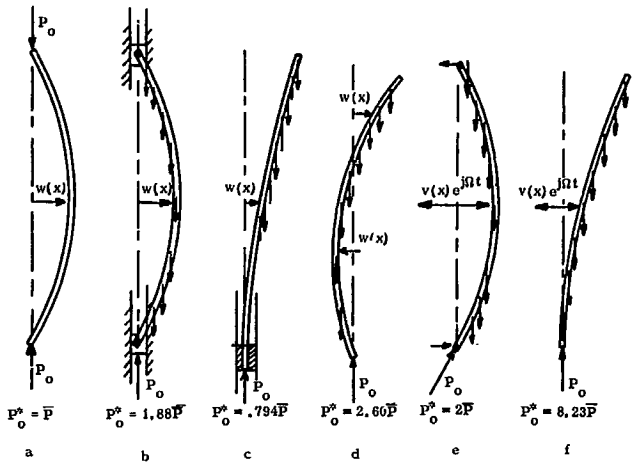

FIGURE 1. THE CRITICAL THRUST

Case 2. Bar with free-free ends: If the bar is treated as free-free, we may use the bending mode of a free-free bar instead of a sinusoidal mode shape. The solution of equation 1 yields[3]

$$P_o^* = 8.23\bar{P}.$$

B. THE STATIC ELASTIC STABILITY

If the lateral vibration of the bar is disregarded, the deflection of the bar is due to the inertia load of uniform acceleration. Consequently, the deflection does not depend on time, and the differential equation to be dealt with is[4]

$$EI \frac{d^3w}{dx^3} + q(L - x) \frac{dw}{dx} = 0, \qquad (2)$$

where $q = m(P_o/mL)$ is the inertia load. The critical thrusts of the bar for various boundary conditions are given as follows:

Case 1. $w(0) = w'(0) = 0$, as shown in Figure 1c. The critical thrust given by Reference 4, p. 116, is

$$P_o^* = 0.794\bar{P}.$$

Case 2. $w''(0) = w''(L) = 0$, as shown in Figure 1d. Reference 5 gives

$$P_o^* = 2.601\bar{P}.$$

Case 3. $w(0) = w(L) = 0$, as shown in Figure 1b. From Reference 4, p. 122, which uses energy method, we find

$$P_o^* = 1.88\bar{P}.$$

III. ELASTIC STABILITY DUE TO COUPLING OF LONGITUDINAL AND TRANSVERSE VIBRATIONS

In Section II N of equation (1) is treated as the average axial force which does not include the longitudinal stress wave in the bar. To take into consideration the longitudinal vibration given by the equation

$$EA \frac{\partial^2 u}{\partial x^2} = m \frac{\partial^2 u}{\partial t^2}, \qquad (3)$$

we have

$$N(x,t) = EA \frac{\partial u}{\partial x}, \qquad (4)$$

with

$$N(0,t) = -P_o(t) \quad \text{and} \quad N(L,t) = 0, \qquad (5)$$

where EA is the extensional stiffness of the bar. The above relationships and equation (1) indicate that both $u(x,t)$ and $w(x,t)$ depend on the thrust $P_o(t)$. Generally, a rocket engine requires 0.5 to 1.5 seconds to build up to its full thrust power; it then keeps a fairly constant magnitude at its full power. Let us represent the thrust buildup by a simple two-parameter curve in the form

$$P_o(t) = P_o[(1 + \tfrac{1}{2}a)\, t/t_o - \tfrac{1}{2}a\,(t/t_o)^2] \quad 0 \le t \le t_o$$
$$= P_o \quad t \ge t_o \qquad (6)$$

where t_o denotes the thrust buildup time, and the constant a has the value from 0 to 2, as shown in Figure 2.

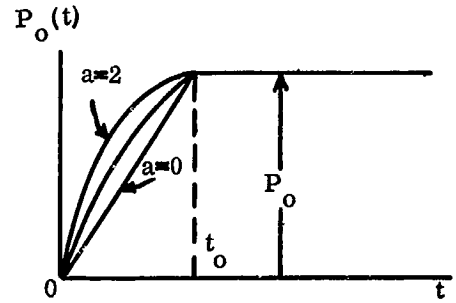

FIGURE 2. THRUST BUILDUP CURVES

Using Laplace transform and Galerkin's technique to solve $u(x,t)$ and $N(x,t)$ from equations (3) and

BLANK PAGE

(5), then w(x,t) from equation (1), we obtain the well-known Mathein equation in the generalized coordinate $f_i(t)$

$$\frac{d^2 f_i}{dt^2} + \Omega_i^2 \left(1 - \frac{P_o}{8.23P} - 2\mu_i \cos\theta_i t\right) f_i = 0 \qquad (7)$$

where Ω_i and θ_i are fundamental natural frequencies of transverse and longitudinal vibrations, respectively, and μ_i is a parametric constant. From equation (7) the stability boundary of θ_i/Ω_i vs. the thrust factor can be plotted. A typical illustration is shown in Figure 3 for $\alpha = 1$ and $\tau_o = \Omega_i t_o = 1$, 3, and 5.

(1) the spacecraft is treated as a hollow, slender cylindrical bar;

(2) the shell effect and local buckling are disregarded; i.e., the cross section is undeformed; and

(3) the linearized piston theory is applicable.

Thus, we may put the aerodynamic pressure and q(x,t) respectively,

$$p = \frac{\gamma p_\infty}{c_\infty}\left(\frac{\partial w_r}{\partial t} - U\frac{\partial w_r}{\partial x}\right) \quad q(x,t) = -2\int_{-\frac{1}{2}\pi}^{\frac{1}{2}\pi} p\cos\theta \, R\,d\theta$$

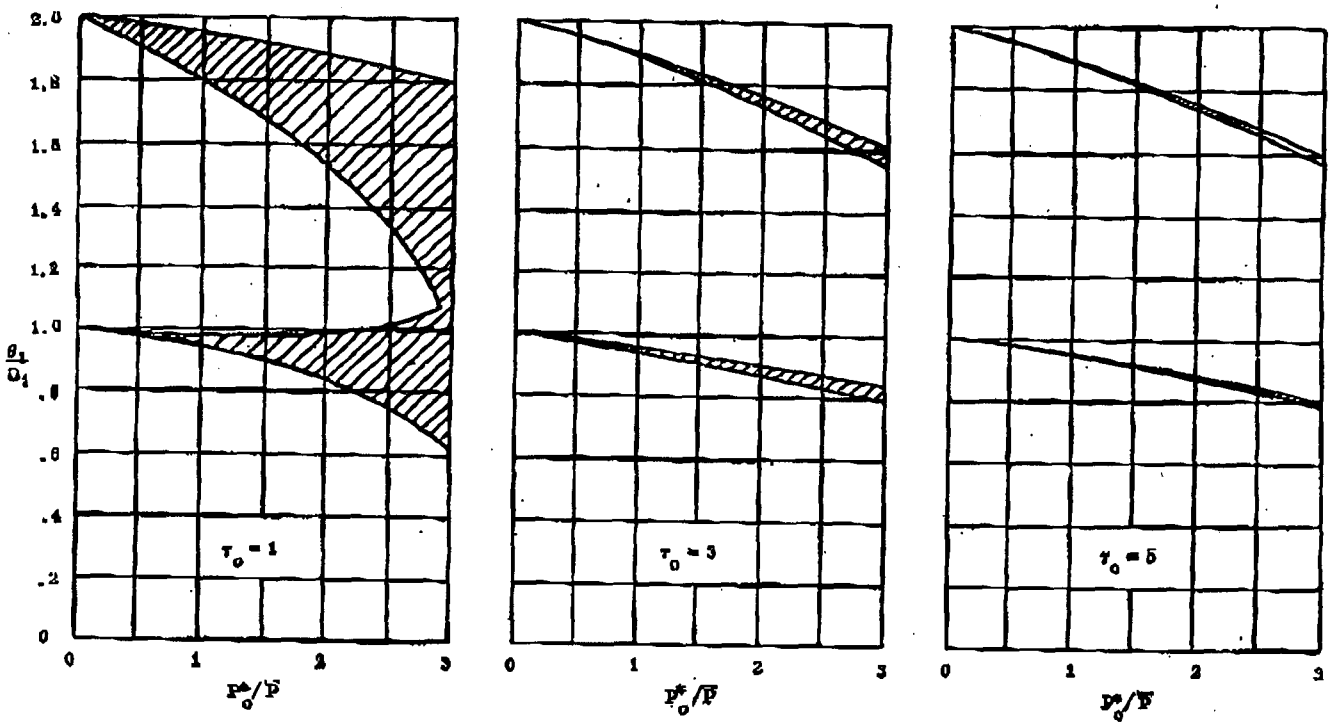

FIGURE 3. THE ELASTIC STABILITY BOUNDARIES

Figure 3 shows that the instability region is larger for smaller thrust buildup time t_o and that the width of the instability band increases with the increase of the thrust P_o.

IV. DYNAMIC ELASTIC STABILITY UNDER AERODYNAMIC LOAD

Now, the term of aerodynamic load q(x,t) exerted on the spacecraft during high speed flight is added on the right-hand side of equation (1). A simplified approach has been used to derive this function under the following assumptions:

and let

$$w_r = \sum_{i=1}^{\infty} v_i(x) f_i(t) \cos\theta$$

where w_r is the radial deformation of the shell structure, U is the velocity of flight, γ is the air constant, p_∞ is the atmospheric pressure, c_∞ is the velocity of sound in air, $v_i(x)$ is the ith free-free bending mode, and $f_i(t)$ is the ith generalized coordinate. Solving the differential equation by Galerkin's method and then applying Routh-Hurwitz criteria to the system of equations of the generalized coordinates, we can calculate the critical thrust as function of flight velocity. An illustration of the effect of aerodynamic load on critical thrust is shown in Figure 4.

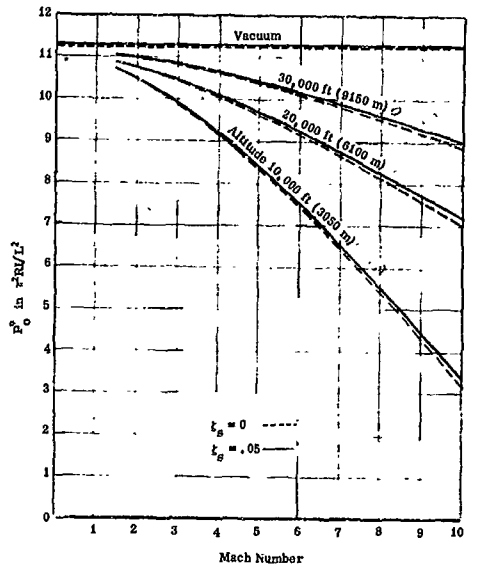

FIGURE 4. CRITICAL THRUST VS. FLIGHT SPEED

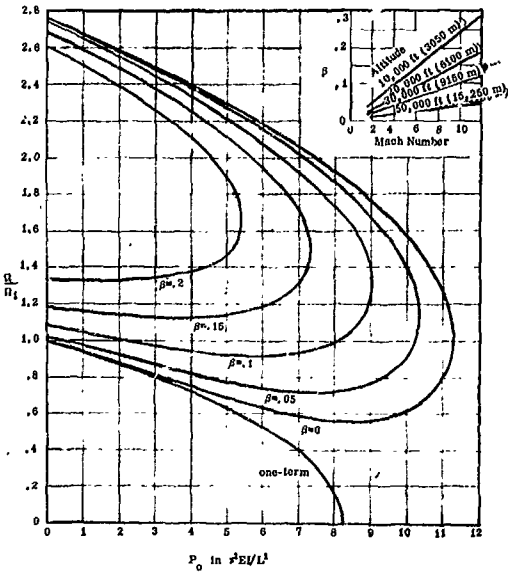

FIGURE 5. VARIATION OF FREQUENCY VS. THRUST

The model used for numerical illustrations in Figure 4, as well as Figures 5 and 6, has the following structural data:

R = 15 ft (4.57 m)

L = 350 ft (107 m)

EI = 50×10^{12} in.^{2}-lb (1.46×10^{10} m^2-Kg)

mgL = 6×10^6 lb (2.72×10^6 Kg)

All these curves are calculated by using the first two generalized coordinates, f_1 and f_2.

From Figure 4 we observe that $P_o^* = 11.23\bar{P}$; this is considerably higher than the value $8.23\bar{P}$ given by given by using f_1 alone. The critical thrust decreases with the increasing of flight velocity, and is not reduced significantly by the structural damping.

A. VARIATION OF FREQUENCY WITH THE THRUST

The frequency of transverse vibration of the rocket under the action of a constant thrust varies with the magnitude of the thrust as shown in equation (7). The frequency ratio, frequency with thrust P_o to frequency with zero thrust, vs. the thrust P_o is plotted for various aerodynamic parameter β as shown in Figure 5. The lower curve, which does not depend on β, is obtained when f_1 is used alone. The value of β plotted against flight velocity is shown in the upper right-hand corner.

In Figure 6 the variation of frequency is plotted vs. β with the thrust factor $K(= P_o/\bar{P})$ as a parameter.

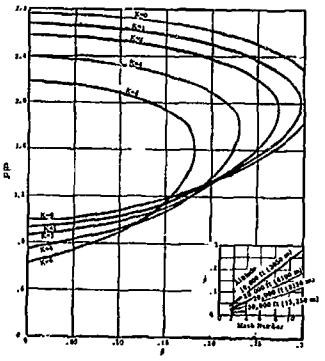

FIGURE 6. VARIATION OF FREQUENCY VS. β

V. CONCLUSIONS

To sum it up, the following findings may be significant:

1. The critical thrust of a free-free bar under an axial thrust is four times greater than that of a supported-supported bar under a conservative force.

2. The region of elastic stability of a rocket decreases with the thrust buildup time.

3. The critical thrust decreases rapidly at high supersonic speed and low flight altitude.

4. Structural damping does not have significant effect on the critical thrust.

V. REFERENCES

1. Bolotin V. V., Nonconservative Problems of the Theory of Elastic Stability, English Translation, The MacMillan Co., N. Y., 1963.

2. Bolotin, V. V., The Dynamic Stability of Elastic Systems, English Translation, Holden-Day, Inc., San Francisco, 1964.

3. Liu, C., Elastic Stability of A Slender Bar With Free-Free Ends Under Dynamic Loads, NASA TM X-53367, December 10, 1965.

4. Timoshenko, S., Theory of Elastic Stability, McGraw-Hill, N. Y., 1936.

5. Silverberg, S., The Effect of Longitudinal Acceleration upon the Natural Modes of Vibration of a Beam, Space Technology Labs., TR-59-000-00791, August 1959.

UNCITED REFERENCES

1. Hoff, N. J., The Dynamics of the Buckling of Elastic Columns, J. of Applied Mechanics, March 1951, pp. 68-74.

2. Seide, P., Effect of Constant Longitudinal Acceleration on the Transverse Vibration of Uniform Beams, Aerospace Corporation Report No. TDR-169(3560-30)TN-6, October 1963.

3. Beal, T. R., Dynamic Stability of a Flexible Missile under Constant and Pulsating Thrusts, AIAA Journal Vol. 3, No. 3, March, 1965, pp.486-494.

BLANK PAGE

OPTIMIZATION OF SLOSH BAFFLE GEOMETRY

By

H. Buchanan

SUMMARY

This paper describes a method for determining the optimum baffle configuration for suppressing excessive propellant sloshing in the tanks of a large launch vehicle. The optimum geometry for a baffle system is considered to be the one with the least mass which is capable of providing the necessary damping. The analysis considers a cylindrical tank and a baffle system made up of several flat ring baffles mounted horizontally. The basic assumptions are discussed and derivations given of the equations necessary to predict the optimum baffle configuration consistent with adequate strength. Numerical results are presented graphically, and some general conclusions are drawn.

I. INTRODUCTION

The phenomenon of propellant sloshing is particularly important to the design of large liquid-fueled launch vehicles due to the interaction of fuel sloshing with the vehicle's control system. The simplest and most widely used method for reducing the effects of propellant sloshing is by means of a system of baffles. Several baffle configurations have been employed; one of the most common has been the flat ring baffle extending inward from the tank wall. Since high vehicle performance requires that the mass of the vehicle structure be kept at a minimum through efficient design, it is highly desirable to use the most efficient baffle design for the particular propellant tank.

This analysis outlines the basic characteristics of an efficient baffle system and gives insight into the manner in which the weight varies with change in configuration of the system.

LIST OF SYMBOLS

Symbol	Definition
A	Area of single baffle
a	Tank radius
d_n	Depth of nth baffle below equilibrium surface
D	Vertical spacing between baffles
F_1, F_2, F_3	Functions defined by equations (11, 12, 5)
h	Length of portion of tank where damping is required
H	Total length of tank
K	Parameter which describes the critical baffle depth
l_{cp}	Distance from center of tank to center of pressure measured radially
P	Load applied to baffle due to pressure
m	Mass of fluid striking the baffle
$\dot{m}$	Mass rate of flow of fluid striking the baffle
n	Number of submerged baffles contributing to damping
N	Total number of baffles in the system
p	Pressure on baffle
r	Radius from tank centerline to a point on the baffle
s_t	Design stress in tension of baffle material
t	Baffle thickness
v	Velocity of fluid at impact with baffle
w	Baffle width
wt.	Baffle weight
α	Longitudinal acceleration of tank
γ_T	Total fluid damping provided by n submerged rings
ζ_w	Maximum amplitude of fluid oscillation at tank wall
ω	Natural frequency of fluid oscillation

ρ_L Mass density of the fluid

ρ_B Mass density of the baffle material

ν Poisson's ratio

II. ANALYSIS

A. BASIC ASSUMPTIONS

The basic tank configuration is shown in Figure 1 below. The tank is cylindrical with a flat bottom and the baffle system is made up of a series of evenly spaced, solid rings mounted horizontally. These assumptions are based on the conclusion made by Langner [1] that for moderate damping a solid ring baffle system has minimum weight. In arriving at these conclusions, Langner conducted a preliminary analysis of ring and partition baffles, both perforated and solid. He also concluded that, with the exception of very thin baffles where the thickness is limited by manufacturing tolerances, there are no distinct savings in weight to be gained by perforating ring baffles. The analysis provides for an arbitrary region at the bottom of the tank where damping is not required because of the small amount of liquid remaining in the tank.

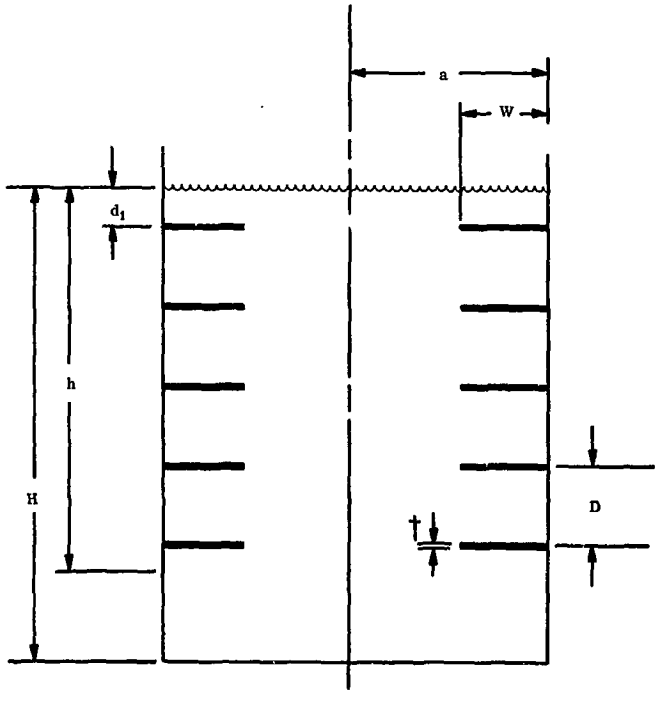

FIGURE 1. TANK AND BAFFLE SYSTEM GEOMETRY

B. DERIVATION OF OPTIMIZING EQUATIONS

1. Damping Law. A damping law for a flat ring baffle mounted in a cylindrical tank was first proposed by Miles [2]; comparison with extensive measurements [3, 4, 5] has confirmed that this relationship gives a resonable approximation of the actual damping. Bauer [6] expanded Miles' equation to account for more than one baffle. In this analysis the contribution to the total damping by exposed or partially exposed baffles is taken into account through the use of an experimentally determined parameter, K, including the combined effects of exposed and unexposed baffles. K is defined below in terms of baffle depth and spacing. The depth, d_1, of the first baffle beneath the undisturbed free surface when the tank is filled is indicated in Figure 2; d_1 corresponds to the fluid level at which the damping provided by the first ring is equal to the minimum provided by the first and

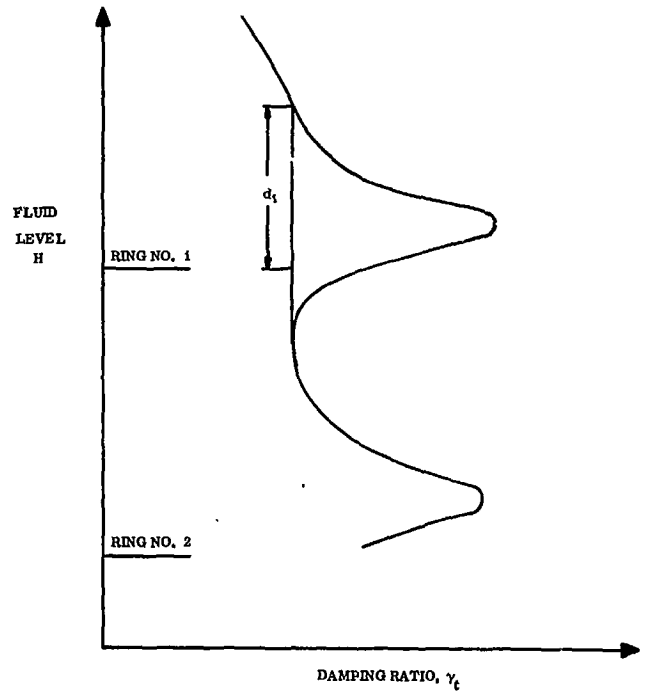

FIGURE 2. TYPICAL VARIATION OF DAMPING RATIO WITH FLUID LEVEL

second rings combined. In this manner, it is possible to insure that the damping provided never falls below a prescribed value. A relationship between d_1 and D can be written

$$d_1/D = K,$$

where K is estimated from experimental data. Then the depth, d_n of the nth ring below the surface is given

by

$$d_n = KD + (n-1)\,D. \qquad (1)$$

The total damping provided by the system of n rings is given by Bauer's expansion of Miles' equation.

$$\gamma_T = \sum_{n=1}^{n} 2.83 \left[\frac{w}{a}\left(2 - \frac{w}{a}\right)\right]^{3/2} \sqrt{\zeta_w/a}\; e^{-4.6\frac{d_n}{a}}. \qquad (2)$$

By substitution for d_n, equation (2) can be rewritten as

$$\frac{\gamma_T \left[\frac{w}{a}\left(2 - \frac{w}{a}\right)\right]^{-3/2}}{2.83\sqrt{\zeta_w/a}} =$$

$$= \sum_{n=1}^{n} e^{-4.6\,[K\,D/a + (n-1)D/a]} \qquad (3)$$

The next step is to determine the dimensionless spacing, D/a, as a function of the dimensionless width, w/a, for given values of the constants K, n and $\gamma_T\sqrt{\zeta_w/a}$; however, because of the form of equation (3), this is difficult to do analytically. By resorting to a curve-fit procedure, a fifth order polynomial for D/a in terms of w/a and $\gamma_T/\sqrt{\zeta_w/a}$ can be found:

$$D/a = a_0 + a_1 F_3 + a_2 F_3^2 + a_3 F_3^3 + a_4 F_3^4 + a_5 F_3^5, \qquad (4)$$

where

$$F_3 = \frac{\gamma_T}{2.83\sqrt{\zeta_w/a}} \left[\frac{w}{a}\left(2 - \frac{w}{a}\right)\right]^{-3/2}. \qquad (5)$$

The coefficients for the terms in equation (4) are determined from the method of least squares and are functions of the values selected for the constants K_1 and n.

2. Pressure Distribution on Baffles. Data from large scale slosh tests [7] indicate that the maximum pressure differentials on ring baffles are experienced when the equilibrium fluid level coincides with the baffle position. It is thought that this pressure is the result of the oscillating fluid striking the baffles from beneath with its maximum kinetic energy. The maximum pressures for this case are found to lie along the tank diameter parallel to the direction of excitation. Assuming that only the first mode of fluid oscillation contributes to the pressure on the baffles, the following procedure can be used to estimate this pressure distribution. If the fluid intersecting the baffle is completely stopped,

$$P = \dot{m}\, v,$$

where

$$V = \zeta\,\omega \quad \dot{m} = \rho_L\, AV \quad \text{Then } p = \frac{P}{A} = \rho_L (\zeta\omega)^2 .$$

From [4]

$$\omega = \sqrt{\frac{\alpha}{a}\,\epsilon \tanh(\epsilon\, h/a)}$$

where for the first mode $\epsilon = 1.84119$ and for the case of $h/a \geq 1.0$, $\tanh(\epsilon\, h/a) \simeq 1.0$. Now by assuming that the liquid surface remains planar, the displacement from the equilibrium position, ζ, at any point is related to the displacement, ζ_w, at the wall by

$$\zeta = r/a\;\zeta_w .$$

The pressure distribution on the baffle is given by

$$p = 1.7506\,\frac{\rho_T \alpha}{a}\left(\frac{\zeta_w}{a}\right)^2 (r)^2 . \qquad (6)$$

Figure 3 shows some of the data from Reference 7 compared to the theoretical values obtained from

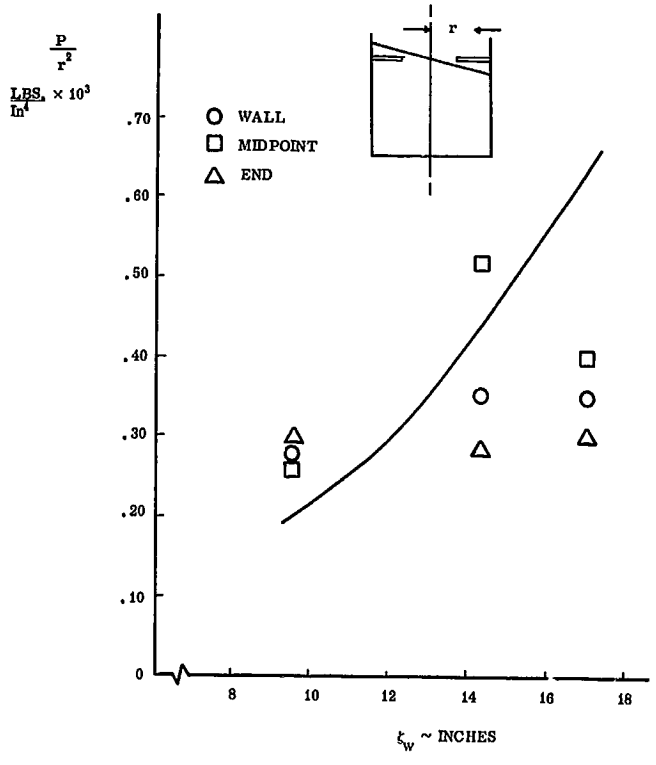

FIGURE 3. BAFFLE PRESSURE VS. AMPLITUDE

equation (6). The predicted pressure is of the correct magnitude, but the variation of pressure with fluid amplitude has not been accurately described. This can probably be traced to the assumption of a planar surface, since after the wave has struck the baffle, its surface would obviously be broken up and made more complex. The degree to which the experimental data can be grouped by dividing by the radius squared suggests that the shape of the distribution on the baffle is essentially correct.

A theory for predicting the pressure distribution as a result of continuous flow past a ring baffle has been presented by Liu [9]. While this method seems to work well for the case of the baffle being completely submerged, Junkins [7] showed that for the case being discussed here the pressure prediction fell well below measured data. Therefore, for the purpose of gaining insight into the optimization problem, equation (6) will be considered adequate.

3. Loading due to Pressure. The pressure distribution given by equation (6) applies along the diameter parallel to the direction of excitation as indi- by Figure 4. The relative magnitudes of the pressures

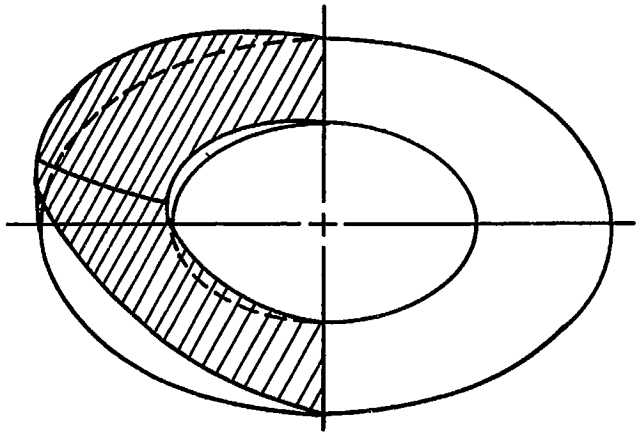

FIGURE 4. PRESSURE DISTRIBUTION ON A RING BAFFLE

in the distribution are greater than those on any other diameter since the fluid amplitude at the wall is a maximum. To apply the existing equations for stresses in flat rings [8], it was necessary to assume that this distribution was made uniformly on all diameters. This assumption is somewhat conservative but is a reasonable approximation of narrow rings. The total load due to this pressure distribution can be found by integrating over the entire baffle.

$$P = 2\pi \int_{r_1}^{a} p\, r\, dr = .$$

$$= 10.99 \frac{\alpha}{a} \left(\frac{\zeta_w}{a} \right)^2 \rho_L \int_{r_1}^{a} r^3\, dr, \qquad (7)$$

where

$r_1 = a - w.$

Then

$$P = 2.748\, a^3\, \rho_L\, \alpha \left(\frac{\zeta_w}{a} \right)^2 [1 - (1 - w/a)^4]. \qquad (8)$$

The center of pressure can be found in like manner by integrating the moment over a unit arc length.

$$\frac{l_{cp}}{a} = 0.800 \frac{[1 - (1-w/a)^5]}{[1 - (1-w/a)^4]}. \qquad (9)$$

By assuming that the baffle derives its principal strength from resistance to bending, it is possible to make use of the equations for bending stress as applied to the equivalent system shown in Figure 5. After

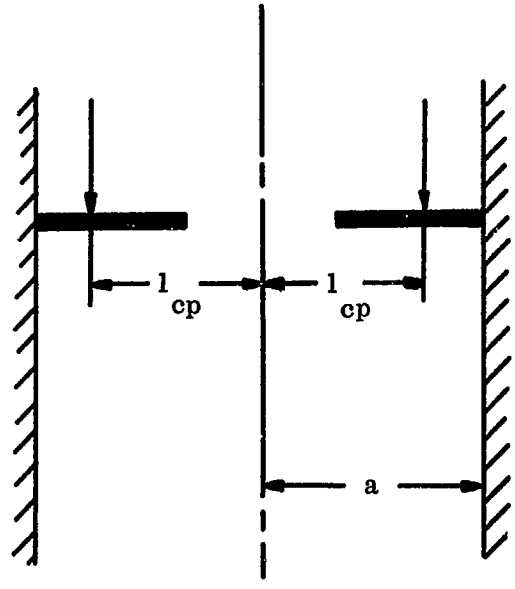

FIGURE 5. EQUIVALENT MANNER OF LOADING (OUTER EDGE FIXED)

substitution of equations (8) and (9), this appears in the form

$$s_t = \frac{a^3\, \rho_L\, \alpha\, (\zeta_w/a)^2}{t^2} 0.65616\, F_1(1 - F_2)], \qquad (10)$$

where

$$F_1 = \frac{(\frac{1}{\nu} + 1)}{\frac{1}{\nu}} 2 \left(\log \left(\frac{1}{l_{cp}/a}\right) + \log \left(\frac{l_{cp}}{a}\right)^2 - 1\right] \left[1 - (1 - w/a)^4\right] \quad (11)$$

$$F_2 = \frac{(\frac{1}{\nu} - 1) - (\frac{1}{\nu} + 1)(1 - w/a)^2}{(\frac{1}{\nu} - 1) + (\frac{1}{\nu} + 1)(1 - w/a)^2} . \quad (12)$$

If equation (10) is solved for t, the result is given by

$$t = \left(\frac{\zeta_w}{a}\right) a \sqrt{\frac{\rho_L \alpha a}{s_t}} \left[0.65616 F_1 (1 + F_2)\right]^{\frac{1}{2}} . \quad (13)$$

The total weight of the baffle system is

$$Wt. = N \rho_B \alpha t [\pi a^2 - \pi (a - w)^2] . \quad (14)$$

However, the number of baffles, N, can be written in terms of their spacing as

$$N = h/d .$$

By substituting this and the expression for t given by equation (13), it is possible to write a dimensionless weight parameter of the form

$$\frac{Wt.}{\alpha \rho_B a^3 (h/a)(\zeta_w/a)\sqrt{\rho_L \frac{\alpha a}{s_t}}} =$$

$$= 0.810 \pi \frac{[F_1 (1 + F_2)]^{\frac{1}{2}} [1 - (1 - w/a)^2]}{D/a} \quad (15)$$

where D/a is given by equation (4). Since this weight parameter contains all the arbitrary quantities pertinent to the baffle material and the fluid, the configuration for which the parameters are a minimum will be the optimum baffle configuration regardless of the material or fluid to be used. The only parameter appearing on the right side of equation (15) which is not a function of the geometry of the system is

$$\frac{\gamma_T}{\sqrt{\zeta_w/a}} .$$

III. DISCUSSION OF RESULTS

The results of a number of cases which have been examined using the methods developed above are discussed briefly. Since there is some question as to the validity of the damping law when applied to very wide baffles, only values of w/a up to 0.20 have been included. However, this includes the range of practical interest since nothing seems to indicate any advantages for very wide ring baffles. The constant K was assigned a value of 0.55 after an examination of the experimental data of Reference 5 . Poisson's ratio was assumed to be equal to 1/3 since this corresponds roughly to most metals that might be considered.

Figure 6 shows the typical variation of the weight parameter with w/a. The shaded area indicates the range of values for w/a which cannot produce the required damping regardless of the number of such baffles

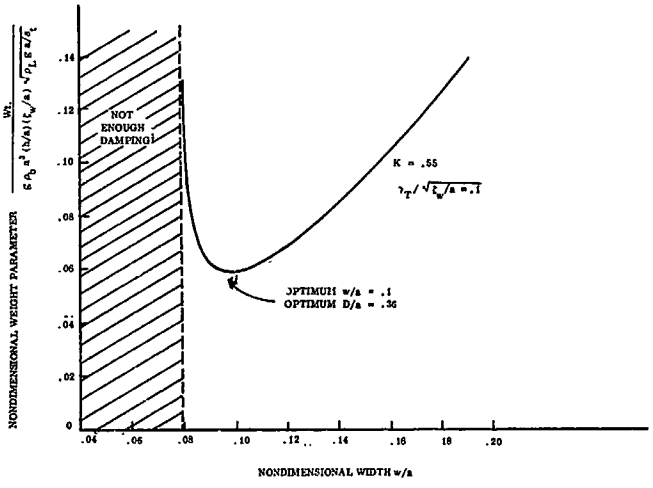

FIGURE 6. NONDIMENSIONAL WEIGHT PARAMETER VS. NONDIMENSIONAL WIDTH

used. A value of 0.10 was selected for the parameter $\frac{\gamma_T}{\sqrt{\zeta_w/a}}$ which contains both the desired damping and the maximum fluid amplitude. In addition, only the first three submerged baffles were assumed to contribute to the damping. The optimum baffle geometry produces the minimum value of the weight parameter as indicated in Figure 6. By constructing several such curves and by selecting from each the minimum value of the weight parameter, the optimum geometry may be presented as a function of the parameter $\frac{\gamma_T}{\sqrt{\zeta_w/a}}$.

The variation of the optimum value of nondimensional width and nondimensional spacing with $\frac{\gamma_T}{\sqrt{\zeta_w/a}}$ is shown in Figures 7 and 8, respectively. Figure 7 indicates that as the parameter $\frac{\gamma_T}{\sqrt{\zeta_w/a}}$ increases so

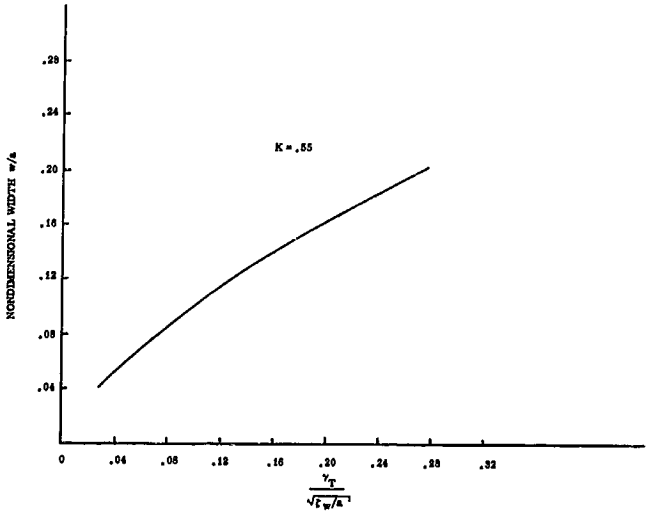

FIGURE 7. VARIATION OF OPTIMUM NONDIMENSIONAL WIDTH WITH $\frac{\gamma_T}{\sqrt{\zeta_w/a}}$

does the optimum value of w/a. Figure 8, however, seems to indicate that the optimum value of D/a is a constant for all the values of $\frac{\gamma_T}{\sqrt{\zeta_w/a}}$ considered.

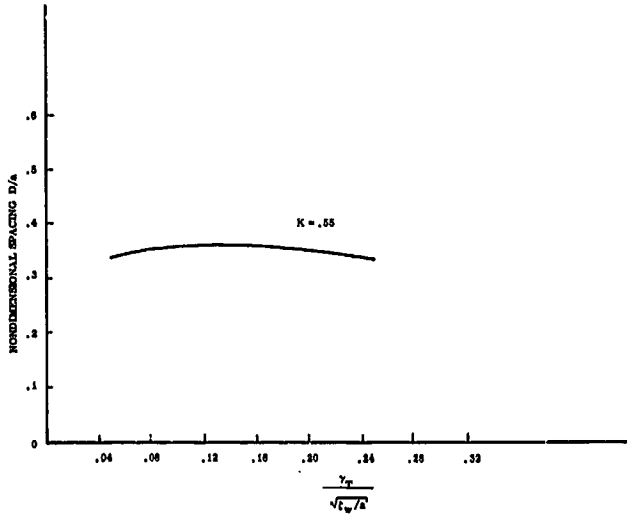

FIGURE 8. VARIATION OF OPTIMUM NONDIMENSIONAL SPACING WITH $\frac{\gamma_T}{\sqrt{\zeta_w/a}}$

IV. REFERENCES

1. Langner, C. G., A Preliminary Analysis for Optimum Design of Ring and Partition Antislosh Baffles, Southwest Research Institute Technical Report No. 7, April 1963.

2. Miles, J. W., Ring Damping of Free Surface Oscillation in a Circular Tank, Journal of Applied Mechanics, June 1958.

3. Silveira. M. A., Stephens, D. G., and Leonard, H. W., An Experimental Investigation of the Damping of Liquid Oscillations in Cylindrical Tanks with Various Baffles, National Aeronautics and Space Administration, NASA-TN-D-715.

4. O'Neil, J. P., Final Report on an Experimental Investigation of Sloshing, Space Technology Laboratories, STL/TR-59-0000-09960.

5. Abramson, H. N., Ransleben, G. E., and Garza, L. R., A Theoretical and Experimental Study of Fuel Sloshing, Southwest Research Institute.

6. Bauer, H. F., The Damping Factor Provided by Flat Annular Ring Baffles for Free Fluid Surface Oscillations, MSFC, Rept. No. MTP-AERO-62-81.

7. Junkins, J. L., Comparison of Results of Sloshing Experiments using a 40 Percent Scale Model of the S-IC Booster LOX Tank to Analytical Results (to be published as a NASA Technical Note).

8. Roark, R. J., Formulas for Stress and Strain, McGraw-Hill Book Company, Inc., 1964.

9. Liu, F. C., Pressure on Baffle Rings due to Fuel Sloshing in a Cylindrical Tank, R-AERO-4-64, MSFC.

VIII. ORBIT THEORY AND PREDICTION

SATELLITE SHADOW TIME

By

P. E. Dreher

SUMMARY

Analytical methods have been developed to determine the time spent in shadow by an earth-orbiting satellite. The length of the shadow time is a function of the particular orbit under consideration (i.e., semi-major axis and eccentricity) and of the orientation of the orbit with respect to the sun. The technique as developed was programmed on the GE-225 and a general parameter study for two different orbits was performed. The umbra transit times are as great as 12 hours for certain orbit orientations and less than 0.5 hour for other orientations. The penumbra transit time is generally less than 30 percent of the umbra transit time.

The effects of the refraction of the sun's rays by the earth's atmosphere on these transit times can be significant. Since the refraction method has not been incorporated in the computer program, only one case was evaluated. For this particular case the umbra transit time was reduced approximately 300 percent.

I. INTRODUCTION

Presented are some of the results of a study performed by Northrop Space Laboratories, Huntsville Department, for the Operations Studies Branch, Aero-Astrodynamics Laboratory, under Contracts NAS8-11111 and NAS8-20082. "Satellite Shadow Time for Earth Orbital Flights," [1], presents some of these results.

For an earth satellite dependent upon onboard solar cells for energy, the length of time spent in the earth's shadow during each orbital revolution is critical. Consequently, prior knowledge of the shadow history for the orbit under consideration is necessary in the design of the onboard energy supply.

An analytical method has been developed for determining the time an earth-orbiting satellite will remain in the earth's umbra and penumbra while traveling in a specified elliptical orbit. The analytical equation for the orbit ellipse under consideration is solved simultaneously with the equation for the shadow cone to obtain the intersection points. The eccentric anomaly corresponding to each shadow intersection point is used in Kepler's equation to determine the shadow transit time for the given ellipse.

The effect of atmospheric refraction on this shadow time has been investigated using Fermat's optical path length principle. The umbra transit time is determined considering the satellite to traverse the umbra formed by the refracted rays rather than the straight rays.

II. ANALYTIC FORMULATION OF SHADOW TRANSIT TIME

For this analysis the following assumptions were made:

1. The earth is a perfect sphere of radius r_E.
2. All perturbational forces are neglected.
3. The sun is a perfect sphere of radius r_S.
4. The earth-sun separation is a constant distance d_S.
5. The relative motion between the sun and earth during shadow transit time is negligible.

The earth's umbra in space can be represented by a circular cone as shown in Figure 1. The trace of the circular cone on the orbital plane will be a conic section, the exact form depending on the relative orientation of the orbital and ecliptic planes. To have transit time in umbra, the trace of the circular cone on the orbital plane must intersect the orbit ellipse in two points which are located on the umbra boundary.

To determine the intersection points of the circular cone trace and the orbit ellipse, the analytical equations for each conic section are solved simultaneously. Such a simultaneous solution yields all intersection points of the two complete conic sections. The two intersection points which lie on the umbra boundary define the shadow time history.

It is convenient to define two coordinate systems, one in which the circular cone can be easily described by an analytical equation and another in which the elliptical orbit can be similarly described. Two such systems are the $\{X\ Y\ Z\}$ and the $\{X_E\ Y_E\ Z_E\}$ systems

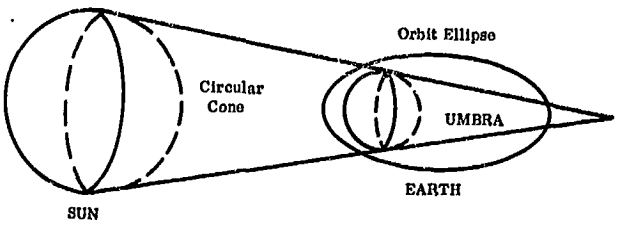

FIGURE 1. CONE REPRESENTATION OF UMBRA

shown in Figures 2 and 3. The {X Y Z} system is a rotating geocentric ecliptic coordinate system with the X-axis pointing directly away from the sun, the Y-axis pointing to the ecliptic north, and the XZ-plane being

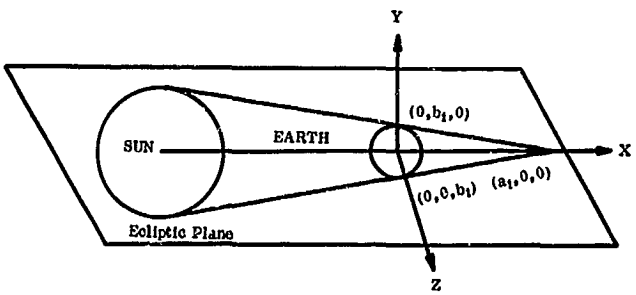

FIGURE 2. {X Y Z} COORDINATE SYSTEM

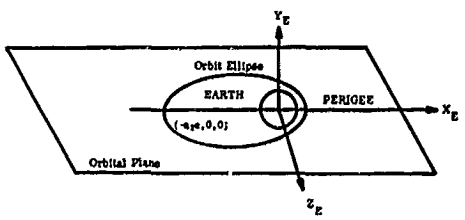

FIGURE 3. $\{X_E\ Y_E\ Z_E\}$ COORDINATE SYSTEM

the ecliptic plane. The $\{X_E\ Y_E\ Z_E\}$ system is a rotating geocentric orbital coordinate system with the Z_E-axis pointing to perigee, the Z_E-axis pointing along the semi-latus rectum to a true anomaly of 270°, the $X_E\ Z_E$-plane being the orbital plane, and the Y_E-axis completing the right-hand system. The orthogonal transformation from the {X Y Z} system to the $\{X_E\ Y_E\ Z_E\}$ system is developed by means of three successive rotations through the angles:

β, the angle between the sun and the ascending orbital node (the intersection of the ecliptic and the orbital plane) measured in the ecliptic plane

i, the inclination between the ecliptic and the orbital plane

γ, the angle between the ascending orbital node and $\vec{R}_p$, the vector through perigee, measured in the orbital plane.

The standard equation for the circular cone in the {X Y Z} system is

$$\frac{(X-a_1)^2}{a_1^2} - \frac{Y^2}{b_1^2} - \frac{Z^2}{b_1^2} = 0 ,$$

where

$$a_1 = \frac{r_E\ d_S}{r_S - r_E}$$

and

$$b_1 = \frac{r_E\ d_S}{\sqrt{d_S^2 - (r_S - r_E)^2}} .$$

The standard equation for an ellipse in the $\{X_E\ Y_E\ Z_E\}$ system is

$$\frac{(X_E + a_2 e)^2}{a_2^2} + \frac{Z_E^2}{b_2^2} = 1 ,$$

where

$$a_2 = \tfrac{1}{2}(R_a + R_p)$$

$$b_2 = \sqrt{R_a \times \vec{R}_p}$$

$$e = \frac{R_a - R_p}{R_a + R_p}$$

R_a = apogee distance

R_p = perigee distance.

The cone equation can be transformed to the coordinate variables of the $\{X_E\ Y_E\ Z_E\}$ system. The resulting transformed equation in the orbital plane, i.e., the $X_E\ Z_E$ - plane, and the standard equation for an ellipse in the $\{X_E\ Y_E\ Z_E\}$ system are solved simultaneously to yield all intersection points of the cone trace and orbit ellipse. Since the sun is always located on the negative X-axis (by coordinate system definition), a shadow point must have a positive X-component. To select the shadow points, it is sufficient to transform all the intersection points to the {X Y Z} system and eliminate those with a negative X-component. The two shadow points are designated as $(X_{E1}, 0, Z_{E1})$ and $(X_{E2}, 0, Z_{E2})$. The satellite will spend time in umbra for the orbit under consideration if and only if two

BLANK PAGE

real shadow points exist. The eccentric anomaly corresponding to each shadow point is

$$E_1 = \cos^{-1}\left(\frac{a_2 - r_1}{a_2 e}\right)$$

$$E_2 = \cos^{-1}\left(\frac{a_2 - r_2}{a_2 e}\right) ,$$

where

$$r_1 = \sqrt{X_{E1}^2 + Z_{E1}^2}$$

$$r_2 = \sqrt{X_{E2}^2 + Z_{E2}^2} .$$

The transit time from perigee to a shadow point is determined from Kepler's equation

$$T_i = \frac{E_i - e \sin E_i}{\sqrt{K/a_2^3}} , \quad i = 1, 2$$

where K = earth's gravitational constant. From these times the umbra transit time $DT\mu$ can be determined:

$$DT\mu = |T_1 - T_2| .$$

A similar procedure is followed to determine penumbra transit time because the earth's penumbra is also represented by a circular cone (Fig. 4):

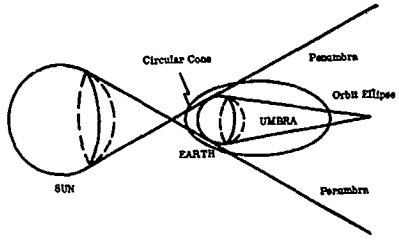

FIGURE 4. CONE REPRESENTATION OF PENUMBRA

$$\frac{(X - a_1')^2}{a_1'^2} - \frac{Y^2}{b_1'^2} - \frac{Z^2}{b_1'^2} = 0,$$

where

$$a_1' = \frac{r_E d_S}{r_E + r_S}$$

$$b_1' = \frac{r_E d_S}{\sqrt{d_S^2 - (r_E + r_S)^2}} .$$

This technique as presented was developed for general studies of shadow time histories as a function of parameters defining the orbital plane orientation with respect to the sun. To study specific trajectories, transformations must be established between the {X Y Z} system and the systems in which trajectory data are available, e.g., the $\{X_E\ Y_E\ Z_E\}$ and {X' Y' Z'} systems. The {Z' Y' Z'} system is a space-fixed geocentric ecliptic coordinate system with the X'-axis pointing to the vernal equinox, the Z'-axis pointing north and the X' Y'-plane being the ecliptic plane. The relative orientation of the {X' Y' Z'}, {X Y Z} and $\{X_E\ Y_E\ Z_E\}$ systems is shown in Figure 5.

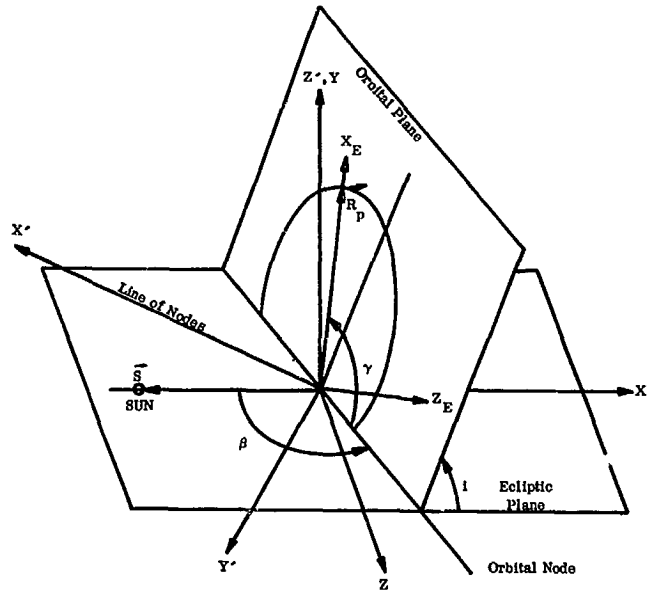

FIGURE 5. RELATIVE ORIENTATION OF {X Y Z}, {X' Y' Z'}, AND $\{X_E\ Y_E\ Z_E\}$ COORDINATE SYSTEMS

The inclination, i, can be determined by a spherical trigonometric consideration of the intersection of the equatorial, ecliptic, and orbital planes as shown in Figure 6. The inclination of the orbital plane, I, the inclination of the equatorial plane to the ecliptic, ρ, and the angle between the line of nodes and the ascending node, L, are known quantities.

Once the available trajectory data are used to determine the parameters β, γ, and i, these parameters, along with the specified apogee and perigee

distance R_a and R_p, can be used to compute the shadow transit time.

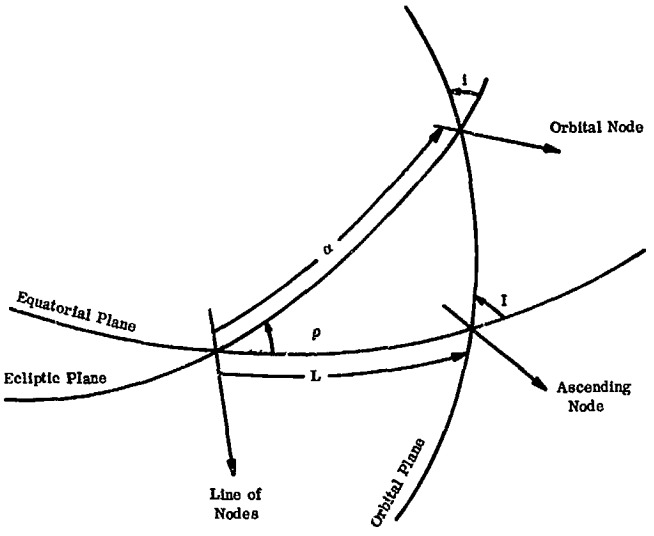

FIGURE 6. EQUATORIAL, ECLIPTIC AND ORBITAL PLANES

Because the inclination, i, generally varies only slightly with time, a general parameter study was done varying β and γ and holding i constant. Two different orbits were considered with the results shown in Figures 7 and 8.

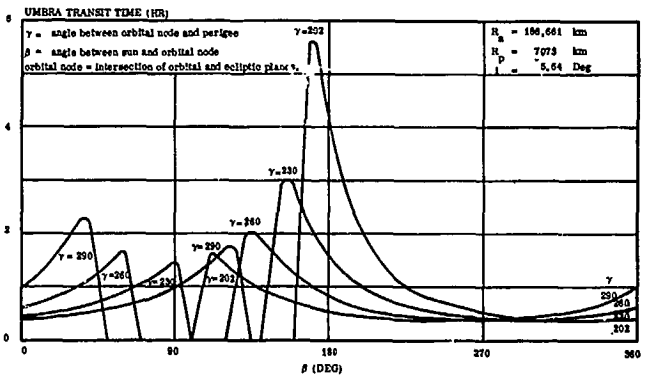

FIGURE 7. GENERAL PARAMETER EFFECTS FOR 1/8 LUNAR PERIOD ORBIT

Figure 7 shows the umbra transit time over the range of 0° to 360° for β and over the range 202° to 290° for γ. The orbit considered was a preliminary 1/8 lunar period orbit with apogee = 186,661 km and perigee = 7073 km. On the launch date, γ = 202°, and one year later, γ = 290°. As seen in Figure 7, the umbra transit time varies from 0.5 hours to 5.6 hours depending on the value of β .

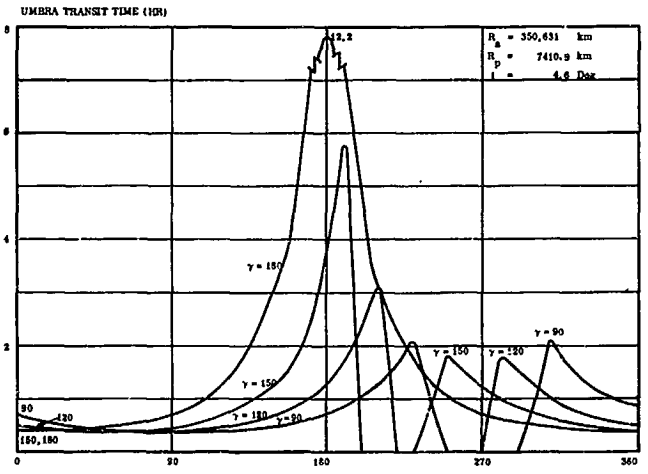

FIGURE 8. GENERAL PARAMETER EFFECTS FOR 1/3 LUNAR PERIOD ORBIT

Figure 8 shows the umbra transit time for a preliminary 1/3 lunar period orbit with apogee = 350,631 km and perigee = 7410.9 km. A general parameter study was done for this orbit over the range of 0° to 360° for β and 90° to 180° for γ. The maximum shadow time occurred for γ and β = 180; this is logical since this placed the sun on the orbital node and placed apogee in shadow (directly behind the earth from the sun). This case represents the maximum shadow time possible for a given orbit. This was not the case for the 1/8 orbit considered because actual γ conditions were used, and the minimum value of γ was 202°. This meant that apogee was not directly behind the earth from the sun. The maximum shadow time is also a function of apogee altitude. A difference in apogee altitude from 186,661 to 350,631 km changed the maximum shadow time from 5.6 hr to 12.2 hr.

Figure 9 shows the transit time through umbra and the transit time through umbra plus penumbra. The time spent in partial shadow (penumbra) is generally less than 30 percent of the time spent in umbra.

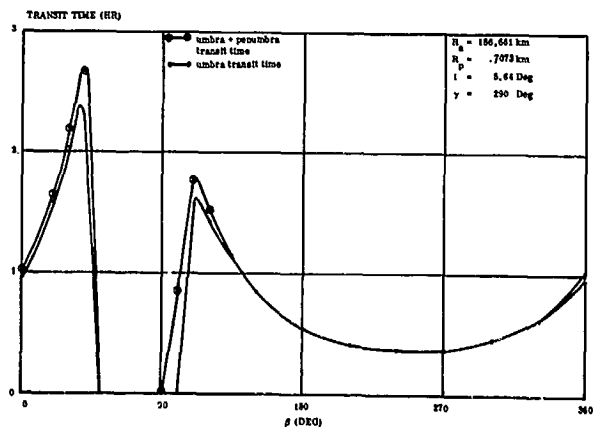

FIGURE 9. COMPARISON OF UMBRA AND PENUMBRA TRANSIT TIMES

Figure 10 shows the umbra transit time for a particular trajectory, the 1/8 lunar period orbit. For this case actual trajectory points were used, and the values of i, β, and γ, corresponding to these points were computed. The maximum shadow time was 1.82 hours with the minimum 0.36 hours.

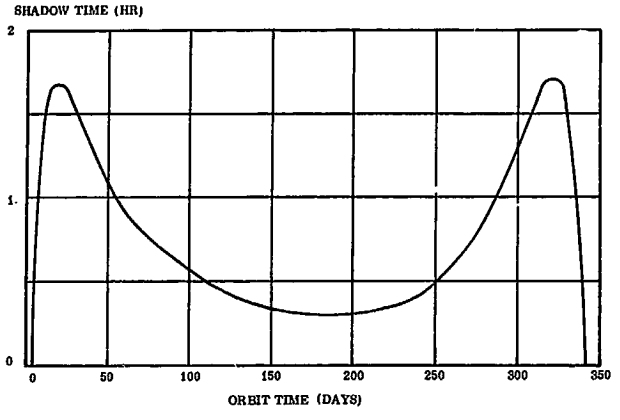

FIGURE 10. UMBRA TRANSIT TIME FOR 1/8 LUNAR PERIOD ORBIT

III. REFRACTION EFFECT ON TRANSIT TIME

In the previous discussion, the light rays from the sun are assumed to travel in straight-line motion. But the rays are refracted as they pass through the earth's atmosphere because they travel between media of different densities. The resulting path is one which satisfied Fermat's principle for optical path length. The umbra is no longer a circular cone whose XY trace is a straight line, but a surface whose XY trace is the curve describing the path of a refracted ray, as shown in Figure 11. For simplification, this portion of the study was confined to the two-dimensional space, i.e., the XY-plane.

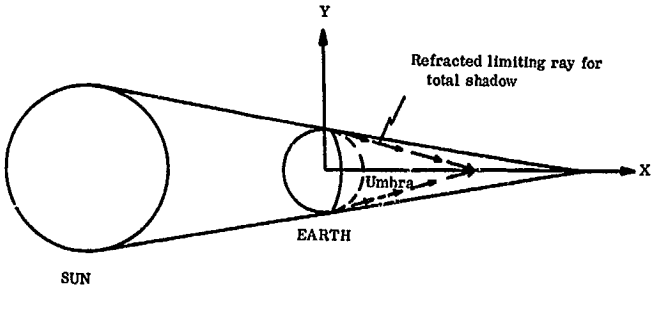

FIGURE 11. REFRACTED RAY FORMATION OF UMBRA

The following assumptions were made:

1. The earth's atmosphere is formed by an infinite number of successive strata, each of uniform density. By passing to the limit in which the number of strata becomes infinite and the differences in density in two consecutive strata infinitesimal, one has the case of the continuously varying density of the atmosphere.

2. The successive strata are all concentric with the center of a spherical earth.

3. The values of the atmospheric density at the surface of the earth [2] are

$$\rho_o = 0.0027 \text{ slug/ft}^3 .$$

4. The value of the refractive index at the surface of the earth [2] is

$$n_o = 1.00029 .$$

5. The atmospheric density model can be expressed as

$$\rho(r) \sim \frac{1}{e^r} .$$

6. The relation between the refractive index and the atmospheric density is given by Sellmeier's equation [6]

$$n^2(r) = 1 + C\,\rho(r),$$

where

$$C = \frac{n_o^2 - 1}{\rho_o} .$$

7. The upper limit of the atmosphere is

$$h = 6419.719 \text{ km.}$$

To determine the refracted ray equation, Fermat's principle is used. The path of a light ray is such that the integral

$$1 = \int_A^B n\,ds$$

is an extremum [4], where

1 = optical path length

n = refractive index

ds = differential of arc length along the path A B. Calculus of variations techniques were used to determine the optical path, this path being that of the refracted ray.

As seen in Figure 12, the refraction angle ξ can be defined as

$$\xi = \theta_o - 90° - \phi_o ,$$

where

$$\phi_o = \cos^{-1} \frac{n_o r_E}{h} .$$

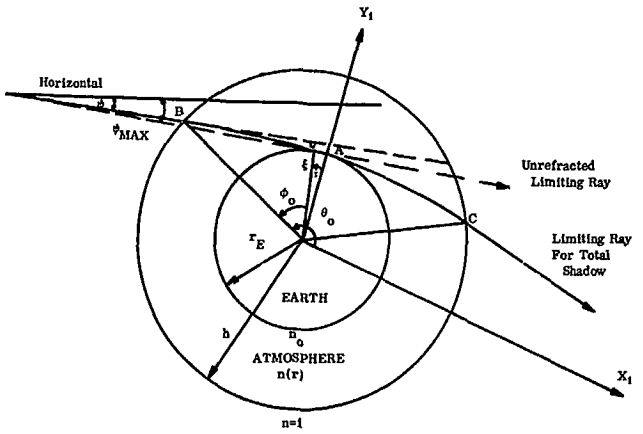

FIGURE 12. MODIFIED PATH OF THE REFRACTED RAY

The angle θ can be determined from a definite integral that is a function of the refraction index, n, the atmospheric density model, and the constants n_o, r_E, and h. This integral can be solved numerically by using Simpson's Method or the Modified Gaussian Method. The value of the refraction angle, ξ, was found to be 38.8 .

The other variable used in the analysis is ψ, the angle made by the limiting ray with the horizontal before refraction. In the case where refraction is neglected, the limiting ray makes the maximum angle with the horizontal as shown in Figure 12. The maximum value of ψ was determined geometrically, and found to be $\psi_{MAX} = 15'$.

Figure 12 shows that the ray which was refracted by the atmosphere proceeds in straight-line motion after leaving the earth's atmosphere (at point C). An analytical equation describing the resulting straight ray in the {X Y} system solved simultaneously with the orbit ellipse equation will give the intersection points necessary for the computation of umbra transit time.

Numerical results were obtained for one trajectory with $R_a = 186,360.0$ km and $R_p = 6545.0$ km. In this two-dimensional case, apogee was considered to be directly opposite the sun ($\beta = 180°$, $\gamma = 180°$) so that the shadow time neglecting refraction was the maximum possible for this orbit. The results were

Umbra time, neglecting refraction 8.03 hr ($\psi = \psi_{MAX}$)

Umbra time, considering refraction 3.22 hr ($\psi = 1.2'$)

Umbra time, considering refraction 2.67 hr ($\psi = 6.2'$)

Umbra time, considering refraction 2.3 hr ($\psi = 11.2'$)

Since this part of the analysis has not been incorporated in the computer program, no other cases have been studied. It is not known whether consideration of atmospheric refraction reduces the umbra transit time by such a large amount for other orbit orientations.

These numerical results show that atmospheric refraction has a major effect on the formation of the earth's umbra. This should not be surprising, for during a total lunar eclipse the moon remains dimly visible because some of the sun's rays are refracted by the earth's atmosphere and reach the moon [5].

IV. REFERENCES

1. Satellite Shadow Time for Earth Orbital Flights. Northrop TM, no. 88.

2. White, J. F., ed.: Flight Performance Handbook for Powered Flight Operations. John Wiley & Sons, Inc., 1963.

3. Pars, L. A.: An Introduction to the Calculus of Variations. John Wiley & Sons, Inc., 1962.

4. Rossi, R.: Optics. Addison-Wesley Publishing Company, Inc., Reading, 1957.

5. Struve, O.; Lynds, B.; Pillans, H.: Elementary Astronomy. Oxford University Press, 1959.

6. Ditchburn, R.: Light. Interscience Publishers, 1959.

BLANK PAGE

IX. PUBLICATIONS AND PRESENTATIONS

A. PUBLICATIONS

TECHNICAL MEMORANDUM X-53187

January 13, 1965

CISLUNAR METEOROID IMPACT AND PUNCTURE MODELS WITH PREDICTED PEGASUS SATELLITE PUNCTURES

By

Charles C. Dalton

George C. Marshall Space Flight Center
Huntsville, Alabama

ABSTRACT

The author's previous model for the variation of meteoroid impact flux with respect to distance from the earth in cislunar space is simplified and corrected for the increase in the inferred mass of a meteoroid due to the new pressure values in the U. S. Standard Atmosphere, 1962. A new model for the corresponding puncture flux is developed as a function of material parameters and thickness by interpreting Explorer XVI puncture data in relation to the revised model for impact flux and to extrapolated results from the Martin Company's multivariate analysis of laboratory hypervelocity impact data.

During one year after a Pegasus satellite has been deployed in an orbit with perigee and apogee heights of 505 and 740 kilometers, the number of punctures in the 16 sheets of the 0.0015-inch sensor, the 34 sheets of the 0.008-inch sensor, and the 366 sheets of the 0.016-inch sensor are predicted to be approximately 5430, 41, and 38, respectively, when the extra material in the bonded capacitors is considered. The estimated masses of the meteoroids which can just puncture these sensors when they have the mean values of density (0.44 gram per cubic centimeter), velocity (26.7 kilometers per second), and impact angle ($\pi/4$ radian) are $10^{-7.84}$, $10^{-5.85}$, and $10^{-4.98}$ gram.

TECHNICAL MEMORANDUM X-53188

January 15, 1965

DYNAMIC TEST RESULTS OF SAD-8,9

By

Gale R. Ernsberger

George C. Marshall Space Flight Center
Huntsville, Alabama

ABSTRACT

Dynamic tests were performed on a full scale prototype of the Saturn SA-8 and 9 flight vehicle to determine the body bending and torsional dynamic behavior. A full scale prototype was vertically suspended in the test tower and excited by shakers mounted at the engine gimbal planes. The vehicle's dynamic response at various applied forcing frequencies was recorded by vibration pickups. This report presents the SAD-8 & 9 dynamic test results in terms of resonant frequencies, mode shapes, generalized masses, damping coefficients and response (amplitude and phase) curves.

TECHNICAL MEMORANDUM X-53193

January 27, 1965

(MMC) - S-IV/APOLLO SEPARATION AND VENTING STUDY FOR SA-9 VEHICLE

By

D. O. McNiel and W. H. Harmon

George C. Marshall Space Flight Center
Huntsville, Alabama

ABSTRACT

This report presents the results of a separation (MMC) - S-IV/Apollo and venting study for the predicted Saturn SA-9 flight. Results in this report are subject to the restrictions that residuals are only vented in the gaseous state. There are two primary objectives of this study, the first of which is to assure adequate separation distance between the two vehicles [(MMS) - S-IV and Apollo boilerplate] and the second of which is to determine a confidence level that excessive angular rates and angular accelerations will not occur during and following (MMC) wing deployment. Results indicate that predicted (3 σ) angular rates and regular accelerations do not exceed the limits established by the (MMC) Project Office of 6 deg/sec resultant angular velocity and .15 deg/sec^2 resultant angular acceleration. The maximum predicted (3 σ) resultant angular rate occurs after all residuals have been depleted and is 4.7 deg/sec. Predicted resultant (3 σ) angular acceleration during and

following (MMC) wing deployment do not exceed 0.005 m/sec^2. The minimum (nominal - RSS) separation distance between the (MMC) - S-IV and Apollo boilerplate at initiation of wing deployment is 64, which is a sufficient distance to prevent collision of the two vehicles during this operation.

TECHNICAL MEMORANDUM X-53203

January 29, 1965

SA-9 FINAL PREDICTED TRAJECTORY PART I. NOMINAL TRAJECTORY

By

Gerald Wittenstein

George C. Marshall Space Flight Center
Huntsville, Alabama

ABSTRACT

This report presents the final nominal predicted trajectory for SA-9. It is the first part of a two part presentation of the SA-9 Final Predicted Trajectory. Part II will present the dispersion analysis associated with the nominal trajectory and will be published as a separate report (Part II. Nominal Trajectory and Dispersion Analysis).

The SA-9 vehicle is to be flown over the Eastern Test Range (ETR) with a flight azimuth of 105 degrees East-of-North. Also included in Part I is a discussion of the vehicle and mission objectives, the trajectory shaping and constraints, and a description of the vehicle configuration.

Primary objectives for SA-9 are to place the Pegasus (MMC) satellite into an elliptical orbit, to further flight test the vehicle system, and to further man-rate the Saturn class vehicle. The primary objective of the Pegasus satellite is to obtain information on micrometeoroids for near-earth orbits.

The depleted S-IV stage and payload, which includes the Pegasus satellite and an Apollo boilerplate, are to be inserted into an elliptical, low-earth orbit, with perigee and apogee altitudes of 500 km and 750 km, respectively. The nominal lifetime for this orbit is well in excess of one year.

Information contained in this report may be considered applicable for SA-8 and SA-10 flight profiles until superseded.

TECHNICAL MEMORANDUM X-53209

February 16, 1965

THE EFFECTS OF INTRODUCING OPTIMIZATION INTO A FAMILY OF SATURN IB FIRST STAGE TRAJECTORIES

By

John B. Winch and Gary McDaniel

George C. Marshall Space Flight Center
Huntsville, Alabama

ABSTRACT

This report presents a study of the effects of introducing lift into a family of Saturn IB first stage gravity tilt programs. In this family of trajectories the vehicle is constrained to fly a nonlifting trajectory profile after a "kick" has been given shortly after launch to initiate tilting. Lift is thus introduced into this family of trajectories using a calculus of variations technique at 60, 65, and 70 seconds which correspond to times prior to and after Mach 1 and the max q time points. The cutoff weight into orbit for these optimized trajectories indicates that an increase of as much as 500-600 pounds over the nominal zero-lift trajectory may be obtained while the structural loadings are still realistic.

TECHNICAL MEMORANDUM X-53214

March 8, 1965

JET PENETRATION INTO A LIQUID

By

H. G. Struck

George C. Marshall Space Flight Center
Huntsville, Alabama

ABSTRACT

This investigation is concerned with the phenomenon of a gas jet impinging on, and penetrating into, a liquid. The study is restricted to the case of a round jet of subsonic and supersonic velocities penetrating the liquid at right angles. The phenomenon was analyzed from two viewpoints. The first, a stagnation

pressure analysis, related the depth of the surface depression or cavity to the stagnation pressure based on the centerline velocity of the jet in the neighborhood of the surface. The second, a displaced liquid analysis which takes the mixing process of the jet into account, related the weight of the liquid displaced from the cavity to the momentum of the jet. It was attempted to derive scaling laws from these investigations to predict penetration depth of full-scale rocket motors of space vehicles launched from platforms built over a water surface. Splash heights were also analyzed and correlated.

TECHNICAL MEMORANDUM X-53215

March 12, 1965

LAUNCH VEHICLE GUIDANCE EQUATIONS FOR THE SATURN IB SA-201 MISSION

By

Isaac E. Smith and F. Don Cooper

George C. Marshall Space Flight Center
Huntsville, Alabama

ABSTRACT

This report defines and describes the Launch Vehicle Guidance Equations for the Saturn IB SA-201 mission, to satisfy document #15 of the Apollo Mission Planning and Trajectory Documentation Plan.

TECHNICAL MEMORANDUM X-53216

March 12, 1965

THE SOLAR FLARE ENVIRONMENT

By

W. T. Roberts

George C. Marshall Space Flight Center
Huntsville, Alabama

ABSTRACT

Of all the natural environments of extraterrestrial space, probably the most hazardous is the radiation to be encountered. The three main sources of radiation are galactic cosmic rays, Van Allen belt particles, and solar flare particles. Galactic cosmic rays are very high energy particles, but since their flux is low, they will not be considered in this analysis. The Van Allen belt particles will not be considered since we are specifically interested in the environment encountered at some distance from earth greater than about fifteen earth radii. Thus, we are left with the solar flare as the main contributing source of intensive radiation.

Discussed is the solar atmosphere including the photosphere, chromosphere, and corona. Most of the main structures found within these areas are mentioned, and some are elaborated on.

Next are described the various types of solar flares which have been observed. The problem of constructing a solar flare "model" is discussed, and percentile curves based on presently available data are suggested as a solution. These curves are drawn for the 99.9 percentile, 90 percentile, 67 percentile, and 50 percentile groups.

Probabilities of solar flare occurrence, and methods now being used as a basis for studies on solar flare prediction are considered. It is concluded that even accurate solar flare predictions cannot alleviate the amount of shielding required for a long duration extraterrestrial mission.

A few of the complications involved in solar flare shielding calculations are covered, and a possible means of approach to these problems is suggested for future extraterrestrial missions.

TECHNICAL MEMORANDUM X-53222

March 22, 1965

MONTE CARLO PERFORMANCE ANALYSIS COMPUTER PROGRAM WITH PROGRAMMED MIXTURE RATIO

By

Roy C. Lester

ABSTRACT

This report presents a detailed description of a Fortran IV computer program which uses the Monte Carlo technique to establish the stage residual and a

total payload distribution for a vehicle with up to ten stages. The Monte Carlo technique employs the sampling of the independent engine and vehicle parameters, and, by the use of a large number of cases, is used to establish the probability distribution for stage residual and total payload.

TECHNICAL MEMORANDUM X-53225

March 25, 1965

THE FIRST STAGE TRAJECTORY OPTIMIZATION OF THE SATURN V VEHICLE

By

Gary McDaniel

George C. Marshall Space Flight Center
Huntsville, Alabama

ABSTRACT

The effects of introducing optimum angle of attack programs into a family of Saturn V first stage trajectories are presented. These angle of attack programs were determined by a calculus of variations technique [1] such that the cutoff weight into a 100 nautical mile circular orbit was maximized. In this family of first stage trajectories, the vehicle was constrained to fly a nonlifting trajectory profile (except during the time when small angle of attack programs were induced shortly after launch to initiate tilting) until the optimization was introduced at 48, 72, and 88 seconds. The results of the study indicate that between 1500 and 5000 pounds of cutoff weight in a 100 nautical mile circular parking orbit can be gained as compared to the optimized nonlifting trajectory. The resulting trajectories show significant increases in the dynamic pressure and large $q|\alpha|$ products which led to using a $q|\alpha|$ constraint to reduce the structural loadings. Additional studies are required to determine the structural loadings and the control requirements associated with the introduction of the optimization.

TECHNICAL MEMORANDUM X-53235

April 9, 1965

SA-9 FLIGHT TEST DATA REPORT

By

H. J. Weichel

George C. Marshall Space Flight Center
Huntsville, Alabama

ABSTRACT

This report is a presentation of certain flight mechanical data obtained from the SA-9 flight test. Digitized data are presented in graphical form. Also included are schematic drawings showing the instrument location on the vehicle.

The intention of this report is to present the digitized data in an easy-to-read form for use by design and technical personnel. This report is to supplement the Saturn SA-9 Flight Evaluation Report and many other reports published by the various laboratories.

TECHNICAL MEMORANDUM X-53242

April 15, 1965

SA-201 LAUNCH VEHICLE REFERENCE TRAJECTORY (U)

By

Joseph W. Cremin and William M. Gillis

George C. Marshall Space Flight Center
Huntsville, Alabama

ABSTRACT

Presented is the official launch vehicle reference trajectory for the first R&D flight of the Saturn IB: The various launch vehicle (S-IB and S-IVB stage), spacecraft, and system constraints that have produced this trajectory shaping are reported in addition to an unofficial representation of the Apollo Command and Service Module (CSM) powered flight. The nominal launch vehicle mission is the injection of a partially fueled CSM into an earth intersecting ellipse. The SM is ignited after a specified coast phase and propels the CM to atmospheric reentry conditions, that will provide an evaluation of the heat shield ablator performance at high heat rate conditions.

TECHNICAL MEMORANDUM X-53244

April 15, 1965

HARDWARE AND GUIDANCE SCHEME ERROR ANALYSIS FOR SA-201 EVALUATED AT S-IVB CUTOFF

By

A. W. Deaton

ABSTRACT

This technical memorandum presents the inaccuracies in velocity and displacement of the Saturn IB SA-201 vehicle at S-IVB stage cutoff caused by hardware and guidance scheme errors. The hardware errors include such effects as stabilized platform drift and accelerometer measurement inaccuracies.

TECHNICAL MEMORANDUM X-53251

April 30, 1965

SATURN SA-9/PEGASUS A POSTFLIGHT TRAJECTORY

By

Jonathan B. Haussler and Robert H. Benson

George C. Marshall Space Flight Center
Huntsville, Alabama

ABSTRACT

This report presents the postflight trajectory for the Saturn SA-9/Pegasus A test flight. Fourth of the Block II series, SA-9 was the first vehicle to carry a Pegasus payload. Trajectory dependent parameters are given in earth-fixed, space-fixed ephemeris, and geographic coordinate systems. A complete time history of the powered flight trajectory is presented at 1.0 sec intervals from first motion to S-I/S-IV separation and at 5.0 sec intervals from S-I/S-IV separation to insertion. Tables of insertion conditions and various orbital parameters are included in a discussion of the orbital portion of flight.

TECHNICAL MEMORANDUM X-53255

May 5, 1965

MEASUREMENT RELATIONSHIPS FOR PEGASUS-TYPE METEOROID EXPERIMENTS

By

Charles C. Dalton

George C. Marshall Space Flight Center
Huntsville, Alabama

ABSTRACT

In Pegasus-type meteoroid measurement satellite experiments, where vehicle attitude information is available without information about the meteoroid closing velocity vector, the probable radiant and the puncture flux enhancement factor for sporadic meteors should be based on the assumption that velocity vectors for ambient meteoroids are isotropically distributed. Then, although half of the meteoroids which impact onto a flat transducer are more than 45 degrees from the normal, those within 45 degrees puncture three times more effectively than the others, and half of the puncturing meteoroids are less than 33.5 degrees from the normal when the earth is below the surface horizon. This distribution also implies that the flux of puncturing meteoroids is five times greater than the flux of incident meteoroids with mass equal to or greater than the mass of the almost-puncturing meteoroid with the average values of density, velocity, and impact angle.

The formulas for the celestial coordinates of the probable radiant of a puncturing meteoroid have been corrected for earth-shielding. This correction is important near the earth even under nominal circumstances; e.g., when the orbit height is 500 kilometers, the radius of the earth's disk (as seen from the vehicle) is 70 degrees. In that case, when the elevations of the earth's center are 0, 15, 30, 45, and 60 degrees, the probable radiants are deflected 5, 10, 20, 39, and 80 degrees, respectively, by the earth-shielding effect.

TECHNICAL MEMORANDUM X-53257

May 11, 1965

HEAT TRANSFER IN THE VICINITY OF A TWO-DIMENSIONAL PROTUBERANCE

By

Ed Murphy

George C. Marshall Space Flight Center
Huntsville, Alabama

ABSTRACT

Empirical equations are presented which will estimate the ratio of protuberance-to-flat-plate heat transfer coefficients for supersonic flow in the vicinity of two-dimensional protuberances in a turbulent, supersonic boundary layer. The equations were derived from experimental heat transfer data taken around several two-dimensional protuberances, i.e., a 1 × 2-inch (2.5 × 5 cm) stringer, a 2 × 4-inch (5 × 10 cm) stringer with and without a 30-degree wedge, and a one-quarter cylinder forebody. Important parameters in the equations are boundary layer thickness, protuberance geometry, Reynolds number, and Mach number. Using the equations, the average deviation between estimated and experimental ratios is from -9 to +15 percent.

TECHNICAL MEMORANDUM X-53258

May 12, 1965

A THREE-DIMENSIONAL ASCENDING ITERATIVE GUIDANCE MODE

By

Isaac E. Smith

George C. Marshall Space Flight Center
Huntsville, Alabama

ABSTRACT

This report discusses a novel computational procedure for implementing three-dimensional, path adaptive guidance in upper stage vacuum flight. The procedure is characterized by a minimum number of preset values, on-board computation of guidance parameters, and reasonably close adherence to trajectories determined by calculus of variations methods, both as to trajectory shape and payload capability. Using average gravity magnitude and direction approximations, a partially closed form solution to the equations of motion is obtained. The solution yields a "time-to-go" and a steering function. The steering function consists of a thrust attitude and a turning rate.

TECHNICAL MEMORANDUM X-53259

May 12, 1965

NASA'S 150-METER METEOROLOGICAL TOWER LOCATED AT CAPE KENNEDY, FLORIDA

By

John W. Kaufman

George C. Marshall Space Flight Center
Huntsville, Alabama

and

Lester F. Keene

John F. Kennedy Space Center

ABSTPACT

This report describes the basic functional operations of the 150-meter NASA Meteorological Tower Facility located in the Merritt Island Launch Area, Cape Kennedy, Florida. Meteorological instrumentation and data acquisition schemes for obtaining lower atmospheric profile measurements of temperature, winds, and humidity are discussed. Specific information on such matters as meteorological sensor response, electronic circuitry of the meteorological facility, and explicit details of recorder systems has purposely been omitted.

TECHNICAL MEMORANDUM X-53261

May 14, 1965

SOME PRACTICAL ACCURACY CONSIDERATIONS OF SMOKE TRAIL WIND PROFILE DATA

By

Dennis W. Camp

and

James R. Scoggins

George C. Marshall Space Flight Center
Huntsville, Alabama

ABSTRACT

Wind velocity profiles measured simultaneously by the smoke trail/photographic method by different camera pairs, and photographs reduced twice for the same trail are analyzed to determine the relative accuracy of the smoke trail wind data. Arithmetic means, standard deviations, and extremes are given for the differences between five pairs of profiles. Also presented are relative RMS errors in wind speeds, relative RMS errors in shears over height increments of 25, 50, 100 and 200 m, and maximum shear differences for each case. The computed RMS differences in wind speeds are generally less than 1 m/sec, errors in wind shear vary to approximately 60 percent of the values used in vehicle design studies, and relative RMS errors in wind speeds range from approximately 0.1 to 0.7 m/sec. The sources of the errors are not isolated. These errors will probably be reduced as more experience is gained in data reduction and quality control procedures are improved.

TECHNICAL MEMORANDUM X-53262

May 17, 1965

SA-8 OPERATIONAL TRAJECTORY

By

Pamelia B. Pack

and

Gordon W. Solmon

George C. Marshall Space Flight Center
Huntsville, Alabama

ABSTRACT

This report presents the operational predicted trajectory for Saturn I vehicle SA-8 to be flown over the Eastern Test Range. Included is a discussion of the vehicle and mission objectives, the trajectory shaping and constraints and a brief description of the vehicle. Wind limit criteria and range safety aspects are also summarized.

A successful flight will insert the depleted S-IV stage and payload into an orbit with perigee and apogee altitudes of 510 km and 754 km, respectively. This orbit has a nominal lifetime of 1200 days.

The payload consists of an Apollo boilerplate (BP-26) and a Meteoroid Technology Satellite (Pegasus). BP-26 is used to simulate the characteristics of an Apollo spacecraft whose ultimate mission will be a manned lunar landing and return to earth. After insertion into orbit, Pegasus will be exposed and, after wing deployment, will transmit micrometeoroid data to earth upon telemetered command.

TECHNICAL MEMORANDUM X-53263

May 17, 1965

SA-9, 8 AND 10 DISPERSION ANALYSIS

By

Gerald Wittenstein and Jerry D. Weiler

George C. Marshall Space Flight Center
Huntsville, Alabama

ABSTRACT

This report replaces the Part II portion of the SA-9 Final Trajectory. The data used to generate the analysis presented here are based on final SA-9 data. The only differences in the flights of SA-9, 8, and 10 will be a shift in the nominal similar to the shift described in this report.

A detailed discussion of dispersions, their philosophy, and application with respect to a nominal trajectory is presented. A brief description of the SA-9 nominal trajectory is contained as a reference in this report.

It is felt by the authors that the group of trajectories presented in the dispersion analysis is representative and yields a satisfactory envelope for the remaining Block II flight profiles (SA-8 and SA-10). Considering the vehicle ± 2 σ perturbations, all mission objectives and requirements will be met with a high level of confidence.

TECHNICAL MEMORANDUM X-53264

May 21, 1965

LAUNCH VEHICLE CONTROL SYSTEMS RESEARCH

By

J. A. Lovingood

George C. Marshall Space Flight Center
Huntsville, Alabama

ABSTRACT

Three areas of launch vehicle control research are discussed: adaptive bending stabilization, adaptive load relief, and a minimax control problem. For each of these problems, factors which motivate the research, specific systems which have been investigated by contractors, and the status of these investigations are presented. In conclusion the future direction of the Aero-Astrodynamics Laboratory's research program is outlined.

TECHNICAL MEMORANDUM X-53221

May 21, 1965

AUXILIARY ESTIMATING FUNCTIONS FOR DOUBLY TRUNCATED NORMAL SAMPLES

By

J. David Lifsey

George C. Marshall Space Flight Center
Huntsville, Alabama

ABSTRACT

When sampling procedures on a random variable X are such that the resulting sample consists of N measured observations for which $X_\alpha < X < X_\beta$, and no information is known for $X < X_\alpha$ and $X > X_\beta$, the sample is said to be doubly truncated at the known terminals X_α and X_β. To calculate maximum likelihood estimates of the mean and standard deviation of a normally distributed population from doubly truncated samples, it is necessary to solve simultaneously a pair of rather complex nonlinear estimating equations. Since every estimate is a function of the sample values and must be regarded as an observed value of a certain random variable, there are no means of predicting in a given case, the true population value assumed by the estimate. The "goodness" of an estimate cannot be judged from individual values, but only from the distribution of the values which it will assume in the long run, i.e., from its sampling distribution. Some estimate of the variance of these sample estimates is needed. Values of auxiliary functions required to obtain, from doubly truncated normal samples, maximum likelihood estimates of parameters of the parent population and the asymptotic (large sample) variances and covariance of these estimates are given.

TECHNICAL MEMORANDUM X-53266

May 24, 1965

LAUNCH VEHICLE GUIDANCE EQUATIONS FOR THE SATURN IB SA-202 MISSION

By

Isaac E. Smith and F. Don Cooper

George C. Marshall Space Flight Center
Huntsville, Alabama

ABSTRACT

This report defines and describes the Launch Vehicle Guidance Equations for the Saturn IB SA-202 mission, to satisfy document #15 of the Apollo Mission Planning and Trajectory Documentation Plan.

TECHNICAL MEMORANDUM X-53268

May 25, 1965

A METHOD OF IMPLEMENTING CUTOFF CONDITIONS FOR SATURN V LUNAR MISSIONS OUT OF EARTH PARKING ORBIT ASSUMING A CONTINUOUS GROUND LAUNCH WINDOW

By

F. Don Cooper

George C. Marshall Space Flight Center
Huntsville, Alabama

ABSTRACT

This report demonstrates a method of implementing cutoff conditions for the Saturn V lunar

mission out of earth parking orbit assuming a ground launch window of four and one-half hours.

TECHNICAL MEMORANDUM X-53245

May 26, 1965

ESTIMATION IN MIXTURES OF POISSON AND MIXTURES OF EXPONENTIAL DISTRIBUTIONS

By

A. Clifford Cohen, Jr.*

George C. Marshall Space Flight Center
Huntsville, Alabama

ABSTRACT

In the analysis of experimental data, many of the distributions encountered are the result of combining two or more separate component distributions. Estimation in these compound or mixed distributions is therefore of particular interest to aerospace scientists. Estimators are derived for the parameters of a compound Poisson distribution with probability density function

$$f(x) = \alpha \frac{e^{-\mu}\mu^{x}}{x!} + (1-\alpha)\frac{e^{-\lambda}\lambda^{x}}{x!}, \quad x=0,1,2,\ldots$$

and for a compound exponential distribution with probability density function

$$f(x) = \alpha(1/\mu)e^{-x/\mu} + (1-\alpha)(1/\lambda)e^{-x/\lambda}, \quad x \geq 0$$

where α is the proportionality factor ($0 \leq \alpha \leq 1$) and where μ and λ are component parameters. In addition to the more general case in which all parameters must be estimated from sample data, several special cases are considered in which one or more of the parameters are known in advance of sampling.

* Professor of Mathematics, University of Georgia, Athens, Georgia. The research reported in this paper was performed under NASA Contract NAS8-11175 with the Aerospace Environment Office, Aero-Astrodynamics Laboratory, Marshall Space Flight Center, Huntsville, Alabama. Mr. O. E. Smith and Mr. J. D. Lifsey are the NASA contract monitors.

TECHNICAL MEMORANDUM X-53271

May 26, 1965

ANALYSIS OF WIND TUNNEL DATA FOR SEVERAL BECKMAN & WHITLEY SERIES 50 AND CLIMET MODEL C1-14 ANEMOMETERS

By

Dennis W. Camp

George C. Marshall Space Flight Center
Huntsville, Alabama

ABSTRACT

This report presents results of wind tunnel test data for several Beckman & Whitley Series 50 and Climet Model C1-14 anemometers. The primary purpose of the wind tunnel testing was the determination of the following two response parameters: the distance constant and the damping ratio of the anemometers.

The dependence of the distance constant on the electronic filter used to filter the output signal of the wind speed sensor is discussed. The importance of the distance constant in measuring the fluctuations of the wind is illustrated by showing how this parameter affects the frequency response curves of the anemometers. The average values of the distance constants were found to be 1.14 m for the Beckman & Whitley Series 50 and 0.73 m for the Climet Model C1-14.

The damping ratio, in agreement with theory, is shown to be independent of wind speed. The values obtained for this parameter were 0.59 for the Beckman & Whitley Series 50 and 0.47 for the Climet Model C1-14 anemometers.

TECHNICAL MEMORANDUM X-53272

May 26, 1965

THE EFFECT OF TRUNCATION ON TESTS OF HYPOTHESES FOR NORMAL POPULATIONS*

By

Britain J. Williams

George C. Marshall Space Flight Center
Huntsville, Alabama

ABSTRACT

The loss of power involved in using the usual tests of hypotheses for complete normal populations when, in fact, the population is a truncated normal one is examined. The technique employed is to obtain an asymptotic expansion of the distribution of sums of samples of size n drawn from a truncated normal population. An electronic computer is then employed to consider enough terms of this expansion to obtain the desired accuracy for the loss function, which is tabulated as a function of selected truncation points and sample sizes.

---

* The research reported in this paper was submitted as a Ph. D dissertation in statistics at the University of Georgia, Athens, Georgia. This research was performed under NASA Contract NAS8-11175 with the Aerospace Environment Office, Aero-Astrodynamics Laboratory, Marshall Space Flight Center, Huntsville, Alabama. Mr. O. E. Smith and Mr. J. D. Lifsey are the NASA contract monitors. The author is currently with the RCA Service Company, Missile Test Project, Patrick AFB, Florida.

TECHNICAL MEMORANDUM X-53273

May 27, 1965

SPACE ENVIRONMENT CRITERIA GUIDELINES FOR USE IN SPACE VEHICLE DEVELOPMENT (1965 Revision)

By

Robert E. Smith

George C. Marshall Space Flight Center
Huntsville, Alabama

ABSTRACT*

This document provides guidelines on interplanetary space, terrestrial space, near-Venus space, near-Mars space, lunar atmosphere and surface, Venus atmosphere and surface, and Mars atmosphere and surface environmental data applicable for Marshall Space Flight Center space vehicle development programs and studies related to future NASA programs.

This report establishes design guideline values for the following environment parameters: (1) meteoroids; (2) secondary ejecta; (3) radiation; (4) gas properties; (5) magnetic fields; (6) solar radio noise; (7) winds; (8) wind shear; (9) clouds; (10) ionosphere; (11) albedo; (12) planetary surface conditions; (13) planetary satellites; (14) composition of the planetary atmospheres; (15) temperature; and (16) astrodynamic constants. Additional information may be located in the references cited.

Extensive use was made of the data prepared by the Planetary Atmosphere Section, ASTD, Space Environment, Manned Spacecraft Center, Houston, Texas, to insure compatibility of both development and study effort between Marshall Space Flight Center and the Manned Spacecraft Center, especially in those areas where there are insufficient data to make definite conclusions.

---

* This document supersedes and should be used in lieu of NASA TM X-53142, September 30, 1964.

TECHNICAL MEMORANDUM X-53275

June 8, 1965

PRELIMINARY SURVEY OF OPTIMUM THRUST LEVELS FOR THE HG-3 HIGH PRESSURE LOX/HYDROGEN ENGINE AS APPLIED TO AN UPRATED SATURN V VEHICLE

By

Emsley T. Deaton, Jr. & Neva H. Huffaker

George C. Marshall Space Flight Center
Huntsville, Alabama

ABSTRACT

Results of a design point survey are presented, determining the optimum thrust levels for the HG-3 engine when used for mission profiles applicable to the Saturn V class of vehicles. The configuration designated MLV-SAT V-3 from the Saturn V Improvement Studies was used for the trajectory analysis, with the J-2 engines replaced by the HG-3 engines in the second and third stages.

A new design point engine was selected with the results of the survey, and trajectory optimizations for appropriate mission profiles were completed for this new engine.

TECHNICAL MEMORANDUM X-53283

June 18, 1965

STATIC LONGITUDINAL STABILITY AND AXIAL FORCE CHARACTERISTICS OF A 4.33-CALIBER BLUNT CYLINDER WITH A 30° SLOTTED FRUSTUM AFTERBODY OVER A MACH NUMBER RANGE OF 0.50 TO 4.96

By

Robert E. Pitcock

George C. Marshall Space Flight Center
Huntsville, Alabama

ABSTRACT

Wind tunnel tests were conducted to determine the static longitudinal stability and axial force characteristics of a proposed Saturn IB camera capsule configuration consisting of a blunt cylinder with a 30° slotted frustum afterbody. Tests indicated this configuration to be statically stable about a center of gravity located 2.43 calibers forward of the base throughout the test Mach number range of 0.50 to 4.96. Maximum stability margin exists at approximately Mach 0.95 with minimum stability margin existing from about Mach number 1.20 to 4.96.

TECHNICAL MEMORANDUM X-53288

June 28, 1965

DETERMINATION OF AERODYNAMIC FORCE AND HEAT TRANSFER PROPERTIES FOR A CONCAVE HEMISPHERICAL SURFACE IN FREE MOLECULE FLOW

By

Clarence Ray Wimberly

George C. Marshall Space Flight Center
Huntsville, Alabama

ABSTRACT

The methods and equations are presented for the aerodynamic force and heat transfer properties of a concave hemispherical surface at an arbitrary angle of attack in free molecule flow. The effect of multiple reflections is taken into account by assuming a cosine distribution after each collision. It is assumed that the emission of molecules from the surface is purely diffuse, and that the reflecting molecules are perfectly accommodated to the surface conditions. The resulting equations are not in closed form, but have been solved numerically for some typical values of the molecular speed ratio and surface-to-ambient-temperature ratio. It is found that under the above conditions the heat transfer characteristics are the same as those of a convex hemisphere. The drag is increased slightly over its counterpart, while the total lift is shown to be very small and would be zero except for interreflected molecules.

TECHNICAL MEMORANDUM X-53289

June 29, 1965

HARDWARE AND GUIDANCE SCHEME ERROR ANALYSIS FOR SA-202 EVALUATED AT S-IVB CUTOFF

By

P. D. Brandon

ABSTRACT

This technical memorandum presents the inaccuracies in velocity and displacement of the Saturn IB SA-202 vehicle at S-IVB stage cutoff caused by hardware and guidance scheme errors. The hardware errors include such effects as stabilized platform drift and accelerometer measurement inaccuracies.

B. PRESENTATIONS

SPHERICAL BALLOON WIND SENSOR BEHAVIOR

By

James R. Scoggins

ABSTRACT

Response characteristics of freely rising superpressured spheres of different configurations are discussed. Wind profile data measured by the superpressured balloon method, the smoke trail method, the AN/GMD-1 rawinsonde system, and from low-level oper-air tests were used in the analysis. Results are reported on data measured at Huntsville, Alabama, at night during stable conditions to an altitude of 120 m and at Cape Kennedy to an altitude of 12 km. The results show that: (1) the average drag curve for a freely rising 2-m diameter, smooth superpressured sphere differs considerably from the drag curve obtained in wind tunnels using smaller spheres; the average value of the drag coefficient is larger over all Reynolds numbers except near the transition region; (2) the drag coefficient for roughened spheres is nearly independent of the Reynolds number but decreases slightly as the Reynolds number decreases; (3) the addition of surface roughness elements reduces the aerodynamically induced horizontal motions of the smooth sphere; and (4) the average aerodynamic lift force, which acts primarily in the horizontal direction and is responsible for the aerodynamically induced horizontal motions, is negligible indicating that it does not act in any preferred direction.

SUMMARY OF SATURN I BASE THERMAL ENVIRONMENT

By

Robert G. Payne and Ira P. Jones, Jr.

ABSTRACT

Research and development flights of the Saturn I have established the base thermal environment of eight-engine LOX/RP-1 propelled vehicles. Plume radiation levels, total heating rates, and base gas temperatures have been measured on the first stage of the Block I and II vehicles. Also some heating data were obtained for the six-engine LOX/LH_2, S-IV second-stage base. Discussion of flight instrumentation, data reduction techniques, and evaluation problems is presented along with a correlation of the flight results to both long and short duration model tests. Maximum base heating rates occurred at liftoff for both total and radiation heating with a lower secondary peak occurring when the reverse flow from the inboard engines became choked. Maximum flame shield total heating rates were approximately three times (75-100 W/cm^2) the heat shield values for the S-I base. Base gas temperatures varied widely with maximum values of 1300°K for the heat shield and 2100°K for the flame shield. Block II flight data for the S-I stage were generally lower than the Block I results. S-IV stage base heat rates varied with radial distance from the center and flight time from 2 to 0.5 W/cm^2 and agreed well with short duration model tests results.

Orbital Tracking and Decay Analysis of the Saturn I Flights. H. F. Kurtz, Jr., Chief, Operations Studies Branch, M. Naumcheff, Chief, Orbit Determination Section, and A. R. McNair, Chief, Mission Studies Section, Marshall Space Flight Center, Huntsville, Alabama.

The successful skin-tracking of the first three Saturn I orbital flights by a network of FPS-16 and FPQ-6 radars is discussed, and the effective atmospheric drag force acting on the orbiting vehicles is presented as determined through use of the radar data for orbit determination. The feasibility of skin-tracking the Saturn vehicle in orbit was proven on the flight of SA-5, the first Saturn I orbital vehicle. Skin-track data has since reliably been obtained on vehicles SA-6 and SA-7. Error characteristics of the data are presented, which show it to be of comparable quality to that obtained with beacon tracking by the same radars. The root-mean-square of the gross error residuals obtained during orbit determinations using the skin-track data averaged about 30 m in slant range and 0.03 degrees in the azimuth and elevation angles. Atmospheric drag data derived from the orbit determinations are presented, with a discussion of the methods used. The data show current atmospheric density values and drag characteristics of the Saturn vehicles, and lead to an increase in the accuracy and confidence of orbital lifetime predictions for such vehicles.

Presented to AIAA, Huntsville, Alabama, February 15 - 17, 1965.

ON THE CALCULATION OF DYNAMIC STABILITY DERIVATIVES FOR POINTED BODIES OF REVOLUTION IN SUPERSONIC FLOW

By

Max F. Platzer
NASA, George C. Marshall Space Flight Center

and

Gilbert H. Hoffman
Lockheed Missiles and Space Company
Huntsville, Alabama

ABSTRACT

This paper reviews two linearized approaches to calculate the dynamic stability derivatives of slowly oscillating pointed bodies of revolution in supersonic flow, namely, (a) a generalized Karman-Moore approach and (b) a generalized Adams-Sears approach.

The Karman-Moore approach is a purely numerical method, whereas Adams-Sears' quasi-slender body theory leads to analytical closed form solutions for the stability derivatives. Four configurations are investigated in more detail, the cone, the convex and concave parabolic ogive and a typical reentry body. Comparison with other theories and experiment is made, thus giving an insight into the range of applicability of both theories.

Presented at Second Technical Workshop on Dynamic Stability Testing, Arnold Engineering Development Center, Tullahoma, Tennessee, April 21 - 23, 1965.

ON LINEARIZED COMPRESSIBLE FLOW OVER PULSATING AND OSCILLATING BODIES

By

M. F. Platzer

ABSTRACT

The paper presents a new and unified approach to the calculation of linearized sub- and supersonic flow over pulsating and oscillating low aspect ratio bodies extending K. Oswatitsch's and F. Keune's theories for steady flow to these unsteady flow cases.

It is shown that the sub- and supersonic flow over low aspect ratio wings at zero angle of attack, whose skin executes symmetric pulsations, is in a first approximation given by two terms; namely, a crossflow and a spatial influence. This spatial influence reduces the flow around pulsating wings to the flow around the equivalent pulsating body of revolution. A similarly characteristic structure of the flow field is found also for the higher order flow terms for both pulsating and oscillating flow. To examine its range of validity this approximation theory is applied to configurations for which exact solutions of the unsteady linearized potential equation can be found. Such exact solutions do exist for the infinitely long tube and ribbon exhibiting a harmonic standing pulsation or oscillation and the paper discusses these solutions in more detail. Furthermore, the slowly oscillating body of revolution is studied by investigating three different body configurations; namely, a cone, a convex parabolic ogive and a concave parabolic ogive. The stability derivatives are evaluated and compared with results from other theories.

Presented at the 7th International Aeronautical Congress, Paris, June 14 - 16, 1965.

SOME RESULTS OF AN ANALYTICAL AND EXPERIMENTAL INVESTIGATION TO DETERMINE HEAT TRANSFER IN THE NOZZLE OF SOLID PROPELLANT ROCKET MOTORS

By

Ewell Roger Heatherly

ABSTRACT

The combustion chamber of a solid propellant rocket motor contains a mixture of fuel and oxidizer in solid form arranged in a pattern to produce a nearly constant chamber pressure and temperature during the firing period. The firing duration is a function of amounts and types of fuel, oxidizer, and additives, as well as grain size and configuration of the combustion chamber and the nozzle.

The nozzle controls the quantity of gas flow and guides the thrust. Since the gas temperature is above the values for which metals retain their structural integrity, some provision must be made to cool the

nozzle. In general, there are three basic methods of cooling nozzles which are functions of the firing duration. For a very short duration of firing, the heat sink method of thermal protection is used, taking advantage of transient heat transfer. For a moderate length of firing, an ablative nozzle may be used. The heat is carried away by actual sublimation, melting, evaporating, or charring of the surface of the nozzle. The ablation products tend to act as a buffer layer for areas downstream, similar to transpiration cooling. For long firing durations, transpiration cooling may be used.

The design of solid propellant motors is dependent on an accurate prediction of the nozzle wall heat flux. The heat flux into the nozzle wall or surface of the protective layer is a function in various degrees of the following:

1. Physical properties of gas constituents.
2. Chemical kinetics during expansion.
3. Metal additives in the propellant.
4. Local flow pattern and properties in the nozzle.
5. Boundary layer thickness and growth.

The prediction of the heat transfer to the heat sink nozzle wall is especially complicated in that it requires some knowledge of the accumulation of metal oxide on the walls (aluminum, in this investigation), which increases resistance to heat flow to the nonablative nozzle.

In the present study, which employs both experimental and analytical methods, a mathematical model is developed for the heat sink nozzle which combines the heat transfer due to convection, conduction, and radiation and also includes the heat flow resistance due to the oxide layer. Ten subscale solid propellant motors were test fired to obtain experimentally the nozzle temperatures which verified the theoretical temperatures computed by use of the mathematical model. Computer programs were used to predict nozzle temperature, heat transfer coefficient, resistance to heat flow due to oxide deposit, and gas properties. The selection of the proper technique for each mode of heat transfer required a literature search and an evaluation of the relative merits of various methods of study.

Although at first the closed form heat conduction solutions already available [1,2,3] were considered, these were subsequently discarded because the tests showed that the boundary conditions were dependent on time. An available numerical computer program capable of creating a wide variety of boundary conditions has been outlined in Chapter II-A and was chosen for use in this analysis.

Several empirical methods [4-9] were available for estimating the coefficient of convective heat transfer, but these were found to be insufficient to describe the details of the environment to which the nozzle was subjected. Bartz and his co-workers [10-14] solved the integral boundary layer momentum and energy equations to produce nozzle convective heat transfer relations. Because of its wide use in industry and good correlation with test data, this method was used in the calculations.

The contribution of radiative heat transfer to the nozzle heating problem is generally small in comparison to that of convective heating. References 15 through 18 are used in the present study to calculate the radiative heat transfer due to the aluminum oxide particles and the products of combustion.

Presented in partial fulfillment for M.S. at the University of Alabama, Tuscaloosa, Alabama, June 1965.